**UNIVERSIDAD POLITÉCNICA DE MADRID**
**ESCUELA TÉCNICA SUPERIOR DE INGENIERÍA AERONÁUTICA Y DEL ESPACIO**


# Development of elastic wave propagation techniques for Structural Health Monitoring

## D O C T O R A L  T H E S I S

Submitted for the degree of Doctor by:

**Fernando Sánchez Iglesias**
Master Universitario en Sistemas Espaciales

Madrid, 2025


UNIVERSIDAD POLITÉCNICA DE MADRID
ESCUELA TÉCNICA SUPERIOR DE INGENIERÍA
AERONÁUTICA Y DEL ESPACIO

**Doctoral Degree in Aerospace Engineering**

# Development of elastic wave propagation techniques for Structural Health Monitoring

## D O C T O R A L  T H E S I S

Submitted for the degree of Doctor by:

**Fernando Sánchez Iglesias**
Master Universitario en Sistemas Espaciales

Under the supervision of:
Dr. Antonio Fernández Lopez

Madrid, 2025

Title: Development of elastic wave propagation techniques for Structural Health Monitoring

Author: Fernando Sánchez Iglesias

Doctoral Programme: Doctorado En Ingeniería Aeroespacial

Thesis Supervision:

Dr. Antonio Fernández López, Profesor Titular de Universidad, E.T.S.I. Aeronáutica y del Espacio (Supervisor)

External Reviewers:

Thesis Defense Committee:

Thesis Defense Date:

*A Julia.*

# Acknowledgement

Firstly, I wish to remark my gratitude to my family and friends, whose unwavering support, patience, and encouragement have been a constant source of motivation.

I am also thankful to Airbus for aiding with the environment used to carry out some of this work; the assistance of the Getafe HPC team was instrumental for the FEM simulations. Special thanks go to my Airbus colleagues and peers: Jaime, Rubén, Rosa, Eduardo, and many others, for their collaboration, discussions, and shared experiences, which enriched this project and made the process enjoyable.

And finally, I would like to express my gratitude to Antonio, whose guidance, knowledge, and support have been invaluable throughout this project. His ideas, feedback, and, of course, discussions and difference of opinions, encouraged me to refine my work and achieve the best possible outcome.

# Abstract

Simulation of elastic wave propagation is crucial for the development of an accurate structural monitoring system. The high cost and complexity of experimental tests and the great causality that exists in the damage that light-weight structures can suffer highlight the importance of simulations, and especially in composite material structures in which certain types of damage such as debondings or delaminations can go unnoticed in routine visual inspections.

This thesis explores the development of a methodology for analyzing the propagation of elastic waves in thin-walled structures. A multipurpose, efficient, and scalable development is proposed, so that it can cover multiple use cases, service conditions, position, and types of damage. With the final objective of being able to limit the experimental task to a few validation cases.

To achieve this objective, an extensive literature review and an evaluation of the most widely used simulation methods have been proposed. Likewise, emphasis has been placed on the analysis of numerical methods such as finite elements and based on this a new methodology based on ray tracing has been designed.

Ray tracing is a method of calculating the propagation of waves through a medium in which regions of different propagation speeds, absorption characteristics, and reflective surfaces may exist. Under these circumstances, wavefronts can bend, change direction, or reflect off surfaces. Currently the method is widely used in problems of electromagnetism, oceanic acoustics, or more recently in computer graphics rendering and, therefore, this thesis considers the use of this methodology for the calculation of wave propagation in thin-walled structures of application aeronautics.

The results obtained demonstrate the effectiveness of this method in calculating wave propagation, considering transmission, reflection, and damping in both metal and composite material structures.

Taking into account representative structural details such as changes in thickness or stiffeners, a series of representative laboratory case studies of metallic and composite aeronautical structures have been analyzed. Likewise, the possibility of predicting the possible effect that the presence of damage or imperfections in the structure may have on the signal was verified using added masses and verified against real damage from impacts.

The developed methodology has been contrasted with other simulation methods such as finite elements. Thus, comparable or even more precise results have been obtained in some cases, which have improved their computing time by several orders of magnitude. Based on the above, this methodology demonstrates its suitability and application possibilities for training artificial intelligence systems.

# Resumen

La simulación de propagación de ondas elásticas es crucial para el desarrollo de un sistema preciso de monitorización estructural. El alto coste, complejidad de ensayos experimentales y la gran casuística que existe en los daños que pueden sufrir las estructuras ligeras ponen de manifiesto la importancia de realizar simulaciones, principalmente, en estructuras de material compuesto en las que ciertos tipos de daño como despegados o de laminaciones pueden pasar desapercibidos en inspecciones rutinarias.

Por medio de la presente tesis, se plantea el desarrollo de una metodología de análisis de propagación de ondas elásticas en estructuras de pared delgada. Se plantea un desarrollo multipropósito, eficiente y escalable, de modo que pueda cubrir múltiples casos de uso, condiciones de servicio y posición y tipo de daños. Con el objetivo final de poder limitar la tarea experimental a unos pocos casos de validación.

Para lograr dicho objetivo, se ha planteado una extensa revisión literaria y una evaluación de los métodos de simulación más usados. Asimismo, se ha hecho énfasis, en el análisis de métodos numéricos tales como los elementos finitos y en base a esto, se ha diseñado una metodología nueva basada en el trazado de rayos.

El trazado de rayos es un método para calcular la propagación de ondas a través de un medio en el que pueden existir regiones de diferentes velocidades de propagación, características de absorción y superficies reflectantes. En estas circunstancias, los frentes de onda pueden curvarse, cambiar de dirección o reflejarse en las superficies. Actualmente el método es ampliamente utilizado en problemas de electromagnetismo, acústica oceánica o más recientemente en renderizado de gráficos por ordenador y por ello, esta tesis se plantea el uso de esta metodología para el cálculo de la propagación de ondas en estructuras de pared delgada de aplicación aeronáutica.

Los resultados obtenidos demuestran la eficacia de este método en el cálculo de propagación de ondas, considerando transmisión, reflexión y amortiguamiento tanto en estructuras metálicas como de material compuesto.

Teniendo en cuenta detalles estructurales representativos como cambios de espesor o rigidizadores, se han analizado una serie de casos de estudio de laboratorio representativos de estructuras aeronáuticas metálicas y de material compuesto. Del mismo modo, se verificó la posibilidad de predicción del posible efecto que pueda tener en la señal la presencia de daños o imperfecciones en la estructura usando masas añadidas y verificando contra daños reales de impactos.

La metodología desarrollada se ha contrastado con otros métodos de simulación como los elementos finitos. Así, se ha obtenido resultados comparables o incluso más precisos en algunos casos mejorando en varios órdenes de magnitud su tiempo de computación. Por lo expuesto, esta metodología demuestra su idoneidad y sus posibilidades de aplicación para entrenamiento de sistemas de inteligencia artificial.

# Table of Contents

# List of Figures

# List of Tables

# Abbreviations and acronyms

**AD** Accidental Damage

**AI** Artificial Intelligence

**ANN** Artificial Neural Network

**BC** Boundary Condition

**BEM** Boundary Element Method

**BVID** Barely Visible Impact Damage

**CAD** Computer-Aided Design

**CBM** Condition Based Maintenance

**CNN** Convolutional artificial Neural Networks.

**CFRP** Carbon Fiber Reinforced Plastic

**DAQ** Data AcQuisition system

**DSF** Damage Sensitive Feature

**ED** Environmental Damage

**EM** ElectroMagnetic

**EOC** Environmental and Operational Condition

**EW** Elastic Waves

**FBG** Fiber Bragg Grating

**FD** Fatigue Damage

**FEA** Finite Element Analysis

**FEM** Finite Element Method

**FFT** Fast Fourier Transform

**HPC** High Performance Computing

**IC** Initial Condition

**IoT** Internet of Things

**ML** Machine Learning

**MRO** Maintenance, Repair and Overhaul

**NDI** Non-Destructive Inspection

**NDE** Non-Destructive Evaluation

**NDT** Non-Destructive Testing

**OD** Operational Damage

**ODE** Ordinary Differential Equation

**PDE** Partial Differential Equation

**PIML** Physiscs-Informed Machine Learning

**PWM** Pulse-Width Modulation

**PWVD** Pseudo Wigner-Vile Distribution

**PZT** Lead zirconate titanate

**RID** Reduced Interference Diagram

**ROM** Reduced Order Model

**RPAS** Remote Piloted Aerial System

**SAFE** Semi-Analytical Finite Element

**SCC** Stress Corrosion Cracking

**SEM** Spectral Element Method

**SFEM** Stochastic Finite Element Method

**SHM** Structural Health Monitoring

**SNR** Signal to Noise Ratio

**STFT** Short Time Fourier Transform

**STMM** Stiffness Transfer Matrix Method

**TFD** Time–Frequency Distribution

**TFR** Time–Frequency Representation

**TMM** Transfer Matrix Method

**ToF** Time of Flight

**UAV** Unmanned Aerial Vehicle

**UPM** Universidad Politécnica de Madrid

**UV** UltraViolet

**WFD** Widespread Fatigue Damage

**WVD** Wigner-Vile Distribution

# Chapter 1

# Introduction

## 1.1 General

Aircraft structures, like all mechanical systems, are constantly exposed to various external factors that impact their service life. Loads and environmental conditions are among the key contributors to the degradation of aircraft components. Regular inspections or automated data collection are essential for tracking the structural health of critical components. This research presents several targeted solutions for the structural health monitoring (SHM) of aircraft components to help identify and detect structural deterioration.

Carbon Fiber Reinforced Plastic structures are widely used in various industries: aerospace, automotive, sports equipment, and civil engineering because of their high strength-to-weight ratio and other desirable mechanical properties, and their usage has increased dramatically in recent years. Thanks to improvements in the structural analysis discipline, an engineer can ensure that they meet their respective safety, performance, and durability requirements in their intended applications; crucial for industries such as aerospace where lightweight, high-strength materials are essential for achieving optimal performance and efficiency.

However, even when they present all these significant advantages, lightweight composite structures may require special attention because, unlike traditional metallic structures, they are subject to a much wider range of failure modes specific to them, such as delaminations, fiber breakage, matrix cracking, and impact-induced damage (Guinard et al., 2002; X. Li et al., 2019; Tuo et al., 2019; J. Wang et al., 2017), some of which may be difficult to assess by visual inspection. Therefore, new and affordable systems must be developed to study the performance of these structures in service.

In this framework, SHM could perform a crucial function, employing various sensing technologies, data acquisition systems, and signal processing techniques to monitor the structure periodically or in real time. There are two primary approaches in the field of SHM: data-driven and model-driven (*Guidelines for Implementation of Structural Health Monitoring on Fixed Wing Aircraft*, 2021). Data-driven methods are supported directly on structural data, from which they can deduce the normal operational state of a structure, typically using machine learning processes. On the other hand, model-driven methods use simulations to determine

the health condition of a structure by directly comparing the predictions of the models with the actual structural information taken from the sensors (Barthorpe, 2010).

The extraction of damage-sensitive features from the structure and the analysis of these features can be used to detect, quantify, and determine the location and severity of damage, and, in addition, the system could be used to capture real-time events and evaluate them (Seno et al., 2019), or even be able to even consider the effect of corrosion (Wu et al., 2023) and environmental factors (García Alonso, 2016).

To achieve this, the system must be fed with data from a sensor network which must be permanently installed in the structure. There are many types of sensors currently available in the industry, one of the most common are piezoelectric (i.e. PZT) sensors or FBG that are based on ultrasonic inspections, which have historically proven to be a reliable and inexpensive way of evaluating manufacturing defects or in-service damages, and are ideal for lightweight structures, as elastic waves can travel large distances with very low attenuation and are very sensitive to typical damages of interest (Ostachowicz et al., 2009).

Therefore, a significantly complex structure could be inspected with a very small number of sensors (Farrar and Worden, 2006; Qing et al., 2019); employing elastic waves with a distributed piezoelectric actuator/sensor network based on the pitch-catch method has proven to be very successful for impact damage detection (Charles H. Keilers and Chang, 1995; Lin et al., 2001) and even for other nontypical damages such as crack and corrosion localization (Zhao et al., 2007). These SHM systems could present many cost advantages compared to traditional inspection methods and could also be used to improve the life prediction of the structure based on its usage (Farrar and Worden, 2006; Fernández López, 2009).

Having the ability to extract the relevant damage identification parameters and achieve the objective of these systems still requires a significant effort, in terms of signal analysis and interpretation (Aloisio et al., 2020; Mendler et al., 2021) and must be supported by relevant test experience. However, due to the high cost of physical tests, numerical simulation can be especially helpful in predicting the propagation of elastic waves and may help improve the accuracy of these systems (de Luca et al., 2018). These data-driven methods, also called physics-informed machine learning systems, are an emerging methodology that can also significantly aid in the interpretation of SHM data. The basic idea consists of combining physics-based models with data-driven ones, taking advantage of both to improve predictive capacity in an SHM setting (Cross et al., 2021).

Numerical simulations provide a very effective way to capture and understand the structural behavior in terms of elastic wave response; general purpose computational codes such as time domain spectral finite element methods (Kudela et al., 2018a, 2018b) or explicit finite element methods (de Luca et al., 2018; F. Li et al., 2018; Ong et al., 2016; Sánchez Iglesias and Fernández López, 2020) are commonly used to calculate the wave propagation, and have proven to be a useful tool when used for training of a physics-informed machine learning model (Svendsen et al., 2023).

However, along with other significant drawbacks, these methods tend to be computationally intensive, especially for large and complex structures. Long computation times and high memory requirements may limit their efficiency and are usually not suitable for real-time or

iterative analyses.

For these reasons and also to increase the reliability of simulations, there have been multiple attempts to solve the problem without resorting to finite elements in the literature, either analytically (Chiappa et al., 2021; X. He et al., 2022; K. B. Kim et al., 2022) or using statistics or artificial intelligence (Buckley et al., 2022; Nguyen et al., 2019); some of these methods are able to achieve very good results, but the algorithms studied tend to be too complex to generalize or limited in applicability.

Therefore, this thesis presents an attempt to implement this ray-tracing methodology to solve the elastic wave propagation problem. The implementation is validated against a battery of physical tests and other numerical methods, and it explores the possibility of using this method for the development of physics-informed AI for SHM systems.

## 1.2 Objectives

This thesis places its focus on the applicability of SHM techniques in the aerospace sector, starting from the state-of-the-art of the technology, mainly in the field on guided elastic waves measured with piezoelectric transducers.

The objective of this thesis relies on the development and implementation of a structural integrity monitoring system based on a dense network of distributed sensors that can support early detection of defects, thus reducing maintenance costs and time. This system will be based on the following lines of research:

- Study of the elastic wave propagation over complex structures and the possible effect of structural details on the propagation and modes.
- Analytical study of a simplified wave propagation model capable of considering these effects and validation of said model through finite element simulations and physical tests.
- Evaluation of the influence of damage on elastic waves: its effect on the different modes of propagation, the energy dissipated and the detection capacity of the system, the effect will be evaluated both by analysis and experimentation.
- Development of analytical compensation methods for geometric effects, such as changes in thickness or curvature and/or environmental effects that may affect wave propagation to be implemented in the analytical model.

Furthermore, to achieve these objectives, the development and testing of a data processing methodology using artificial intelligence techniques is explored, to identify and locate structural damage. The deployment of a neural network-based data processing model, trained with experimental and theoretical results, would facilitate the classification of the origin of the damage, its location within the structure, identification of the affected area, and assessment of the impact on the safety of the aircraft. Additionally, a series of physical tests is proposed to progressively validate the system properties and to verify finite element models and analytical methods. These tests will explore wave propagation characteristics across various typical

geometries of aeronautical structures made of metallic and composite materials, including the following:

- Thickness changes and variable thickness.
- Curvature and changes in curvature.
- Stiffening elements (stringers, frames...).
- Boundary conditions, free edges, etc...
- Representative damages, present in the structure and comparison with intact structure.

These tests can also be used to evaluate the specific damages of the composite material (delaminations, porosity, etc.) and its effect on the different modes of propagation, extracting representative damage characteristics to be able to tune the numerical model in order to represent them.

The numerical model should be able to accurately represent the wave propagation efficiently, but also it must be suitable to bridge some significant problems detected in other numerical methods such as finite elements or spectral elements, summarized as follows:

- Computational complexity: numerical methodologies tend to be computationally intensive, especially for large and complex structures. Long computation times and high memory requirements may limit their efficiency and are usually not suitable for real-time or iterative analyses.
- Grid or element discretization: discretizing the structure into grids or elements may result in some loss of accuracy, difficulties in capturing fine details, or aliasing effects on high frequencies. The choice of grid or element size can affect the accuracy and computational cost of the analysis and is usually a limiting factor for the maximum scale of structures to be analyzed. In the case of explicit finite element methods, signal aliasing limits the maximum element size to a very small magnitude, typically on the order of one millimeter, needing millions of elements in order to study a standard aeronautical component.
- Material damping or boundary damping: Introducing damping elements, either as dashpots or material damping, significantly increases the algorithm complexity, making it exponentially more costly to solve problems where this effect is relevant to the solution.
- Curvature, boundaries, or non-uniform material properties may be difficult or nearly impossible to model with spectral elements due to the complexity of the analytical formulation.

To achieve these objectives, a simulation methodology for the propagation of elastic waves based on the ray-tracing method is proposed; the ray-tracing method simulates the elastic wave propagation by projecting rays from a source, calculating their interactions with surfaces, and evaluating reflection and diffraction. This can predict how elastic waves behave in complex environments by evaluating the acoustic behavior of the component with a significantly low computational cost.

This methodology will be studied and validated against the set of tests on characteristic aeronautical structures described above, both metallic and composite materials, taking into account structural details such as changes in thickness or stiffeners. These tests will consider the presence of real and simulated damage.

Additionally, for a new method to be widely adopted, it must show clear benefits compared to existing approaches; therefore, a comparative study is also proposed between the developed ray-tracing methodology and other conventional numerical methodologies such as finite elements to evaluate factors like computational time, resource efficiency, and ease of implementation. If the ray-tracing method yields similar or better results than these other well-established methods, it will enhance its credibility and validate and promote the use of the method.

### 1.2.1 Thesis structure

To effectively implement the objectives outlined in the previous section, the study presented in this thesis is structured around three distinct approaches or profiles. Each of these approaches has been carefully developed to address various aspects of the research goals, providing a comprehensive framework for exploring the subject matter.

The first profile is theoretical; it addresses the scientific field that supports the thesis, the objectives and the necessary resources to accomplish them, placing an emphasis on the ray-tracing method and its theoretical background and consistency, but also comparing the methodology with others that are also used to solve the same problem in the literature. This profile also includes the definition and planning of the test in order to obtain valid experimental data, the setup and design of the numerical FEM models used to support the validation, and the subsequent processing of all of these data.

The second profile is experimental; it focuses on the tests carried out to adjust and validate the methodology, hardware, software, and processes developed that complement the required use. The objective of this profile is to obtain useful experimental information that supports the theoretical analysis and validates the methodology.

The third profile is operational. In this part, it is verified, using both theoretical support and experimental data, that the proposed models fulfill their function with verifiable accuracy.

All of this content is organized into the following six main chapters.

1 **Introduction:** Presents the motivation, objective, and conceptual definitions used in the thesis.

2 **State of the art:** Contains an in-depth study of the current and past technological developments in the field of structural health monitoring, specifically in elastic wave simulations and the ray-tracing methodology.

3 **Materials and methods:** This chapter presents the experimental framework, the FEM simulations performed, the theoretical basis and implementation of the ray-tracing methodology used in the thesis and the validation and verification strategy of the method.

4 **Results:** The ray-tracing methodology is evaluated against the tests and FEM simulations for the test cases described and the results from each method is shown and compared.

5 **Discussion:** A discussion of the accuracy and applicability of the results is presented, discussing the main advantages and limitations of the methodology and comparing them with other methods present in the literature.

6 **Conclusions:** The main conclusions derived from the study are presented and supported, along with a series of suggestions that may be helpful in orienting future studies on this topic.

In addition, five more complementary sections or annexes are added to the thesis to support the study and conclusions.

### 1.2.2 Resources

This thesis is carried out in the composite materials unit (CCMSS) of the department of Materiales y producción Aeroespacial of Escuela Técnica Superior de Ingeniería Aeronáutica y del Espacio.

The laboratory has everything necessary to carry out the tests and subsequent analysis and data processing, including:

Sensors:

- FBG sensors to obtain the deformation field of the structure.
- Piezoelectric PZT transducers for the generation of elastic waves and correlation of results from FBGs.
- Strain gauges to measure static deformation.
- Thermocouples for temperature measurement.

Data acquisition equipment:

- Optical Backscatter Reflectometer (OBR) for FBG sensors.
- Data acquisition cards (DAQ) for piezoelectric transducers.

Computers to control data acquisition, processing and generation of models, with the necessary software environments for these tasks:

- The Mathworks, MATLAB for data acquisition and information processing.
- FEM software (Nastran / Abaqus / RADIOSS) for the explicit simulation of wave propagation and validation of the tests and methodology to be developed.

Manufacturing and instrumentation of components and representative parts for testing; in metal and composite material.

## 1.3 Design of aeronautical structures. General concepts

Through history, aeronautical design has continually evolved guided by two premises: the first is structural weight savings, since lower weight will improve load capacities and reduce fuel consumption (and therefore costs), improving the operational profitability of aircrafts. The second is the high demand for safety and reliability, a primary and nonnegotiable requirement within air transport. The importance of structure in the design of an aircraft is such that most of the advances that have occurred in aeronautics in the last 40 years are inextricably linked to advances in materials and new structural designs and to advances in power plant design (Arnaiz, 2002; Niu and Niu, 1999).

The current state of aeronautical structural design is based on the use of composite materials on a monolithic design of semi-monocoque structures (Figure 1.1). The integrity of the structure is proven by resistance, rigidity, fatigue behavior, damage tolerance, and a maintenance plan based on these criteria, especially those of tolerance to damage (Donaldson, 2008). Thus, at a structural level, the biggest changes in recent times have been introduced by the material, whose characteristics have a marked influence from the preliminary design to the maintenance process, including manufacturing (Megson, 2007).

**Figure 1.1:** A350 section 19 hybrid composite structure (Fualdes, 2016)

At this point, where current design approaches have reached maturity, some of the new aeronautical design proposals tend to try to adopt certain solutions based on nature, arguing that thousands of years of evolution can provide valid solutions to certain problems. This reasoning is common in other branches of science, and in the field of structures, architecture is the branch that has tried the most to use structural mimicry, improving structural and environmental performance. In aeronautics, it could already be considered that the microstructure of composite materials is similar to the structure of plants, such as bamboo, in which rigid materials are combined with the function of supporting loads and others with the function of distributing them uniformly, similar to what the fibers and the matrix would be.

The new generation structures, which introduce a greater degree of mimicry, are known as 'intelligent structures'. Intelligent structures are those that adopt some traits typical of human beings, those that can condition their functions as a structure, that is, maintain structural integrity so that they can perform the function assigned to them in the most efficient way possible. In this way, an intelligent structure is expected to be able to sense-measure the conditions of its environment (which in human beings would correspond to the nervous system), to evaluate it autonomously (for which both preset responses and as those learned in similar situations) and respond appropriately to it, normally warning of the situation so that an external agent can act appropriately or reacting the structure itself through actuators coupled or integrated to it (corresponding to the motor system in the body). In addition, if necessary, structures could allocate their own resources to repair themselves, although this has only been achieved to a very limited extent in living beings (Fernández López, 2009).

## 1.4 Maintenance of aeronautical structures

Since the beginning of aviation, aeronautical design has evolved from the design of elements with 'unlimited life' to the present day with techniques based on maintenance and reliability plans. Maintenance Repair and Overhaul (MRO), as an inherent part of the design, has been adapted according to the conditions imposed by costs and materials at all times (Vieira and Loures, 2016).

The supply chain of the aerospace industry is highly complex. Every aircraft component must be certified by airworthiness authorities, which impose strict standards to ensure safety. Given the rigorous requirements for supplier qualification, only a small number of companies are authorized to provide parts and services within the industry (Bales et al., 2004). This constraint limits the options available when selecting suppliers for new aircraft programs, reducing the ability to negotiate favorable commercial terms. Furthermore, many system suppliers operate across different sub-tiers, making them suppliers to their competitors, which can strain relationships and potentially affect the end customer.

Currently, a maintenance program must meet the following objectives derived from the historical evolution that aircraft maintenance and operation have undergone.

- Detect deterioration before it can affect airworthiness or require repairs that could have significant economic consequences. Maintain the levels of reliability (economy) and safety inherent in the original design. Today, inspections are determined by the time interval between detectable damage and critical damage (unable to withstand the load limit).
- Restore safety and reliability when the level has deteriorated.
- Obtain the necessary information to improve the design if reliability is not adequate. Determine the threshold intervals from which inspections must be performed and the type of inspection.
- Obtain these objectives with the minimum total cost, including the cost of maintenance and residual failures.

To achieve these purposes, two types of maintenance work can be differentiated:

- **Scheduled:** it refers to any maintenance task assigned on a regular schedule. This could be a reoccurring or one-time task. Scheduled maintenance usually occurs regardless of if the asset is in need of repairs. This is because part of the point of a maintenance schedule is to reduce the amount of repairs and downtime of the equipment needed.

  Scheduled maintenance tasks are designed to optimize the amount of time required to keep the plant operating. allowing more resources to be allocated and preventing equipment failures.

- **Unscheduled:** Born from abnormalities found during operation or maintenance. It is any maintenance task that is needed unexpectedly or is the result of a mechanical or structural failure that was not anticipated.

Structural maintenance will be based on the following parameters for the calculation of maintenance indexes. These indexes attempt to objectively assess the difficulties in detecting damage to the structure (Fernández López, 2009):

- Distance to the item to be inspected (Access Index).
- Existing structural and systems congestion in the area (Access Index).
- Size of the area to be inspected (Practicability index).
- Lighting available (condition index).
- Surface condition (condition index).

The knowledge of the state of the structure that the SHM provides us primarily results in its maintenance. If the SHM operated with high reliability, the evolution of the current maintenance philosophy would be evident, from the current one based on inspections every certain number of flight hours, in which the inspection of the structure and pertinent repairs are carried out, to a maintenance system based on the real state of the structure, given by the network of integrated sensors, which would degenerate into stoppages solely for the repair of the structure.

This may be one of the biggest problems and risks that the development of SHM has: although it may seem obvious, since we are surrounded by examples of this type of operation (in fact, we ourselves are), it means a radical change with the techniques of design used to this day, since in addition to providing solutions, it introduces new problems not necessarily related to the monitoring system. In aeronautical design, where the guarantee of safety is an indispensable condition, the main application of SHM techniques is as a structure inspection tool which, unlike current ones, is integrated into the structure itself. This is why it is necessary to investigate more in-depth the characteristics of aeronautical maintenance (Staszewski et al., 2003).

## 1.5 Monitoring a structure

Boller and Buderath, 2007 define structural monitoring as ensuring structural integrity regardless of the type of plant and its structure, differentiating the parameters that must be measured to do so. There are a multitude of structures that may be monitored, such as civil or naval structures. AS stated previously, this thesis will focus on the aerospace industry, specifically commercial aircraft.

Both metallic and composite aircraft structures can present in-service conditions and failure modes that are generally complex and may not be accurately predicted in the design phase. Due to this, the aerospace industry typically uses conservative statistical tools based on predicted time or usage patterns to determine scheduled maintenance procedures (Aktepe and Molent, 1999). These procedures are usually overly time-consuming, labor intensive, and in some cases very expensive. In addition to this, as structures age, maintenance service frequency and costs have to increase as performance and availability decrease significantly.

Monitoring a structure consists of observing via specialized equipment the evolution of one or many physical parameters of a structure in order to detect possible abnormalities. The correct behavior of a monitoring system implies a measurement of all inputs that can affect the structure being monitored in addition to the response of the said structure to these inputs (Glisic and Inaudi, 2003). With this information, the system may suggest decisions to be taken in order to operate the structure in a set of limits for safety and efficiency. The basic elements of any general monitoring system are shown in Figure 1.2.

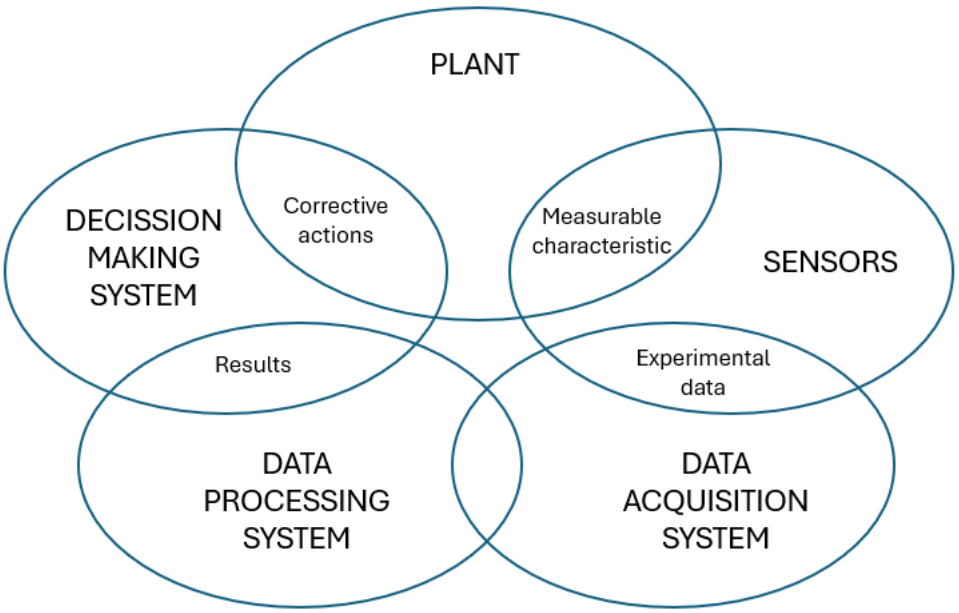


**Figure 1.2:** Monitoring concept (García Alonso, 2016)

In the case of aerospace structures, SHM systems comprise a set of novel techniques that allow evaluating the structural integrity and reliability of a component in a precise and on-demand

way (Furkan Kosova and Hakk, 2024). They can be viewed as an evolution to the traditional non-destructive techniques (NDT) for structural inspection, which targets the same objective: ensuring the safety and reliability of an aerospace structure.

Many specific events can be monitored during the aircraft lifecycle, such as the ones shown in Figure 1.3. These events could be different depending on the location in the aircraft, as each location could be subjected to different environmental loading conditions, and therefore there must exist an optimal SHM system that must be different for each area of interest and each event to be monitored.

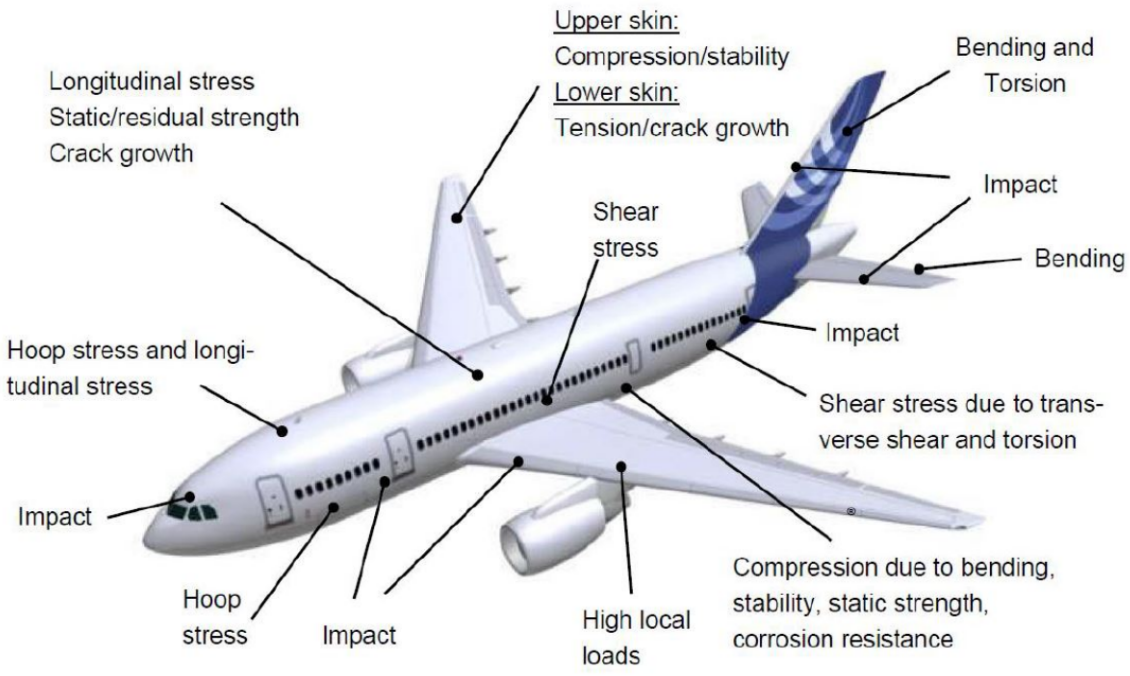


**Figure 1.3:** Events or effects to be monitored on an aircraft (Assler and Telgkamp, 2004).

Considering the origin of these events, they can be grouped in at least one of the following categories (*Guidelines for Implementation of Structural Health Monitoring on Fixed Wing Aircraft*, 2021):

- Fatigue Damage (FD)
- Accidental Damage (AD)
- Environmental Damage (ED)
- Operational Damage (OD)

The advantages of the integrated sensor network for detecting defects must outweigh the disadvantages derived from the introduction of a permanent system in the aircraft. These are summarized in Table 1.1

**Table 1.1:** Main advantages and disadvantages of an integrated sensor network (Fernández López, 2009)

| Advantages | Disadvantages |
|---|---|
| Fewer inspections, increasing operation time. | Additional weight of the sensor network and monitoring equipment; |
| Shorter inspection time | Cost of inspection equipment |
| Fewer man-hours spent on maintenance | SHM system maintenance and calibration times |
| Exact determination of service life | Difficulties introduced to normal aircraft operation |

In order to function, a monitoring system will measure all the inputs that affect the monitored plant, as well as the outputs. With all this information, a series of actions will be taken to ensure the operation of the plant within predetermined limits of safety and efficiency.

From a conceptual point of view, monitoring systems can be considered as feedback control systems. They differ from these in characteristic times and in the way they act on the plant (García Alonso, 2016); with respect to the temporal scale, the monitoring systems studied here evolve over very long periods of time compared to a usual mathematical control system, as the time scale is typically of the order of magnitude of the operating life of the structure (Farrar et al., 2002). In a spatial scale, these systems can operate both in a microscopic or material structure level and evolve up to a macroscopic or detectable level; at this point, when the change is sufficient to affect a measurable parameter, the monitoring system can detect and control it.

## 1.6 Structural health monitoring definition

The basis of a SHM system applied on an aeronautic structure is to build a similar system to a human nervous system in which nerves (sensors) monitor the state of critical parts or organs of the body. Similarly to this nervous system, the SHM could acquire information from a network of sensors in the aerospace structure and assess its state (da Silva et al., 2014; Speckmann and Roesner, 2006).

SHM technologies for aircraft are being developed to have a reliable system that can be used for the early detection of cracks and delaminations in CFRP, as well as corrosion or crack growth problems in metallic structures. The ideal system would be integrated into the aircraft structure and provide instantaneous measurements and data processing. A second but also prominent option is the creation of an implemented SHM system that could be used exclusively during maintenance, that is, when the aircraft is out of service, considering the usage of additional NDT methods but being able to simplify or increase the process reliability (Assler and Telgkamp, 2004).

SHM applications in aircraft are still in an experimental phase. There are different reasons for this, firstly, the lack of technical maturity, related to (Pitropakis, 2015):

- Solutions proposed only solved isolated problems
- Difficulties to match all natural environmental conditions
- Measured data are difficult to interpret due to the complex nature of aircraft parts

In addition, the lack of acceptance by end users, driven by skepticism toward new technologies, can be addressed through technical solutions that effectively meet the challenges of aircraft operations. Another key issue is the difficulty of interpreting the data collected from complex aircraft components. This challenge can potentially be mitigated by increasing the number of sensors and improving data processing techniques. And finally, as with every new technology, a complicated and long-term certification process should be expected.

In this way, SHM only makes sense if the fault that can be detected affects safety and increases reliability, since if it does not affect safety, it is not necessary to introduce a system of such complexity, and in this case the only way to make it profitable is by improving reliability. Despite the undeniable interest in this technology, its state of development is immature for aeronautical applications, since despite the existence of a multitude of monitoring techniques and the resources invested in the subject, the high requirements of reliability, weight and integration into the structure, in addition to the special working conditions typical of the aeronautical environment, very few of the techniques, which have been in development for more than 20 years in laboratories, have been implemented in the industry, and there is only a small set of examples that have proven to be effective: such as the Health and Usage Monitoring Systems (HUMS), certified for use in helicopters to detect signs of possible failure on its rotor gearboxes components (C. Adams, 2012) or the Honeywel's Central Maintenance Computer (CMC) first installed in a Boeing B777 aircraft and the Aircraft Management Operations Support System (AMOSS) developed for the Boeing B787 aircraft (Gorinevsky et al., 2005).

From a practical point of view, we focus on a low-level interpretation of the system. SHM can be considered a technique divided into five levels of action (Farrar and Worden, 2006; Rytter, 1993):

1. Existence of damage. Alert on the presence of an anomaly.
2. Location of the damage. Spatial situation of the detected anomaly.
3. Characterization. Type of anomaly detected and its severity.
4. Prognosis. Evaluate the moment in which the said anomaly becomes critical.
5. Repair. Correction of the anomaly.

This is consistent with the definition presented in Speckmann, 2007 that considers the SHM discipline as an evolution of nondestructive inspection (NDI) techniques, in which the sensors are permanently attached to the structure asn the system is working in real time during the operation of the aircraft. An SHM system, therefore, implies an observation of the structure over time using periodically sampled response measurements from an array of

sensors that must be permanently installed; the extraction of damage-sensitive features from these measurements, such as the ones shown in Figure 1.4, and the statistical analysis of these features can be used to determine the current state of system health and use this information to assess the state of the entire structure and drive the maintenance program.

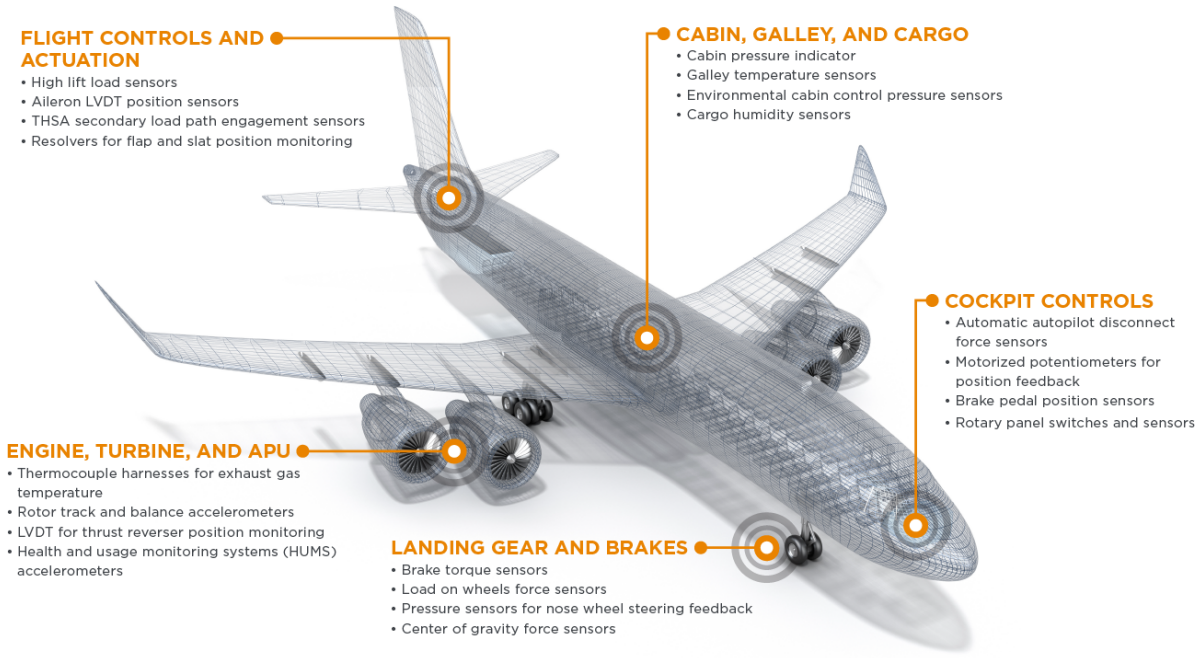


**Figure 1.4:** Possible areas and applications that could potentially be sensorized on an airplane ("Sensors for aerospace applications", 2024).

SHM can also be considered as part of a strategy implementation process to identify abnormal operation of an aerospace, civil, or mechanical infrastructure, plant, or structure (Farrar and Worden, 2006). This definition implies the comparison between two states of the said structure, one as a reference considered 'healthy' and another that is verified and the system decides whether it is considered "healthy" or damaged. It also implies a periodic observation of the said structure. This process or strategy would have three fundamental elements:

- Usage Monitoring History of the structure's use.
- Damage Diagnosis Current state of the structure. Most authors consider SHM to be fundamentally part of this task.
- Damage Prognosis Future state of the structure

It is possible to consider SHM from different points of view, depending on the author. Typically, from a functional point of view, SHM is defined as either operational load monitoring or damage detection. These two groups will include the following SHM main branches:

**Operational monitoring:** using indirect measurements that could indicate the presence of FD / AD / ED / OD, ie, to measure the loads of the structure for fatigue monitoring.

- **Usage Monitoring:** how the structure is being used compared with a reference in terms of typical flight parameters
- **Operational Loads Monitoring:** how the structure is used compared with a reference in terms of loads

**Damage detection:** by mains of direct measurements of FD/AD/ED/OD, i.e., measure local strains in stress concentration detail to detect a crack.

- Events and Damage Diagnosis: which is the current health status of the structure
- Prognosis: how will be the structure behavior according to: past usage and health status, current health status and scheduled future usage

### 1.6.1 Different SHM levels and uses

When considering a generic SHM system, there are many different techniques that can provide completely different results. The implementation of a SHM system can be done at different levels of complexity as required by the system to be inspected. These levels can be categorized as follows (Rytter, 1993, Ihn, 2013):

- **Level 1: Detection** At the most basic level, the method is able to detect an event and the possibility of this event to cause a damage to the structure. It's the most basic level of information that can be provided by an SHM system and can be used to raise the possibility of damage and need for inspection by a more complex method.
- **Level 2: Location** The method gives information about the probable location of the damage. Damage localization is more complex than detection and requires a denser sensor network or more sophisticated algorithms to pinpoint the area of concern. Techniques like guided wave propagation (e.g., Lamb waves) or triangulation using multiple sensors are often employed for this purpose.
- **Level 3: Assessment** After detecting and localizing the damage, the next step is to give information about the size and severity of the damage, such as crack length, depth, or the degree of material degradation. This may help to evaluate the reliability and safety level of a structural component and assess the need of repairs or replacement. The assessment can be made via a combination of the following two strategies:
  - Using the location and geometry of the damaged area, the damage severity can be extrapolated based on known data from the structure.
  - Using the measurements obtained from the sensor network by evaluating the signal variation between the intact and damaged structure.

  The Assessment or quantification is critical for decision-making, as it provides actionable information about whether the damage requires immediate repair or if it can be monitored over time.
- **Level 4: Prognosis** The method gives information about the efect of the damage to the structure. Once the damage has been completely described, it is also possible to evaluate the influence of this damage in the future operation of the structure and its

possible consequences. A system able to operate at this level should be able to provide the operator with with information in terms of safety, structural properties or remaining life and requirements for a future maintenance operation.

- **Beyond Level 4: Self-Healing Structures** Though not commonly included as a "level" of SHM, recent research focuses on self-healing materials and structures that can autonomously repair damage. In such systems, SHM plays a role in detecting damage and triggering the healing process. This area is still in its infancy but represents the next frontier in SHM development (Correa et al., 2017).

The higher the level, the more complex the SHM system becomes, and it is clear that to achieve a higher level, the system must also be able to reach the previous levels. Depending on the mission needs and the characteristics of the structure to be monitored, the SHM system may perform at a certain level. Additionally, not all levels are equally developed nowadays, and especially level 4 may present some complications that currently may be difficult to fully achieve.

### SHM Axioms

As with any other discipline, the process of implementing a complete SHM system, whether it is for aerospace, civil, or mechanical engineering, can be subject to a number of basic truths or axioms. Worden et al., 2007 defines the following set of eight fundamental axioms; although no claims are made about whether this may form a complete set. It is possible that there are other fundamental truths that have been omitted.

- Axiom I. All materials have inherent flaws or defects. In many engineering materials, nano/micro-structural defects can often be incorporated into average material properties, such as yield stress or fatigue limit, and are not typically classified as "damage." However, in certain cases, such as with composite materials, void content must be considered as initial damage. Under dynamic loading, there is no way to prevent damage progression from voids or the resulting degradation of the material's properties.
- AxiomII. The assessment of damage requires a comparison between two system states. In this case, the comparison is between a state considered healthy, in which there is damage to the structure that does not compromise its integrity, and a damaged state, which compromises its integrity (as previously mentioned, present or future).
- Axiom III. Identifying the existence and location of damage (SHM levels 1 and 2) can be done in an unsupervised learning mode, but identifying the type of damage present and the damage severity (SHM level 3) can generally only be done in a supervised learning mode.
- Axiom IVa. Sensors cannot measure damage, only DSFs. Feature extraction through signal processing and statistical classification is necessary to convert sensor data into damage information.
- Axiom IVb. Without intelligent feature extraction, the more sensitive a measurement (DSF) is to damage, the more sensitive it is to changing operational and environmental conditions (EOC). This axiom can be combined with Axiom VI, indicating that the

greater the sensitivity of the DSF to damage, the more sensitive it is to noise.

- Axiom V. The length- and time-scales associated with damage initiation and evolution dictate the required properties of the SHM sensing system. Again, it can be combined with Axiom VII which establishes an inverse proportionality relationship between the size of the damage to be detected and the working frequency of the selected SHM technique.
- Axiom VI. There is a trade-off between the sensitivity to damage of an algorithm and its noise rejection capability.
- Axiom VII. The size of damage that can be detected from changes in system dynamics is inversely proportional to the frequency range of excitation. In ultrasonic NDT, the diffraction limit is typically associated with the smallest flaw size that can be detected in relation to the ultrasonic wavelength; this limit implies that flaws approximately the size of half a wavelength are detectable. This implies that if instrumentation is capable of detecting extremely small scattering signals, such as very low reflection coefficients, then even very small flaws can be identified. However, scattering becomes significant when the flaw size is comparable to the wavelength, making it beneficial to use shorter wavelengths for detecting smaller flaws.

Although these axioms may not be a closed group and may grow or be modified, they can provide a basis for SHM technologies and a starting point for research.

### SHM in a maintenance program

Considering an SHM system as a viable part of a maintenance process implies that the system must be able to contribute to at least one of the following items (Fernández López, 2009):

- Detecting the structural deterioration before it may affect the aeronavegability or require repairs that may have significant economic repercussions and preserve the reliability and safety levels for which the structure has been designed.
- Restore the safety and reliability of the structure when its deteriorated.
- Obtain the necessary information to improve the design if the reliability is not adequate. Determine the basis, interval and type of inspections.
- Achieve this objectives with the minimum total cost, including the cost of maintenance and residual failures.

SHM techniques have a very clear application in the three first objectives; having an integrated sensor network, it is possible to inspect the structure in shorter intervals or even in a continuous way; in this way, damage tolerance criteria may evolve with the new information of viability indexes, even redefining the maintenance operations. SHM may improve damage detection and traceability, resulting in more intelligent maintenance of the structure.

Having the possibility of detecting damage at a more early stage, reliability of the structure will be improved with a more preventive and less costly maintenance, also the repairs may be more specific and efficient as there would be more information of the damage available.

Being able to register the state of the structure in a quantitative way also may provide additional information to revise the design conditions. Additionally, an SHM system may record information about applied loads or operational cycles to which the structure may be subjected due to the sensor network of the system. This information could be used to improve both the design in the primary structure components and the modification of damage tolerance criteria in secondary structure.

The usage of a SHM system can allow for the evolution from a scheduled maintenance of an aerospace structure to a CBM. In a CBM, the structure is serviced on-demand according to the aircraft operation and the resulting state of the structure. The CBM could potentially save maintenance costs with the same level of safety and reliability or could even improve under certain conditions (Ihn, 2013).

However, even though the benefits of SHM are clear, they must be compared with the more traditional NDT, currently used in most aerospace applications. The main advantages of SHM, as described by Fernández López, 2009 could be summarized as follows:

- Reduced number and time of inspections, increasing operational time.
- Reduced man-hours of time dedicated to the maintenance of the structure.
- Increased accuracy to the estimation of the in-service life of the component.
- Potential failure may be detected earlier and with greater accuracy,

Although the main disadvantages of an SHM system could be reduced to:

- Increased weight due to the sensor network and monitoring equipment.
- Cost of monitoring equipment.
- The maintenance and calibration time of the SHM system may impact the operational time of the structure.
- Additional complications in the normal operation of the system.
- As the system is integrated into the structure, a failure of the structure can also produce a failure of the SHM sensor network, which can increase the cost and complexity of the repair.
- Replacement of structural elements also requires the replacement and calibration of its integrated sensors.

Therefore, it is possible that the complications and disadvantages that an SHM system may introduce outweigh the benefits. The system only makes sense when it increases safety and reliability of the structure; otherwise, such a complex system may not be needed; additionally, the reliability of these kind of systems is crucial for them to be profitable, as they must be able to surpass greatly the current NDT techniques reliability levels.

## 1.7 Guided elastic waves

One of the most widely studied methods for SHM in aircraft is damage detection using ultrasonic guided elastic waves. In recent years, numerous articles and books have explored this approach, highlighting its various applications and affirming its potential (H. Cho and Lissenden, 2012; Philibert et al., 2022; Yoon et al., 2012).

The method relies on transmitting guided ultrasonic waves, which interact with defects or discontinuities in the material by reflecting off or passing through them. Elastic waves are particularly well suited for inspecting large, plate-like areas commonly found in aircraft due to their long-range sensitivity. Their ability to detect damage is based on changes in their waveform as they travel through the material, with these alterations occurring because their propagation characteristics are directly influenced by the material's mechanical properties.

Elastic waves in solids can be summarized in the basis of its particle motion, as shown in Table 1.3. They can be broadly classified into two main types: longitudinal waves and transverse waves. In longitudinal waves, the particle motion occurs parallel to the direction of wave propagation, compressing and stretching the material as the wave travels, similar to sound waves in air. These are also called P-waves (primary waves) and are typically the fastest type of elastic wave. In contrast, transverse waves or S-waves (secondary waves) involve particle motion perpendicular to the wave direction, producing shear stress within the material. S-waves are slower than P-waves and can only propagate through solids, not fluids. At the surface of a solid, there are surface waves, including Rayleigh waves and Love waves. Rayleigh waves combine longitudinal and vertical motion, producing an elliptical particle trajectory (Telford et al., 1990), while Love waves involve horizontal shear motion (Love, 2015), and finally, at the interface of two solids there is a particular kind of wave, described by Stoneley and Baker, 1924, that can propagate along the boundary.

**Table 1.3:** General types of elastic waves in solids

| Wave types | Particle movement |
|---|---|
| Longitudinal | Parallel to wave propagation |
| Transverse - Shear | Perpendicular to wave propagation, in plane. |
| Transverse - Lamb | Perpendicular to wave propagation, out of plane. |
| Surface - Rayleigh | Elliptical orbit, perpendicular to surface |
| Surface - Love | Elliptical orbit, parallel to surface |
| Stoneley wave | Wave guided along interface |

Waves in metallic plates were among the first guided waves to be analyzed by Lamb, 1917, and have been extensively studied in the literature since then for their applications in SHM (Kessler et al., 2002; Su et al., 2006; Worlton, 1961). This section presents an overview of the nature of guided elastic waves and the main features that can be used for event or damage detection.

### 1.7.1 Fundamentals of Lamb waves

The characteristic equations that were initially established by Horace Lamb in 1917 (Lamb, 1917) and further developed by Mindlin, 1951 for waves propagating in an infinite plate. These equations were derived by setting up formalism for a solid plate having infinite extent in the x- and y- directions, and thickness $2h$ in the z-direction (Achenbach, 1973) and describe two modes of propagation: symmetric (S0) and anti-symmetric (A0), as follows:

$$\text{Symmetric:} \quad \frac{\tanh qh}{\tanh ph} = -\frac{4k^2qp}{\left(k^2+q^2\right)^2}$$

$$\text{Anti-symmetric:} \quad \frac{\tanh qh}{\tanh ph} = -\frac{\left(k^2+q^2\right)^2}{4k^2qp}$$

$$p^2 = k^2 - \frac{\omega^2}{c_L^2},\ q^2 = k^2 - \frac{\omega^2}{c_T^2},\ \text{and } k = \frac{\omega}{v_p}$$

where $k$, $c_L$, $c_T$, $c_P$ and $\omega$ are the wavenumber, velocities of longitudinal and transverse modes, phase velocity and wave circular frequency, respectively.

The equations are derived by establishing a formalism for a solid plate with infinite dimensions in the $x$ and $y$ directions and a thickness $h$ along the $z$-axis and proposing sinusoidal solutions to the wave equation, resulting in the propagation modes shown in Figure 1.5. The complete derivation of the equations is performed in Annex C.

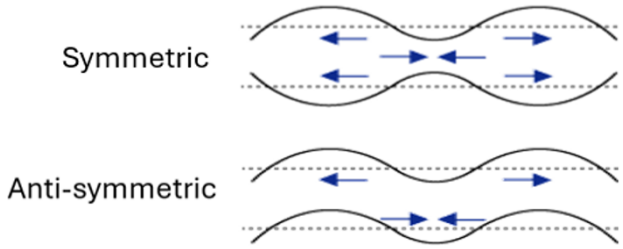


**Figure 1.5:** Lamb wave propagation modes ("Modes of Sound Wave Propagation", n.d.)

By definition, Lamb waves have no particle motion in the y-direction. Motion in the y-direction in plates is found in the so-called $Sh$ or shear-horizontal wave modes. These have no motion in the x- or z-directions, and are thus complementary to the two Lamb wave modes. Although this wave mode is not generally used for SHM applications, in the case of isotropic plates, the velocity of the first order shear propagation mode $Sh0$ has been mathematically proven to be equal to the anti-symmetric (bending) propagation mode $A0$ (Conry, 2005).

The equations imply that Lamb waves, regardless of mode, are dispersive; resulting in a propagation speed that depends on the frequency. This dependency is shown in Figure 1.6 for an aluminum plate.

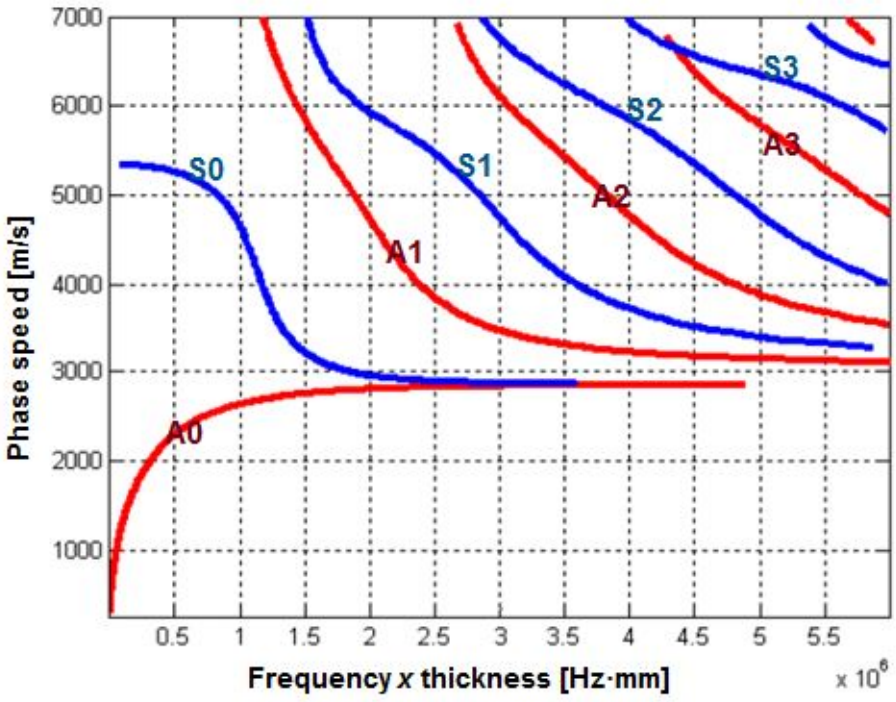


**Figure 1.6:** Lamb wave dispersion curves in aluminium (García Alonso, 2016).

For orthotropic materials such as CFRP, the velocity of Lamb waves is not uniform in all directions due to the directional dependence of material properties (mainly stiffness and density). The main directions of interest are usually aligned with the material's principal axes (along fibers, across fibers, and through thickness). The velocities are therefore determined by solving a system of equations that relate the material's orthotropic elastic constants to the wave's frequency and wavenumber. An attempt to solve the propagation speeds using the TMM method is shown in Annex D.

Lamb waves differ from standing waves because the motion of the particles at an arbitrary point in space is not periodic; they are then a particular case of traveling waves and give a very good approximation of the elastic wave propagation speeds in thin plate objects, however, as the infinite plate is nowhere to be found in reality, the term Guided Lamb Waves (GLW) is more commonly used to refer to this real phenomena, as its refers to Lamb-like waves that are guided by the finite dimensions of real objects. By definition, Lamb waves do not have a particle motion in the transversal direction. This motion is found in the so-called shear wave modes (*Sh*), which have no motion in the longitudinal or vertical directions, and are thus complementary to the Lamb wave modes. These waves can be generated by either active interrogation with sensors or as a result of the environment on the structure, such as an impact.

Lamb waves traveling in thin composite plates are very sensitive to defects or damages (Ostachowicz et al., 2009). This opens a wide field of applications for structural health monitoring, especially for composite structures, as they are prone to damage, such as delaminations, that

are not easily detected by visual inspection techniques; or structures for space applications that cannot be inspected during their service life (Charles H. Keilers and Chang, 1995; Lin et al., 2001).

Computational simulations provide a very effective way to capture and understand structural behavior in terms of elastic wave response; general-purpose computational codes such as time-domain spectral finite element methods (Kudela et al., 2018a, 2018b) or explicit finite element methods (de Luca et al., 2018; F. Li et al., 2018; Ong et al., 2016) are commonly used to calculate wave propagation. However, these codes require a large amount of computational resources and may become a problem in large and complex structures. For this reason, it is important to derive solutions on simple structures and understand the local behavior of the wave when facing structural detail before attempting to simulate a complete aerospace structure.

### Wave propagation maps

Wave propagation maps are graphical or analytical representations of how waves (such as mechanical, acoustic, or electromagnetic waves) travel through a medium. In the context of SHM, wave propagation maps are primarily used to visualize and analyze how stress waves, like ultrasonic waves or guided Lamb waves, move through a structure. These maps help in understanding the interaction between waves and structural elements, such as boundaries, defects, and material interfaces.

The knowledge of propagation velocities for each propagation mode of a guided elastic wave can allow tracing of the evolution of the wave front between a source point and a potential sensor that could capture the signal. These sources could be artificial sources generated by a controlled actuator to inspect the structure or external sources such as impact, crack growth, or environmental conditions.

The primary goal of wave propagation maps in SHM is to illustrate the spatial distribution of wave energy over time, enabling the identification of regions where EW are reflected, scattered, or absorbed. These maps can be helpful for locating potential defects, assessing structural integrity, and guiding sensor placement.

Propagation maps can be calculated analytically or numerically knowing the propagation velocities of the waves and the structure and material properties and design. The simulation can be used to compute an estimation of the time when the elastic wave is expected to reach the sensors and allows to optimize the computation window for the signal processing on an in-service event.

Wave propagation maps can be understood with an increasing level of complexity, grouped in the following levels:

1. **Wavefronts:** the wavefront which represent the leading edge of a wave as it travels through the material. These wavefronts can be circular (in isotropic materials where waves propagate uniformly in all directions) or more complex in anisotropic materials, such as composites, where wave speed varies with direction.

   The philosophy adopted to generate these propagation maps is described in Muñoz

Chamorro, 2018, discretizing the wave front at multiple spatial points with the objective that at the time of representation the change in shape and speed of the wave front can be appreciated. Structural details such as thickness changes or borders must be taken into account when computing the propagation of the wave.

2. **Reflection and refraction:** Waves reflect off boundaries, cracks, or material interfaces. Wave propagation maps highlight these reflection points, showing how the wave path is altered by structural features or defects. For example, waves encountering a boundary may reflect back into the structure, while encountering a defect can cause scattering in multiple directions.

   Can be accurately performed with numerical methods such as explicit FEM or analytical methodologies.

3. **Scattering from Defects:** Defects, such as cracks or voids, could scatter waves in various directions. Propagation maps can be used to visualize this scattering behavior, helping to locate and assess the severity of damage. A defect may cause multiple secondary wavefronts to emerge, which can be traced back to identify the damage location.

   More complex methodologies such as Finite elements or spectral elements are required to accurately represent this, often requiring specific element formulations to better characterize the damage (Shen and Giurgiutiu, 2016).

Reflection and Refraction: Waves reflect off boundaries, cracks, or material interfaces. Wave propagation maps highlight these reflection points, showing how the wave path is altered by structural features or defects. For example, waves encountering a boundary may reflect back into the structure, while encountering a defect can cause scattering in multiple directions.

### 1.7.2 Elastic wave damping and composite materials

In mechanical systems, damping is often understood as the irreversible conversion of mechanical energy into other energy forms. In materials and structures, this typically involves the transformation of mechanical energy into thermal energy, although other conversions, such as electromagnetic or piezoelectric, can also be considered damping. A common method to estimate damping is to calculate the ratio of dissipated energy to stored energy (Bert, 1973).

An ideal linear damped system of one degree of freedom is governed by the following equation:

$$m \cdot \ddot{u} + c \cdot \dot{u} + k \cdot u = 0\,; \quad \ddot{u} + 2\zeta\omega_n \dot{u} + \omega_n^2 u = 0 \tag{1.1}$$

where:

- $k$, $c$, $m$ Are the stiffness, damping and mass of the structure respectively
- $\omega_n$ Is the natural frequency of the system, defined as $\omega_n = \sqrt{k/m}$
- $\zeta$ Is the critical damping ratio, defined as $\zeta = c/c_{cr}$, with $c_{cr} = 2k/\omega_n$.

The critical damping ratio $\zeta$ can have a significant influence on the response of a system; it is

said that a system is said to be under damped when $\zeta < 1$, critically damped when $\zeta = 1$ and over damped when $\zeta > 1$. A typical response for each of these cases is shown in Figure 1.7.

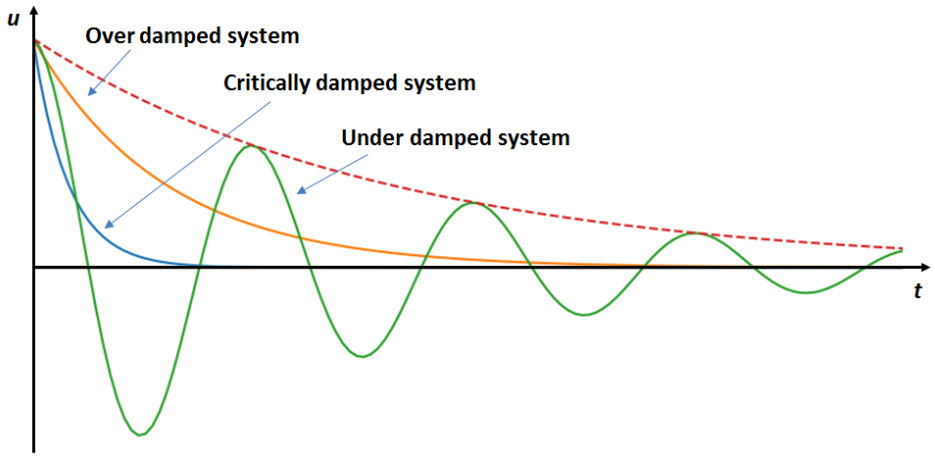


**Figure 1.7:** Effect of the critical damping ratio on the response of a 1 degree of freedom system

Compared to metals, composite materials typically exhibit greater damping capacity, primarily due to the viscoelastic nature of their polymeric matrix. Like other performance parameters of composites (e.g., stiffness, strength, density) the effective damping capacity is dependent on not only the damping properties of the constituent materials, but also microstructural details such as fiber volume fraction, fiber orientation, ply stack up, fiber packing array, and weave pattern in woven composites (Bednarcyk et al., 2016).

Similarly to stiffness and strength, damping can be optimized by carefully selecting the constitutive parameters of the composite, including fiber aspect ratio, stacking sequence, and the properties of the constituents (Treviso et al., 2015). However, in many cases, achieving optimal damping properties results in compromised performance in terms of strength and stiffness, requiring a trade-off. Optimization of strength and damping in composite structures falls outside the scope of this review, which focuses on describing the impact of structural and operational parameters on the dissipative behavior of composite materials.

The damping mechanisms in composite materials are different, more complex and usually more severe than those of conventional metals. This is due to the multiple energy dissipation sources that can be present in a composite structure and are not present in metals, such as:

- The visco-elastic nature of the matrix. Usually, the main contributor to the damping of the laminate (Chandra et al., 2003), although the damping of the fibers may also be significant in some cases.
- Interphase damping. The interphase between the fiber and the matrix presents some unique characteristics and in some cases a significant thickness that may influence the damping of the composite (Gibson and Hwang, 1991).
- Coulomb friction due to slip in unbounded regions of the fibre-matrix interface (Sun et al., 1985). It refers to the frictional resistance that occurs when the fiber and matrix within a composite material slide relative to each other at their interface; under cyclic

loading (e.g., vibrations or impacts), frictional forces generate heat and dissipate energy, reducing the vibrational response of the composite.

- Damping due to damages or imperfections. Composite materials are usually more prone to damages than traditional metallic structures; even when these damages may be small and negligible form a structural point of view, they can still dissipate energy and present some special mechanisms unique to composites.
- High vibrations. Viscoelastic damping is another unique characteristic of composite materials (Kenny and Betti, 1995).
- Temperature changes that may produce thermo-elastic damping (Curtis and Moore, 1988; Kenny and Betti, 1995).

At the macromechanical level, damping mechanisms can be estimated based on fiber lay-up sequences (R. Adams and Maheri, 1994; Berthelot and Sefrani, 2004). Conversely, at the micromechanical level, the damping behavior can be related to the microstructures of fiber composites, including factors like fiber volume fraction and interface properties (Chandra et al., 2002; Finegan and Gibson, 2000; L. He and Liu, 2005; Hwang and Gibson, 1993; Kaliske and Rothert, 1995).

In the case of impact detection, the damping characteristics of a structure become crucial in the response measured in the sensors, during this thesis the piezoelectric sensors will be mainly explored. Previous efforts have been made to characterize the damping parameters of composite materials for numerical simulation (Gresil and Giurgiutiu, 2014), although there exists many different approaches to study the passive response of the sensors under impact excitation.

Systems used for structural applications tend to have a very small value of structural damping, and the signals measured by piezoelectric sensors under low-energy impacts usually behave as an under-damped system. For these kinds of systems, the solution of Eq. 1.1 can be written as:

$$u(t) = \mathrm{e}^{-\omega_n \zeta t}\left(u_0 \cos \omega_D t + \frac{\dot{u}_0 + \zeta \omega_n u_0}{\omega_D} \sin \omega_D t\right) \tag{1.2}$$

where $\omega_D$ is the damped natural frequency, such as: $\omega_D = \omega_n \left(1 - \zeta^2\right)^{1/2}$

Advanced polymer composites exhibit strong anisotropy, affecting both their stiffness (moduli) and damping properties. As a result, there is no single damping value that can be universally applied; instead, each vibration mode will have its own specific damping value (R. Adams and Maheri, 2003).

A simple model for implementing structural damping in an explicit simulation could be the one proposed by Strutt [Rayleigh], 1877, also studied in Gresil and Giurgiutiu, 2014; Ramadas et al., 2011 for lamb wave simulations, which defines the critical damping ratio $\zeta$ as a function of the mass and stiffness matrix in the following manner:

$$[C] = \alpha [M] + \beta [K] \tag{1.3}$$

where $[C]$ is the damping matrix, $[M]$ is the mass matrix, $[K]$ is the stiffness matrix and $\alpha$ and $\omega$ are two parameters of the damping model, that in the case of a one degree of freedom system can be defined as:

$$\zeta = \frac{\alpha}{2\omega} + \frac{\beta\omega}{2} \tag{1.4}$$

Therefore, knowing the average frequency of the oscillation $\omega$, both the $\zeta$ and the Rayleigh parameters $\alpha$ and $\beta$, can be obtained with a numerical fitting of this model on the test results.

The approach to damped vibrations described in this section is based on data that represent the mechanical and damping properties of the material used. To ensure an efficient design process, it is preferable to rely solely on basic quantities obtained experimentally. Therefore, for composite materials, the characteristics of the individual components, studied as homogeneous macromechanical properties, should provide sufficient information Kaliske and Rothert, 1995.

## 1.8 Sensors for structural health monitoring

As stated in the previous sections, an SHM system relies on real-time data provided by a vast variety of different sensors which must be permanently installed in the structure. These sensors must be able to track various physical parameters and form an integrated system that monitors the structural health of the plant, providing real-time data that is critical for proactive maintenance and ensuring its long-term safety and functionality(*Guidelines for Implementation of Structural Health Monitoring on Fixed Wing Aircraft*, 2021).

In addition to the always desirable characteristics that every sensor must have from a measurement point of view, SHM requires additional characteristics of the sensor network related mainly to its integration into the structure (Fernández López, 2009):

- **Weight**: as low as possible, to introduce the least influences in the operation of the aircraft, in addition to the cost of increasing the weight of the additional structure, not only of the sensor, but of its attached systems (cables, equipment, etc.)
- **Integrability**: Composite materials allow a complete integration of the sensor network into the structure during the manufacturing process, for example, by embedding the sensors in the laminate. In addition, the sensors must withstand the entire manufacturing process.
- **Sensitivity and Resolution:** The desired level of sensitivity and resolution in detecting damage influences the type and number of sensors to deploy. For critical or primary structure where even minor damage could lead to catastrophic failure, highly sensitive sensors with high resolution, such as fiber optic sensors or piezoelectric sensors, might be required. Conversely, for less critical structures, a lower-resolution system with strain gauges or accelerometers might suffice.
- **Durability, lifespan or repairability**: The greatest difficulty for fiber optic sensors is the ability to be repaired if they are embedded in the structure which presents a big limitation in order to implement this type of sensors in the structure. Therefore, sensors

used in SHM need to be durable enough to withstand the operational lifetime of the structure or at least have a service interval that aligns with scheduled maintenance. Wireless sensors that rely on batteries must have long battery life or use energy harvesting techniques to ensure continuous operation without frequent intervention. Similarly, sensors exposed to harsh environments or heavy loads must be robust, and corrosion-resistant sensors are critical for structures exposed to moisture, chemicals, or saltwater.

- Environmental and Operational Conditions: Environmental factors such as temperature, humidity, electromagnetic interference, static or dynamic loads, and vibration levels also play a crucial role in sensor selection. For example, fiber optic sensors are ideal for harsh environments because they are immune to electromagnetic interference and can operate in extreme temperatures. Wireless sensors offer flexibility in environments where cabling is difficult, but they must be able to withstand environmental conditions like dust, moisture or temperature changes that arise in normal aircraft operation.

According to Worden et al., 2007, damage to an aircraft structure can be considered as any change in material, geometric properties, connectivity, or boundary conditions of the structure that adversely affects its current or future operation. In general, damage affecting aeronautical structures can fit into the following categories:

- **Accidental damage**. Fortuitous and unpredictable damage that occurs in the structure.It is usually clasified in one of the following:
  - Impact damage: An external force strikes the aircraft, it could be due to bird strikes or runway debris. One common type of impact damage is foreign object damage (FOD), which results from objects striking the aircraft during takeoff or landing. Aircraft skin, leading edges of wings, and engine inlets are particularly vulnerable to impact damage.
  - Ground handling Damage: improper handling of the aircraft on the ground is a frequent source of accidental damage. This can include collisions with service vehicles, mishandling of tools or equipment during maintenance, or damage caused by improper use of towing or parking mechanisms.
  - Environmental damage: Hailstorms, lightning strikes, extreme temperatures, or high wind speeds can lead to damage, especially on exposed surfaces like wings or stabilizers
  - Maintenance induced damage: Accidents during routine maintenance can lead to damage such as misaligned panels, scratched surfaces, or incorrectly installed parts. Fatigue from repeated maintenance cycles can also accumulate, leading to undetected issues such as fastener damage, sealant wear, or misaligned components.
- **Fatigue damage**. Predictable damage that occurs in the structure derived from the action of cyclic loads on it. For example, a crack that appears on the edge of a hole.
- **Environmental damage**. Damage that gradually occurs in the structure due to the action of the environment in which the structure operates. For example, corrosion, humidity absorption or thermal degradation.

- **Operational damage**. Unpredictable accidental damage that occurs in the structure derived from an anomalous operation of the structure. For example, an overload during a landing maneuver.

This classification does not generate disjoint groups; instead, damage can fall into more than one category. For example, stress corrosion cracking (SCC) is a phenomenon that generates fatigue-like cracks in the area where it appears, in addition to suffering cyclic loads, and operates in a high salinity environment; therefore, it could be considered both as environmental damage and operational damage. However, it is a classification that allows us to correlate damage with SHM techniques in a simpler way.

Damage in a structure may produce a DSF that can be detected by a sensor; however, different types of damage may produce different DSFs, such as the examples shown in Table 1.4, and each DSF is associated with one or more typical sensors directly related to the different SHM techniques.

**Table 1.4:** Typical damages in aerostructures and their associated DSF(García Alonso, 2016)

| Typical damages | Structural shape | Local strain | Strain field | EM interference | Vibration strain | EW strain |
|---|---|---|---|---|---|---|
| Fatigue Cracks | | X | X | X | X | X |
| Corrosion | | | | X | | X |
| Overloading | X | X | X | | X | |
| Delamination | | X | X | X | X | X |
| Debonding | X | X | X | X | X | X |
| WFD | | X | X | | X | X |
| Impacts | X | X | | X | | X |
| Dents | X | X | | X | | X |
| Rivet loss | | X | X | | X | X |
| Porosity | | | | X | | X |
| SCC | | X | X | X | | X |
| Erosion | X | X | X | X | X | X |
| Local bucking | X | X | | | X | |
| Plastic strain | X | X | X | X | | |

In addition to the damage-sensitive characteristic, we must take into account how the presence of damage modifies the said characteristic. This is what we call the damage signature. This signature (distinctive patterns or signals that arise due to specific forms of degradation or

defects) can be the change of some value related to the measurement or signal that we obtain from the damage-sensitive characteristic, such as amplitude, frequency, energy, etc.

The DSF provides a quantitative measure that reflects how sensitive a structure is to various forms of damage, serving as a key indicator for assessing the health of the structure. When combined with the damage signature, this sensitivity information allows for the selection of an SHM technology that is optimized for the specific application.

### 1.8.1 Optimal sensor selection

Optimal sensor selection for Structural Health Monitoring (SHM) is a critical aspect of ensuring accurate, efficient, and cost-effective monitoring of structural integrity over time. The performance of an SHM system largely depends on the type, placement, and configuration of sensors used to detect damage or changes in structural conditions. Selecting the right sensors involves balancing several factors, including the type of damage expected, the material and geometry of the structure, environmental conditions, data acquisition capabilities, and the desired sensitivity and resolution of the monitoring system.

Currently there are a large number of SHM techniques available or in development that can be used to monitor the evolution of damage in materials. Some of these techniques involve acoustic emission (Finlayson et al., 2001; Vandenplas et al., 2004; Wevers et al., 2007), real-time microfocus radiography (Bowman et al., 2003), electrochemical noise measurements (Reynolds et al., 1997), ultrasound (W. L. Liu et al., 2011) or optical fiber sensors (Guo et al., 2011; Lopez-Higuera et al., 2011. New techniques to assess and characterize the extent of damage are also being developed or optimized, such as high-resolution X-ray computer tomography (Knight et al., 2011), optical fibers as smart materials, or others. A summary of these techniques is shown in Table 1.5. These procedures may vary according to the type of damage to be monitored or the scope of the system.

**Table 1.5:** SHM technologies used in aircraft (Qing et al., 2019)

| Monitoring Principle | Sensor | Monitoring object | Mode |
|---|---|---|---|
| Strain | Fiber optic sensor<br>Strain gauges | Loads and impact | Passive |
| Stress waves | Piezoelectric sensors<br>Fiber optic sensors | Impact | Passive |
| Guided waves | Piezoelectric sensors<br>Electro-magnetic sensors | Global / Local dmg | Active |
| Ultrasonics | Piezoelectric sensors/Laser | Local damage | Active |
| EM impedance | Piezoelectric sensor | Local damage | Active |
| Electric resistance | Resistance element | Local damage | Passive |
| Coating monitoring | Nano material | Local damage | Passive |
| Vacuum monitoring | Air / Vacuum tubes | Local damage | Passive |
| Eddy current | Eddy current foil sensors | Local damage | Active |

Once the available SHM sensors / technologies and typical damages have been studied, both

Table 1.4 and Table 1.5 can be cross-examined to evaluate the suitability of each technology to be applied, as shown in Figure 1.8. The most common ones and widely used in the industry could be strain gauges, accelerometers, piezoelectric transducers, etc., each of them have certain advantages or disadvantages that may make them more suitable for specific applications. (UK, 2019).

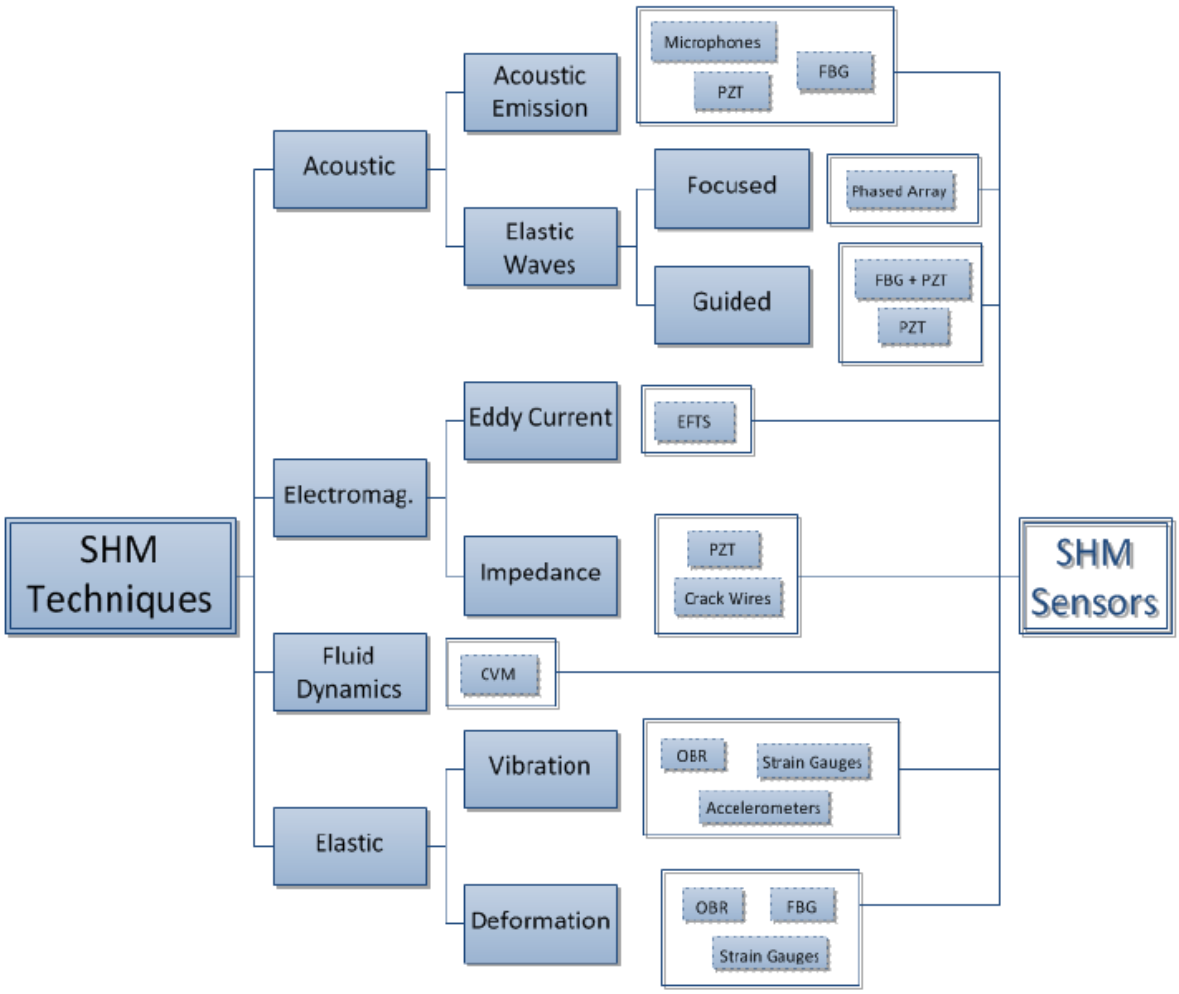


**Figure 1.8:** SHM techniques and applicable sensors (Muñoz Chamorro, 2018)

An SHM system may use one or combine many types of sensors to achieve its objectives. As many sensors are able to detect similar DSF many other factors must be evaluated when selecting the ideal sensor such as cost, state-of-the-art of the technology, weight or complexity of the system. The influence of the sensor itself on the structure (such as the added weight of sensors, equipment and cabling, or stiffness in the case of large sensors), could also be a significant factor to be taken into account in the selection process.

#### Emerging Trends in Sensor Selection for SHM

The field of SHM is rapidly advancing, and new technologies are influencing sensor selection strategies. Some emerging trends include:

- **Smart Sensors and IoT Integration:** Smart sensors equipped with embedded data processing and communication capabilities are becoming increasingly popular. These sensors could potentially preprocess the data, reducing the need for extensive data transfer and analysis in a central system. Integration with the Internet of Things (IoT) allows these sensors to communicate with cloud-based platforms for remote monitoring and management (J. Chen et al., 2024).
- **Energy Harvesting Sensors:** In environments where long-term power sources are unavailable, sensors capable of harvesting energy from structural vibrations, temperature gradients, or light are gaining traction. This can significantly extend the lifespan of wireless SHM systems, reducing maintenance needs (Mo and Davidson, 2013; Zelenika et al., 2020).
- **Machine Learning for Sensor Optimization:** Machine learning is being employed to optimize sensor placement and selection. By analyzing historical data and simulating potential damage scenarios, machine learning algorithms can help determine the most effective sensor types and configurations for specific applications, improving the accuracy and efficiency of SHM systems (Sofi et al., 2022).

### 1.8.2 Elastic waves sensors

As postulated by Worden et al., 2007 Axiom IVa (Section 1.6.1), an SHM system cannot measure damage directly. It can only measure some structural magnitudes influenced by the presence of damage, called Damage Sensitive Features or DSFs. Damage assessment may be made with these features, and in this section the focus is placed on GLW.

Lamb waves can be generated and detected by a wide variety of methods; the most useful ones for SHM are Laser-Based Ultrasonics (LBU), PZT sensors, and ultrasonic probes, inter-digital transducers such as Polyvinylidene Fluoride (PVDF), piezoelectric polymer films, etc. (Rytter, 1993).

Additionally, another novel technique for the detection of guided elastic waves can be the use of fiber optics sensors that are able to provide an excellent time and spatial resolution for the strain field. The combination of these techniques with strain gauges or other traditional monitoring techniques can provide a huge amount of information about the state of the structure. Fernández Díaz-Maroto et al., 2018

#### Fiber Bragg Gratings

Fiber Bragg Gratings (FBGs), are a type of Bragg reflector distributed in a small segment of optical fiber that reflects light at certain wavelengths transmitting the rest. This is achieved by creating a periodic variation in the refractive index of the fiber core that generates a specific dielectric mirror at certain wavelengths.

The fundamental principle behind the operation of an FBG is Fresnel reflection, where light traveling between media of different refractive indices may both reflect and refract at the interface (Paschotta, 2024). The grating in the fiber optics is created using ultraviolet (UV) light to form regions of higher refractive index within the fiber, and the distance between these regions determines the wavelength that will be reflected, known as the Bragg wavelength, as shown in Figure 1.9.

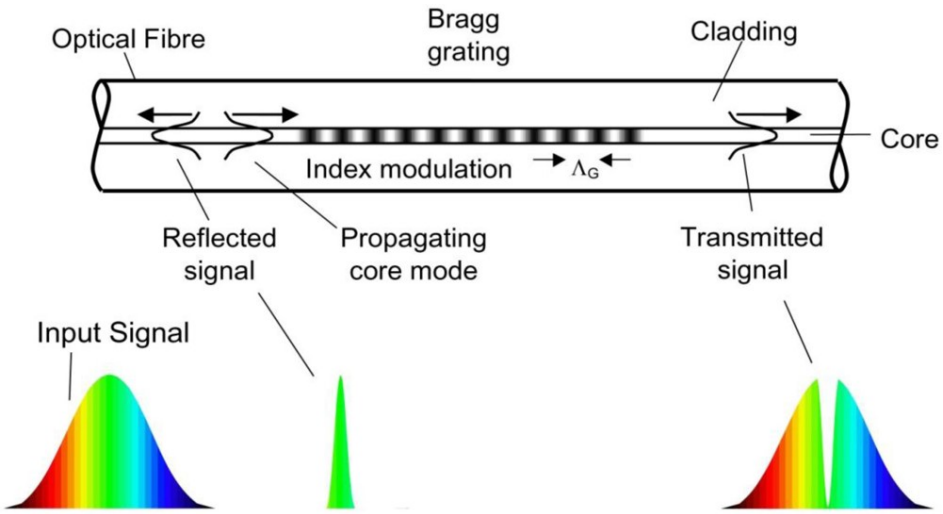


**Figure 1.9:** Schematic diagram of an FBG inside a single-mode optical fiber (Mihailov, 2012).

The Bragg wavelength $\lambda_B$ is given by the relationship:

$$\lambda_B = 2n_e\Lambda \tag{1.5}$$

where $n_c$ is the effective refractive index of the fiber core and $\Lambda$ is the grating period (the distance between adjacent high-refractive-index regions).

Changes in temperature, strain, or pressure cause shifts in the Bragg wavelength, which can be measured and correlated to the physical changes in the environment surrounding the fiber.

The FBG can be used as a local deformation sensor of the structure, since when a deformation is applied to the network, its period is modified so that a variation in the wavelength of reflected radiation is observed, proportional to this deformation (Theodosiou and Kalli, 2020).

### Piezoelectric sensors

Piezoelectricity is the electric charge that accumulates in solid materials in response to applied mechanical stress; it results from the linear electro-mechanical interaction between the mechanical and electrical states in crystalline materials without inversion symmetry (Ikeda, 1996). It is a reversible process: materials that exhibit the piezoelectric effect also exhibit the reverse piezoelectric effect, the internal generation of a mechanical strain resulting from an applied electrical field (Douglas A. Skoog, 2007; Gautschi, 2002). The effect was discovered by Jacques and Pierre Curie in 1880 (Manbachi and Cobbold, 2011).

The direct piezoelectric effect refers to the generation of an electric charge in response to mechanical stress. The converse effect refers to the case in which the strain develops in response to an applied electric field, as shown in Figure 1.10 (J. Li, 2021). The constant of proportionality for both effects is the same and is known as the piezoelectric coefficient $d$ (Heywang et al., 2008; Jaffe, 1958). Since polarization is a vector and stress is a second rank tensor, the piezoelectric constant is expressed as a third rank tensor, although it can be simplified to a second-rank matrix (Newnham, 2005).

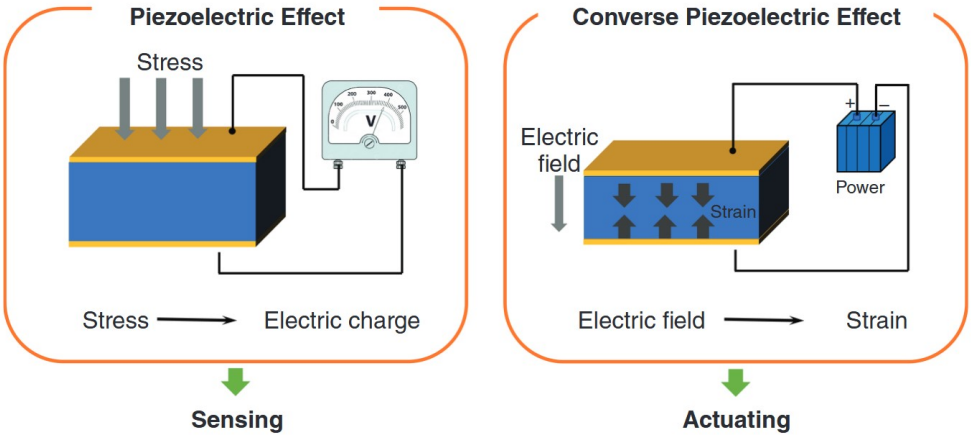


**Figure 1.10:** Direct and converse piezoelectric effect (Rödel and Li, 2018).

In the case of sensors and transducers used for SHM, the most extended piezoelectric material used is Piezoceramic Lead Zirconate Titanate (PZT) and polymer piezofilms (polivinylidene fluoride). This work will focus exclusively on PZT.

The main advantage of these types of sensors compared to other more traditional alternatives such as strain gauges is their extremely high sensitivity to strains (up to values of $5\,\mathrm{V}/\mu\epsilon$) which is six orders of magnitude higher than resistive strain gauges. Furthermore, PZT elements can also generate elastic waves, making them ideal for both event detection and inspection (Gautschi, 2002; Sirohi and Chopra, 2000).

A limitation of piezoelectric sensors is their inability to perform truly static measurements. The application of a static force induces a fixed charge on the piezoelectric material; however, in conventional readout electronics, imperfect insulation and a reduction in internal sensor resistance lead to a continuous loss of electrons resulting in a progressively diminishing signal. Elevated temperatures further exacerbate this problem by decreasing internal resistance and sensitivity. Furthermore, increased pressure loads and temperatures adversely affect the piezoelectric effect, primarily through twin formation, which ultimately reduces sensor sensitivity (Okayasu and Bamba, 2018).

PZT elements provide excellent performance in Lamb wave generation and acquisition and are particularly suitable for integration in a host structure due to their small weight and volume and excellent mechanical strength. Their wide frequency response, low power consumption, and low cost make them ideal for SHM applications (Su et al., 2006). A typical disc-like pzt sensor that could be used for SHM applications is shown in Figure 1.11.

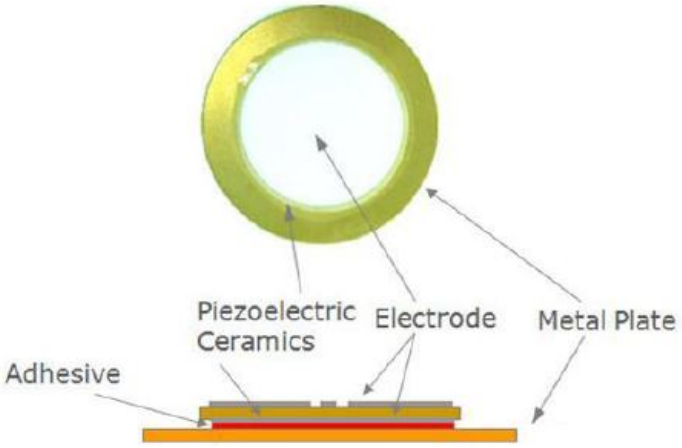


**Figure 1.11:** Disk shaped piezoelectric sensor

Integrated PZT sensors have a finite size, which implies that there will be an interaction between the GLW wavelength and the sensor size. To avoid unwanted couplings, wavelengths greater than the sensor size should always be used to ensure correct acquisition. Previous work by Fernández López, 2009; García Alonso, 2016 indicates that the interrogation pulse wavelength must be at least five times greater than the PZT disk diameter; this must be taken into account when defining the structure interrogation signals for the type of PZT sensors used. An optimal criterion for designing a disk-like PZT is proposed by Kessler et al., 2002, aimed at minimizing geometrical effects and avoiding uneven wave propagation:

$$2R = c_{wave}/f\left(n + \frac{1}{2}\right) = \lambda_{wave} \quad (n = 0, 1, 2, ...) \tag{1.6}$$

where $R$ is the radius of the PZT disk, $c_{wave}$, $f$ and $\lambda_{wave}$ are the wave velocity, frequency and wavelength of the Lamb mode of interest.

Guided Lamb waves generated by PZT unavoidably contain multiple modes, requiring a complex signal processing technique to extract information. Moreover, PZT may also reveal certain non-linear behavior and hysteresis under large strains/voltages or at high temperature. Brittleness, low fatigue life, etc., may be some other concerns that limit application (Schulz et al., 1999). PZT sensors have a maximum working temperature, the Curie temperature (Gautschi, 2002), between 250 °C and 330 °C, above which they lose polarization. This limits the working areas of this type of sensors, although for standard aeronautical structures under their design conditions it is not critical. However, their properties change with working temperature even without reaching the Curie temperature. This implies that it must be an additional factor to consider in the compensation of the EOC, indirectly affecting the interrogations (García Alonso, 2016).

### 1.8.3 Damage detection with piezoelectric sensors

As stated above, a PZT can be operated in either a passive way (Figure 1.12), listening to elastic waves in the structure that are generated by external events, or in an active way, in which some PZT transducers generate the elastic waves while the others listen. The ability of these devices to function as both actuator and sensors is one of the fundamental features that makes them ideal to be applied on an SHM system (Fernández López, 2009).

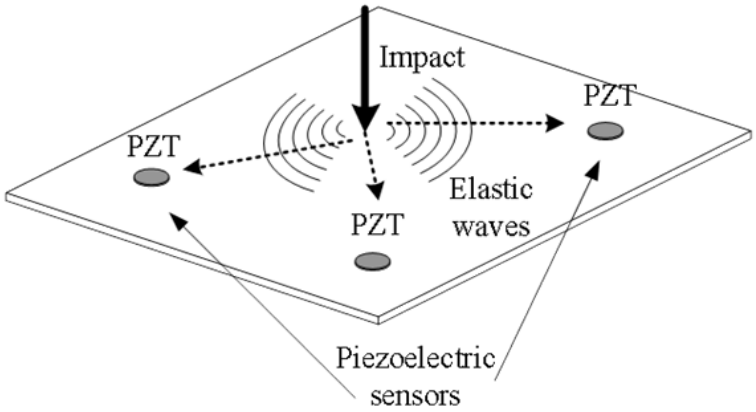


**Figure 1.12:** Passive impact detection with piezoelectric sensors

In the active mode of operation guided elastic waves could be used in two different ways, either the so-called pulse-echo techniques or pitch-catch techniques (IOWA State University, 2024). Pulse echo allows for the use of a single PZT transducer or an array of transducers located in close proximity, capable of emitting the wave, or the wave beam, that travels through the material; its reflections are captured back by the same sensor, as shown in Figure 1.13a. Pitch-catch requires at least the use of two transducers, as the roles of sensor and actuator are separated. For each interrogation, one of them acts as an actuator and the other as a sensor, as shown in Figure 1.13b. This work focuses on the analysis of the pitch-catch technique.

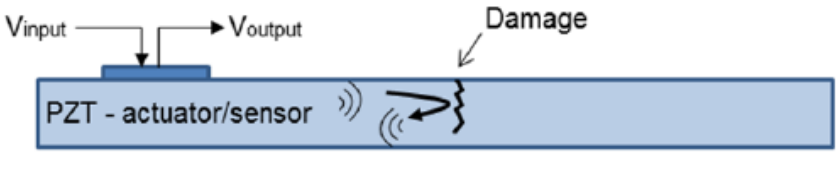


**(a)** Pulse - Echo

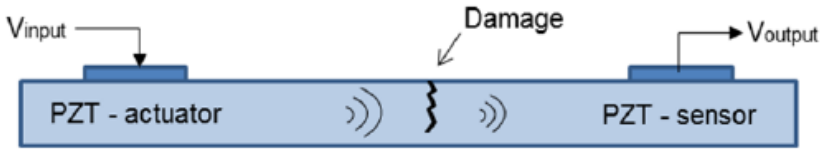


**(b)** Pitch - Catch

**Figure 1.13:** Interrogation techniques with PZT transducers

The signal emitted could be altered by the presence of damage in the structure, as shown in Figure 1.14 for the pitch-catch mode. This alteration can be measured by the sensors, and therefore the damage could be identified.

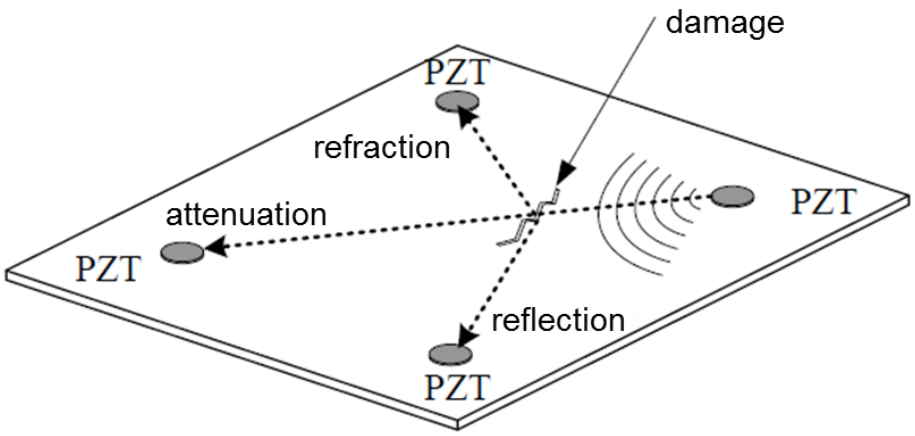


**Figure 1.14:** Damage detection in pitch-catch configuration

The main advantage of the pitch-catch technique is that the signal is only attenuated on its path from the actuator to the receiver, whereas on the pulse-echo technique the signal is reflected back, potentially being attenuated twice and, therefore, reducing the sensitivity of the system as the magnitude of the singal is lower.

Evaluation of the different states of a structure can be performed by comparing the signals measured on piezoelectric sensors, as described in Galarza et al., 2016; Studying the discrepancy of the signals can give information about the state of the structure. An example of signals that are affected by damage is shown in Figure 1.15.

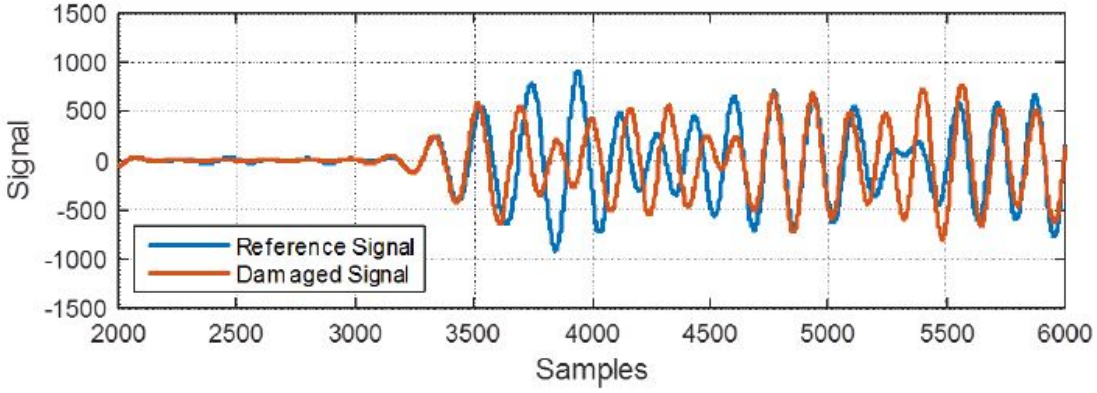


**Figure 1.15:** Example of baseline and damaged situations measured signals with piezoelectric sensors (Muñoz Chamorro, 2018).

## 1.9 Artificial intelligence techniques applied to SHM

Artificial intelligence (AI) refers to the ability of machines, especially computer systems, to demonstrate intelligence. As a branch of computer science, AI focuses on developing technologies and software that allow machines to perceive their surroundings, learn from experience, and make decisions that increase their chances of successfully reaching specific goals (Russell et al., 2020).

AI techniques are those that deal with the study of intelligent systems. An intelligent system could be defined as a certain system that perceives its environment and acts accordingly (Russell and Norvig, 2021). It is a relatively recent discipline (Nilsson, 2009), starting in the mid-1950s and emerging as a binder of a series of novel techniques that materialized during the first half of the twentieth century.

The ability to perceive and act in a specific environment of these systems can be carried out in four different ways:

- Thinking like a human being.
- Thinking rationally.
- Behaving like a human being.
- Behaving rationally.

This subdivision allows for the classification of the different techniques belonging to the field of Artificial Intelligence, both the disciplines on which it is based and those it generates.

AI is increasingly being applied to SHM to enhance the detection, diagnosis, and prediction of structural problems in various systems, such as bridges, buildings, aircraft, and pipelines. SHM involves continuously or periodically assessing the condition of a structure to ensure its integrity and safety. Traditional SHM methods are based on sensors and manual data interpretation, but AI introduces new capabilities that make this process faster, more accurate, and automated (Keshmiry et al., 2024).

In SHM, AI techniques such as machine learning (ML) and deep learning are used to analyze large amounts of data from sensors that monitor vibrations, strain, temperature, and other factors. These AI models can identify patterns, detect anomalies, and predict potential failures long before they occur, often improving human capabilities in terms of speed and precision. For example, neural networks can be trained to recognize subtle changes in vibration patterns that indicate damage, while reinforcement learning can optimize real-time monitoring strategies.

AI can also be used to improve SHM through predictive maintenance, where algorithms forecast the future condition of a structure based on current and historical data. This allows for proactive repairs, reducing downtime and maintenance costs, while increasing safety. Furthermore, computer vision techniques enable automated inspections using drones or robots, where AI can detect surface cracks or corrosion that might otherwise be missed.

### 1.9.1 Artificial intelligence and neural networks

An artificial neural network (ANN) is a computational model inspired by the structure and behavior of biological neural networks found in animal brains (Brahme, 2014).

In many animals, neurons transmit electrical impulses, known as spikes, through a long, slender fiber called an axon. The axon branches out into thousands of terminals, where it connects to the dendrites of other neurons at synapses. The strength of the signal determines how these connections are made and how information is passed between neurons (Figure 1.16). Neurons are highly connected to other neurons from which they receive stimuli from an event as it occurs, or hundreds of electrical signals with the learned information (R. F. López and Fernández, 2008). There are around 1000 billion neurons in the human brain and each one has an association point somewhere in the range of 1000 and 100000.

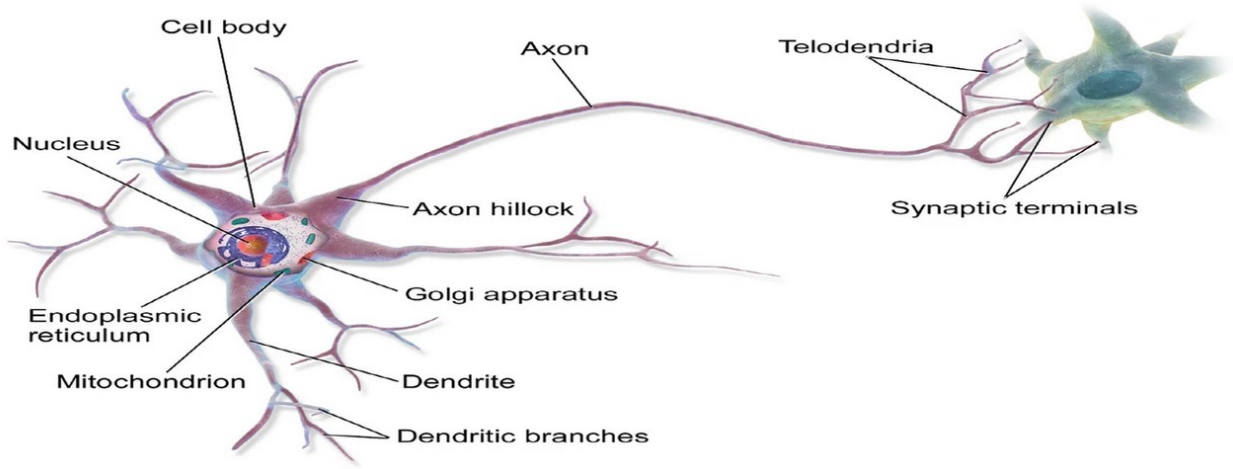


**Figure 1.16:** A graphic representation of a biological neuron (O. López et al., 2022).

An ANN is composed of interconnected units, or nodes, also referred to as artificial neurons, which loosely mimic the function of biological neurons. These neurons are linked by connections, representing synapses through which signals are transmitted. Each artificial neuron receives inputs from other connected neurons, processes the information, and passes a signal to the next set of neurons (Figure 1.17). This signal is a real number, and the neuron's output is calculated using a nonlinear function called the activation function, applied to the sum of its inputs. The strength of each connection, known as a weight, is adjusted during the learning process to optimize the network performance (Bishop, 2016).

The neurons are organized into a series of layers that together form the entire ANN within a system. A layer may contain anywhere from a few neurons to millions, depending on the complexity required for the network to learn hidden patterns in the data. Typically, an ANN consists of an input layer, one or more hidden layers, and an output layer. The input layer receives data from the external environment, which the network needs to analyze or learn from. This data then passes through one or more hidden layers, where it is transformed into useful information for the output layer. Finally, the output layer generates the network response based on the processed input data.

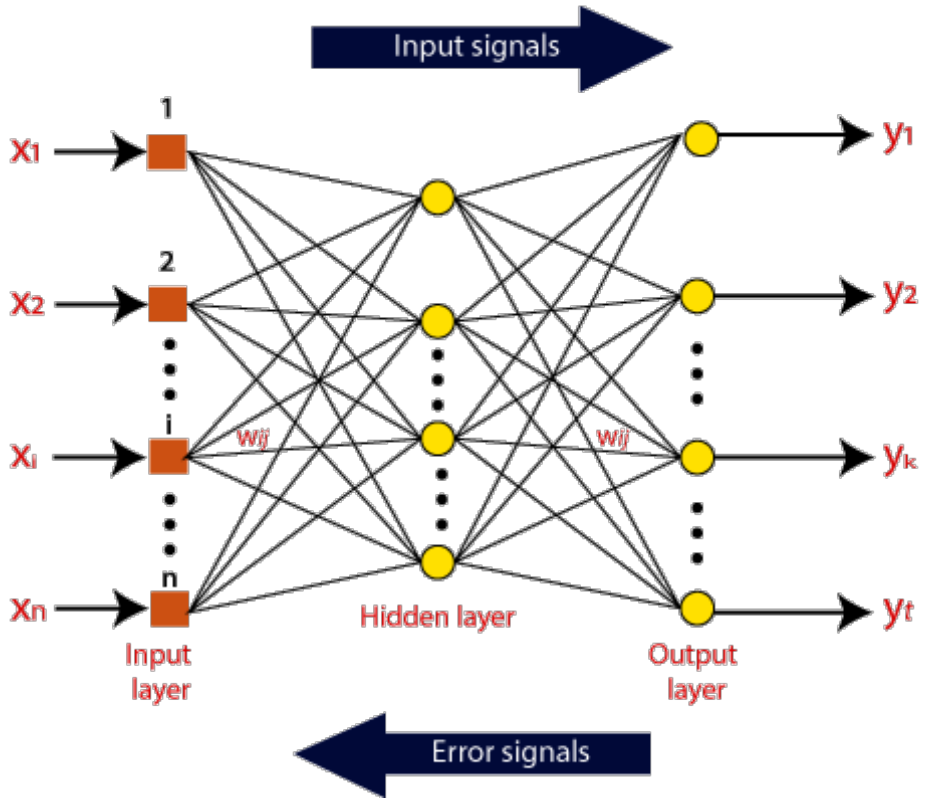


**Figure 1.17:** A graphic representation of an artificial neural network ("Artificial Neural Network Tutorial", 2024).

Artificial Neural Networks are a part of the discipline of Artificial Intelligence, falling within the category of reproduction of human thought. The typical problems of this branch of AI include learning, decision-making, and problem-solving, all through data.

AS a subset of AI, Artificial Neural Networks are highly multidisciplinary ( Buchanan, 2005), here we have classified them within AI techniques but they belong to many other areas, in fact they predate the foundation of AI as such in 1956 Fausett, 1994; Nilsson, 2009. Figure 13 indicates that ANNs also belong to Soft Computing techniquesNilsson, 2009 forming part of a set of different techniques but also with common elements mainly oriented to problem solving according to novel criteria:

- Fuzzy Logic (Zadeh, 1965).
- Genetic algorithms.
- Chaos theory.

Traditionally, SHM techniques based on AI have used functional approximation networks (feedforward backpropagation). However, the question arises as to what conditions the problem at hand and the selected ANN must meet to ensure the existence of solutions. For the selected networks, if a functional relationship. between two data sets is to be found, the following must be met (Fausett, 1994; Gupta et al., 2004):

- Firstly, said relationship exists (causality principle) and is defined in a biunique way even though it cannot be obtained analytically. This is called system identification.
- Stone-Weierstrass theorem. Establishes necessary, but not sufficient, conditions for the chosen neural network to be able to carry out the approximation. These conditions are established for the neural activation function, since the rest of the conditions will be automatically met if the selection is adequate. For use in approximation of feedforward backpropagation network functions, the following can be used, among others:
  - Tangent-sigmoid (a hyperbolic tangent).
  - Radial basis function (a Gaussian).
- Kolmogorov existence theorem for neural networks (Hetch-Nielsen). If the neural network has a minimum of three layers, it can reproduce any multivariate continuous function. In our case, when working with discrete data, this approximation will have an error that can be calculated.

These theorems allow us to select from among all the available ANNs those that have the greatest possibilities to adjust the models we need. We should not forget that these models, defined by their experimental data, must have a biunique relationship between inputs and outputs. This will force us to control the greatest number of variables in the problem that have a significant influence on it.

### 1.9.2 Neural networks in SHM

The last point of this brief introduction to Artificial Intelligence techniques, specifically Artificial Neural Networks, consists of a review of some of the applications of these techniques to the different problems of structural integrity monitoring. The application of these techniques is very varied and ranges from the generation of models of the structure itself to damage detection models. Firstly, we will discuss some applications for usage monitoring or prognosis.

They are mainly applied in the load modeling from aircraft flight parameters. This area is one of the most prolific in the application of ANNs. Examples are found for all types of aircraft, from military aircraft (Gómez Escalonilla et al., 2007; Meadows et al., 2009; Tuck and Kekoc, 2010) to helicopters (A. Liu et al., 2011; Valdes et al., 2011), where they are often combined with genetic algorithms. A more detailed description of the application of ANN and other AI techniques can be found in Schwabacher and Goebel, 2007. Secondly, applications of ANNs to the different SHM diagnostic techniques:

In passive SHM systems:

- Impact detection from the signals of the installed sensors. In this type of system, ANNs use some characteristic of the DSF as input and their output would be directly the position of the damage (del Río Velilla et al., 2024; Possetti et al., 2012). The reason for using this type of model is the high complexity in directly applying a triangulation algorithm from the impact echoes in composite material structures due to the anisotropy of wave propagation and its interaction with the different structural details.

- Energy Characterization of an Impact and Potential Damage Produced. An ANN is trained with impacts at different energies. Using sensor data, a correlation is created by means of an ANN between the impact signature in the DSF for different energies. This creates a kind of classifier that, based on the modification of the eigenmodes, establishes one type of damage or another in the structure (Sofge, 1994).
- Very similar to impact detection is the application of ANN to detect acoustic emission patterns (Kirikera, 2003) (AE) and classify them (Torres-Arredondo et al., 2013). There are examples of applications in which neural networks are used in an unsupervised manner to carry out such classification, AE patterns from a healthy structure and AE patterns from a damaged structure, even considering the EOC (García Alonso, 2016; Pedraza et al., 2023).

In active SHM systems, vibration, GLW, etc.:

- Within the field of vibration SHM techniques, there are examples in which ANNs are used to detect variations in the modal parameters of the structure produced by the presence of damage (Kirkegaard and Rytter, 1994). In this type of application, the neural network is adjusted in a multitude of situations with damage, in a supervised manner, and using FEM models. Measurements are then made on the damaged structure, and the network is fed to check if it detects the damage tested. Within the same technique, the power of ANNs is used to classify the different types of damage detected in a structure under the effect of environmental and operating conditions. This is one of the most complex situations since the EOCs significantly interfere with the damage signatures in the DSF, confusing the classical methodologies (Sohn et al., 2002).
- Systems based on guided elastic waves GLW also use ANNs for the most complex tasks. For example, for the identification and location of the presence of damage (Dworakowski et al., 2015; Su and Ye, 2005). They are also attempted to be used to cover all levels of SHM, even reaching the quantification of the severity of the damage (Sbarufatti et al., 2013), although training the models with FEM and simulating with the real structure. As for unsupervised systems, self-associative networks are used to differentiate the situation without damage from the presence of damage and, within the presence of damage, the different types (Tibaduiza et al., 2013).

  The latter is an example of how ANNs, applied to this type of problem, usually require additional complex preprocessing, such as a principal component analysis, some type of transformation, etc., which help the model to perform the classification. These additional processes help to extract what we have called the damage signature in the DSF (S. Liu et al., 2013). They are very useful in complex details of real structures (Haig and Haig, 2012) using the measured data directly and the models only as a design support for the model.
- For the structural impedance technique. In which the structural and electrical behavior of the sensor is coupled for damage detection, ANNs have also been used. It is an application very similar to pattern detection or classification. In this type of system, an ANN classifies changes in the structural impedance pattern into a series of predefined damages, in a supervised manner (Min et al., 2012).

Two main lines of work are typically used: In the first place, the ANN models are adjusted using physical models such as FEM finite element models (Gopalakrishnan et al., 2011), and then they are fed real data to check their operation. In the second, the experimental data are directly used to adjust the ANN model and also to check its operation (Armijo Torres et al., 2013). These latter are usually combined with complex signal analysis techniques to prepare the information such as the Wavelet Transform and others.

It will be necessary to ensure that the part chosen to be modeled meets the conditions for its realization. The literature establishes which levels of the SHM can be performed in an automatic or unsupervised way and which need to be supervised, thus complying with the applicability at all levels of the SHM (Worden and Manson, 2007).

# Chapter 2

# State of the art

## 2.1 Historical evolution

The evolution of Lamb wave simulation has mirrored advances in computational power, numerical methods, and SHM technology. From its theoretical foundations in the early 20th century, Lamb wave modeling has grown into a sophisticated field enabling the detection of structural defects in various materials and configurations. The state of the art includes high-fidelity simulations, data-driven approaches, and real-time SHM applications, making Lamb wave simulation an essential tool for maintaining the safety and integrity of modern structures.

### 2.1.1 Early Theoretical Developments (1917-1960s)

Early work on elastic waves has been well documented, since first explained by Lord Rayleigh in 1889 who derived the equations for wave propagation along a guided surface (Rayleigh, 1888). This particular case of elastic waves described are known as Rayleigh waves today. Following Rayleigh's work, Horace Lamb, a British applied mathematician, reported the waves discovered in plates in one of his historic publications: *O*n Waves in an Elastic Plate in 1917 (Lamb, 1917), and the waves were named Lamb waves after him. Horace Lamb established the theoretical rudiments of such waves also on solids and spheres (Lamb, 1881). Lamb waves initially garnered little attention because of the highly complex equations required to describe them. However, the topic was revisited by Osborne and Hart in 1945 when they studied Lamb waves generated in structures as a result of underwater explosions (Osborne and Hart, 1945) and their study unveiled much potential for applications of Lamb waves.

In the mid-20th century, as the need for non-destructive evaluation (NDE) grew, Lamb waves became increasingly important for inspecting metals and composites, particularly in industries such as aerospace and civil engineering. Theoretical work during this period focused on extending Lamb's original formulations, but practical simulations were constrained by a lack of computational power. A comprehensive solution to Lamb waves was completed by Mindlin, 1951, followed by considerable detail provided by Gazis, 1958 and Viktorov, 1967 who also first evaluated the dispersive properties of Lamb waves. Firestone and Ling

inaugurated Lamb-wave-based damage detection in the 1940-1950s (Firestone and Ling, 1945, 1951), after which Lamb waves found niche applications in seismology and NDE. In parallel with theoretical development, intensive experimental investigation, for the purpose of understanding fundamentals of Lamb waves, was contributed by Worlton, 1961 and Frederick and Worlont, 1962.

### 2.1.2 Numerical Methods and Advances (1970s-1990s)

The 1970s marked the beginning of significant progress in Lamb wave simulation thanks to the development of numerical methods. Finite element analysis became a powerful tool for modeling complex wave propagation problems in structures (Graff, 2012). These methods allowed for more detailed simulations of Lamb wave behavior, such as mode generation, interaction with boundaries, and reflection/refraction at defects. The Semi-Analytical Finite Element (SAFE) methods made their first appearance in the early 1970s (Aalami, 1973; Lagasse, 1973; Nelson et al., 1971) as an alternative to other methods matrix-based methods whose mathematical framework tends to be ill-suited for structures of increasing complexity.

In the 1980s and 1990s, computational advances made it possible to simulate Lamb waves more efficiently, though high-resolution simulations still required significant computational resources. The development of higher-order models and improved algorithms for solving wave equations expanded the range of materials and structures that could be analyzed, particularly in anisotropic materials such as fiber-reinforced composites or other complex specific problems (G. Liu and Quek Jerry, 2003; Moser et al., 1999). Other similar numerical techniques such as the boundary element method (BEM) have also started to be used in the field (Y. Cho and Rose, 1996).

### 2.1.3 Modern Simulation Techniques (2000s-Present)

By the 2000s, Lamb wave simulation had become a crucial part of SHM systems, driven by improvements in both computational power and sensor technology. The spectral element method, first developed by Maday and Patera, 1989, started to gain traction (Eisenträger et al., 2014; Kudela et al., 2007; Rucka, 2011). Other advanced methods such as time-domain and frequency-domain analyses (Frank Pai et al., 2015), and hybrid approaches combining analytical and numerical techniques (Shang et al., 2023; Svendsen et al., 2023) have also begun to be developed, allowing for more accurate and faster simulations of Lamb waves.

In addition, with the recent developments in artificial intelligence, AI-based surrogate models have started being used to approximate the results of high-fidelity simulations (FEM or SEM). These models are trained on a set of precomputed simulations and then used to predict the outcomes of new study cases with minimal computational effort. Surrogate models can significantly speed up the process of simulating wave propagation, especially for real-time SHM applications (de Paula S. Ferreira et al., 2024; Fakih et al., 2022; Ji et al., 2024).

Recent years have also seen significant improvements in FEM simulation software packages, such as Abaqus, COMSOL Multiphysics, and ANSYS, which now provide integrated environments for Lamb wave analysis, making simulation accessible to more engineers and researchers.

## 2.2 GLW simulation techniques

### 2.2.1 Analytical methods

Analytical methods for solving elastic wave propagation problems focus on finding exact or approximate solutions to the governing equations that describe the motion of elastic waves in solids. These methods are especially valuable for understanding the fundamental behavior of wave phenomena in simple geometries and material conditions.

Most of these analytical methods present approach to solving the elastic wave equation (also known as the Navier-Cauchy equation (Kolsky, 1964)):

$$\rho\ddot{u} = F + (\lambda + 2\mu)\nabla(\nabla \cdot u) - \mu\nabla \times (\nabla \times u) \tag{2.1}$$

where:

- $\lambda$ and $\mu$ are the Lamé parameters describing the elastic properties of the medium (Lyle and Salencon, 2012),
- $\rho$ is the density,
- $F$ is the source function (driving force),
- $u$ is the displacement vector

These analytical methods are highly effective for solving elastic wave propagation problems in idealized conditions and serve as a foundation for understanding more complex numerical methods such as the finite element method (FEM) and the spectral element method (SEM).

1. Separation of Variables

   Separation of variables is a classic technique used when governing equations, such as the wave equation, can be split into independent functions of each coordinate. This method is applicable in simple geometries like rods, plates, or rectangular domains where boundary conditions are well defined. Reduces a complex partial differential equation (PDE) into simpler ordinary differential equations (ODEs) for each spatial coordinate.

   For a 1D problem, assuming a rod of length $l$ undergoing small amplitude vibrations, the translation $u(x,t)$ follows the wave equation:

   $$\frac{\partial^2 u}{\partial t^2}(x,t) = v^2 \frac{\partial^2 u}{\partial x^2}(x,t) \quad \text{for all } 0 < x < l \text{ and } t > 0 \tag{2.2}$$

   were $x$ is the position in the rod, $t$ is the time and $v$ is the wave phase speed.

   The factorized function $u(x,t) = X(x)T(t)$ is a solution to the equation when:

   $$X(x)T"(t) = v^2 X"(x)T(t) \iff \frac{X"(x)}{X(x)} = \frac{1}{v^2}\frac{T"(t)}{T(t)} \tag{2.3}$$

   As both sides of the equation are constant, it is possible to solve the problem as a system of two constant ordinary differential equations, by imposing the boundary conditions.

The method has proven its effectiveness in the study of seismic waves (Cheng and Fomel, 2014; Sánchez Galvis et al., 2017). However, although theoretically possible, its application to GLW is limited due to the high difficulty in introducing the dispersive effect in the formulation (Annex B).

2. Fourier Transform Method

   The Fourier transform is commonly used for solving wave propagation in infinite or semi-infinite domains. By transforming the wave equation from the time domain into the frequency domain, the problem becomes easier to solve, especially for harmonic wave propagation. The inverse Fourier transform then retrieves the time-domain solution. This method is effective for problems involving scattering, reflections, and wave dispersion and can be used to solve the wave equation in infinite domains.

   Assuming the same conditions as lead to eq. 2.2, the basic observation is that for each fixed time point $t >= 0$, the unknown $u(x,t)$ is a function of one variable $x$. Therefore, by the Fourier series theorem and the odd periodic extension trick, $u(x,t)$ has, for each fixed t, a unique expansion of the form[1]:

$$u(x,t) = \sum_{k=1}^{\infty} b_k(t) \sin\left(\frac{k\pi x}{l}\right) \tag{2.4}$$

   The solution $u(x,t)$ is completely determined by the coefficients $b_k(t)$. These coefficients can be found by substituting eq. 2.4 into the wave equation and the problem's boundary conditions and solving the system.

   It could also be used to infer wave propagation velocities based on experimental results, although formulations such as the one presented in Draudviliene et al., 2021 may be done with a different approach.

3. Laplace Transform

   The Laplace transform is used to solve initial value problems by converting the time-dependent elastic wave equation into the Laplace domain. This transforms the PDE into an algebraic equation that can be solved more easily. The inverse Laplace transform is applied to return to the time domain. This method is particularly useful for solving transient wave propagation problems (Gangadharaiah and Sandeep, 2021).

   For example, to solve a simple 1D problem of a plane wave propagating in an infinite medium, as shown in Figure 2.1.

[1]This equation already satisfies a set of boundary conditions, in this case $u = 0$ for $x = 0, l$. Other periodic extensions, such as the even periodic extension, can result in different expansions of $u(x,t)$

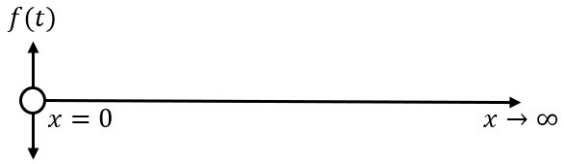


**Figure 2.1:** 1D model of a traveling plane wavefront on an infinite plate.

The wave equation (eq. 2.2) can be solved with the following initial conditions (IC) and boundary conditions (BC):

$$\begin{aligned} \text{BCs:} \quad & u(0,t) = f(t) \\ \text{ICs:} \quad & u(x,0) = 0 \\ & u_t(x,0) = 0 \end{aligned} \tag{2.5}$$

where $f(t)$ is the wave form. The following expression is then obtained by applying the Laplace transform in time to the wave equation:

$$s^2\bar{u}(x,s) - su_t(x,0) - u(x,0) = v^2\bar{u}_{xx}(x,s) \tag{2.6}$$

where $s$ is taken as a constant. Therefore, by substituting the ICs in the previous equation, the wave equation can be transformed into an ODE that can be solved by conventional methods:

$$\bar{u}(x,s) - \frac{v^2}{s^2}\bar{u}_{xx}(x,s) = 0 \tag{2.7}$$

The Laplace transform may also be used to solve coupled thermoelastic equations and reach solutions that may consider dynamic heating effects and thermal waves (Blanchard, 2003).

4. Method of Characteristics

   The method of characteristics (Sasoh, 2020) is a technique used to solve hyperbolic PDEs, like those governing wave propagation. It transforms the PDE into ordinary differential equations along characteristic lines that represent the paths along which information travels. This method is particularly useful for analyzing wavefronts and shock waves in elastic media (Z.-h. Wang et al., 2022).

5. Rayleigh-Lamb Theory

   Rayleigh-Lamb theory is specifically used for solving elastic wave propagation in thin plates. It provides a solution for guided waves propagating in two-dimensional structures. The theory involves solving the wave propagation velocity for the desired material properties and plate thickness and assuming a linear propagation in the structure (Muñoz Chamorro, 2018).

   It can be useful to generate wave propagation maps in a structure, determine times of arrival, perform basic triangulation of damages (Vázquez et al., 2024) and can be enhanced with artificial intelligence techniques to consider EOCs and increase accuracy and reliability(Pedraza et al., 2023).

6. Other GLW analytical solutions

   There are other analytical solutions to the guided Lamb wave propagation problem that have been developed to complement or improve upon the ones mentioned previously; particularly when dealing with specific geometries, boundary conditions, or material characteristics. These solutions often involve different approaches to model wave behavior more effectively in complex environments, either by simplifications of the Navier-Cauchy equation (X. He et al., 2022), to better characterize or enhance some features that may not be immediately available in commercial numerical simulation software, such as viscoelasticity (S.-Y. Kim and Lee, 2009) or other specific behaviors. Or to extend SAFE methodologies to specific geometries or damage modeling Bartoli et al., 2006; Chiappa et al., 2021; Gavrić, 1994.

### 2.2.2 Numerical methods

#### Finite Element Method

Finite Element Method (FEM) is a numerical technique widely used in engineering and applied sciences to solve complex problems involving partial differential equations (PDEs) over complicated geometries; it is commonly used in civil, mechanical, aerospace, and automotive engineering to design and optimize structures, materials, and systems. FEM breaks down a large, complex structure or system into smaller, simpler parts known as finite elements. These elements are interconnected at specific points, called nodes, forming a mesh that approximates the geometry of the structure.

Each element behaves according to the governing physical laws (such as elasticity, heat conduction, or fluid flow), and by solving these equations for all elements together, FEM provides an approximate solution to the entire problem. This method is especially useful for problems that involve stress analysis, heat transfer, fluid dynamics, and electromagnetic fields, where exact solutions are difficult to obtain.

A time domain numerical solution can be obtained using either an implicit or explicit approach.

**Implicit dynamics:** the equations of motion are solved using an implicit time integration scheme, such as the Newmark beta method or the backward Euler method. At each time step, a system of simultaneous equations must be solved, which involves inverting a stiffness matrix. Although this makes each time step computationally more expensive, implicit methods are unconditionally stable, allowing for larger time steps. Although it is generally used to solve linear or non-linear static problems, it is also possible to solve the full equations of motion in an implicit way and therefore solve the GLW propagation problem (X. Liu et al., 2022). The main characteristics of this method are:

- Time stepping: Implicit methods require solving a system of equations at each time step, which can be computationally expensive. Matrix inversion is required for each time step; this makes each time step slower, but larger time steps can be taken.
- Unconditionally stable: Stability is maintained even with larger time steps, although accuracy still depends on the size of the time step.

- Suitable for long-duration simulations: Effective for problems where the time scale is larger and for solving static or quasi-static problems with a steady-state solution.

**Explicit dynamics:** the equations of motion are solved directly using an explicit time integration scheme, typically the central difference method. The key feature of this approach is that the displacement of the system at a given time step depends only on the information from the previous time step. There is no need to solve a system of simultaneous equations, which makes explicit FEM computationally faster per time step. However, small time steps are required for stability, which often requires more steps for long simulations.

The explicit dynamics method has been used extensively for the simulation of GLW propagation in the time domain (de Luca et al., 2018; F. Li et al., 2018; Ong et al., 2016; Sánchez Iglesias and Fernández López, 2020). Its main characteristics are:

- Time stepping: The solution advances in small, incremental time steps. However, since no system of equations is solved at each time step, the method is computationally efficient, and it does not require matrix inversion.
- Conditionally stable: The method is stable only if the time step is smaller than a certain critical value (related to the size of the smallest element and the properties of the material, known as the Courant–Friedrichs–Lewy (CFL) condition (Jacob and L., 2002)).
- Efficient for large-scale, short-duration simulations: Ideal for problems involving high-speed events such as impact, crash simulations, explosions, or other situations involving wave propagation and shocks.

The finite element method is highly flexible and can be applied to problems in 1D, 2D, or 3D, making it suitable for modeling complex geometries and varying material properties. However, FEM models still present a series of significant disadvantages that make them not suitable to be used in some SHM system applications. Some of the most limiting ones could be the following:

- Grid or element discretization: discretizing the structure into grids or elements may result in some loss of accuracy, difficulties in capturing fine details, or aliasing effects on high frequencies. The choice of grid or element size can affect the accuracy and computational cost of the analysis and is usually a limiting factor for the maximum scale of structures to be analyzed.

  Kocbach, 2000 recommended a minimum of 10 elements per wavelength to ensure consistent results in the simulation. The number of elements $M$ that must be used to cover a length $L$ with $P$ elements per wavelength can be obtained by applying the following relationship:

$$M = \frac{PL}{\lambda} = \frac{PLf}{c} \tag{2.8}$$

  where, $c$ is the wave group velocity, $\lambda = c/f$ is the wavelength and $f$ is the frequency, which typically results in element sizes smaller than 1 mm, as shown in Figure 2.2.

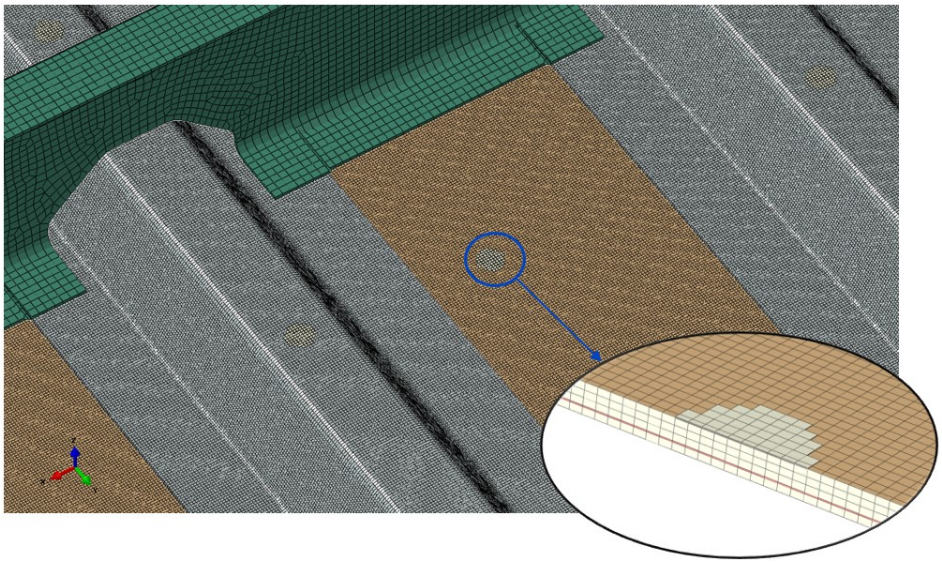

**Figure 2.2:** FEM model of a piezoelectric sensor for GLW simulation (Sánchez Iglesias et al., 2016).

- Computational complexity: methodologies for both explicit and implicit analyses tend to be computationally intensive, especially for large and complex structures. Long computation times and high memory requirements may limit their efficiency and applicability to machine learning approaches.
- Material damping or boundary damping: specifically for the explicit dynamics analyses, introducing damping elements, either as dashpots or material damping, significantly reduces the stable time increment, making it exponentially more costly to solve problems where this effect is relevant on the solution.

### Spectral Element Method

The Spectral Element Method (SEM) is a numerical technique used to solve PDEs, combining aspects of both the Finite Element Method (FEM) and the spectral methods. Like FEM, SEM divides a domain into elements to solve problems in complex geometries, but uses high-order polynomials within each element to approximate the solution, giving it greater precision (Ostachowicz et al., 2011).

In SEM, each element is treated using spectral techniques, where the solution is approximated by a series of high-degree polynomials, often based on Legendre or Chebyshev polynomials. These high-order polynomials allow SEM to achieve exponential convergence for smooth problems, meaning that it can offer very accurate solutions with fewer elements compared to standard FEM. This results in high computational efficiency, especially for problems that require fine resolution or involve wave propagation, fluid dynamics, or elasticity.

SEM is particularly useful in fields like seismology (Xu et al., 2021) and fluid mechanics (Patera, 1984) where both complex geometries and high accuracy are needed. Its combination of FEM's geometric flexibility and spectral methods' precision makes SEM a powerful tool for solving large-scale and high-frequency problems.

It has also been widely used for simulation of GLW and, along with Explicit FEM, is one of the most widely used methods for solving this kind of problems (Han, 2007; Palacz et al., 2020; Schulte and Fritzen, 2010), being able to represent complex geometries and curvature (Matuszyk, 2017), interfaces (H. Chen et al., 2022) and even orthotropic materials (Kudela and Ostachowicz, 2008; Kudela et al., 2018a) with high accuracy, although it presents similar drawbacks as the finite element method and is less flexible in the kind of structures able to represent.

### Stochastic Finite Element Method

Stochastic Finite Element Method (SFEM) is an extension of the traditional Finite Element Method (FEM) used to account for uncertainties in material properties, boundary conditions, loads, and geometry in engineering analysis. Although FEM is a widely used numerical method for solving complex structural and physical problems by dividing a structure into smaller, manageable elements, SFEM goes further by incorporating randomness or uncertainty into these models (Haldar and Mahadevan, 2000; Stefanou, 2009).

In SFEM, parameters such as material strength, elasticity, or external loads are treated as random variables or stochastic fields rather than fixed values. This allows engineers and researchers to perform a more realistic analysis of how uncertainties affect the performance and reliability of a structure or system. SFEM typically involves techniques like Monte Carlo simulations, perturbation methods, or polynomial chaos expansion to propagate uncertainties and evaluate their impact on the system's behavior (Arregui-Mena et al., 2016).

SFEM is particularly valuable in fields like civil engineering, aerospace, and mechanical engineering, where exact conditions are often unknown or variable, and understanding the probability of failure or behavior under uncertain conditions is critical.

It has also been used for SHM to solve some specific problems dealing with high anisotropy of materials and stochastic damage models ("Application of SFEM to SHM: Simplified Damage Models", 2008; Van Pamel et al., 2017).

### Boundary Element Method

Boundary Element Method (BEM) is a numerical technique used to solve PDEs that arise in engineering and physics, particularly for problems involving complex geometries. Unlike the Finite Element Method (FEM), which discretizes the entire volume of a structure, BEM only requires discretization of the structure's boundaries. This makes BEM highly efficient for problems where the domain extends infinitely, such as in acoustic, electromagnetic, or fluid flow simulations.

In BEM, the problem is formulated in terms of boundary integrals rather than volume integrals, which reduces the dimensionality of the problem by one (for example, a 3D problem becomes 2D on the surface). This significantly reduces the computational cost, especially for problems with large or infinite domains, such as the problem shown in Figure 2.3, since only the boundaries need to be discretized. However, BEM is most effective for problems where the material properties are uniform, as it can be more challenging to apply in cases with varying internal properties.

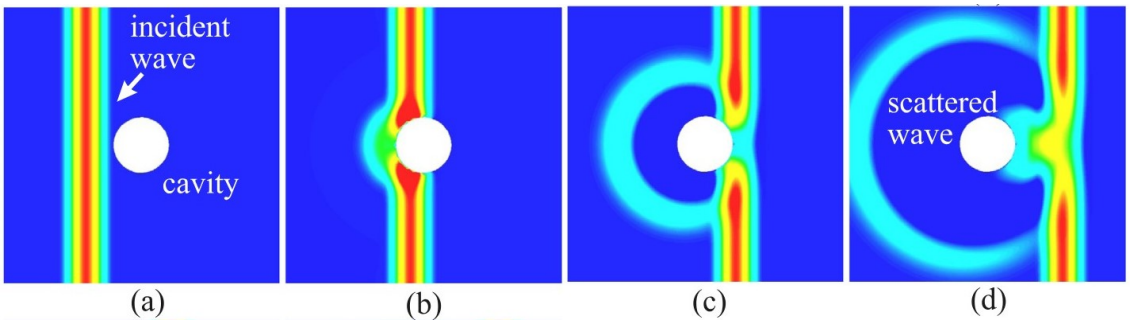


**Figure 2.3:** Simulation of a wave displacement field around a cavity in isotropic material with BEM at times: (a) $t = 0.0$, (b) $t = 1.6$, (c) $t = 3.2$, and (d) $t = 4.8$ (Saitoh, 2024).

Common applications of BEM for EW propagation include seismography (Ge and Chen, 2008) fluid dynamics, and potential flow problems in electromagnetism and acoustics. Its advantages in handling infinite domains and in reducing problem dimensionality make it a powerful tool for certain types of engineering analysis. It has been used in SHM to reduce the domain size (Marrazzo et al., 2023), for GLW propagation (Gravenkamp, 2014), and it could also present some potential benefits when used in combination with FEM or SEM (Ehsani et al., 2023).

### Semi analytical Finite Element methods

The Semi-Analytical Finite Element (SAFE) method has recently emerged as a powerful approach to address wave propagation in dispersive media. It is particularly well-suited for modeling wave transmission along waveguides with arbitrary cross-sections. Initially introduced in the early 1970s as an alternative to matrix-based methods, the SAFE method offers a more flexible mathematical framework. The approach takes advantage of the periodic nature of wave propagation along the guide through analytical representation, while the waveguide's cross-section is discretized using finite elements to account for its specific geometry.

Typical applications of the SAFE method include modeling wave propagation in shell-like structures (Gavrić, 1994) and rails (Gavrić, 1995). A key advantage of this technique is its ability to capture evanescent modes, which are nonpropagating waves that decay exponentially (K. Huang and Dong, 1984). Over the past few decades, the method has been extended to handle damped waveguides with both axisymmetric (Marzani et al., 2008)and arbitrary cross-sections (Bartoli et al., 2006). In several cases, the SAFE method has been successfully applied to solid media, especially in problems involving the interaction between waveguides and fluids (Duan and Kirby, 2019; Kalkowski et al., 2018; Mazzotti et al., 2019). More recently, the SAFE method has been integrated with the Global Matrix Method in a hybrid approach that enforces stress continuity at interfaces within multi-layered structures Joseph et al., 2019.

This hybrid FE-SAFE approaches have enabled the study of guided wave interactions with discontinuities (Karunasena et al., 1995), defects (Benmeddour et al., 2011) or welded sections (Rattanawangcharoen et al., 1997). In regions near singularities, the model employs classical FEM or BEM, while the SAFE formulation is used to effectively describe the far-field behavior

(Galán and Abascal, 2002, 2003). These developments demonstrate the versatility of the SAFE method in addressing increasingly complex wave propagation problems in structural health monitoring and nondestructive testing.

### Ray-tracing

There are, however, other numerical approaches that may breach the problems issued above, specifically, the Ray-Tracing Method; which is based on the assumption that the particle motion can be modeled as a number of idealized narrow beams (rays) advanced through the medium by discrete amounts. Tracing the paths of individual rays provides valuable information about wave behavior, including wavefront curvature, mode conversion, reflection, and transmission as the rays interact with the objects present along their path.

Ray-tracing is widely recognized for its contributions to computer graphics, where it is used to simulate realistic lighting, shadows, and reflections in visual renderings. Due to recent development in high-end graphics card technology, the method has been extensively developed as a computer graphics technique used to simulate the way light interacts with objects in a 3D environment to produce highly realistic images. It works by tracing the path of light rays as they travel through a scene, calculating how they interact with surfaces and materials (through reflections, refractions, or shadows) to determine the final color and brightness of each pixel in an image (Figure 2.4). ray-tracing is widely used in visual effects, rendering, and real-time graphics, especially in movies, video games, and simulations (Aila and Laine, 2009).

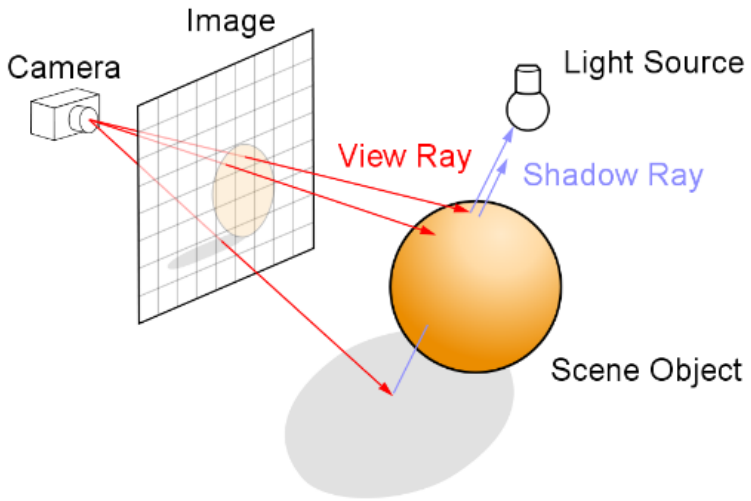


**Figure 2.4:** ray-tracing rendering of an image by casting rays into a scene (Nikodym, 2010)

Because of the complexity of light calculations, ray-tracing is traditionally used in pre-rendered scenes (e.g., movies, visual effects) where rendering time is not a constraint, rather than real-time applications like video games. However, with modern advances, real-time ray-tracing is becoming more feasible, and some graphics cards such as NVIDIA or AMD already have technologies that make it commercially available (Figure 2.5).


**Figure 2.5:** Refraction in the water modeled with NVIDIA real-time ray-tracing rendering technology. Left: Without ray-tracing, right: with ray-tracing (Burnes, 2024)

However, the applications of the ray-tracing method extend far beyond the realm of digital imagery. It can aid in precisely modeling how light interacts with complex surfaces and media, offering insights into the behavior of optical systems. In addition to its role in developing cutting-edge imaging technologies and virtual environments, ray-tracing plays a crucial role in fields that require high precision and accuracy in the manipulation of light. Most commonly associated with the design and analysis of advanced optical systems, ray-tracing is essential for everything from camera lenses to medical imaging devices, ensuring optimal performance and clarity. Modern innovations may highlight its relevance in entertainment and engineering; it has also been continually used historically for science and research in different fields such as astronomy (Peterson et al., 2015) or optical design (Spencer and Murty, 1962); In both applications, ray-tracing helps researchers and engineers design instruments, understand optical phenomena, and create models that predict how light propagates through complex environments.

- **Lens, mirrors and telescope design:** It allows to simulate how light enters a camera or telescope, reflects off mirrors, passes through lenses, and forms images on detectors to ensure that the image is properly focused, sharp, and free of distortion (Fuse et al., 2022; Yu et al., 2023).
- **Analysis of Optical Aberrations:** helps optical designers understand and correct aberrations in lenses and mirrors. Aberrations such as distortion, coma, and astigmatism can degrade the performance of optical systems. ray-tracing allows designers to simulate these effects and find solutions, such as adjusting lens curvatures or introducing corrective elements. For example, correcting chromatic aberration in refractive telescopes (Reshidko et al., 2014) or spherical aberration in reflective telescopes (Elagha, 2017) is crucial for producing sharp and accurate images of distant celestial objects.

- **Non-Imaging Optics:** such as light guides, reflectors, and illumination systems. These systems do not form images but control the distribution of light in a specific manner, such as in LED lighting or solar concentrators. ray-tracing allows to optimize how light is directed and distributed, improving efficiency and performance (Shen et al., 2014).
- **Simulation of Observations and Gravitational lensing:** gravitational lensing is a phenomenon in which light from a distant object is bent by the gravitational field of a massive foreground object. This effect can create multiple images or magnifications of the same object. ray-tracing can be used to predict and analyze the paths light rays take through gravitational lenses, aiding in the interpretation of astronomical data and the study of dark matter and the large-scale structure of the universe (Killedar et al., 2011).

Radiative heat transfer is one of the three modes of heat transfer (along with conduction and convection) and occurs through the emission, absorption, and scattering of thermal radiation. Unlike conduction or convection, which require a medium (like air or a solid) to transfer heat, radiation can occur across a vacuum and is governed by the emission of electromagnetic waves, typically in the infrared spectrum.

The process involves following the paths of thermal radiation rays as they travel from hot surfaces or sources, interact with other surfaces, and are either absorbed, reflected, or transmitted (Figure 2.6). This method is especially useful when dealing with complex geometries or environments where heat transfer is predominantly radiative (Piqueras et al., 2020).

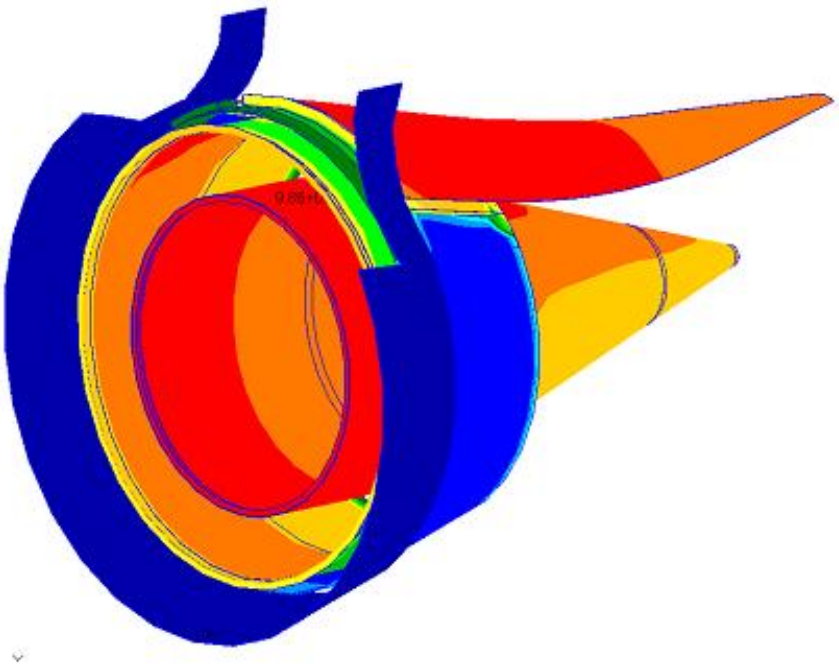

**Figure 2.6:** Radiative heatmap results on aircraft engine. (*ESATAN-TMS 2023 thermal modelling suite*, 2024).

The ray-tracing-based approach offers significant advantages over traditional numerical methods in terms of computational efficiency and ease of implementation, as it is not limited by an element size, although a large number of rays may be limiting in some applications. It is not limited to visual rendering, as it can also be applied to simulate sound propagation in various environments. In the context of acoustics and sound engineering, it involves tracing the paths of sound waves as they interact with the boundaries given by the structure. This technique allows for the modeling of how sound behaves in complex 2D or 3D environments, considering factors such as reflection, diffraction, and absorption.

Similarly to how ray-tracing is used in optics to simulate light, in sonar acoustics, ray-tracing calculates the paths taken by sound waves as they travel through underwater environments (Figure 2.7), taking into account factors such as changes in water temperature, salinity, pressure, and ocean topography (Cerqueira et al., 2020; Hovem, 2010; Officer, 1958).

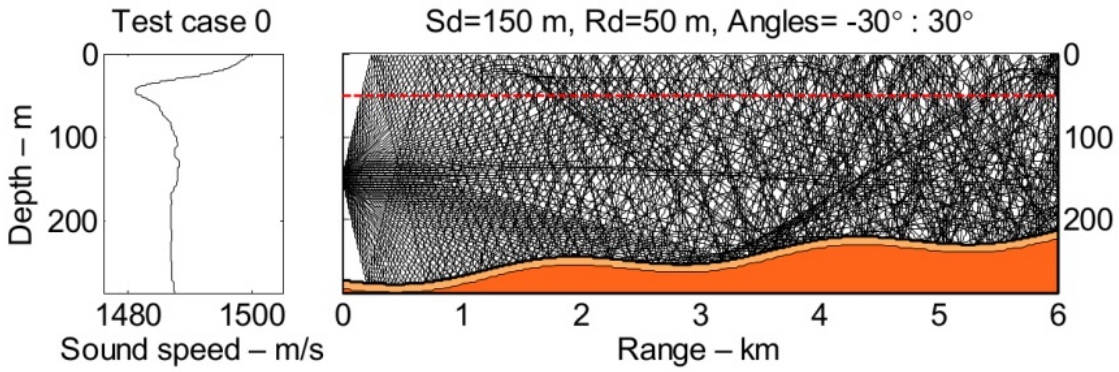


**Figure 2.7:** Sound speed profile and ray traces for a typical underwater sonar acoustics case. The source depth is 150 m and the red dotted line indicates a receiver line at a depth of 50 m. The initial angles of the rays at the source are from –30º to 30º. (Hovem, 2010).

In terms of SHM, the methodology has also been previously used to solve the guided wave propagation problem, and it has proven its effectiveness. Ray-tracing offers a valuable approach for simulating Lamb wave propagation, especially when computational efficiency is a priority. By tracing the paths of waves through complex structures, it could aid in optimizing SHM systems, design nondestructive testing protocols, and understand how waves interact with defects and boundaries (Ogilvy, 1990). Although it may not capture all aspects of wave behavior as fully as more computationally intensive methods, ray-tracing remains an important tool in the study and application of Lamb waves in materials science and engineering.

In elastic wave propagation, the concept of ray-tracing is borrowed from optics, where individual rays are traced as they travel through a medium. For Lamb waves, this involves modeling the wave energy as it travels along specific paths or rays through the structure (Ogilvy, 1992). Each ray represents a small portion of the wavefront, and by tracing a sufficient number of rays, it is possible to simulate the overall wave behavior in a complex medium and reconstruct the elastic wave displacement field (Figure 2.8).

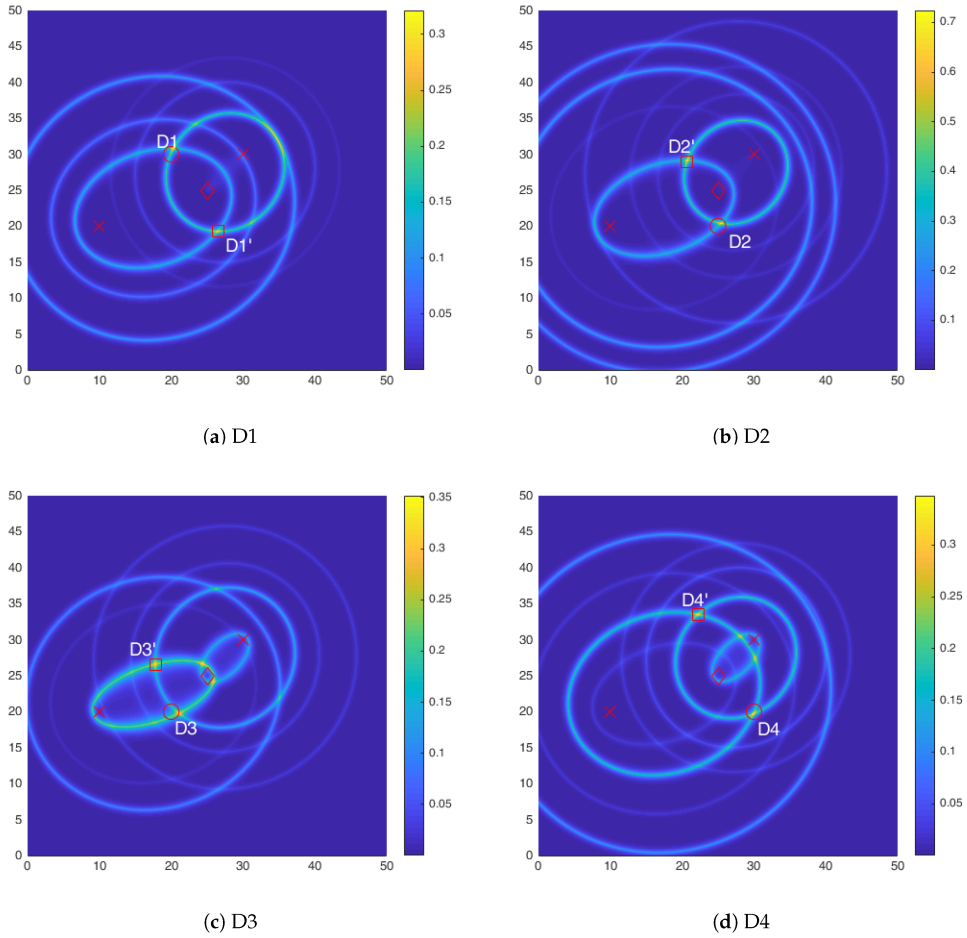


(a) D1 (b) D2

(c) D3 (d) D4

**Figure 2.8:** Ray-tracing based triangulation of damage hotspot for four damage scenarios. (a) D1; (b) D2; (c) D3; (d) D4. (Soman et al., 2020).

The method has been applied to solve multiple problems in the field, such as tracing possible reflections individually implementing a multipath baseline-free damage imaging method (L. Huang et al., 2020), applying it to iterative tomography to reconstruct Lamb wave velocity maps (Malyarenko and Hinders, 2001), using two-step algorithms to identify possible propagation paths and computing the sensors signals Heinze et al., 2014, tracing reflections from an initial ray beam in inhomogeneous media in CFRP (Qin et al., 2024) or ceramic materials (Shivaprasad et al., 2016), or even to aid in the interpretation of experimental results (Soman et al., 2020).

However, when applied for GLW propagation, ray-tracing could present some challenges or limitations, such as:

- **Accuracy:** While ray-tracing is efficient, it may not capture the full physics of Lamb wave propagation, especially for complex wave interactions. It is typically less accurate than full numerical methods such as FEM when modeling highly dispersive or strongly scattering environments.

- **Complex Boundary Conditions:** Modeling Lamb wave interactions with complex geometries or boundaries using ray-tracing can be challenging. In these cases, hybrid methods that combine ray-tracing with other numerical techniques are sometimes used.
- **Wave Amplitude:** ray-tracing focuses primarily on wave paths and phase, but it may not accurately model changes in wave amplitude or energy dissipation, which are important for detecting small defects.

### 2.2.3 Artificial intelligence training approaches

The application of artificial intelligence (AI) to guided Lamb wave propagation has gained significant attention in recent years, particularly in the development of surrogate models, as traditional numerical methods, such as FEM, SAFE or SFEM, can be very computationally expensive when dealing with GLW in large or complex structures, high-frequency waves, or they can present limitations to model complex material or structural behaviors (contacts, riveted joints, etc.).

Surrogate models serve as simplified representations or approximations of complex numerical simulations. Instead of performing detailed computations for every new simulation, these models are trained to predict the outcome based on a relatively small set of training data, significantly reducing computational time while maintaining accuracy (Ranftl and von der Linden, 2021). AI-based surrogate models use machine learning (ML) to learn the underlying patterns of wave propagation, enabling near-instant predictions (Diaw et al., 2024).

Although, by definition, pretty much any AI algorithm could be used as a surrogate model, the following techniques are commonly used in literature:

- Artificial Neural Networks (ANNs): Neural networks, particularly deep learning models, are frequently employed to approximate the behavior of Lamb waves. By training on a dataset generated from high-fidelity numerical simulations (e.g., FEM or SAFE), a neural network can learn to predict wave behavior, including the dispersion characteristics, interaction with defects, and mode conversions, in real time. This allows for quick evaluation of the Lamb wave responses under various conditions, such as changes in material properties, geometry, or wave frequency (Dadras Eslamlou and Huang, 2022).
- Convolutional Artificial Neural Networks (CNNs): CNNs are effective in processing large amounts of spatial data, such as Lamb wave fields. For example, CNNs can be trained on wavefield images or sensor data to detect and classify defects in structures. These models are particularly powerful in capturing features of wave propagation and scattering that are otherwise difficult to describe analytically (Kneifl et al., 2024; Silionis et al., 2024; Sony et al., 2021).
- Gaussian Process Regression (GPR): GPR is another technique used to build surrogate models for guided wave propagation. It offers a probabilistic approach, in which predictions come with an associated uncertainty measure. GPR models are effective when the dataset is small, as they can efficiently interpolate between known data points to predict Lamb wave behavior under untested conditions (Marrel and Iooss, 2024).

- Reduced-Order Models (ROMs): AI is also applied to create reduced-order models that compress complex Lamb wave simulations into lower-dimensional representations while retaining essential features. These models allow for faster simulations of wave propagation in large or multi-layered structures. ROMs, combined with neural networks, can significantly speed up iterative processes such as defect localization or material characterization (Sánchez Iglesias et al., 2017; Torzoni et al., 2023).

Physics-informed machine learning (PIML) is an emerging paradigm that integrates physical laws into machine learning models. This approach is especially useful in complex fields like GLW propagation, where purely data-driven methods might struggle due to a lack of interoperability or require extensive training data, while traditional numerical methods can be computationally expensive (Cross et al., 2021).

By embedding known physical principles into machine learning models, physics-informed neural networks or other PIML techniques can provide more efficient and accurate solutions, for SHM and NDT. These methods reduce reliance on large datasets and ensure that predictions remain physically consistent, making them highly suitable for real-world scenarios (Pinello et al., 2024).

# Chapter 3

# Materials and methods

## 3.1 Experimental work

This chapter details the experimental investigations conducted to validate the theoretical and numerical analyses of guided Lamb waves presented in the preceding sections. The experimental work presented in this study is centered on validating and refining the simulation techniques used for SHM, both via FEM and with the ray-tracing model, introduced later. The testing campaign will focus on generating reliable and reproducible data on guided Lamb wave behavior in a controlled environment, providing a baseline for evaluating how elastic waves propagate through various materials and interact with defects. Another objective is to assess the accuracy and effectiveness of piezoelectric transducers (PZTs) sensors in detecting and characterizing wave signals and validate the simulation sensor model, ensuring precise measurements of waveforms, amplitudes, and time of flight (ToF).

The key focus of this section relies on comparing the experimental data with the predictions from ray-tracing simulations to validate the computational models. This comparison is essential to determine the accuracy of the model in predicting wave paths, reflections, and mode changes caused by defects or structural features. The experimental work seeks to refine these models by adjusting for any discrepancies between predicted and measured wave propagation behavior.

The experiments performed are grouped into the following main groups or sets:

- Aluminum plate: a simple rectangular homogeneous aluminum plate used to validate the numerical methodologies studied in this thesis and to better understand basic GLW propagation and damping mechanisms.
- Square composite panels: Two panels of a standard quasi-isotropic CFRP laminate, intended to validate the GLW propagation in orthotropic materials and to evaluate the effect of a T-shaped stiffener on the waves.
- UAV wing lower cover demonstrator: Intended to validate the method in a representative CFRP aeronautic structure and to evaluate the effect of thickness changes, the presence of damages, both simulated (with added masses) and real (using a gravity impactor), and

the accuracy and viability of implementing the SHM system in small-scale structures.

The experiments aim to highlight the sensitivity and limitations of Lamb wave-based SHM systems. By exploring wave interaction under different conditions and damage scenarios, the work seeks to optimize sensor placement, improve damage detection algorithms, and better understand the mechanics of wave propagation in complex structures.

The main objectives of the experiments include:

- Mode Identification and Validation: To excite and isolate specific Lamb wave modes predicted by theoretical models and study their propagation and damping within the structure.
- Defect Detection and Localization: To evaluate the interaction of Lamb waves with simulated defects and measure reflections, mode conversions, and scattering effects.
- Numerical model validation: The experiments aim to replicate representative aeronautic structures and serve as a validation benchmark for the numerical models tested in this thesis.

All experimental work presented in this thesis is performed with piezoelectric (PZT) transducers, due to their many advantages for SHM, as described in Section 1.8.2, such as their low cost, simplicity in post-processing sensor data, and the ability to generate and receive GLW with the same transducer.

### 3.1.1 Active interrogation tests

The main goal of active interrogation is to detect, localize, and characterize potential damage within a structure. By actively introducing a known excitation (GLW for this case study) into the structure, an SHM system could monitor how these waves propagate and interact with the material. Reflections, scattering, or changes in the wave characteristics, when compared with a previous measurement, can indicate the presence of damage, as elastic waves will behave differently when passing through intact versus damaged areas.

In active interrogation, elastic waves are generated using a PZT transducer actuator. The installation of these sensors is described in Annex E. Due to the piezoelectric effect, the PZT transducer converts electrical energy into mechanical vibrations, which in turn generate guided waves that propagate through the material, and, at the same time, the same sensor can be used to measure those waves.

Once the wave is generated, it propagates through the material. The wave interacts with any boundaries, defects, or heterogeneities in the material, which may cause reflections, mode conversions, scattering, or attenuation. In the presence of crack, delamination, or other forms of damage, the behavior of the wave will change. These changes are key indicators of potential structural issues.

Other PZT sensors placed on the structure can detect transmitted and reflected waves. The sensors convert mechanical vibrations back into electrical signals, which can be recorded and analyzed by the DaQ system.

### Input signal analysis

The active emission tests are performed with the Acellent Technologies SCANGENIE (Figure 3.1), which is a purpose-built "active" acousto-ultrasonic DAQ from a network of PZT sensors mounted or embedded within a structure. It supports up to 64 PZT channels and can interface with additional types of sensors such as smart layers (*Scangenie setup and operation guide*, 2007).


**Figure 3.1:** Acellent Technologies ScanGenie DAQ.

A summary of the main ScanGenie system specifications is shown in Table 3.1.

**Table 3.1:** Acellent Technologies ScanGenie specifications summary (*Scangenie setup and operation guide*, 2007).

| **Characteristic** | **value** |
|---|---|
| Interrogation signal type | BURST3, BURST5, BURST10 or custom up to 1024 points |
| Max interrogation frequency | 700 kHz |
| Analog channels | 64 (Input / Output) |
| Sampling rate | 48 Msp |
| Output signal voltage range | $\pm 75$ V |
| Digital-Analog converter | 12 bit adjusted to $\pm 1$ V |
| Maximum acquisition datapoints | 32000 (per channel) |

The hardware can be controlled with proprietary software: Accellent Access(*Acess 2.0 user's manual*, 2007) that can export the data in a Matlab dataset.

For the input signal, in the case of active interrogation, a tone burst ($s(t)$) named with the convention BURST-$n$ is generated by modulating a sinusoid of frequency $f$ with a Hann window, where $n$ represents the width of the window in number of periods.

$$s(t) = \text{Hann}(n/f) * (\sin(2\pi f t)) \tag{3.1}$$

A 250 kHz BURST-3 signal in its time domain, as generated by the Acellent SCANGENIE DaQ, is shown in Figure 3.2a and its FFT in Figure 3.2b.

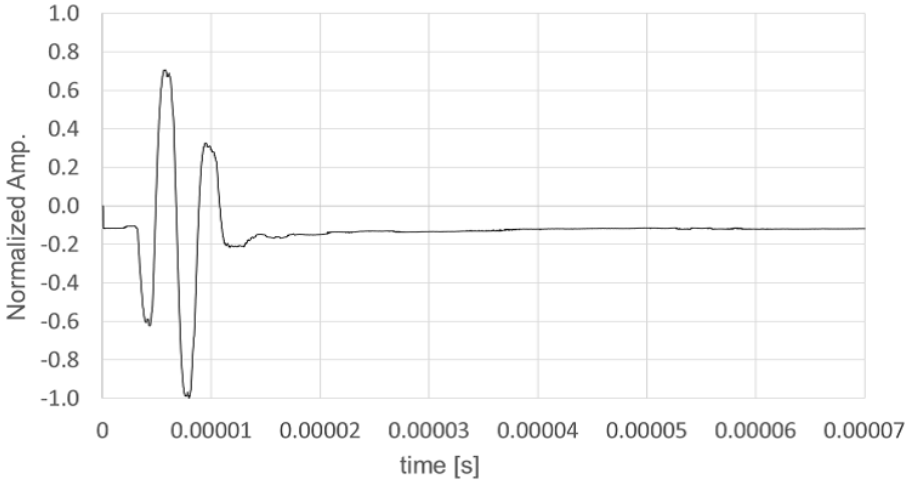


**(a)** BURST-3 signal, as generated by SCANGENIE

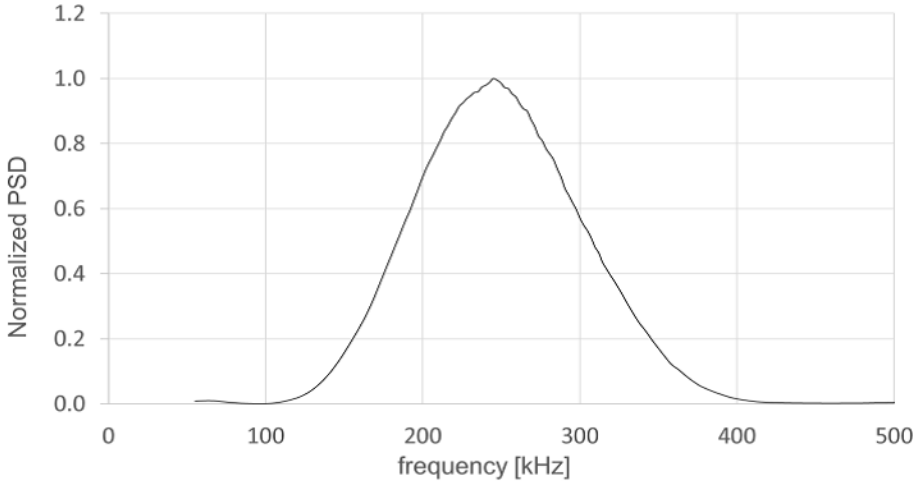


**(b)** Frequency spectrum (Power Spectral Density) for the BURST-3 signal

**Figure 3.2:** BURST-3 input signal for active interrogation at 250 kHz

All tests are performed with a three-cycle burst signal (BURST-3), with an amplitude in a range from 10 V to 50 V peak to peak. The frequency of the excitation studied is comprised in the range of 100 kHz to 500 kHz.

### Rectangular aluminum plate

The methodology is first validated against a physical test on a 2023-T3 rectangular aluminum plate of aeronautic grade, as shown in Figure 3.3.

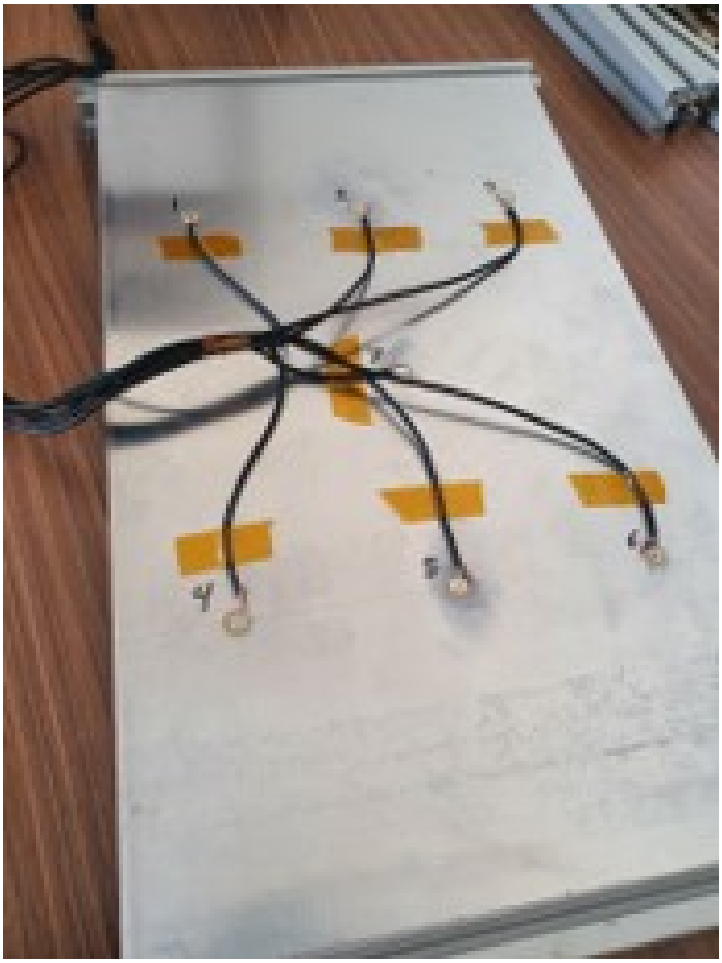

**Figure 3.3:** Underside of the aluminum plate and PZT sensors.

Aluminum, known for its lightweight properties, high strength-to-weight ratio, and corrosion resistance, is a critical material in many industrial applications. When employed in thin plate structures, such as aircraft skins, aluminum is particularly well-suited for inspection using Lamb waves; therefore, this aluminum plate configuration could represent an ideal medium for studying guided wave behavior due to their simple geometry and widespread use in engineering.

The plate used in the experiment is simply supported along two of its edges to create a boundary condition that approximates the structural constraints commonly encountered in practical applications. Although the presence of simply supported boundaries may introduce localized effects such as reflections and mode conversions, these influences are considered negligible for the purpose of the simulation and are not explicitly modeled. Instead, a uniform energy loss assumption is adopted to account for wave attenuation at the boundaries,

simplifying the computational analysis.

The experimental setup is instrumented with an array of seven piezoelectric sensors, which are evenly distributed across the test specimen to ensure comprehensive spatial coverage and accurate wave detection. Each sensor consists of an 8 mm PZT ceramic wafer bonded to a 12 mm diameter bronze backing disc. This configuration is selected to enhance both sensitivity and robustness, providing reliable performance for the excitation and detection of guided Lamb waves. The sensors are evenly distributed on the plate, as shown in Figure 3.4. Data is recorded with an Acellent SCANGENIE DaQ system, with a sampling frequency of 48 Msps.

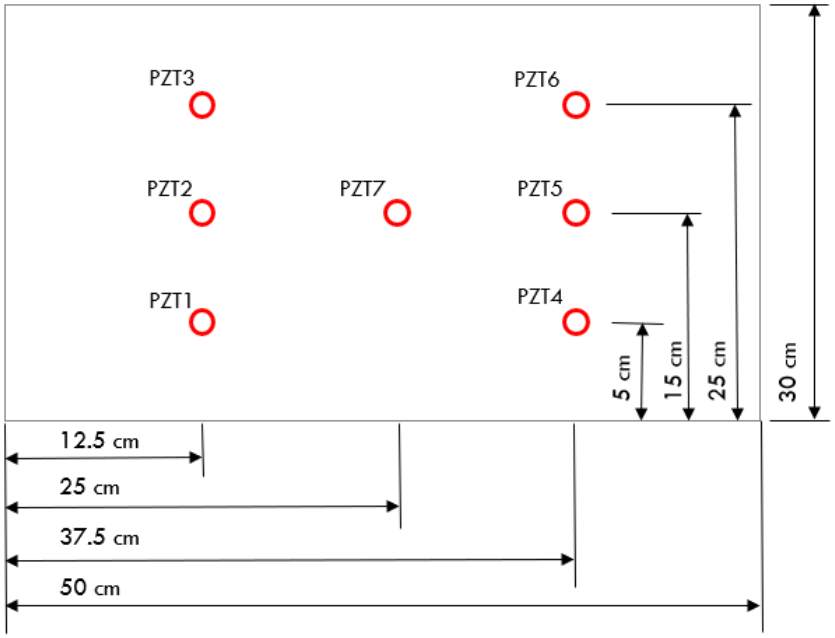


**Figure 3.4:** Schema of the aluminum plate dimensions and PZT transducers positioning.

Additional considerations are made to minimize extraneous influences that could affect the experimental measurements. The sensor cabling and associated instrumentation weight is assumed to have a negligible effect on wave propagation and is therefore excluded from the numerical simulation. This approach helps maintain consistency between the experimental and simulated conditions, ensuring that any discrepancies observed can be attributed to intrinsic material properties or wave interactions rather than external artifacts.

The test configuration involved applying a burst of three signals at frequencies ranging from 100 kHz to 500 kHz, with increments of 50 kHz between each frequency step. Each frequency burst was averaged over three signals to ensure precision and consistency in the results (Figure 3.5). Data acquisition was performed at a high sampling rate of 48 MS/s, with 32000 sampling points collected per signal. The tests were carried out at three different voltage levels: 15 V, 25 V, and 50 V. This setup resulted in a total of 1323 time histories per configuration, providing comprehensive data for analysis on multiple frequencies and voltages.

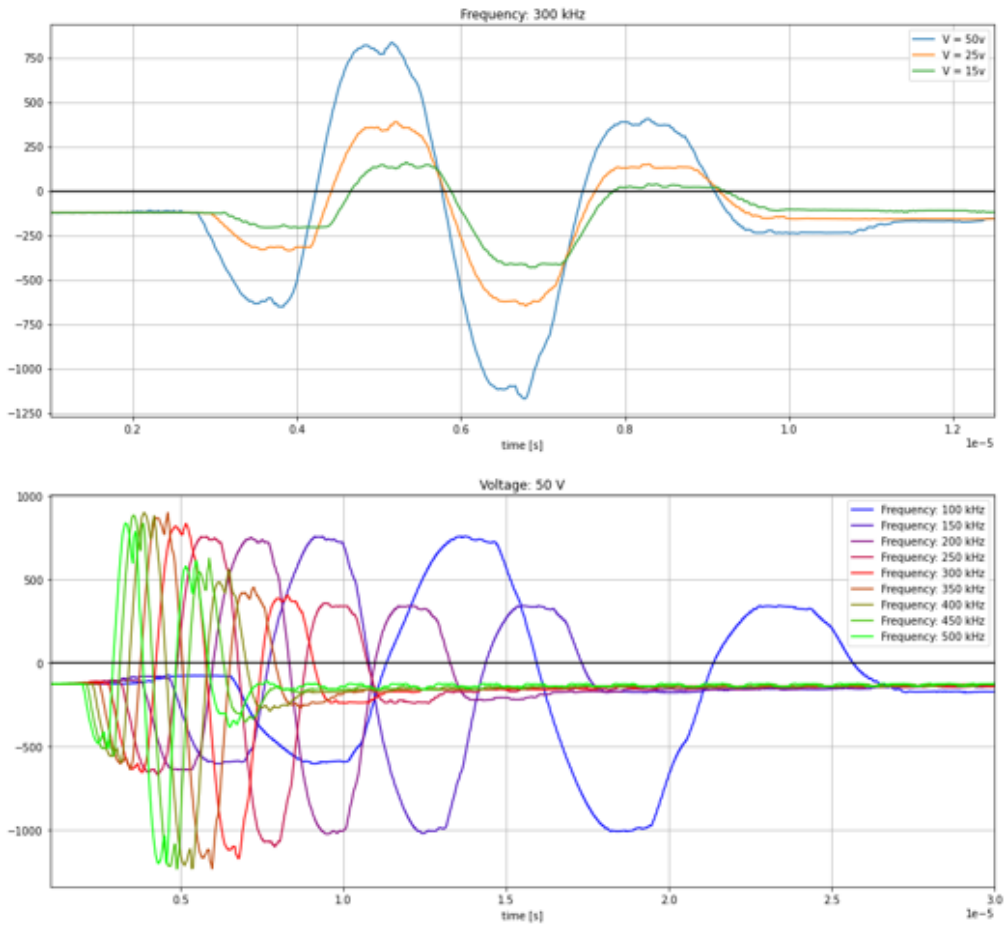


**Figure 3.5:** SCANGENIE input signal time-histories used for the parametric study, highlighting the differences in signal amplitude and frequency.

In the experimental analysis, the paths from sensor 5 to 7 and from 6 to 4 were identified as the most representative in capturing the damping effects (Figure 3.6), when the plate is only clamped on one side (referred to as configuration $C1$). The signal measurements for the path 6-4 are shown in Figure 3.7.

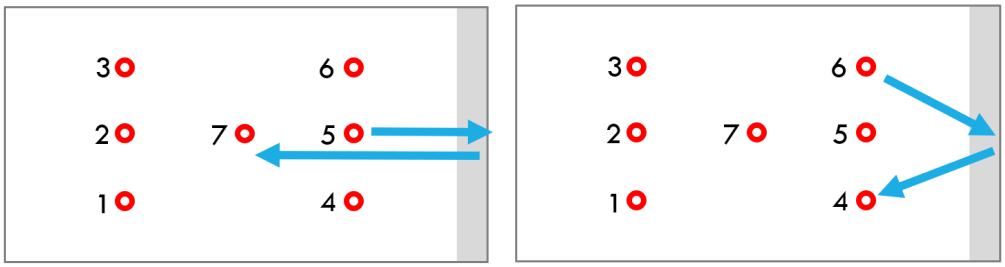


**(a)** Path $PZT5$ to $PZT7$. **(b)** Path $PZT6$ to $PZT4$.

**Figure 3.6:** Schema of relevant wave propagation paths for config. C1.

The interpretation of the sensor data is done with the help of the analytic signal. An analytic

signal is defined in terms of a real part and an imaginary part; its magnitude is related to the magnitude spectrum, and its phase angle its phase spectrum. Features, such as standard deviation of amplitude, standard deviation of phase, and signal energy, can be extracted from these spectrum.

The real and imaginary parts of the analytic signal are related by the Hilbert transform; which takes a function $u(t)$ of a real variable and produces another function of a real variable $H(u)(t)$. The Hilbert transform can therefore be thought of as the convolution of $u(t)$ with the Cauchy kernel, $h\left(t\right) = \frac{1}{\pi t}$, and it is written explicitly as:

$$H\left(u\right)\left(t\right) = \frac{2}{\pi} \lim_{\varepsilon \to 0} \int_{\infty}^{\varepsilon} \frac{u\left(t-\tau\right) - u\left(t+\tau\right)}{2\tau} d\tau \tag{3.2}$$

Taking the real function $u(t)$ as the signal measured in the system, it is possible to apply this methodology to obtain additional information and help visualize the data. The Hilbert transform has been historically widely used for signal processing in many disciplines, and particularly for SHM can be extremely useful to interpret the signal results (Pines and Salvino, 2006).

The absolute value of the Hilbert transform gives a representation of the instantaneous amplitude of the function, as shown in Figure 3.7 where it is plotted alongside the signal from the raw sensors to aid in its visual interpretation.

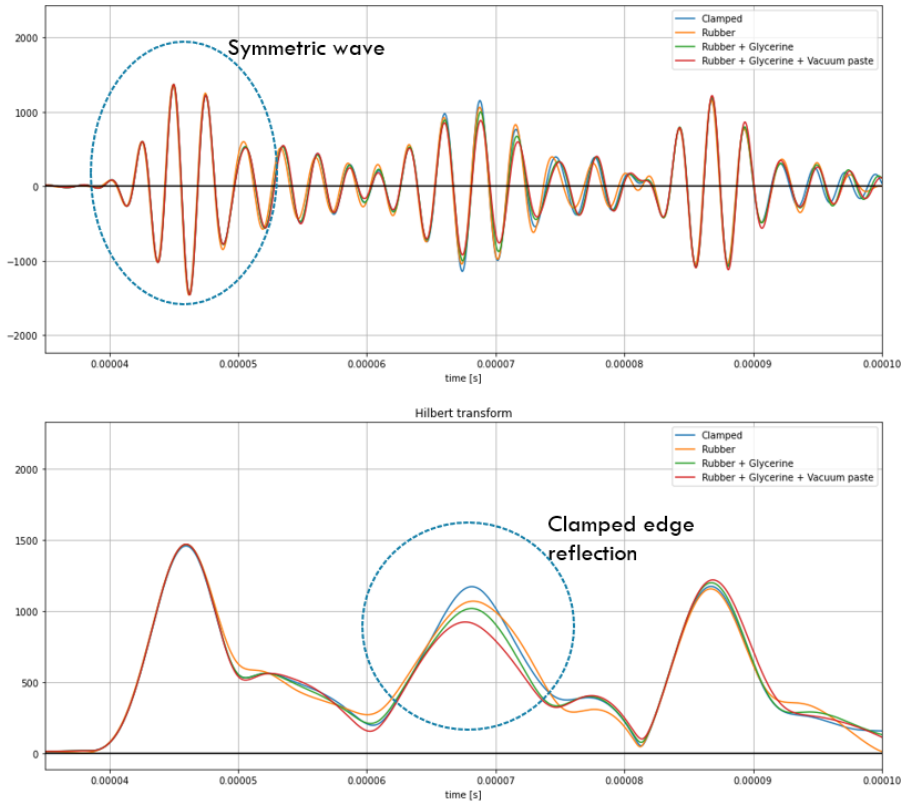


**Figure 3.7:** Signal results of path $PZT6$ to $PZT4$ for config. C1. Comparative of different damping strategies.

This is then compared with a clamped edge with vacuum paste as shown in Figure 3.8, to isolate the damping effect of the vacuum paste.

**Figure 3.8:** Detail of clamped edge and vacuum paste damping setup.

The effect is compared in Figure 3.9, for the clamped edge, the clamped edge with rubber, and the clamped edge with rubber and glycerine. It can be observed that the absorbed energy on the first reflected wave increases with the complexity of the damping mechanism.

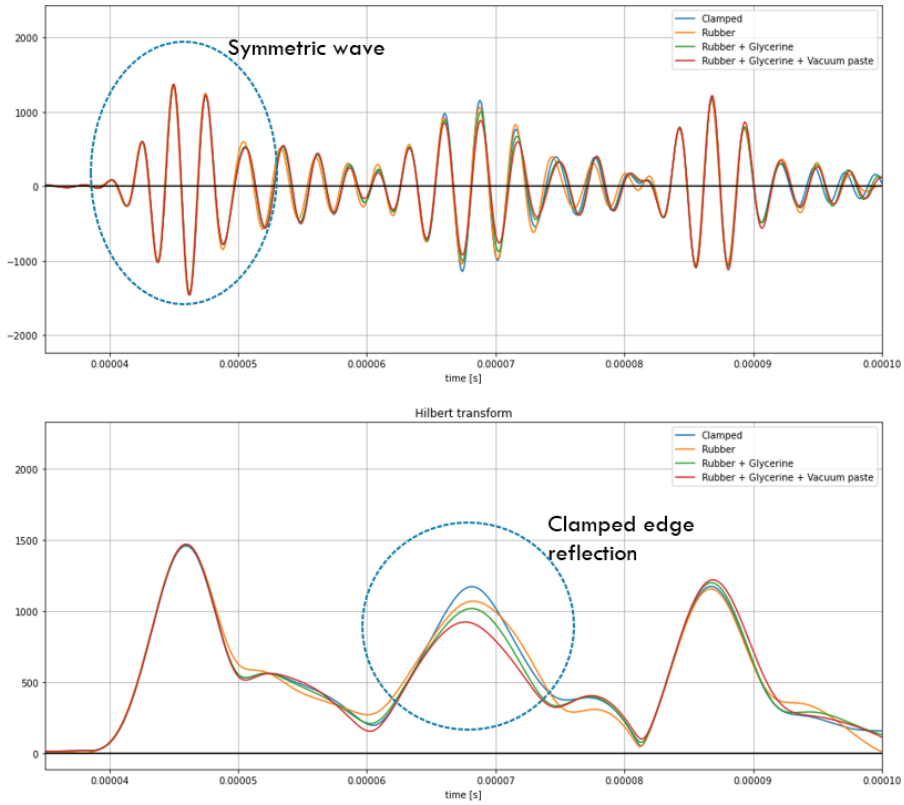


**Figure 3.9:** Signal results of path $PZT6$ to $PZT4$ for config. C1. Comparative of different damping strategies.

The experiment is continued with additional testing configurations with vacuum paste damping on 1, 3 and 4 sides of the plate, named $C1$, $C2$, $C3$, and $C4$ respectively (Figure 3.10).

Each configuration, with increasing vacuum paste length, allows for a systematic comparison of how damping on various sides of the plate influences wave attenuation. By analyzing these setups, it is possible to understand the relationship between the extent of vacuum paste application and the resulting damping efficiency.

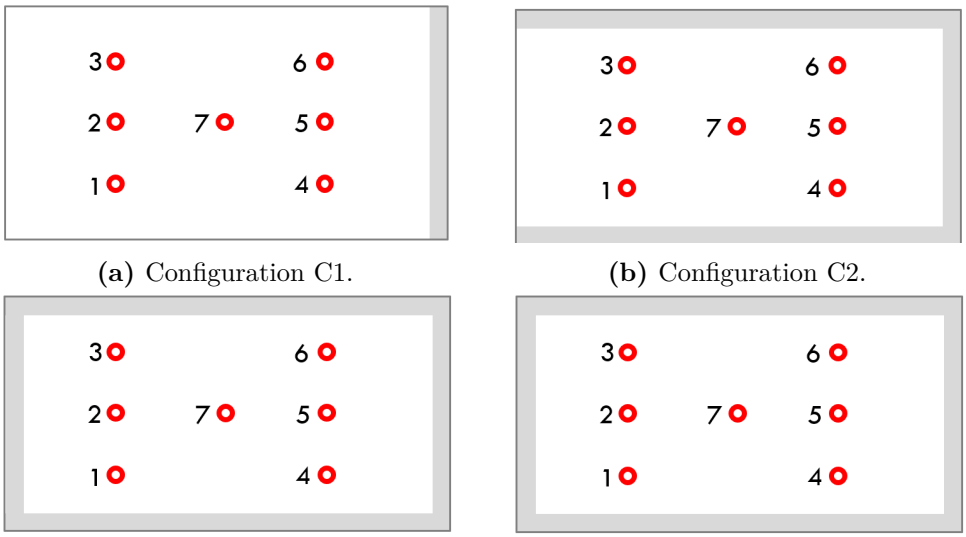


**(a)** Configuration C1. **(b)** Configuration C2.

**(c)** Configuration C3. **(d)** Configuration C4.

**Figure 3.10:** Aluminum plate boundary damping configurations tested.

The signal measured for configuration C1, with vacuum paste on a single side, is shown in Figure 3.11, compared to the free-free state of the plate.

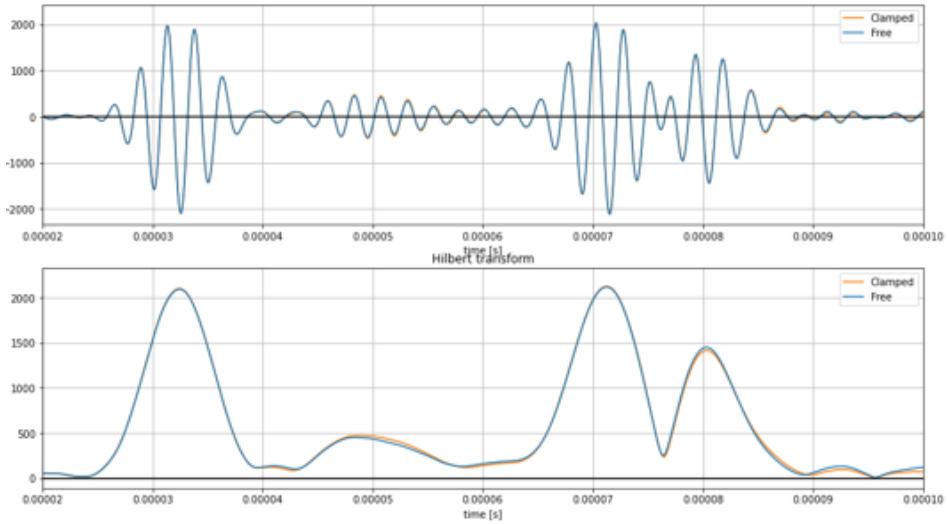


**Figure 3.11:** Signal results of path $PZT5$ to $PZT7$ for config. C1.

The piezoelectric sensor signals obtained for all the configurations studied are compared in Figure 3.12 for a frequency of 350 kHz.

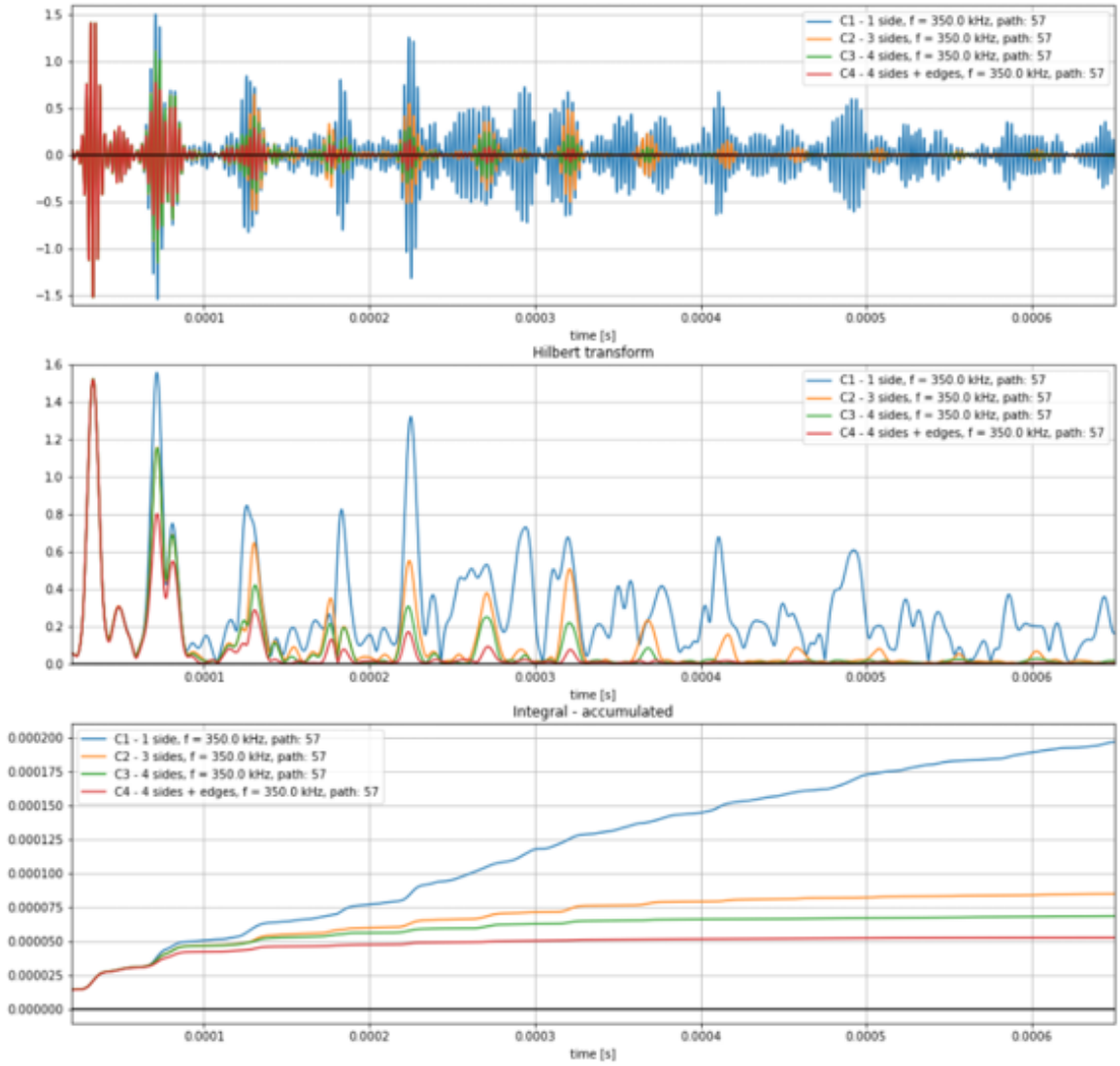


**Figure 3.12:** Signal results of path $PZT5$ to $PZT7$ for all configs (C1-C4).

The data show that a simple clamped edge had very little effect on wave attenuation. Despite the mechanical restriction at the edges, the absence of additional damping materials, such as rubber strips or coupling agents at the other edges, meant that the GLW experienced minimal energy loss as they propagated through the plate. This highlights the importance of incorporating dedicated damping materials to achieve significant attenuation, as clamping alone does not sufficiently dampen wave propagation.

The accumulated integral of the signal remains constant after a certain point in time, as shown in Figure 3.12 (without accounting for sensor crosstalk). This note that after this point, the energy of remaining reflections is absorbed by the damping material, and therefore the contribution to the signal is negligible.

Normalizing these integral data by the maximum input signal voltage allows a consistent comparison across different test conditions; this is shown in Figure 3.13, and the results are shown in Figure 3.14 for a number of relevant frequencies. Normalization thus highlights the existence of a relationship between the signal amplitude, the frequency, and the attenuation, in addition to the influence of the material properties and setup.

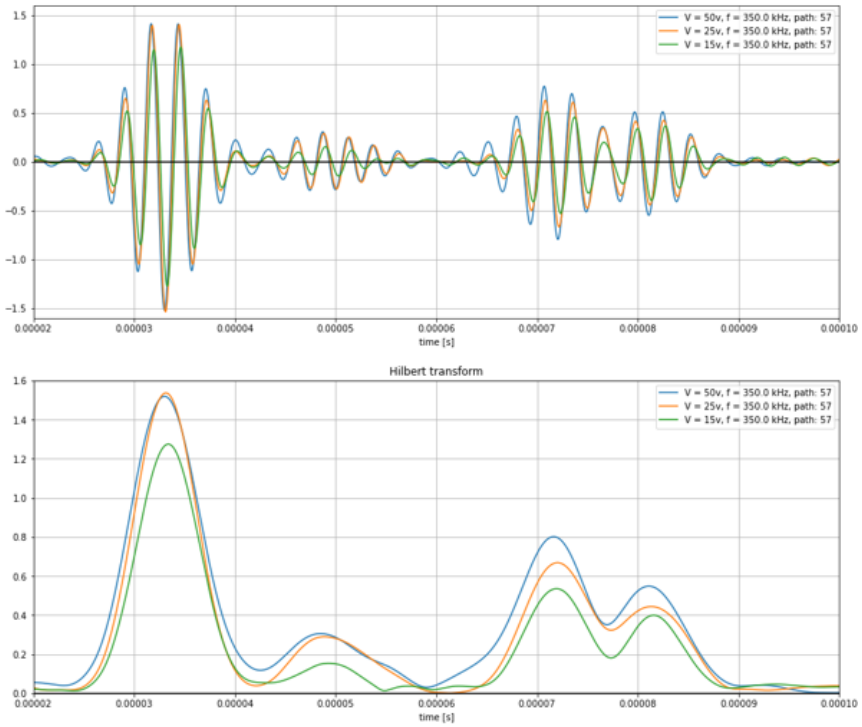


**Figure 3.13:** Signal results of path $PZT5$ to $PZT7$ for config C4. Comparative of input voltage values.

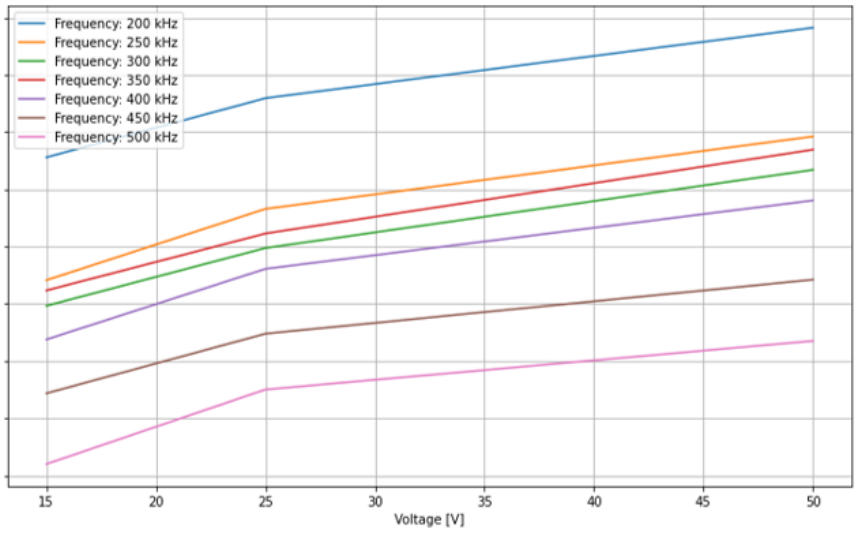


**Figure 3.14:** Normalized signal integral value results of path $PZT5$ to $PZT7$ for config C4. Comparative of input frequency.

### Composite wing demonstrator

The Remotely Piloted Aircraft System (RPAS) LIBIS, designed by *Departamento de Aeronaves ETSIAE* (Figure 3.15) is designed to provide a flexible platform for configuration and operation for university based research projects. It features a combination of an unconventional tandem wing configuration with a pusher propeller for cruise flight as fixed-wing, four adjustable VTOL rotors for rotary-wing operation and a 2.5 m wing span.

All the structural components are made of composite materials, with similar structural configuration than a real aircraft (stiffeners, stringers, frames and a torsion box in the wing) and all joints between sub-elements are adhesive.

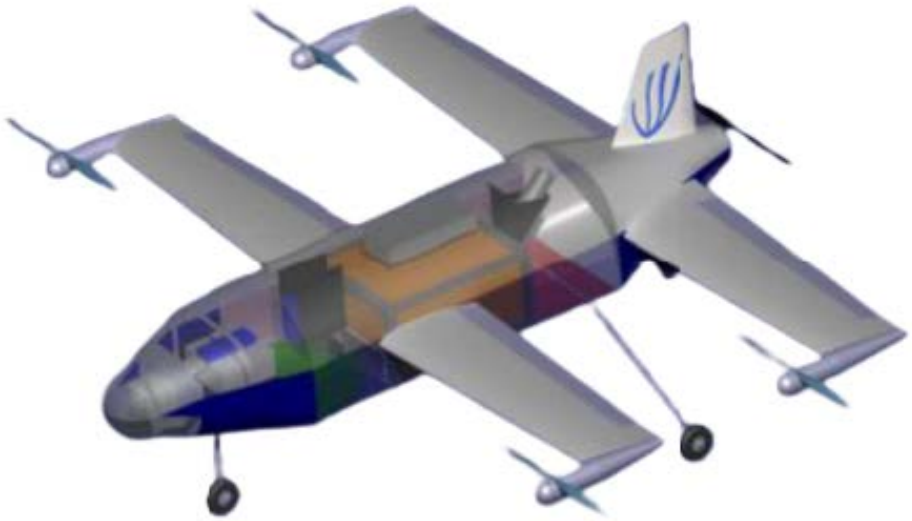

**Figure 3.15:** Design of the RPAS-LIBIS.

The study is conducted on a specimen of the RPAS-LIBIS front right wing's lower cover, which features a composite curved structure with three distinct sections with gradual thickness transitions between them, as shown in Figure 3.16.

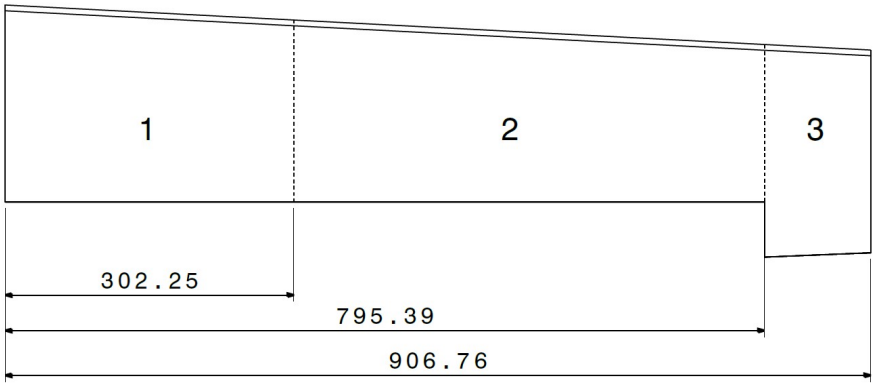


**Figure 3.16:** Dimensions and laminate zoning for the RPAS-LIBIS wing lower cover.

The wing lower cover is fabricated entirely in CFRP Hexcel IM7/8552 (Hexcel Corporation, 2024) and its stacking layup for each section is shown in Table 3.3.

**Table 3.3:** RPAS-LIBIS wing lower cover laminate sequences (del Río Velilla, 2022).

| **Zone** | **1** | **2** | **3** |
|---|---|---|---|
| **Sequence** | $[0, 90, \pm 45, 0]S$ | $[0, 90, 0]\$$ | $[0, 90]\$$ |
| **Number of layers** | 10 | 5 | 3 |
| **Thickness** | 1.8 mm | 0.9 mm | 0.54 mm |

The specimen is instrumented with an array of 8 piezoelectric transducers (8 mm PZT ceramic wafer, over a 12 mm bronze disc), shown in Figure 3.17, and the data is again recorded with the same Acellent SCANGENIE system, using a sampling frequency of 48 MHz (Sánchez Iglesias et al., 2024).

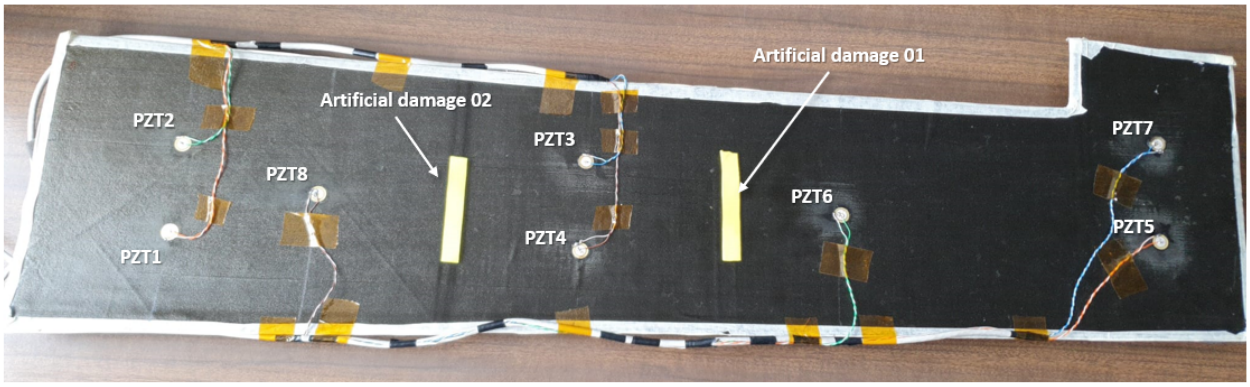


**Figure 3.17:** Example test configurations evaluated on LIBIS wing prototype showing transducers and artificial damages location and numbering.

Artificial damages have been introduced in the specimen as shown in Figure 3.17. They are introduced with 8 cm long, 1 cm thick strips of vacuum paste stuck on the inner side of the laminate, with an average mass of 5 g; they function as added masses in order to alter the dynamic behavior of the structure. Given that the structural integrity of the CFRP remains intact under the vacuum paste, it is considered that the effect of adding the masses could show a higher resemblance to the effect of a delamination or matrix failure rather than a fiber breakage, although other types of damages may have a similar effect (J. Ma et al., 2023; Zeng et al., 2022).

Three sets of tests were performed considering the intact structure, the structure with artificial damage 01 and the structure with artificial damage 02. The input signal used consist on a 40 V BURST3 at 350 kHz and test results are presented as an average of 3 runs, these parameters are not a limitation of the simulation method, instead they are selected based on the best experimental result data available.

### Stiffened composite plates

T-Shape stiffeners are widely used in aerospace structures, being one of the most common solutions for the stiffening of thin panels. In the case of composite structures, these stiffeners are typically bonded to the structure, not needing rivets for the union, and therefore providing support along all of its length and a uniform behavior and interaction with the guided elastic waves. For these reasons, an experimental campaign intended to characterize this behavior has been performed in this project, described in this section.

The CFRP experimental test campaign is carried out on two square composite plates with a side length of 726 mm one of them with a stiffener in the center. The panel has a 7-ply symmetric quasi-isotropic laminate of AS4/8552 with the following layup: (+45, -45, 90, 0)$ resulting in a total thickness of 1.288 mm. The flat panel used for the tests is shown in Figure 3.18a.

The stiffener has a symmetric 11-ply laminate of AS4/8552 with the following layup: (+45, -45, 0, 0, 0, 90)$ and doubles in the central web. A picture of the stiffened panel is shown in Figure 3.18b.

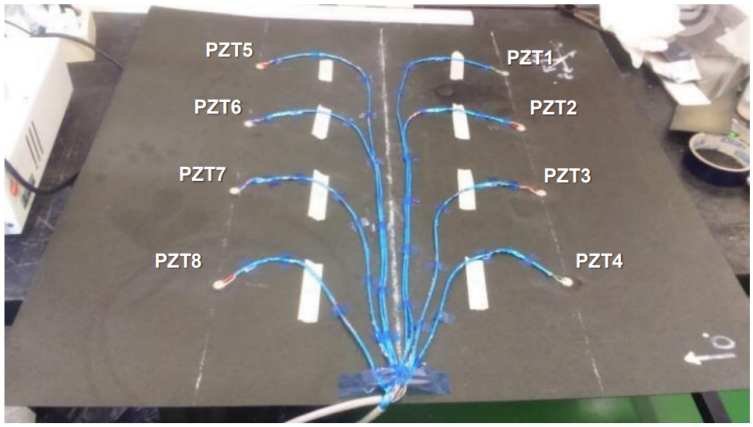


**(a)** Non-stiffened panel

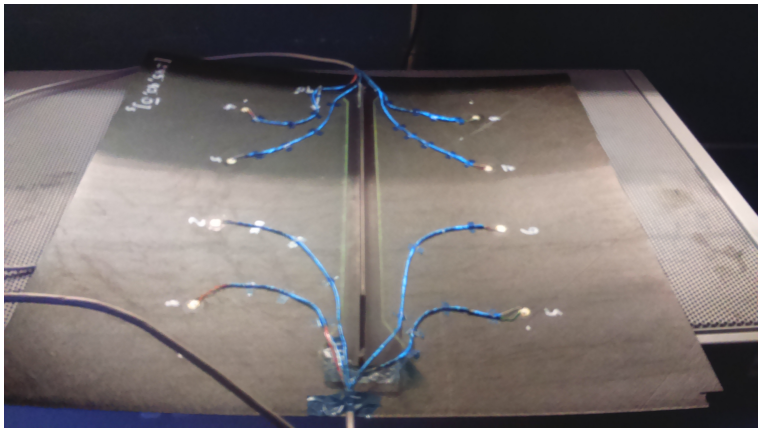

**(b)** Stiffened panel

**Figure 3.18:** Test specimens for the active interrogation test for the composite stiffened plate case study

Both plates are instrumented with an array of eight piezoelectric transducers; its location and numbering are shown in Figure 3.19.

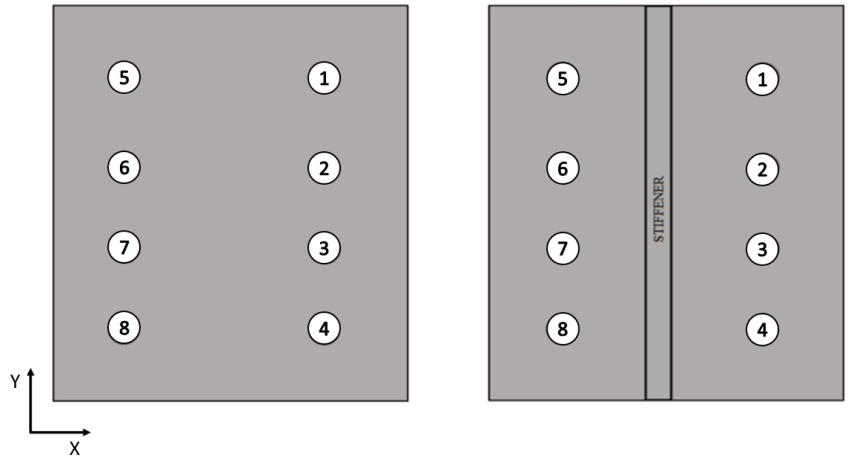


**Figure 3.19:** PZT sensors position and numbering for the flat plates.

The exact position of the PZT sensors has been measured experimentally and is shown in Table 3.4. The accuracy with respect to the ideal position is smaller than 10 mm, therefore, for the Finite Element model simulation it has not been considered and the ideal position has been used; this may create small discrepancies in the arrival times and dispersion measured.

**Table 3.4:** Exact position of the PZT sensors on the flat plates. Aguilar Redondo, 2019

| | **Without stiffener** | | **With stiffener** | |
|---|---|---|---|---|
| | x [mm] | y[mm] | x [mm] | y[mm] |
| PZT 1 | 143 | 183 | 145 | 183 |
| PZT 2 | 293 | 181 | 292 | 185 |
| PZT 3 | 430 | 182 | 434 | 185 |
| PZT 4 | 575 | 183 | 579 | 186 |
| PZT 5 | 145 | 546 | 143 | 547 |
| PZT 6 | 295 | 548 | 295 | 547 |
| PZT 7 | 435 | 547 | 437 | 549 |
| PZT 8 | 583 | 548 | 584 | 549 |

Some additional active interrogation tests are performed with two piezoelectric sensors installed in the stiffener web. Due to the limitations of the data acquisition system, PZT4 and PZT8 are replaced with two new piezoelectric sensors on the stiffener web, as shown in Figure 3.20. The number and position of the PZT transducers are shown in Figure 3.21.

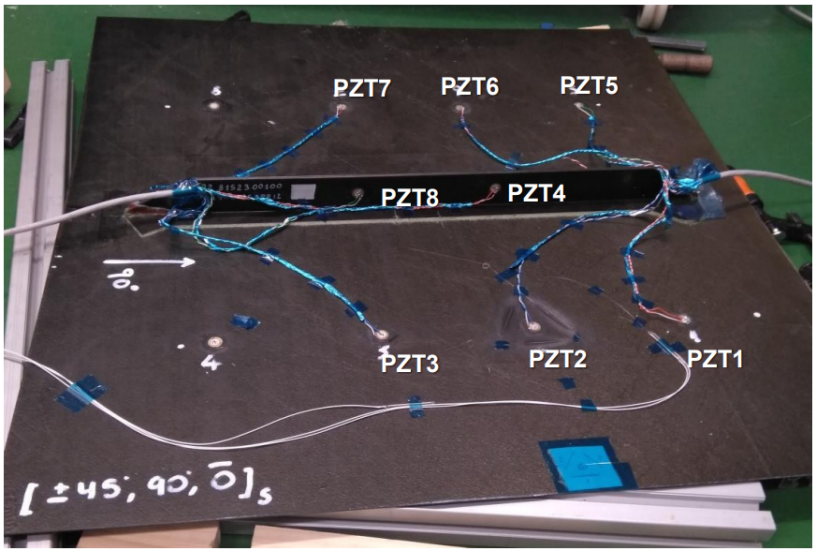


**Figure 3.20:** Experimental set-up for the active interrogation tests with PZT sensors on the stiffener web.

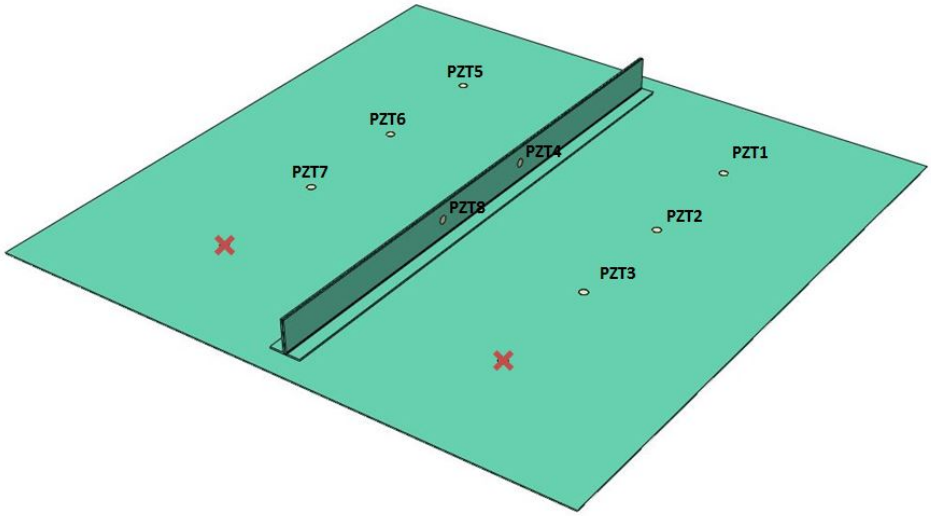


**Figure 3.21:** PZT sensors position and numbering on the stiffener.

This configuration allows for a better understanding of the propagation and interactions of guided elastic waves on the stiffener and the possible mode changes or reflection mechanisms that may occur.

For the active interrogation tests the data is again recorded with the Acellent SCANGENIE DAQ system, measuring a frequency range between 50 kHz and 500 kHz with a 50 kHz step, combining all possible emitting and receiving paths; generating a total of 560 signals. However, for validation with the FEM simulation only the tests at 200-300 kHz are used.

### 3.1.2 Passive - Impact detection tests

Passive impact detection tests are commonly used to monitor and identify the location and severity of impacts on a structure without actively exciting the material. Instead, these tests rely on the structure's response to naturally occurring impacts from external objects or the dynamic response from crack growth os buckling. The sensors placed on the material detect the resulting GLW, capturing the vibration signals that propagate through the structure.

Wave patterns generated by impacts can vary depending on the material properties, thickness, and boundary conditions. GLW in particular are sensitive to changes in material stiffness, thickness, and defects, which makes them useful in detecting impact location and severity.

The impacts for passive tests are done using a Brüel and Kjær instrumented hammer model 8206-003 and the piezoelectric signals and the hammer load cell are recorded with a National Instruments data acquisition card model NI-USB-636.

The National Instruments NI-6366 (*NI 6366 device specifications*, 2023), shown in Figure 3.22, is a DAQ device with simultaneous sampling and multiple functions. It offers analog I/O, digital I/O, and four 32-bit counters/timers for PWM, encoder, frequency, event counting, etc.


**Figure 3.22:** National Instruments NI-6366 DAQ.

When used in active mode, the interrogation of the damage path between the actuator and the sensor is carried out with a continuous pulse train and not individually. This allows interrogation times to be reduced by an order of magnitude from minutes to seconds.

It uses a much lower sampling frequency than the ScanGenie and performs subsequent oversampling that reconstructs the acquisitions made. This allows acquisition equipment to be used at a much lower cost, although it may impact the result quality.

And it allows for the acquisition of elastic waves in real time. It could be used for real-time impact detection. This functionality is not shown since it is outside the scope of the thesis.

Although the SCANGENIE DaQ offers better characteristics, the complications of usage and limitations to its customization, due to it being a proprietary platform, made it impossible to be used for passive impact monitoring, for this reason, the NI-USB-6366, is used in these tests. The technical specifications of the NI-6366 card are shown in Table 3.5.

**Table 3.5:** NI-6366 specifications summary at 25 °C (*NI 6366 device specifications*, 2023).

| **Characteristic** | **value** |
|---|---|
| Analog channels | 8 Input / 2 Output |
| Sampling rate | 2 Msp Input / 3.33 Msp Output |
| Input signal voltage range | ±10 V |
| Output signal voltage range | ±10 V |
| Bandwidth | 1 MHz |
| Digital-Analog converter | 16 bit |

As in the active interrogation tests, the CFRP flat plate is equipped with the eight PZT sensor array. These sensors are distributed uniformly across the plate, ensuring comprehensive spatial coverage for data collection and analysis, as illustrated in the previous section.

However, due to specific constraints imposed by the DAQ hardware, it was necessary to make a slight modification to the sensor configuration. In particular, the piezoelectric transducer designated as $PZT1$ was removed from the setup and, in its place, the signal generated by the instrumented hammer was incorporated into the system. This substitution allows the hammer to act as both an excitation source and a data input channel, ensuring compatibility with the available DAQ resources and preserving the integrity of the experimental setup.

The inclusion of the instrumented hammer in the testing procedure provides a controlled and repeatable excitation mechanism. It enables precise timing and amplitude measurements critical for evaluating wave propagation and structural behavior. Additionally, this modification supports the collection of impact response data, which is vital for validating numerical models and assessing material properties. Overall, these adjustments maintain the robustness of the experimental design while accommodating the technical limitations of the instrumentation.

A schematic of the test setup is shown in Figure 3.23 and a picture of the test is shown in Figure 3.24.

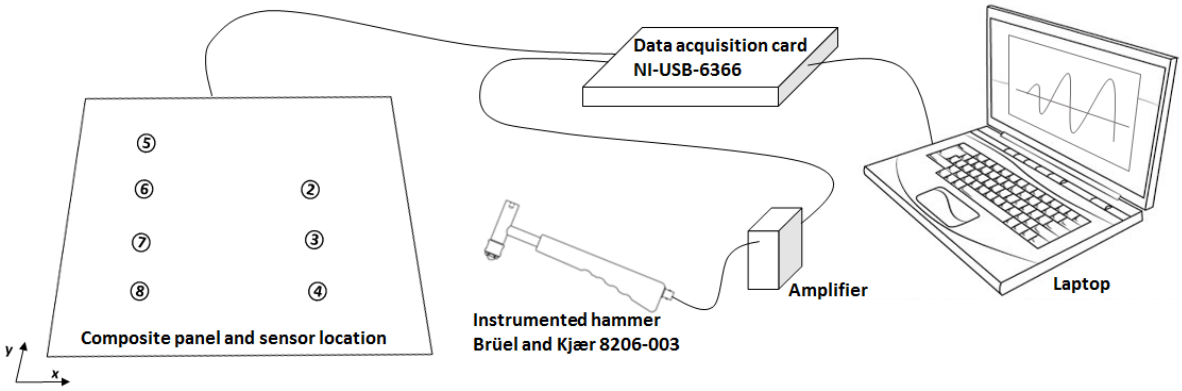


**Figure 3.23:** Experimental set-up schematic (Sánchez Iglesias and Fernández López, 2020).

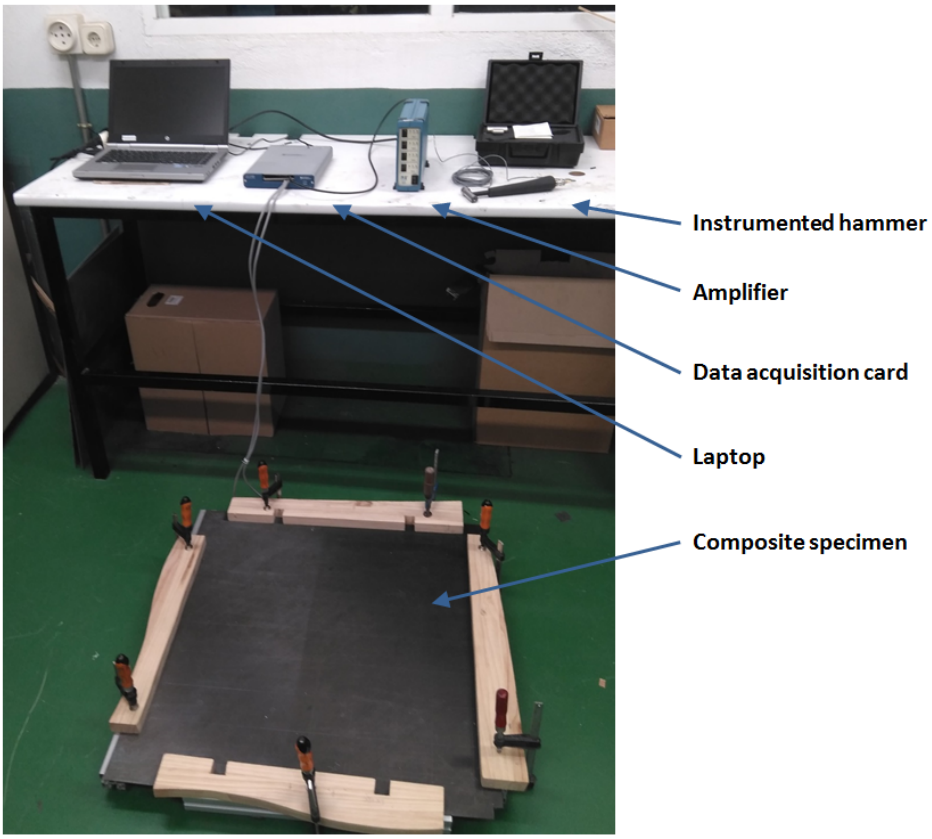


**Figure 3.24:** Experimental set-up picture.

An average impact velocity of 0.5 m/s is estimated from the test results by integrating the imact hammer force and used in the FEM simulation, based on the definition of kinetic energy $E_K = 0.5\,\mathrm{mV}^2$, knowing the mass of the hammer of 0.22 kg. The signals measured on the Hammer and piezoelectric sensor 2 are shown in Figure 3.25 for the aluminum tip.

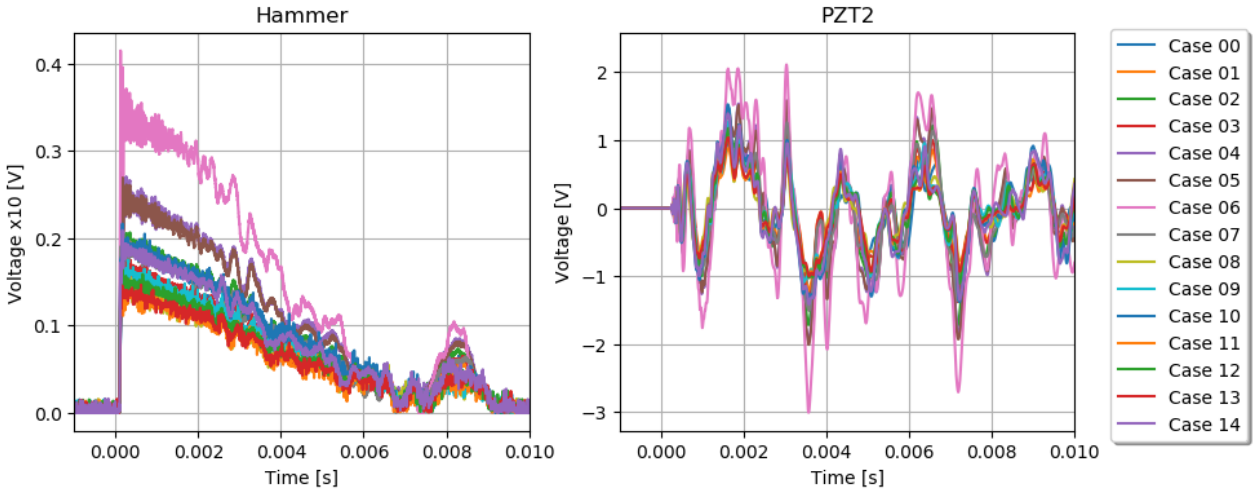


**Figure 3.25:** Hammer force and $PZT$ sensor 2 signal for all valid tests performed with the aluminum hammer tip.

## 3.2 Simulations via the Finite Element Method

Explicit Finite Element Method (FEM) simulations are a numerical technique widely used for modeling and analyzing dynamic problems in engineering and physics, particularly in scenarios involving large deformations, impact loading and propagation of GLW. As Lamb waves exhibit complex behavior, including mode conversion and dispersion, FEM provides a robust framework for accurately modeling these phenomena, while being able to consider the orthotropic material properties of CFRP laminates.

This section describes the results and setup of the simulations, performed according to the Airbus Defence and Space standards (Sánchez Iglesias et al., 2017). The simulations shown here have been generated and run in the Airbus Defence and Space High Performance Computing (HPC) cluster in Getafe, which, at the time of the analyses, had a global theoretical peak of 450 TFLOPs. Due to the size of the results of the simulations, data extraction has also been performed in the cluster.

### 3.2.1 Finite element model description

FEM analysis, described in detail in Sánchez Iglesias, 2020, is done with Abaqus/Explicit version 2017. The composite solid panel is represented with continuum shell elements (SC8R) and conventional 2D shell elements (S4R) are used for the piezoelectric sensors/actuators. As the simulation must be able to represent the elastic wave behavior as it progresses through the panel, an average element length of 1 mm is used in the model; this ensures that an anti-symmetric wave up to a frequency of 200 kHz can be captured by the model using at least 10 elements per wavelength (Kocbach, 2000; Yang et al., 2018).

The orthotropic material properties used for the composite AS4/8552 are introduced in the FEM simulation with a *Lamina* definition, shown in Table 3.7. The laminate stacking is introduced in the element section definition.

**Table 3.7:** AS4/8552 material properties for the FEM model simulation (Hexcel Corporation, 2024)

| Property | Value |
|---|---|
| $E_1$ | 131 000 MPa |
| $E_2$ | 9750 MPa |
| $\nu_{12}$ | 0.3 |
| $G_{12}$ | 4650 MPa |
| $G_{13}$ | 4200 MPa |
| $G_{23}$ | 4200 MPa |

The size limitation to model the elastic wave results in a very large mesh of around 600 000 elements and 1 500 000 nodes. The mesh has been generated approximately uniform for most of the panel, although it is distorted around the piezoelectric sensors to follow its shape (Figure 3.26a).

The stiffener is meshed as an individual part and the interaction with the skin is done through a cohesive contact. A detail of the stiffener mesh is shown in Figure 3.26b.

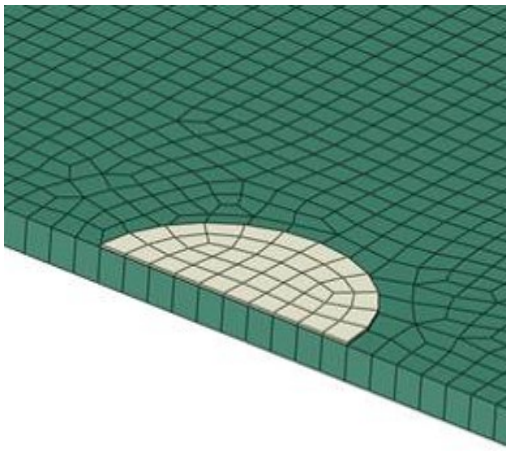

**(a)** Piezoelectric sensor mesh

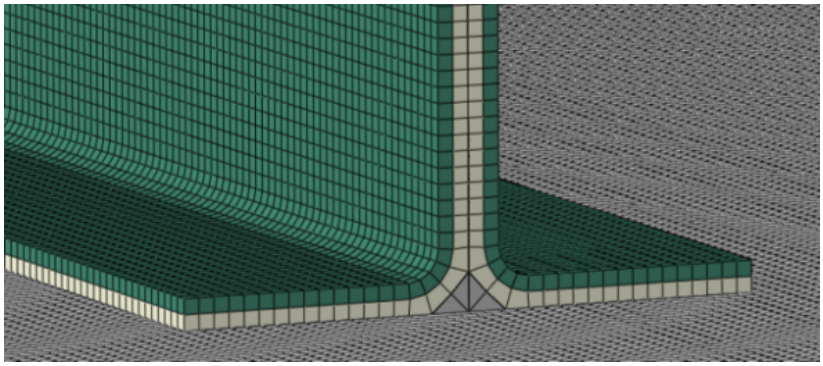

**(b)** Stiffener mesh

**Figure 3.26:** Detail of the FEM model mesh.

Due to the relatively large thickness of the stiffener, it is necessary to employ a mesh composed of two stacked SC8R elements in order to achieve an appropriate representation of the geometry. This approach is taken to prevent the aspect ratio of the elements from becoming excessively high, which could compromise the accuracy and stability of the shell formulation. The use of stacked elements helps to better capture the structural behavior of the stiffener while maintaining a reasonable level of computational efficiency.

It is important to note, however, that the SC8R elements in Abaqus/Explicit do not provide an exact representation of the thickness direction. Instead, the software approximates the stiffness properties in this direction, which introduces a potential limitation in the modeling accuracy (*Dassault Systemes Simulia. Abaqus v. 2017 Documentation*, 2023). As a result, while the elastic wave propagation through the flat panel is expected to be modeled with a higher degree of precision, the propagation through the stiffener thickness may be less accurate due to this approximation.

The stiffener filler is meshed with reduced integration pentahedric elements (C3D6) with average resin properties. Cohesive contact is also definer between both sided of the stiffener. A global view of the finite element model with the stiffener is shown in Figure 3.27.

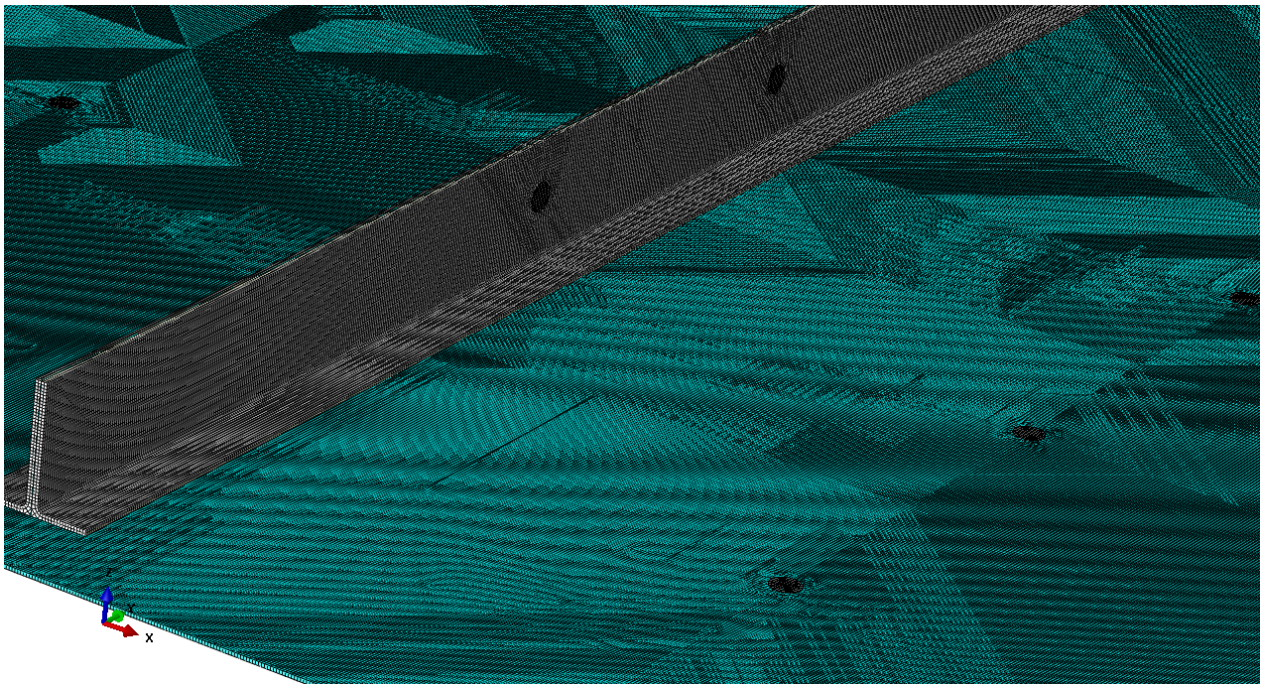

**Figure 3.27:** Mesh for the FEM model of the stiffened flat plate.

Abaqus/Explicit v.2017 does not support piezoelectric behavior, therefore, the input signal is introduced on the piezoelectric actuator as a temperature variation. A uniform thermal expansion coefficient $\alpha_{exp} = 1 \times 10^{-4}\,°\mathrm{C}^{-1}$ is applied to all the elements of the piezoelectric sensors following the theoretical time-history of the *BURST-3* input signal shown in Figure 3.28 for a frequency of 200 kHz.

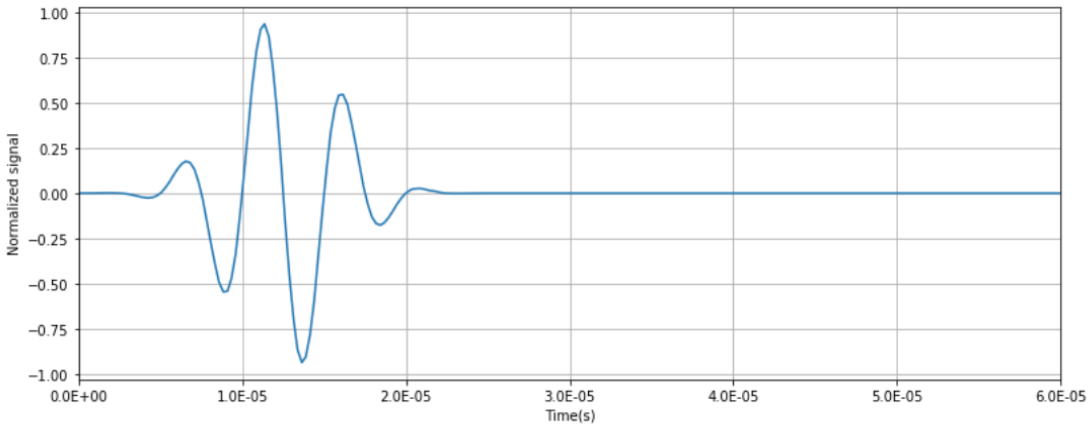


**Figure 3.28:** BURST-3 input signal at 200 kHz applied to the FEM model.

The impactor for the passive test simulations is modeled as a semi-sphere meshed with solid reduced integration hexahedral elements C3D8R as shown in 3.29. A friction-less contact is defined between the impactor and the panel. To ensure a smooth contact force distribution

the element size of the impactor is kept consistent with the panel, with a side length of an average of 1 mm on the surface.

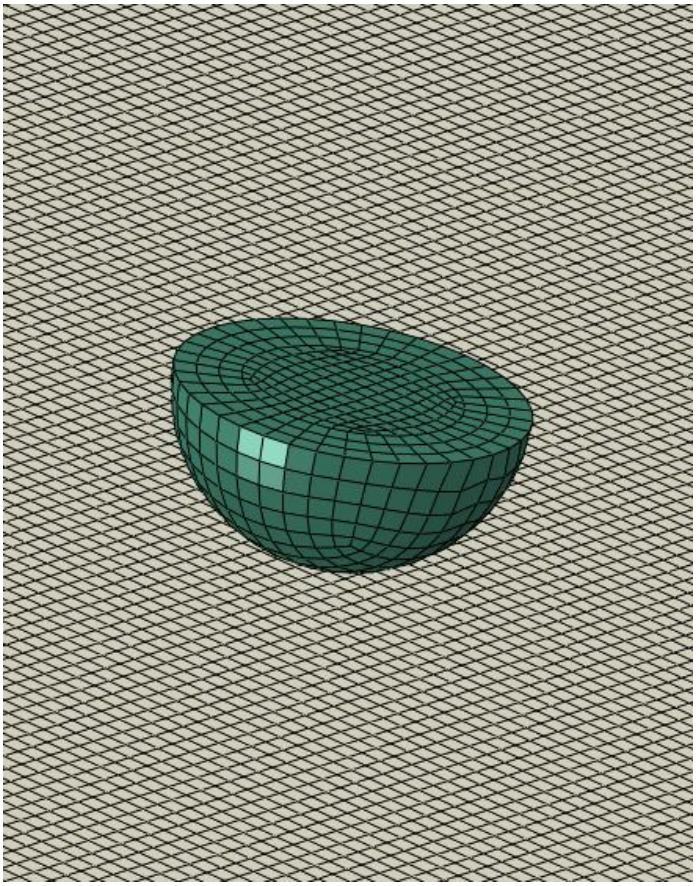

**Figure 3.29:** Detail of the impactor mesh used on the FEM model

In order to obtain the signal in the piezoelectric sensors, the stress measured in the finite element model elements must be converted to voltage. The following relationship can be applied to obtain the electric voltage contribution that could be generated by each element $i$, assuming that the sensor is working on its linear range (Ayers et al., 2003; Erturk and Inman, 2011):

$$V_i = \frac{d_{31}(T_1 + T_2)}{\epsilon_0} \cdot h \tag{3.3}$$

were $T_1$ and $T_2$ are the element stresses in directions 1 and 2, $h$ is the piezoelectric sensor thickness, $\epsilon_0$ is the electric constant and $d_{31}$ is the piezo electric constant, taken from previous validated experimental data.

It is assumed that the contribution to the electric field of each elements representing the piezoelectric sensor is equal per unit of area, therefore the final voltage level, $V$, is obtained as the sum of all elements that represent the PZT transducer:

$$V = (A_{PZT})^{-1} \sum V_i \cdot A_i \tag{3.4}$$

### 3.2.2 FEM model results interpretation

Interpreting the results of FEM simulations for GLW propagation involves analyzing various outputs generated during the simulation to understand the behavior of the waves as they propagate through the structure and its interactions with structural features.

In order to obtain the most useful information from the FEM simulations, the three following variables are observed and compared with the test results, when possible:

- **Average hydro-static strain:** is a measure of the uniform deformation of a material in all directions. It represents the volumetric strain, or how much the volume of a material changes under a given stress state, without accounting for any shape distortion and its calculated as the average of the normal strains in all three principal directions.

  As shown above, the average hydro-static strain can give an estimation of the voltage measured by the PZT transducers. However, due to the input signal intensity not being charazterized in the simulation, the results are normalized by the maximum of the measured S0 wave for a better comparison with the tests.

- **Normal displacement to the sensors:** measured at the nodes located in the center of each sensor.

  Although it does not provide a strictly comparable signal to the PZT measurements, it can give a very good quantitative idea of the wave evolution and behavior, and when evaluating the displacements at opposite sides of the plate its really easy to identify the wave propagation mode, interpreted as follows (Sánchez Iglesias et al., 2017):

  - Opposite direction displacement results imply a symmetric ($S0$)wave mode, as it implies that the material is locally under compressive or tensile stress.
  - Same direction displacements imply an anti-symmetric ($A0$) wave mode, as it implies that the material is locally subjected to bending stress.

- **Global displacement plots:** Can give a global view of the wave propagation, are essential to verify the correct behavior of the simulation, and can help the reader to understand the physical phenomena behind the results plotted with the previous variables studied.

These magnitudes can help to validate the accuracy of the simulations and ensures that the numerical model reflects the real-world behavior of the system.

Both simulations performed with the stiffened and un-stiffened panel are presented in this section and the correlation with the tests has been performed also for both cases. Due to the limitations imposed by the FEM model element size the frequency of the anti-symmetric wave cannot be greater than 200 kHz; as shown in Aguilar Redondo, 2019 lower frequencies present an undesirable interaction between the $S0$ mode and the electromagnetic crosstalk for shorter distances of the transducers, therefore, all simulations are performed at an input frequency of 200 kHz.

### 3.2.3 Validation of FEM model analysis on test specimens

Validation is a crucial phase in the finite element analysis (FEA) process, as it ensures that the FEM model accurately reflects the real-world behavior of the structure or material being studied. In order to assess the accuracy and reliability of the simulation, it is necessary to compare the FEM results against the experimental data, as described in the previous section. By validating the model with physical test results, any discrepancies between predicted and observed behaviors can be identified, allowing model refinement and increased confidence in its predictive capabilities. This process not only confirms the model's ability to simulate realistic GLW propagation conditions, but also strengthens its potential for use in design, optimization, and SHM applications.

In this section, the results will be presented when using the PZT in the skin as actuators. To reduce the number of plots, only the actuators PZT1 and PZT2 are considered. As the plate has geometrical symmetry and the laminate is quasi-isotropic, it is considered that the results when actuated from the other transducers will not vary significantly.

#### Non-stiffened panel results

Results and validation for the flat (unstiffened) panel are shown in this section. The vertical displacement results of the simulation at $t = 0.068\,\text{ms}$ while emitting a 200 kHz BURST-3 signal from $PZT2$ is shown in Figure 3.30. The different propagation modes are identified in the figure.

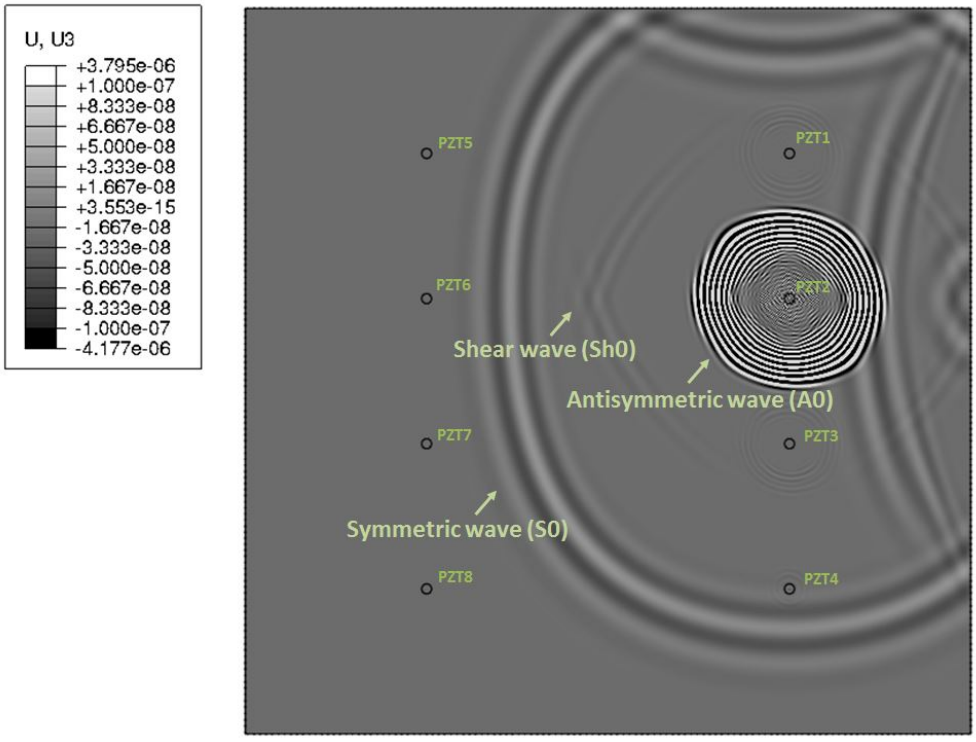


**Figure 3.30:** Active interrogation results for the flat composite panel - Actuator $PZT2$ at a time $t$ =0.8 ms. Lamb wave propagation modes are highlighted in the figure.

The comparison of the active interrogation signals for the flat panel is presented in Figure 3.31 and Figure 3.32. Duplicated or redundant paths are not shown, and paths between consecutive sensors/actuators are also not shown, as the crosstalk overlaps the symmetric wave on the experimental results.

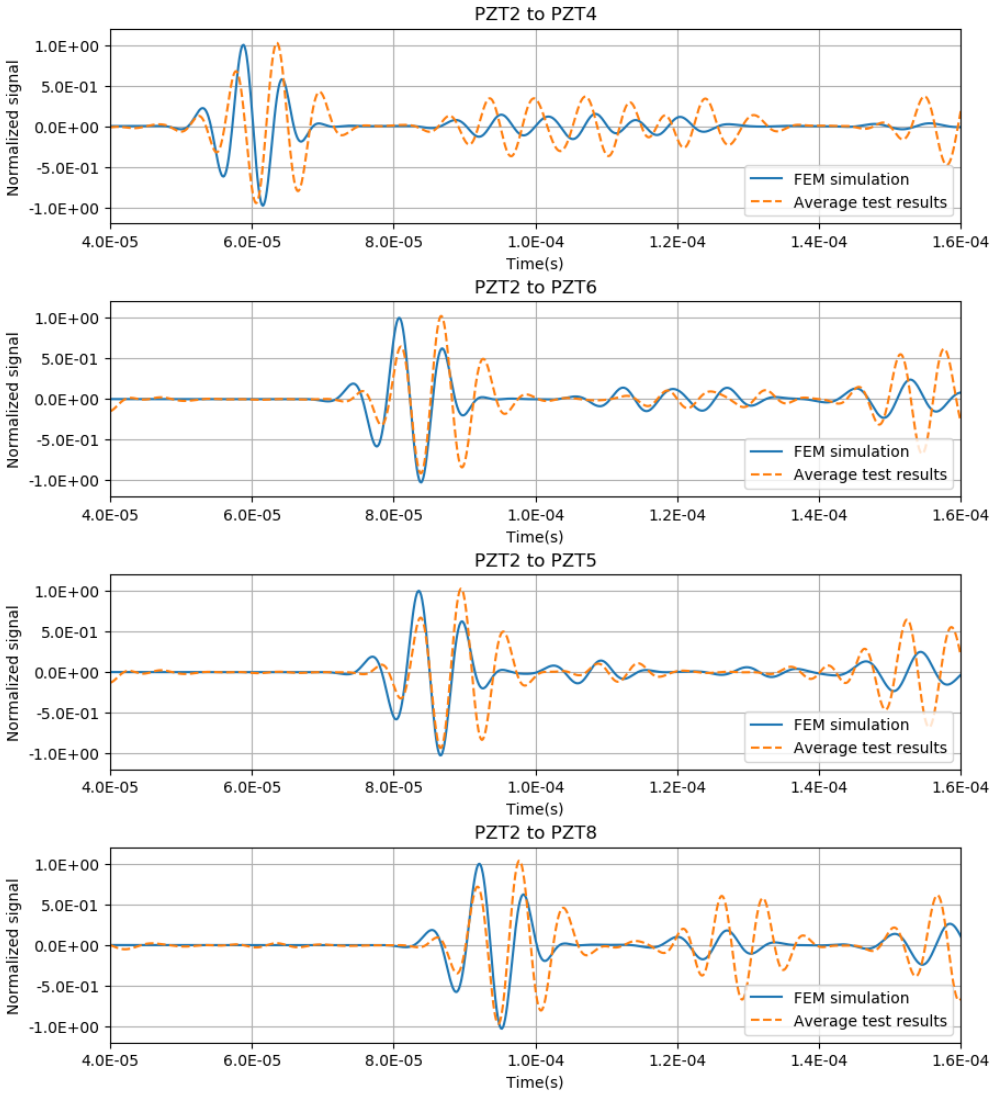


**Figure 3.31:** Active interrogation results for the flat composite panel - Actuator PZT2.

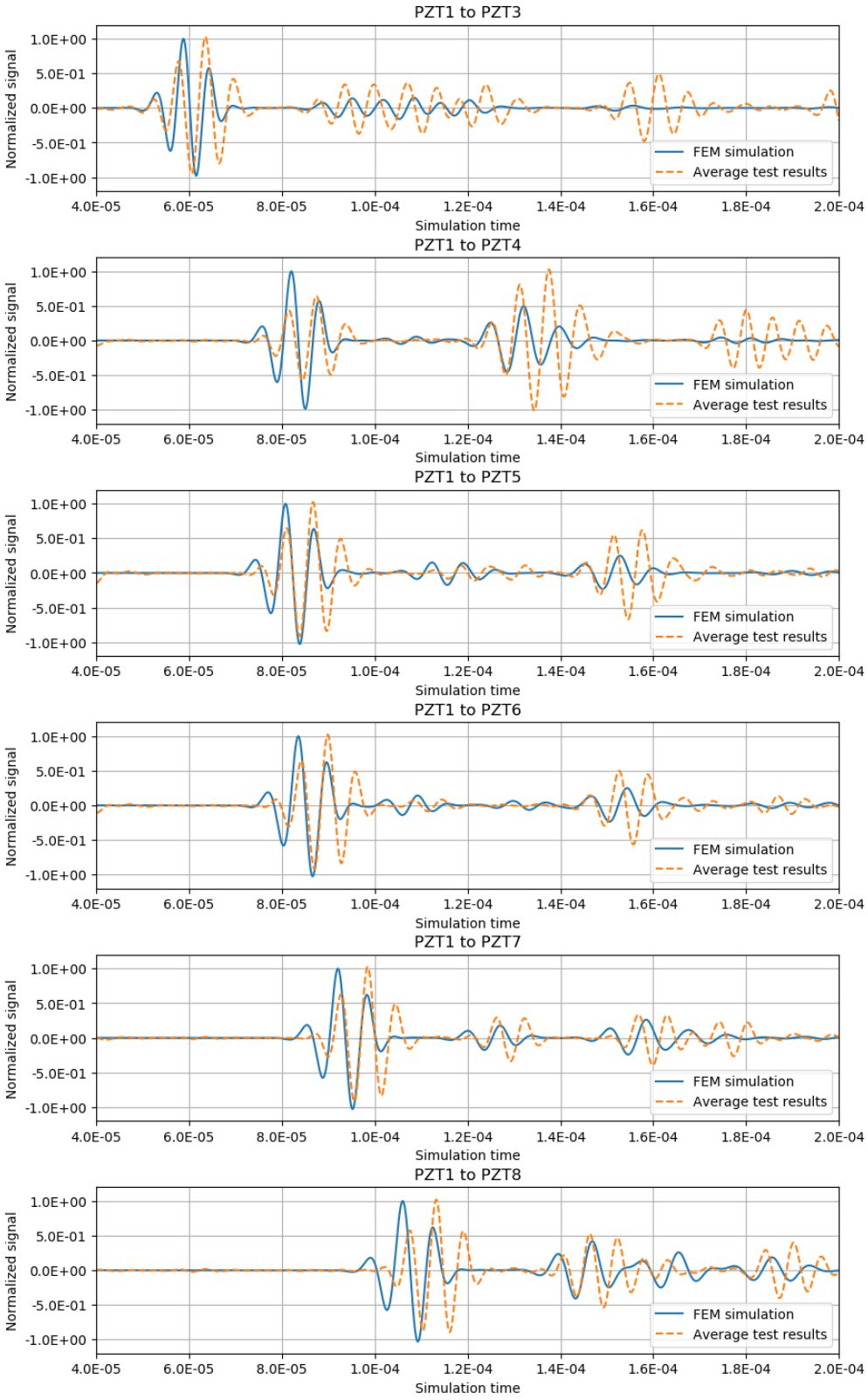


**Figure 3.32:** Active interrogation results for the flat composite panel - Actuator PZT1.

The wave velocity measured at the tests compared with the simulations and the analytical solution presented in Muñoz Chamorro, 2018 is shown in Figure 3.33 as a function of the material angle. The simulation shows very good agreement with the test results and the analytical model.

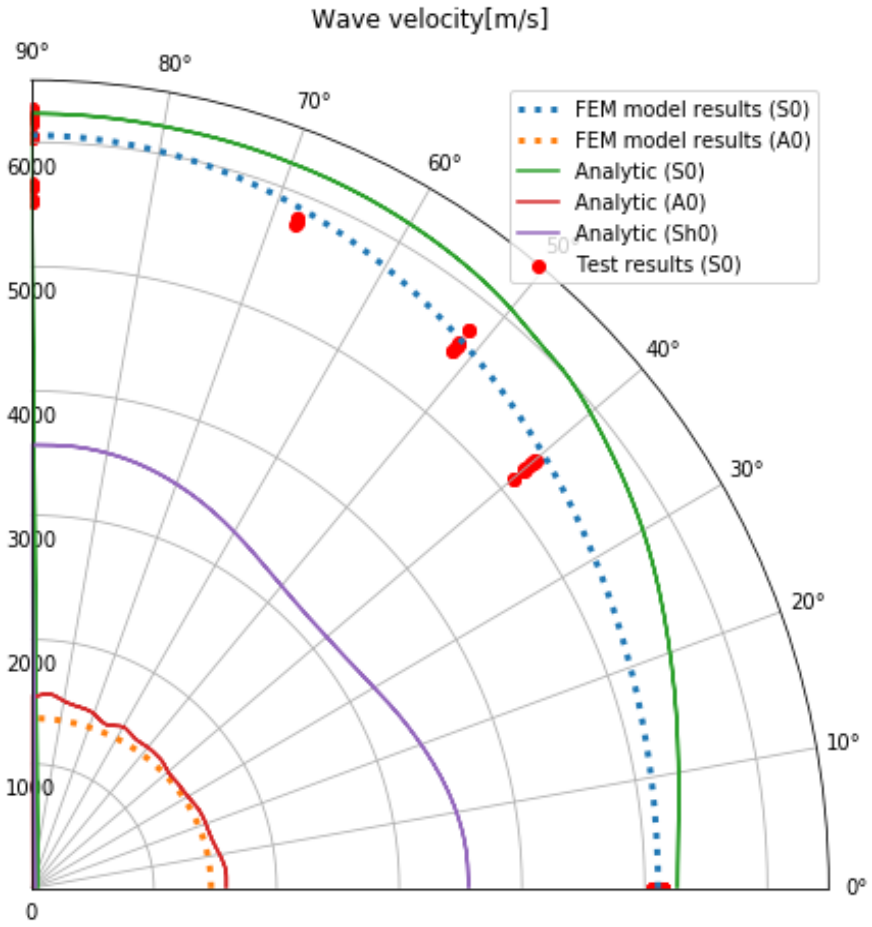


**Figure 3.33:** Wave velocity comparison for the flat composite panel for an input frequency of 200 kHz.

### C3D8R element modeling

This section presents an attempt to validate the modeling of the panel with 7 C3D8R elements to simulate the propagation of elastic waves. Each element represents a single ply of the composite material, with its respective orientation. The material definition needs additional terms to simulate the out-of-plane behavior of the elements, therefore, an Abaqus **Elastic, type=Engineering constants* model definition is used; with its properties shown in Table 3.8 (Hexcel Corporation, 2024).

**Table 3.8:** AS4/8552 material properties for the FEM model simulation with C3D8R elements.

| Property | Value | Property | Value | Property | Value |
|---|---|---|---|---|---|
| $E_1$ | 131 000 MPa | $E_2$ | 9750 MPa | $E_3$ | 8500 MPa |
| $\nu_{12}$ | 0.3 | $\nu_{13}$ | 0.3 | $\nu_{23}$ | 0.3 |
| $G_{12}$ | 4650 MPa | $G_{13}$ | 4200 MPa | $G_{23}$ | 4200 MPa |

The results of an active interrogation of a 200 kHz BURST-3 on PZT2 are shown in Figure 3.34, compared to the experimental results.

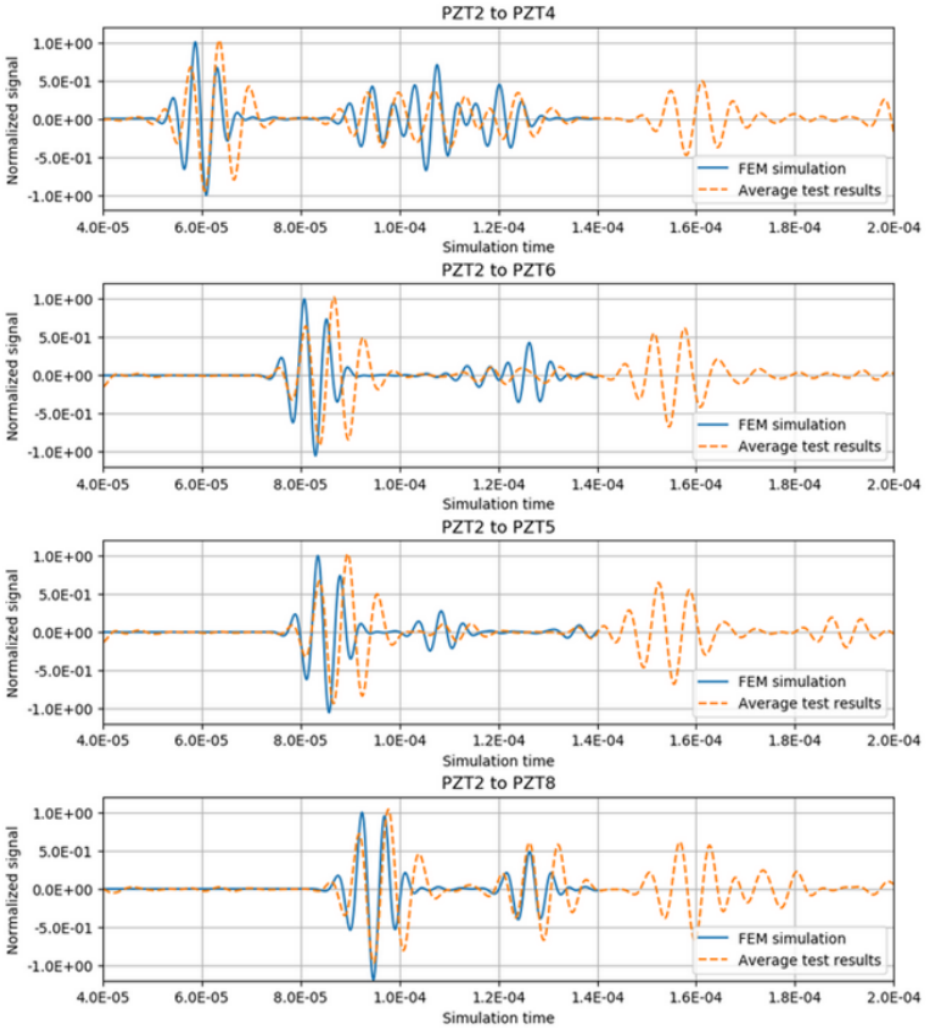


**Figure 3.34:** Active interrogation results for the flat composite panel with C3D8R elements - Actuator PZT2.

It is clear that the results present a good correlation, with a quality similar to that obtained with the SC8R representation shown in the previous sections. Further studies are recommended as this modeling may provide a better representation of the wave interaction with out-of-plane elements, such as stiffeners.

### Stiffened panel comparative

The following figures show a comparison of the propagation of elastic waves under the stiffener.

- Figure 3.35 shows the results at a time of 0.807 ms. The symmetric wave has reached the stiffener; it propagates with very little attenuation, and the energy lost in the tests is mostly due to the viscous dissipation of the adhesive, which is not simulated.
- Figure 3.36 shows the displacement at a time of 2.090 ms. At this point the A0 wave has reached the stiffener, and it can be seen that most of its energy is being reflected back.

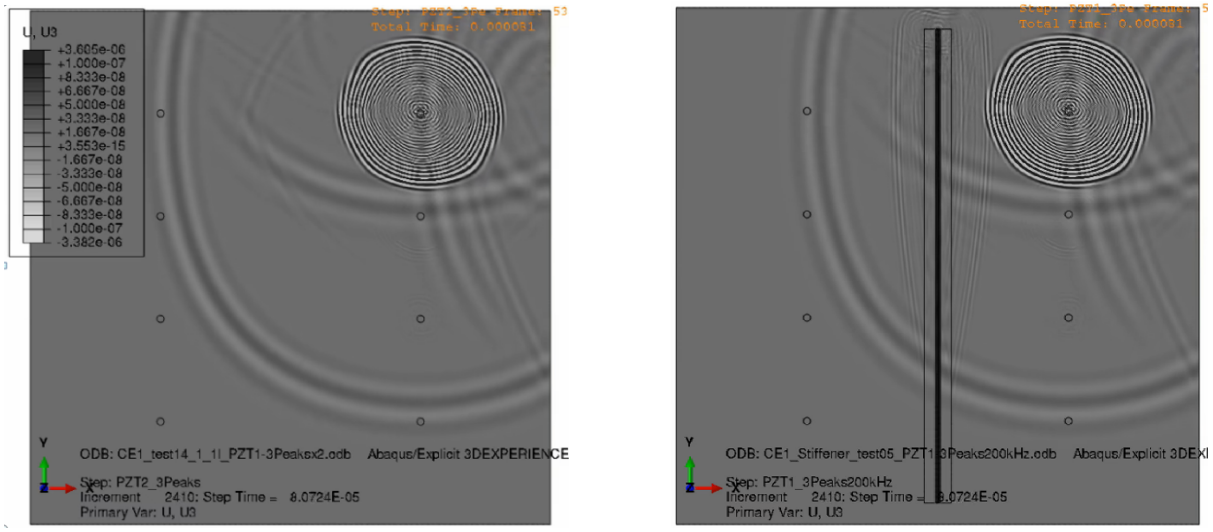


**(a)** Unstiffened panel **(b)** Stiffened panel

**Figure 3.35:** FEM model vertical displacements at $t = 0.807\,\text{ms}$

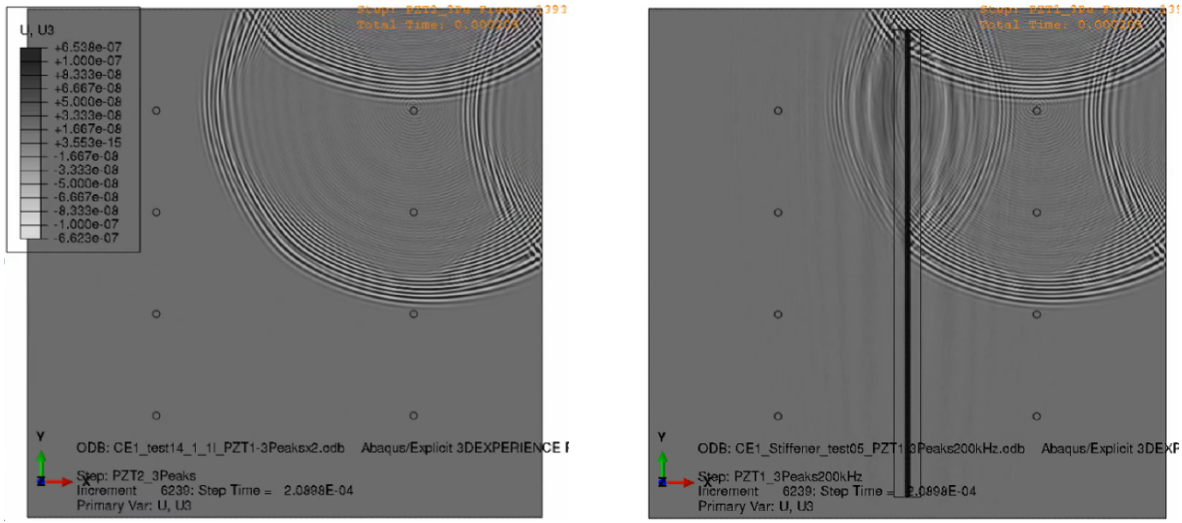


**(a)** Unstiffened panel **(b)** Stiffened panel

**Figure 3.36:** FEM model vertical displacements at $t = 2.090\,\text{ms}$

A more detailed view of the simulated interaction of the elastic waves with the stiffener is shown in Figure 3.37, displaying an evolution of the elastic wave at four consecutive instants of time; mode shapes in the reflections can be appreciated in the figure.


**(a)** $t = 3.63 \times 10^{-5}\,\mathrm{s}$

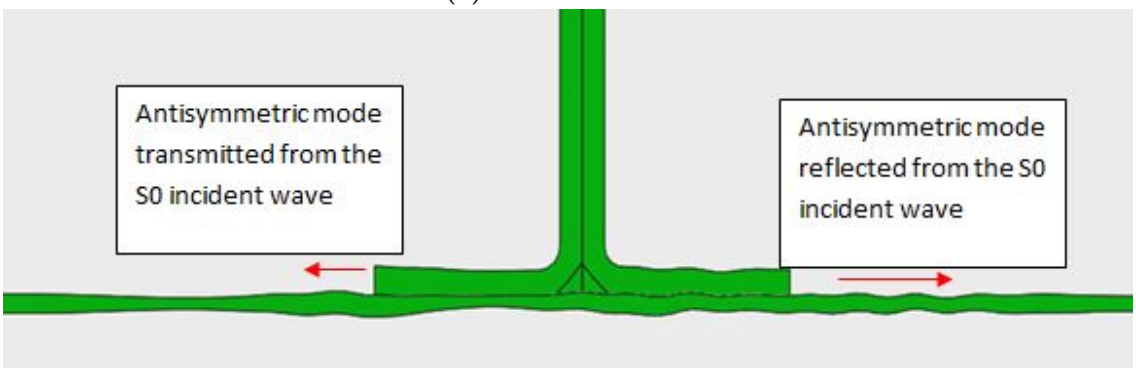


**(b)** $t = 5.36 \times 10^{-5}\,\mathrm{s}$

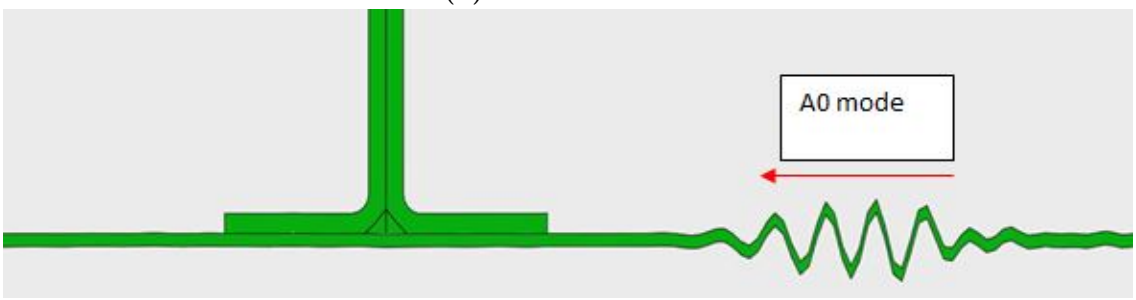


**(c)** $t = 1.00 \times 10^{-4}\,\mathrm{s}$

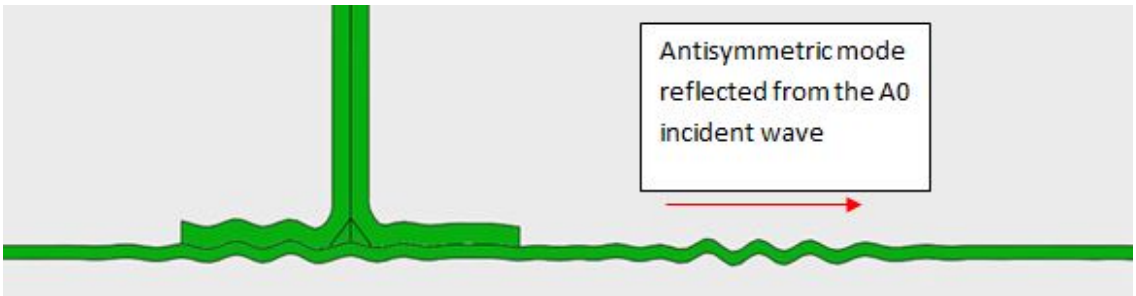


**(d)** $t = 1.46 \times 10^{-4}\,\mathrm{s}$

**Figure 3.37:** FEM model results detail of the elastic wave interaction with the T-shape stiffener.

It can be seen in the previous figures that the perturbation of the stiffener on the symmetric wave is very small. It is also interesting to see how the symmetric wave is accelerated along the length of the stiffener, although, due to its size this effect is not easy to appreciate. Figure 3.38 shows a detailed view of the interaction at $t = 0.06\,\text{ms}$.

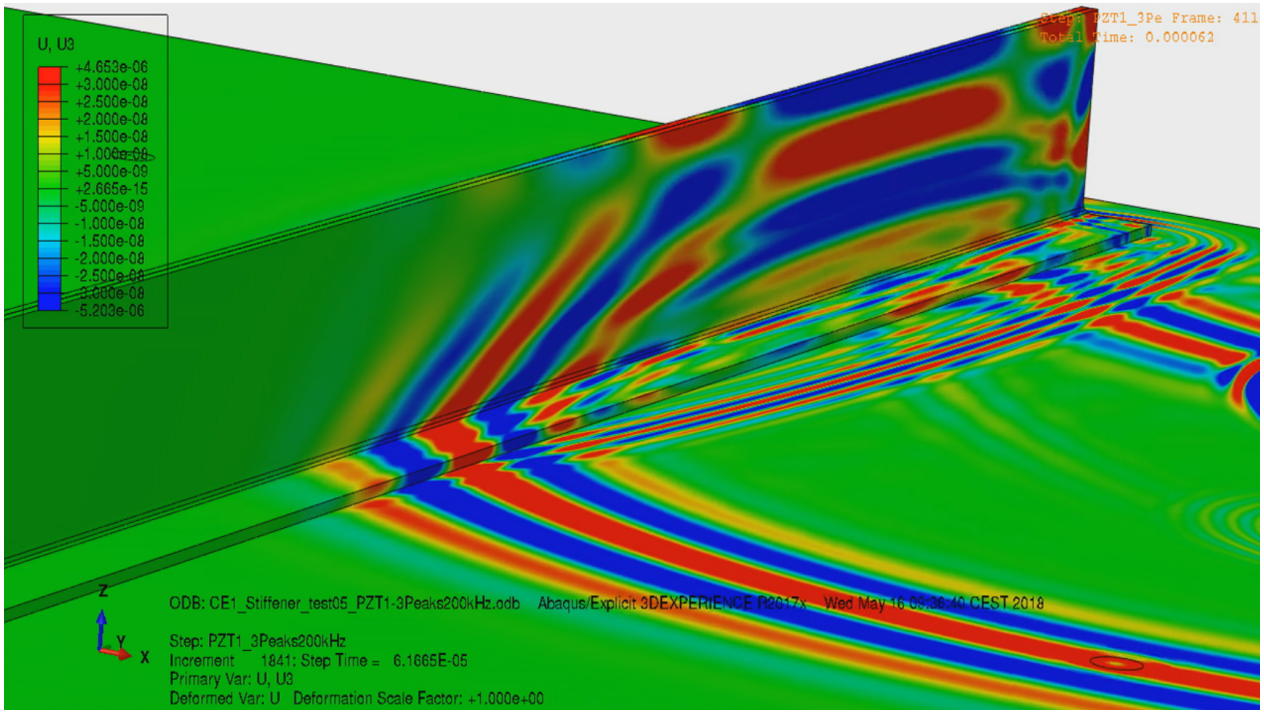


**Figure 3.38:** Detail of the interaction of the symmetric wave with the stiffener

The test validation is shown in Figures 3.39 and 3.40 when emitting form the piezoelectric transducers PZT1 and PZT2 located in the composite skin. The simulation predicts a very accurate result except for the paths that corss under the stiffener, as discussed before.

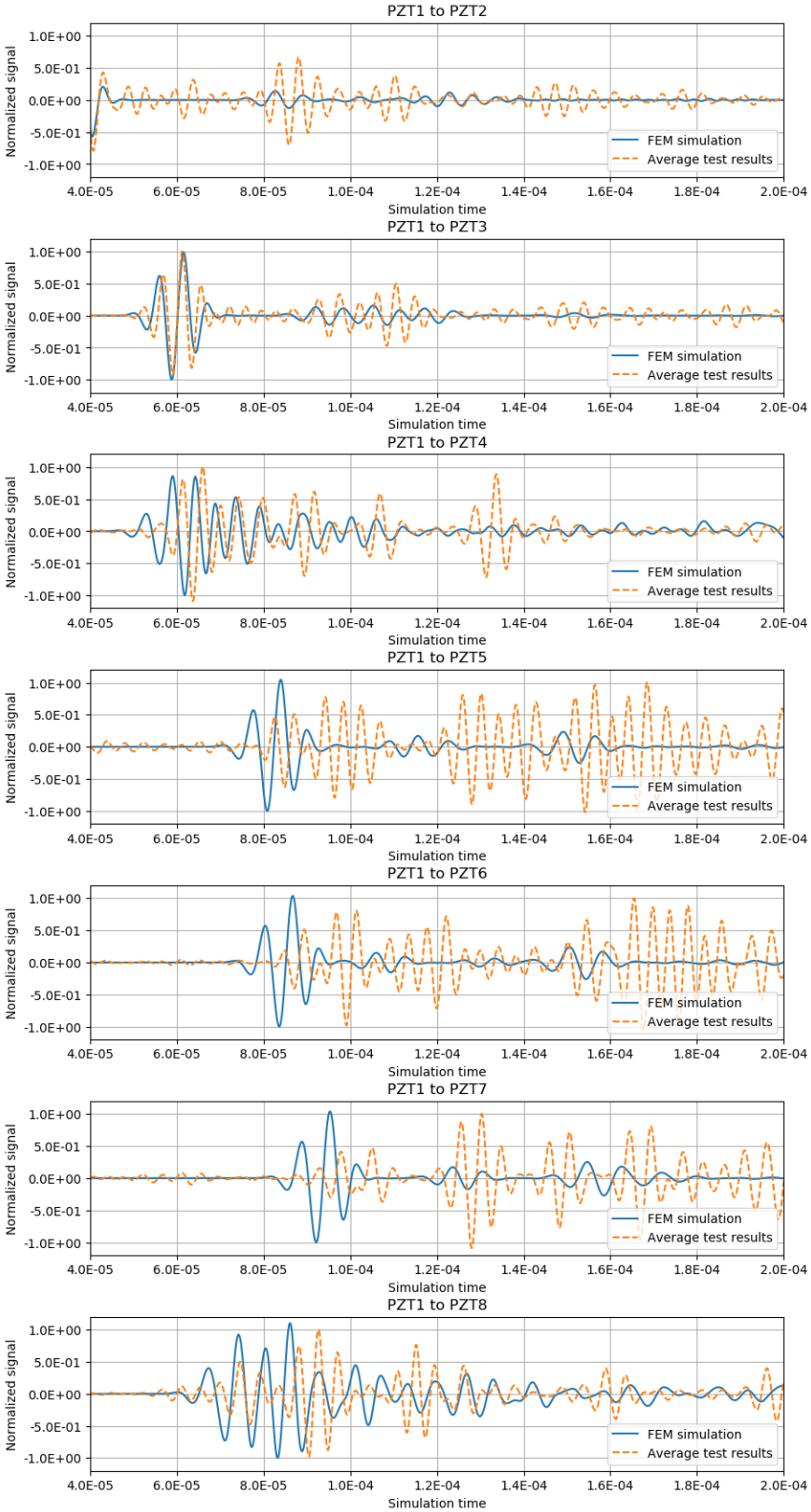


**Figure 3.39:** Active interrogation results for the flat composite panel and comparison with the test results - Actuator PZT1.

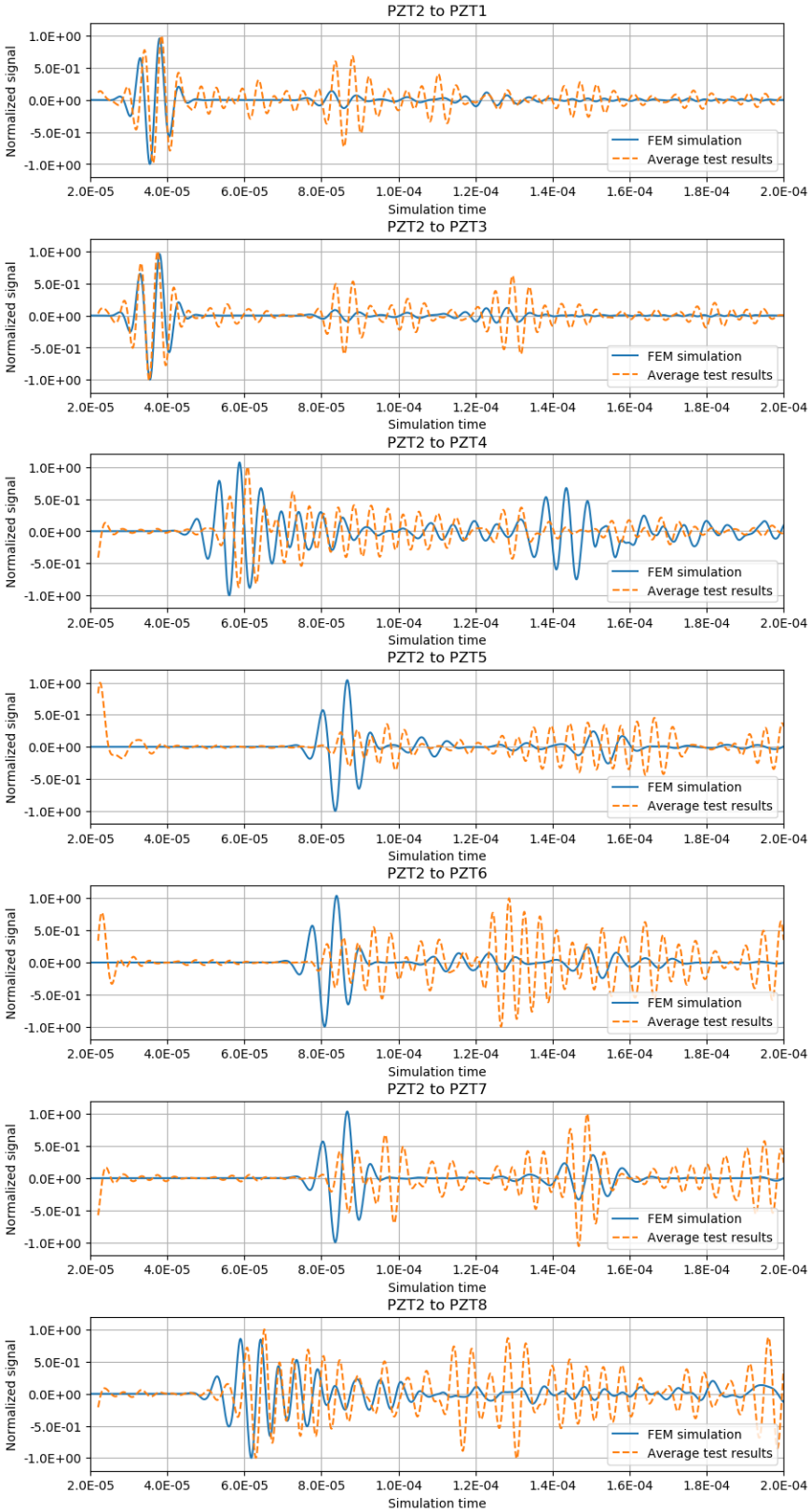


**Figure 3.40:** Active interrogation results for the flat composite panel and comparison with the test results - Actuator PZT2.

### Single mode excitation

When emitting with a single piezoelectric sensor, due to its location on one side of the plate, and therefore, its relative offset with the mid-plane, the resultant stress distribution is a combination of both tension and bending, with generates all possible GLW propagation modes.

As proven by Fernández López, 2009 it is possible to generate pure bending or tensile stress distributions with piezoelectric sensors at opposite sides of the plate that could generate isolated $SA0$ and $S0$ propagation modes (Figure 3.41).

- If both sensors generate the signal in phase the resulting stress field is uniform, resulting in the generation of a pure $S0$ mode.
- if both sensors generate the signal in contra-phase the resulting stress field has a pure bending shape, resulting in the generation of a pure $A0$ mode.

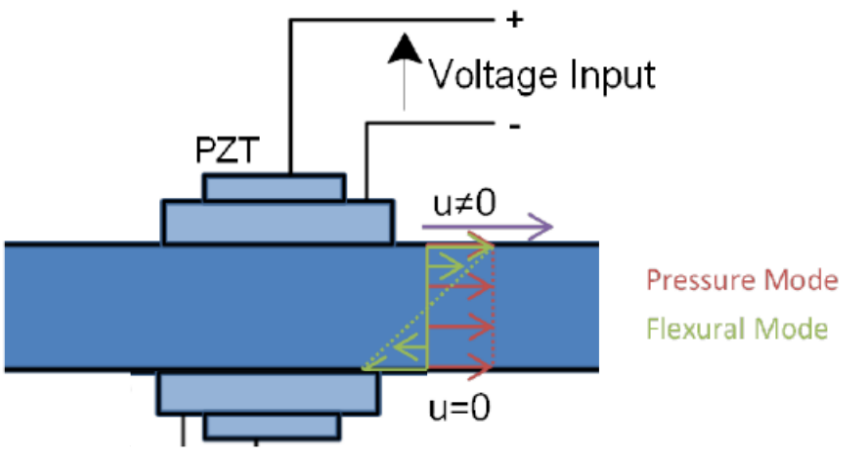


**Figure 3.41:** Stress distribution for the A0 and S0 modes.

Figures 3.42 and Figure 3.43 show the displacement results for these pure $S0$ and $A0$ modes respectively when emitting the wave from the location of transducer $PZT2$ in the unstiffened panel. To facilitate the interpretation of the results, displacements at both the top and bottom node are plotted.

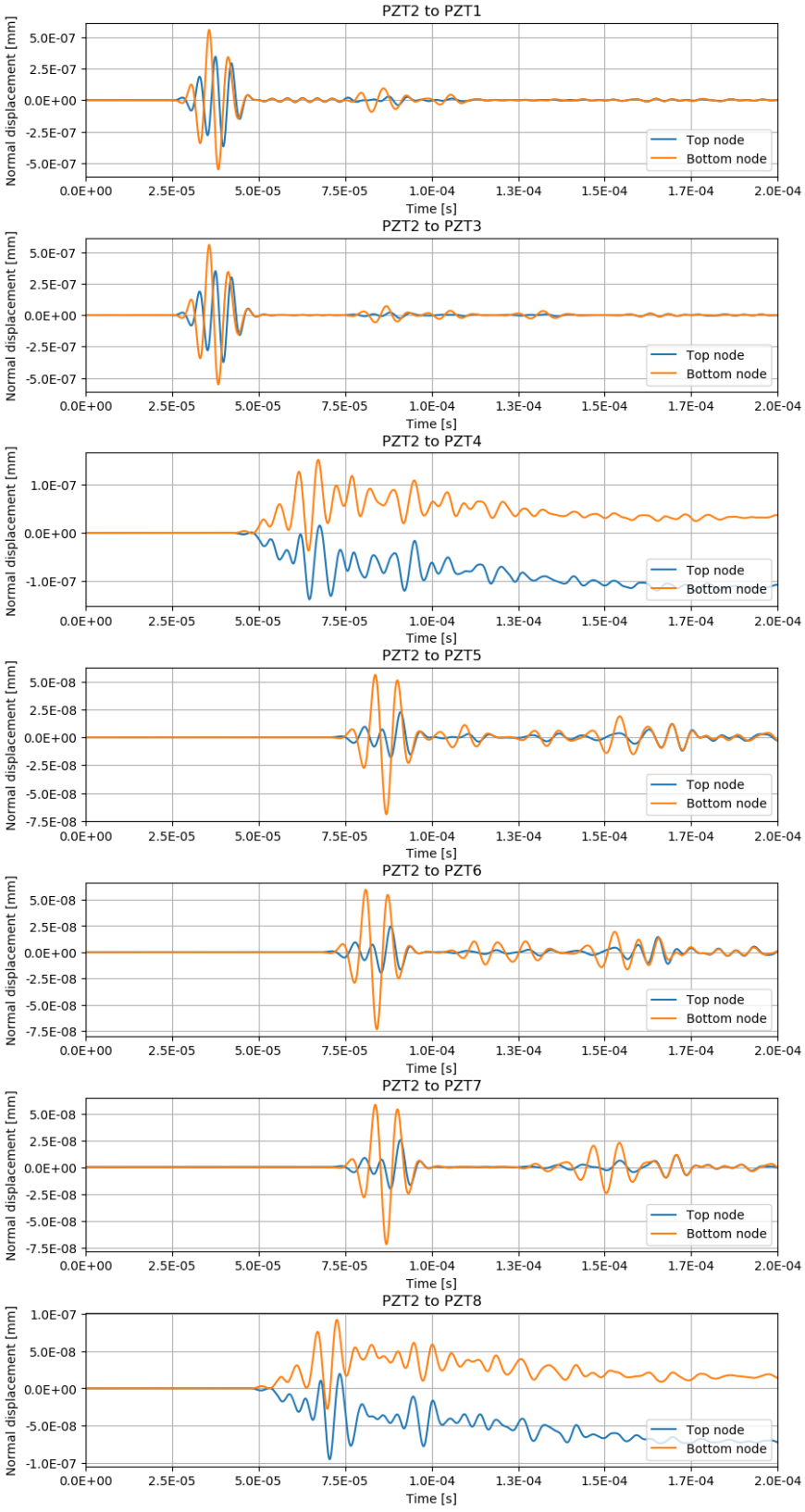


**Figure 3.42:** Active interrogation results in phase for the flat composite panel - Actuator PZT2. Displacement on top and bottom node

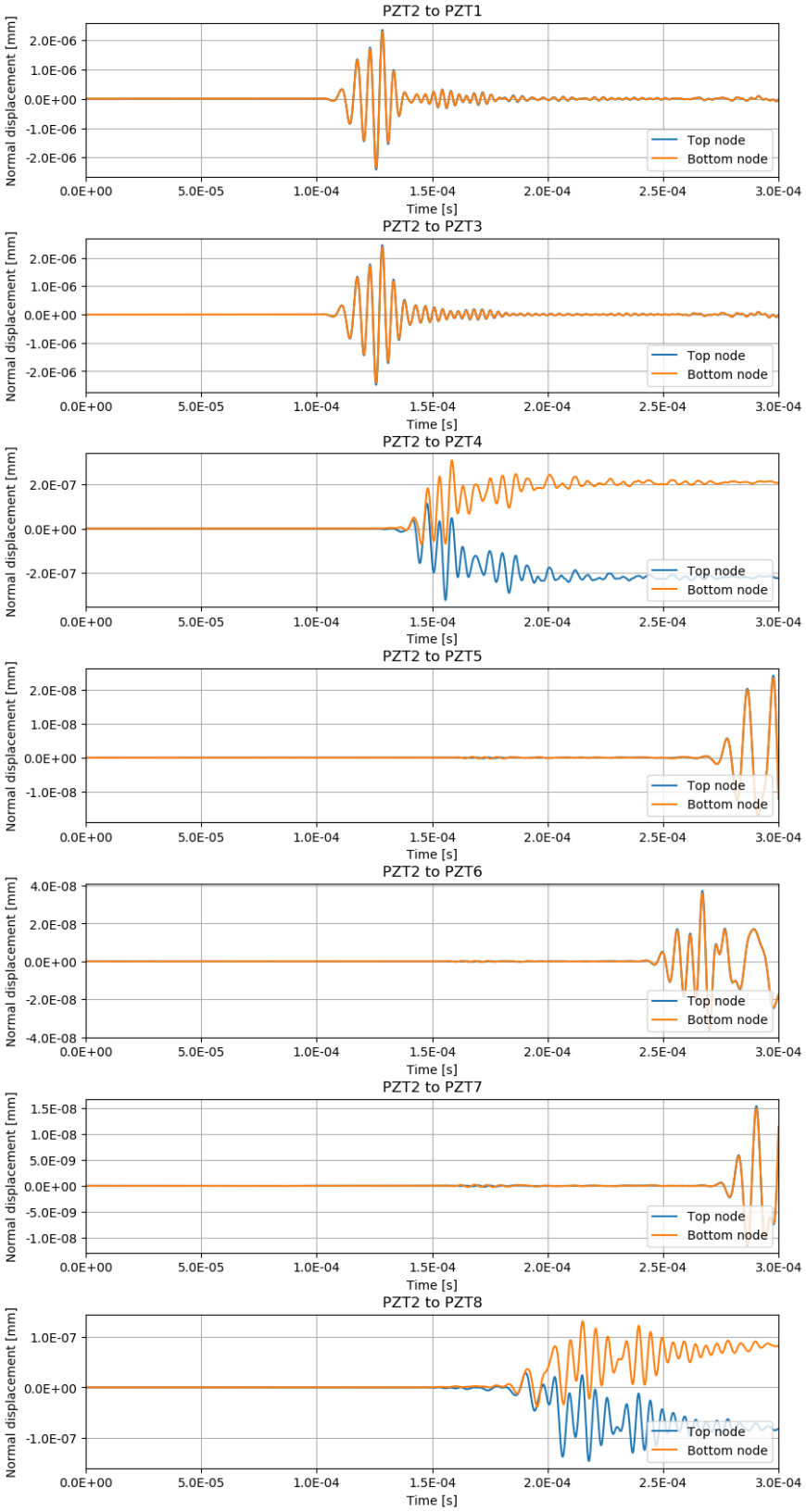


**Figure 3.43:** Active interrogation results in contra-phase for the flat composite panel - Actuator PZT2. Displacement on top and bottom node

### Piezo-electric sensors on stiffener

This section presents the results when the actuator is located in the stiffener. As the panel is symmetric, only the condition of actuator PZT4 has been simulated. The evolution of the displacements at three successive time points is shown in Figure 3.44.

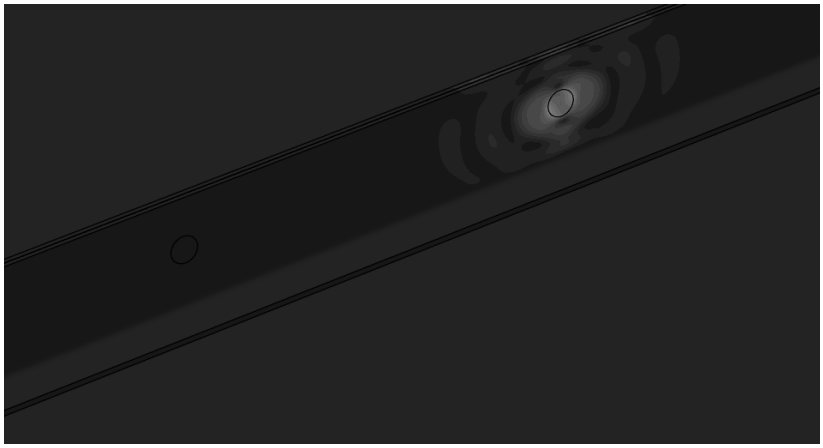

**(a)** $t = 1.6805 \times 10^{-5}\,\mathrm{s}$

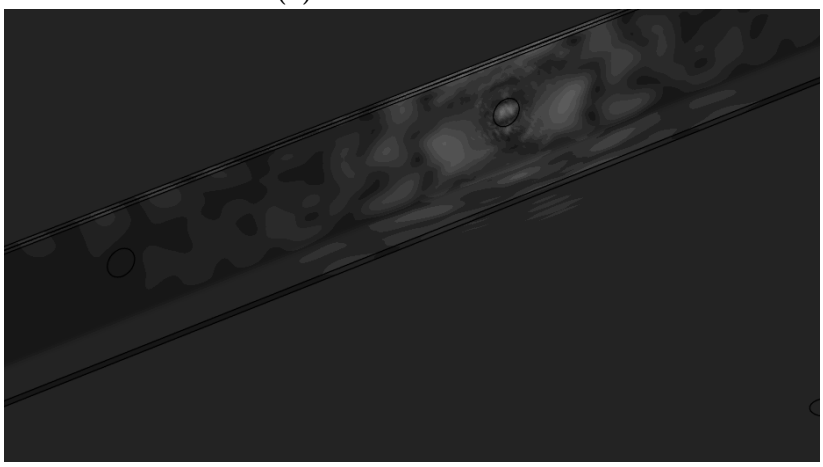

**(b)** $t = 3.5271 \times 10^{-5}\,\mathrm{s}$

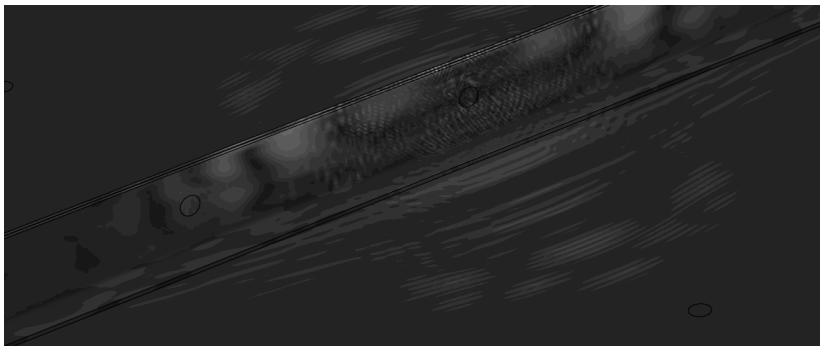

**(c)** $t = 1.1056 \times 10^{-4}\,\mathrm{s}$

**Figure 3.44:** Evolution of the displacement plot of the elastic waves on the stiffener when emitting from PZT4 at different time intervals.

The behavior of the simulation under these conditions is explained below:

- **Solution at** $t = 1.6805 \times 10^{-5}$ s. Shown in Figure 3.44a. The signal is being generated in transducer $PZT4$. As the dimensions of the Transducer are of a similar order than the plate the reflections with both the free edge and the base start interacting with the wave from the start.
- **Solution at** $t = 3.5271 \times 10^{-5}$ s. Shown in Figure 3.44b. The wave propagates both through the stiffener, reaching sensor $PZT8$ and through the base of the stiffener into the panel. The velocity of the wave is higher in the stiffener due to its increased stiffness.
- **Solution at** $t = 1.1056 \times 10^{-4}$ s. Shown in Figure 3.44c. The interaction of the reflections at both the base and top of the stiffener with the generated signal create a very large intensity of high frequency components that the simulation is not able to represent, this generates a large amount of noise that masks the true signal seen in the structure. Luckily, the noise propagates at a lower velocity than the elastic waves, therefore the initial part of the signal measured in the transducers of the plate is not significantly altered.

As in the previous section, both the symmetric and anti-symmetric pure wave modes are generated with transducer $PZT4$. The displacements results are shown in Figure 3.45 and Figure 3.46. As described below, the reflections on the stiffener generate a high amount of noise in the response of the sensors; this effect can be seen in the path from $PZT4$ to $PZT8$. Paths from the stiffener to the skin do not suffer from this effect in a significant manner.

Even considering the issues with the noisy response described before, the results present an acceptable match due to the fact that the piezoelectric sensor integrates the wave strains in an area and this phenomena is replicated in the simulation, reducing the effect of the high frequency noise. The comparison with the tests results for actuator $PZT4$ is shown in Figure 3.47.

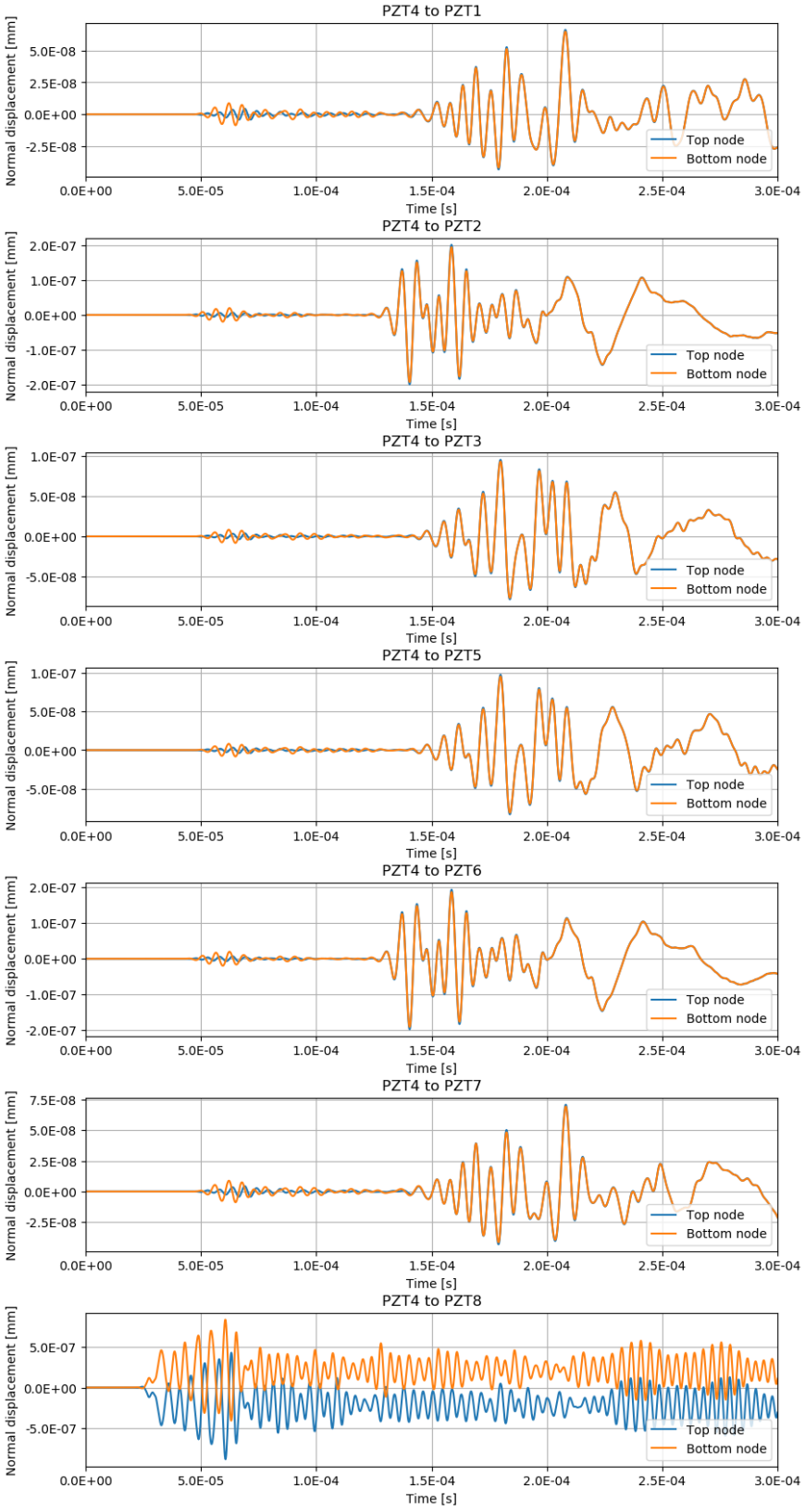


**Figure 3.45:** Active interrogation in phase results for the flat composite panel - Actuator PZT4. Displacement on top and bottom node.

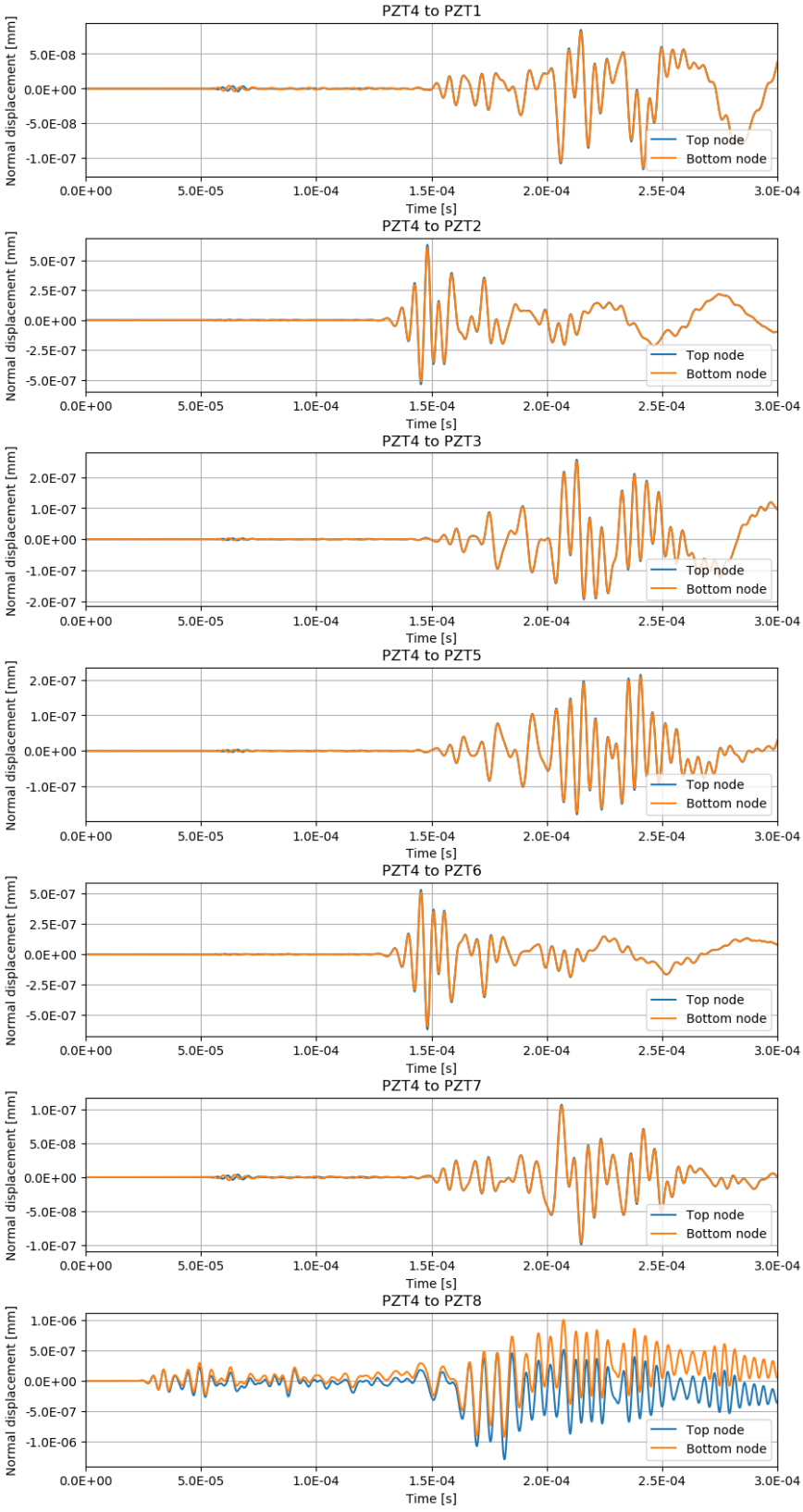


**Figure 3.46:** Active interrogation results in contra-phase for the flat composite panel - Actuator PZT4. Displacement on top and bottom node.

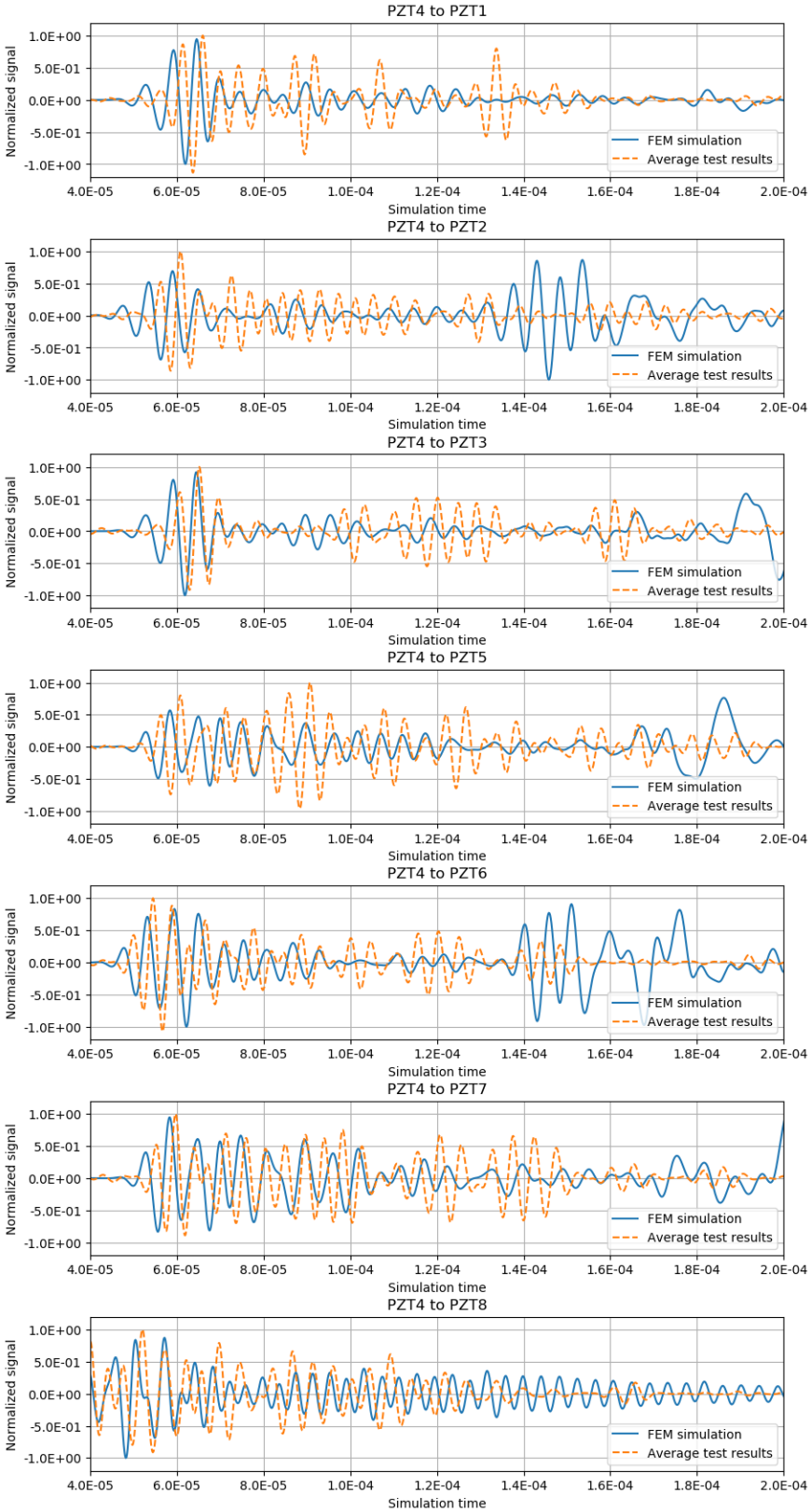


**Figure 3.47:** Active interrogation results for the flat composite panel and comparison with the test results - Actuator PZT4.

## 3.3 Signal analysis techniques via time-frequency distributions

A time–frequency representation (TFR) is a view of a signal, taken to be a function of time represented over both time and frequency (Sejdić et al., 2009). This is achieved by using a formulation often called Time–Frequency Distribution (TFD). The analytical formulation of relevant TFD is shown in Annex A.

This section presents an approach to study the frequency content of a signal measured in a PZT sensor with signal processing techniques based in time-frequency distributions. The TFD may give information about the frequency content of a signal and its evolution during time, making them a very promising tool to analyze the signals recorded in an SHM system. A very detailed review of time frequency distributions can be found in Cohen, 1989, and an application of the pseudo Wigner-Ville distribution on signals produced by Lamb Waves is shown in Prosser et al., 1999.

The main drawbacks to these techniques may be the difficulty to interpret the results obtained and the time and storage consumption of these computational methods. This work aims to provide some tools to simplify this first point.

### 3.3.1 Rayleigh damping parameters adjustment via TFD analysis

As stated previously, time frequency distributions can provide a vast amount of information on a time signal; this section presents the application of said distributions to validate a damping model usable with FEM simulation, an example of this procedure is shown in Sánchez Iglesias and Fernández López, 2020 and is replicated in this document.

An approximation of the antysimmetric wave for low frequencies is proposed in Hambric, 2006. This approximation can be compared with the time frequency diagram as follows:

$$c_B = \sqrt[4]{\frac{Eh^2}{12\left(1-\nu^2\right)\rho}(2\pi f)^2} \implies f = \frac{1}{2\pi}\sqrt{\frac{12\rho\left(1-\nu^2\right)}{Eh^2}}\frac{d^2}{t^2} \tag{3.5}$$

where $c_B$ is the anti-symmetric wave speed ($c_B = d/t$), $E$ is the plate stiffness in the direction of the wave to the sensor, $\nu$ is the poisson ratio, $\rho$ is the material density, $h$ is the plate thickness, $d$ is the distance from the impact point to the sensor, $t$ is the time and $f$ is the wave frequency.

The RIDH applied to an example signal obtained from one of the hammer impact tests is shown in Figure 3.48.

As shown in Prosser et al., 1999, the initial part of the RIDH corresponds to the dispersion curve of the material for the anti-symmetric wave, and a comparison with the theoretical curve is shown in Figure 3.48b. After a short amount of time the frequency content of the signal stays at a constant value, rather than becoming zero, this is due to the reflections of the wave coming back to the sensor and the response of the structure approaching a normal mode, and its this average frequency the one that dominates the damping of the one degree of freedom system described in section 1.7.2.

After a time of 0.003 s the theoretical dispersion curves predict an arrival frequency of less than 0.1 kHz and its energy or intensity in the RIDH becomes negligible compared with the energy of other frequency components present in the signal. Therefore the average frequency is calculated from this point; this effect is shown in Figure 3.48b.

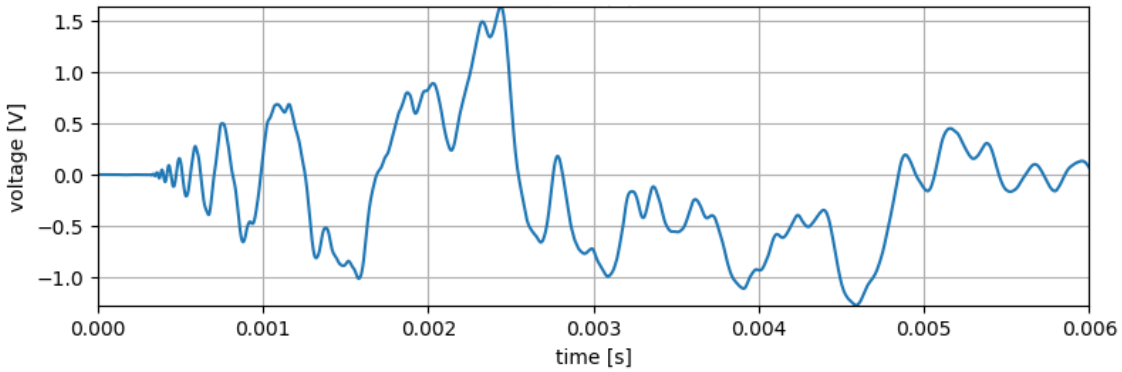


**(a)** Sensor signal

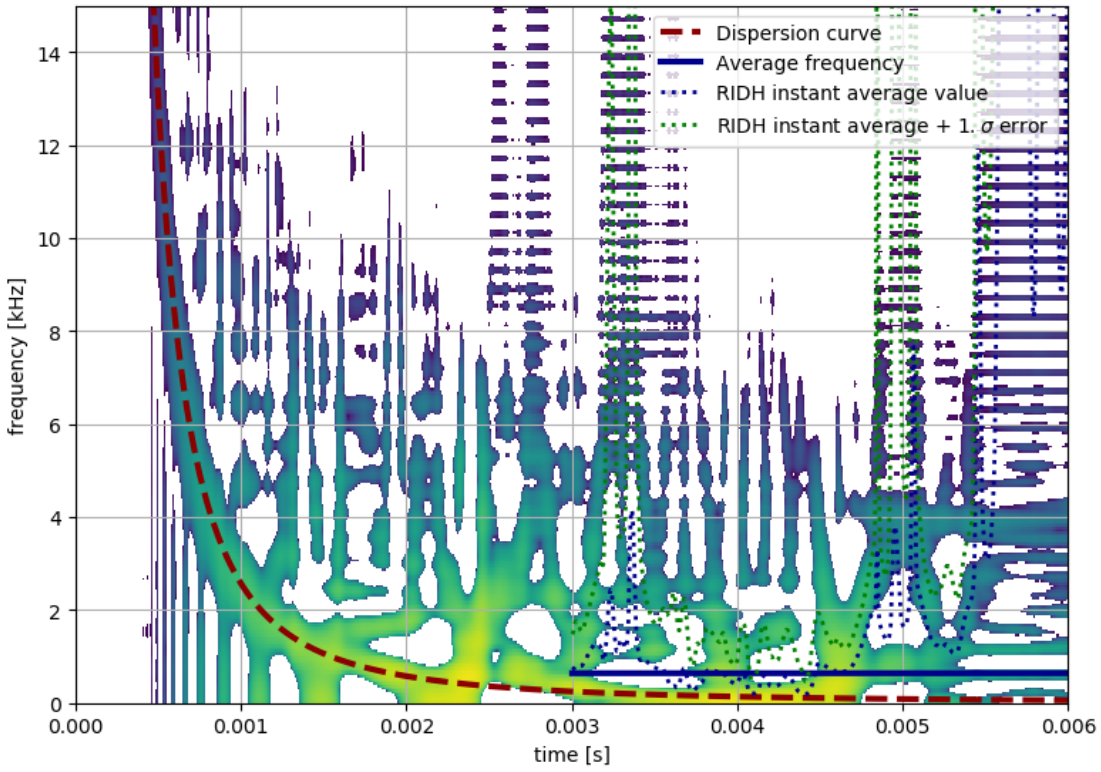


**(b)** $\log RIDH$ plot ($threshold = 0.1$) with theoretical dispersion curve and avg. freq. estimation

**Figure 3.48:** Example of PZT5 sensor signal results with aluminum impactor.

Rubber impactor presents a similar behavior as shown in Figure 3.49, although the measured frequency is lower than in the aluminum case.

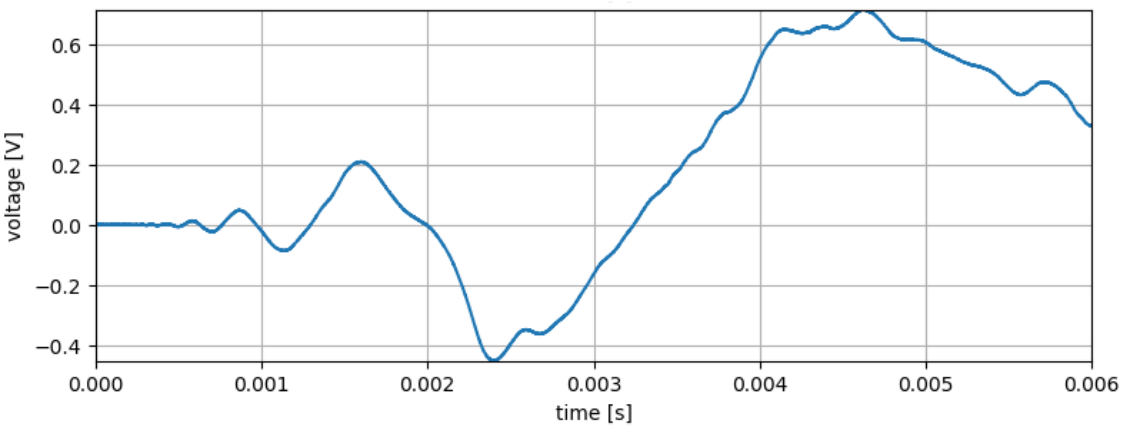


**(a)** Sensor signal

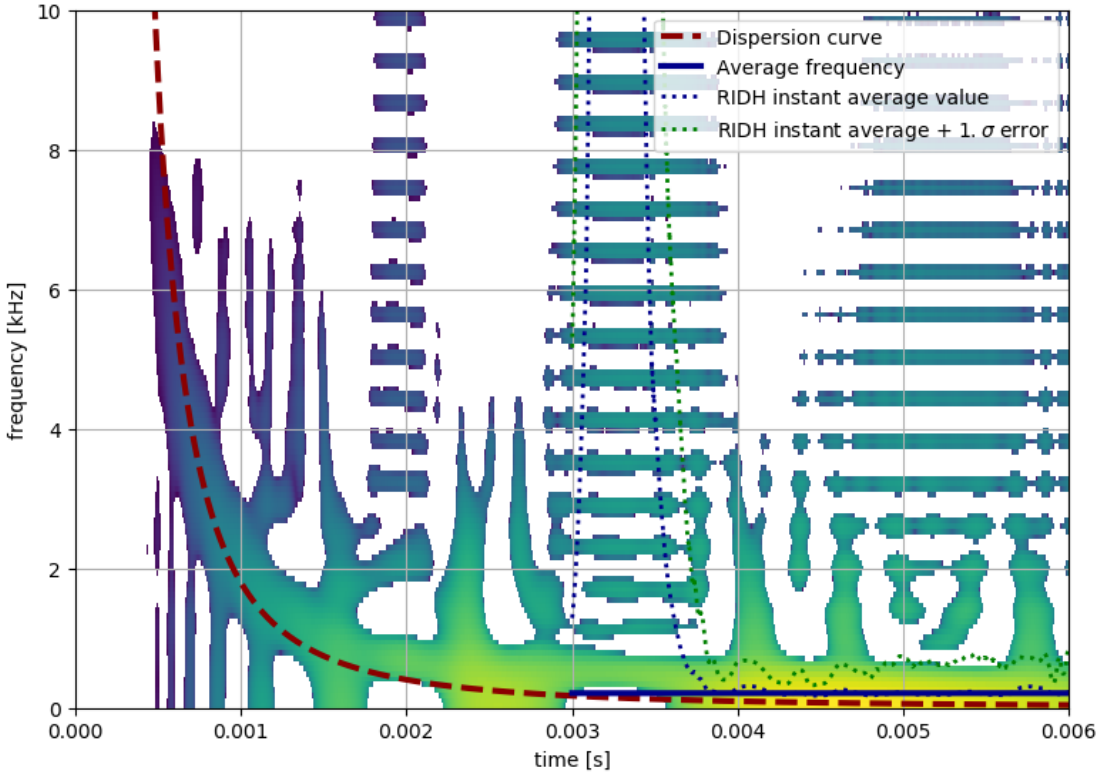


**(b)** $\log RIDH$ plot ($threshold = 0.001$) with theoretical dispersion curve and avg. freq. estimation

**Figure 3.49:** Example of PZT5 sensor signal results with rubber impactor.

As shown in equation 1.2 the peaks of the response of a one degree of freedom system follow an exponential curve. Because it is assumed that the piezoelectric sensor behaves in its linear range during the whole time frame, the following curve is fitted to the area measured in the tests:

$$a = -A_0 \mathrm{e}^{-\omega_D \zeta' t} + C \tag{3.6}$$

where $A_0$ is defined as a funtion of the average absolute voltage, $V_0$, as $A_0 = -V_0/(\omega_D \zeta')$, $\zeta' = \zeta/\sqrt{1+\zeta^2}$ and $C$ is a constant.

The parameters $A_0$, $\zeta'$ and $C$ are adjusted by means of a numerical fitting to match the experimental results. An example of this fitting is shown in Figure 3.50a. The time for the fitting is limited to 0.3 s sufficient to developt the majority of the impact energy in every case. Taking its derivative the curve can be plotted alongside the time history of the impact resulting in: $v = V_0 \exp(-\omega_D \zeta' t)$,

**(a)** Integral of the signal

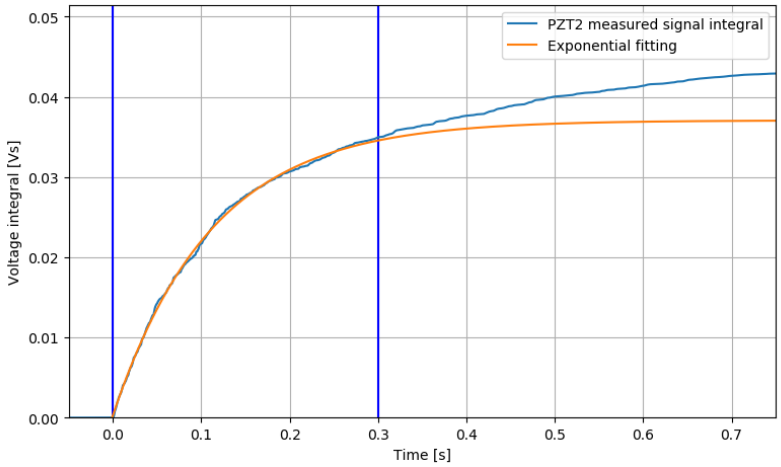


**(b)** Sensor signal

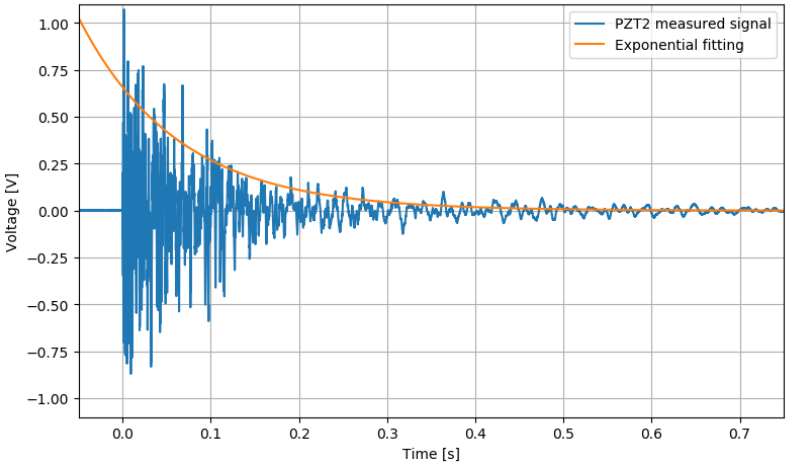


**Figure 3.50:** Exponential fitting adjustment of the piezoelectric sensor signals

The Rayleigh model, described in equation 1.4, is adjusted assuming the frequency $\omega$ obtained with the RID as the average oscillation frequency for each piezoelectric sensor signal and the critical damping factor $\zeta$ obtained with the method above for each sensor and impact performed in the tests.

The measured frequency of the impacts can provide a very good estimation of the Rayleigh $\alpha$ parameter, however, in order to obtain a good accuracy for the $\beta$ parameter additional points

at high frequency are taken from Ben et al., 2012, taking $\zeta = \tan(\delta)/2$ as proposed in Harris and Piersol, 2002. The fitting of the Rayleigh model is shown in Figure 3.51.

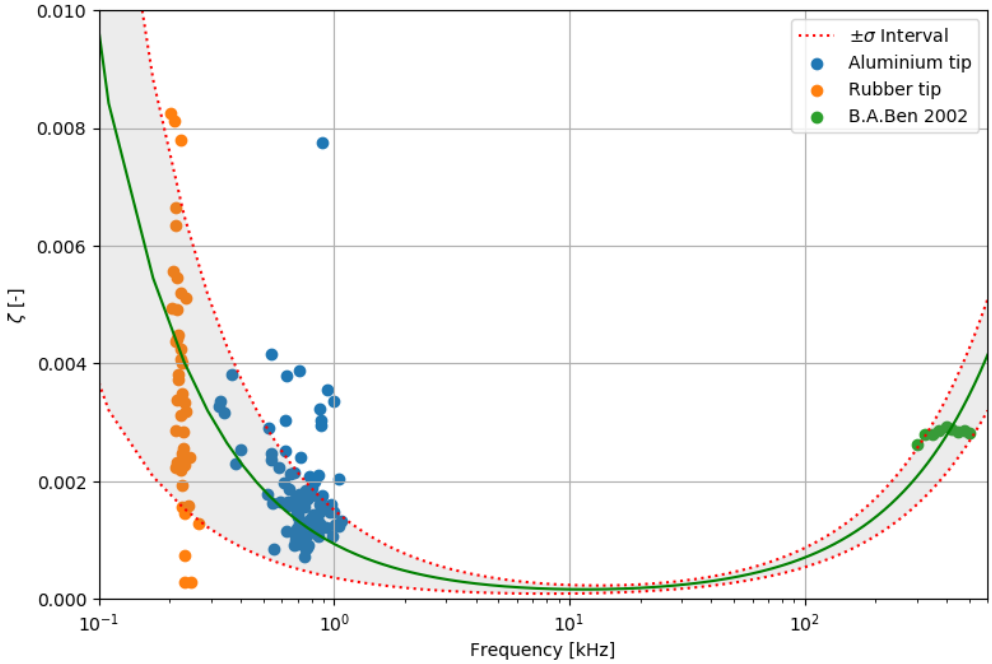


**Figure 3.51:** Rayleigh damping model fitting

The resulting parameters for the Rayleigh damping model are $\alpha = 11.62\,\text{Hz}$ and $\beta = 2.21 \times 10^{-9}\,\text{s}$. These parameters can then be used in a FEM model simulation, the results for a very low energy impact are compared with the test in Figure 3.52.

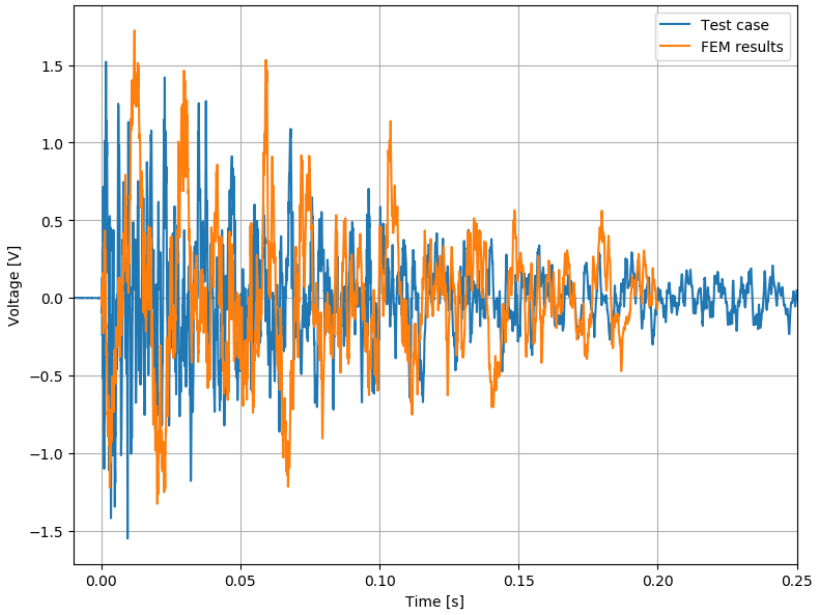


**Figure 3.52:** Results from FEM model and Tests at piezoelectric sensor 2

### Impactor type determination using the RIDH

As an additional result from the previous analysis, it is clear that the oscillation frequency measures in the Aluminum impactor tests is significantly different from the measured in the Rubber impactor. This difference can be plotted as a histogram, based in the number of tests performed and its shown in Figure 3.53.

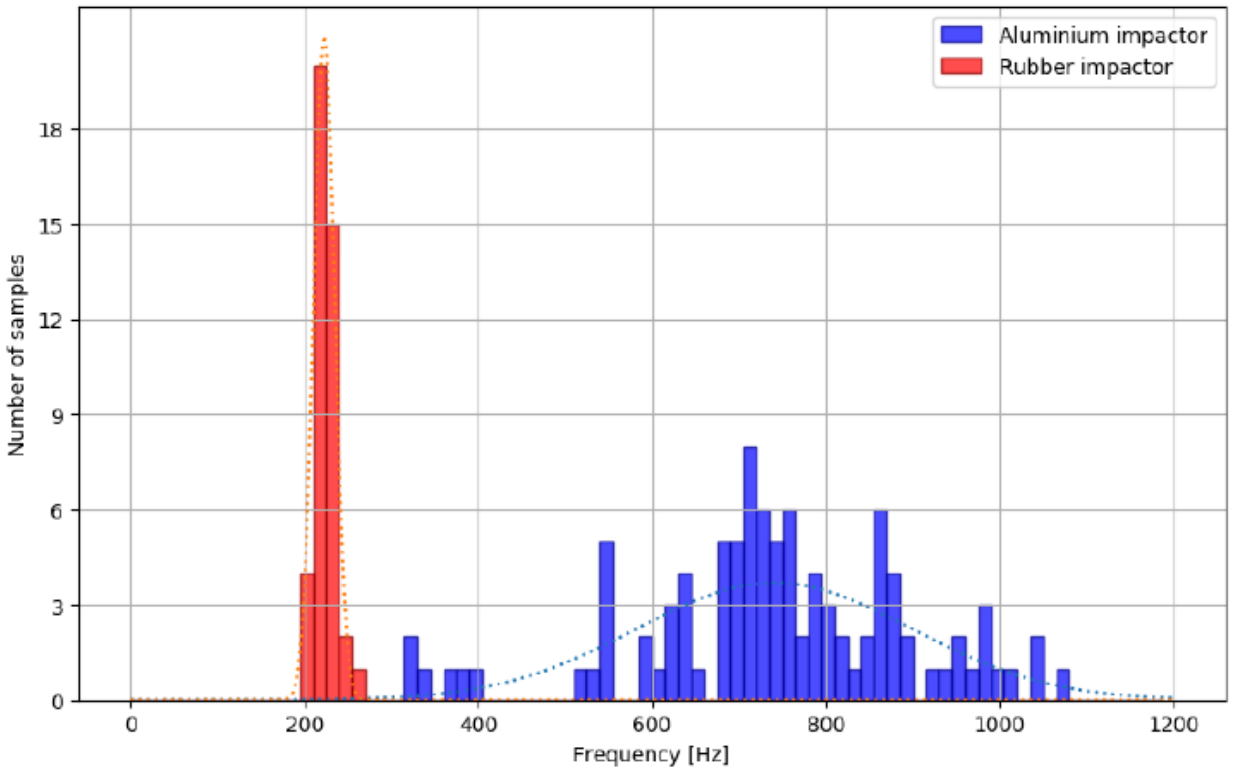


**Figure 3.53:** Histogram of the frequency results for the aluminum and rubber impactors.

The data is also presented in Table 3.9. It is clear from the previous figure that there is a very significant difference in the frequency of the response of the system after an impact due to the impactor's material, potentially allowing the use of time-frequency distributions to obtain this data from a recorded impact in-service as part of an SHM system.

**Table 3.9:** Average frequency results for the aluminum and rubber impactors obtained with the time-frequency distributions

| Impactor type | N | Average frequency [Hz] | Standard deviation [Hz] |
|---|---|---|---|
| Aluminum | 98 | 740.88 | 158.80 |
| Rubber | 42 | 222.98 | 12.07 |

### 3.3.2 Active interrogation signal processing with time-frequency distributions

This section presents an application of the time frequency distribution to the analysis of the signals measured during the active interrogation at the piezoelectric sensors. An example of said signals when emitting a BURST-3 in the flat plate at a frequency of 250 kHz is shown in Figure 3.54.

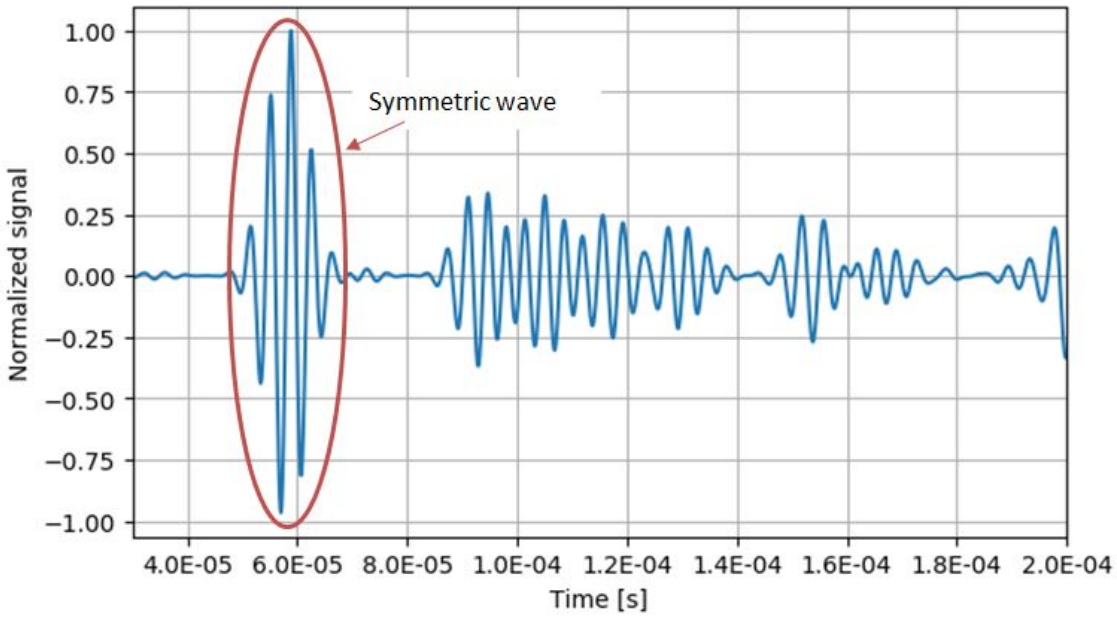


**Figure 3.54:** Input signal

The Wigner-Ville distribution, Pseudo Wigner-Ville distribution and reduced interference distribution are shown in Figures 3.55, 3.56 and 3.57 respectively.

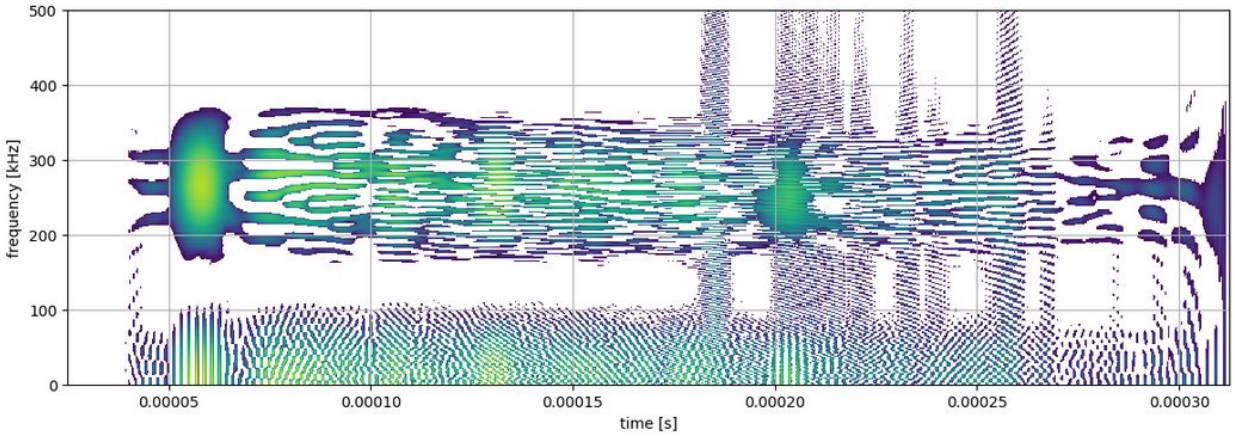


**Figure 3.55:** Normalized Wigner-Ville distribution plot (threshold = 0.001)

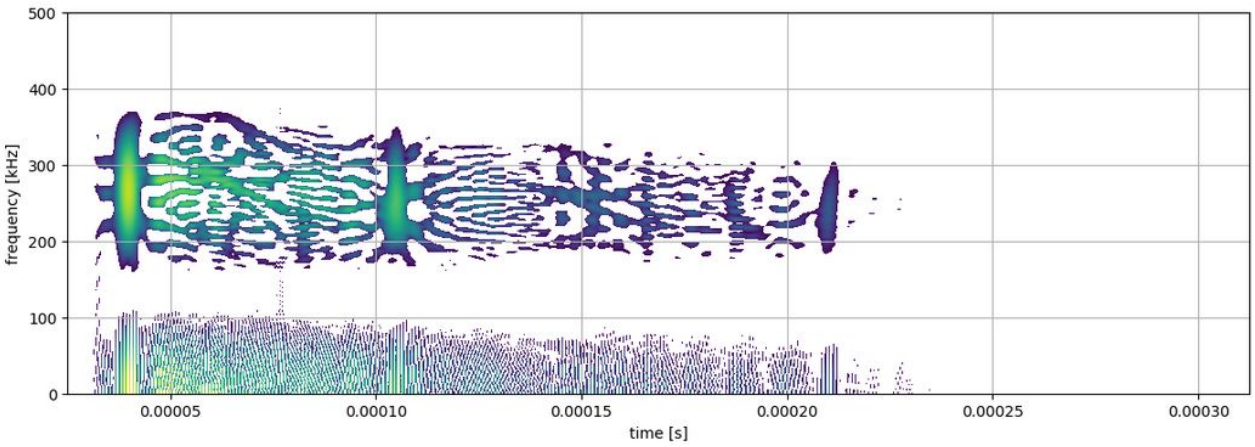


**Figure 3.56:** Normalized pseudo Wigner-Ville distribution plot (threshold = 0.001)

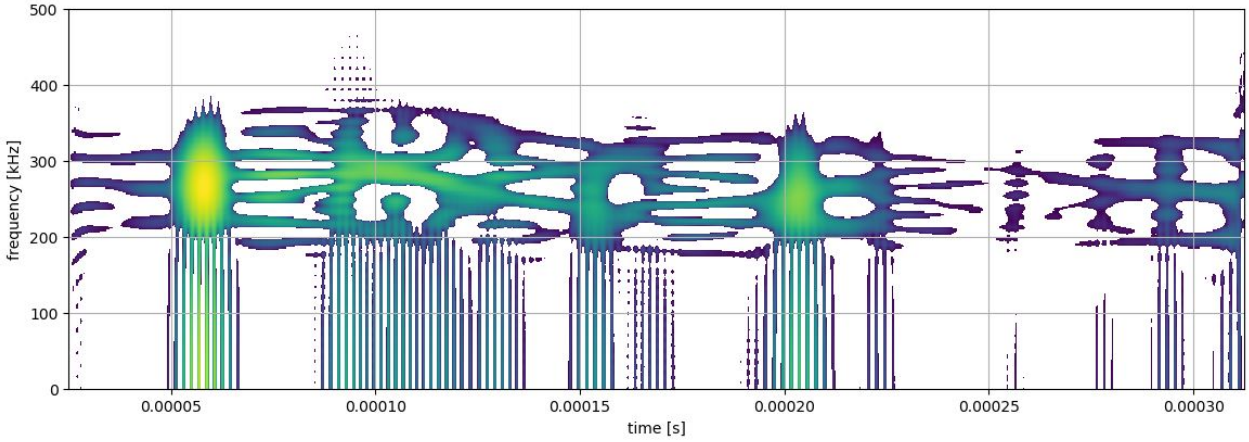


**Figure 3.57:** Normalized reduced interference distribution plot (threshold = 0.001)

Due to an implementation error, the time scale displayed in the PWD distribution shown in Figure 3.56 is half of he real time scale, nonetheless, its clear that the three of them display similar information about the signal.

As it can be seen in the previous figures, the three time-frequency distributions studied display an initial density concentration around the 250 kHz, corresponding to the input frequency. The extent in frequency of this area is similar in all cases, of around $\pm 100$ kHz, consistent with the extent of the FFT of the $S0$ wave, shown in Figure 3.58.

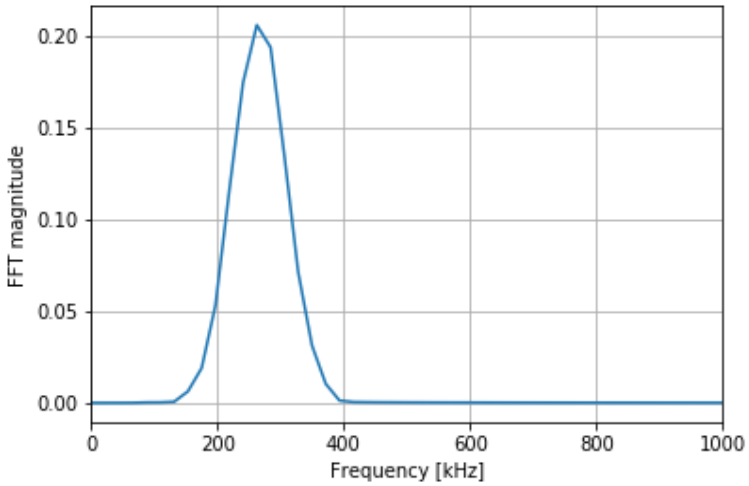


**Figure 3.58:** Fast Fourier transform (FFT) of the measured symmetric wave at 250 kHz

As stated previously, the Wigner-Vile distribution has a very high noise component due to the prescience of undesirable cross-terms in the solution. This can be appreciated in the figures as after the detection of the symmetric wave it is not easy to discern any further characteristics of the wave.

The PWVD also displays a significant amount of noise, specially at lower frequencies, however, as the cross-terms have been significantly reduced the figure appears much *"cleaner"*. Thanks to this reduction of noise it is possible to identify the reflections of the symmetric wave in the distribution.

From the three time-frequency distributions studied, the RIDH is the one that displays the least amount of noise, this is really helpful when identifying the real characteristics of the signal, as with the other distributions the solution does not appear as clearly. The reflections of the wave are clearly separated as independent groups and potentially could allow for machine learning techniques to characterize them and obtain additional information of the signal.

## 3.4 The ray-tracing algorithm

### 3.4.1 Algorithm overview

A wave point source in a medium radiates a spherical wave, which can be considered as a plane wave as soon as the distance r between the source point and the observation point is large enough. This plane wave is characterized by a wave vector defined by these two points. The trajectory of this plane wave when the cone angle is sufficiently small, shown in Figure 3.59, could be approximated by a line or a ray, and therefore, with enough rays, the propagation of the complete wavefront would be approximated accurately (Gengembre and Lhémery, 2000).

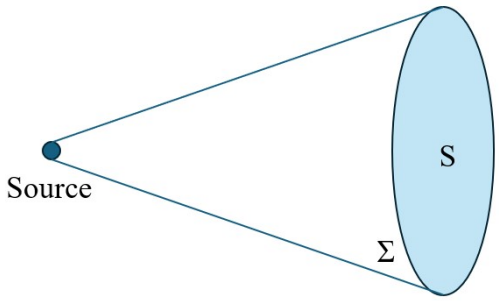


**Figure 3.59:** Cone of energy from a point source transmitted in a ray.

For an elastic-wave-based SHM system design, a wave source could emit a wavefront of energy that travels until it encounters a surface that interrupts its path. These rays would be represented as a stream of energy moving along the same trajectory. In vacuum or a perfect isotropic material, this ray travels in a straight line. When the ray encounters a surface boundary, any combination of four interactions may occur: absorption, reflection, refraction, and fluorescence.

A boundary can reflect all or part of the ray in one or more directions, and if the boundary is transparent or translucent to the wave, it will refract a portion of the beam in a different direction, potentially altering the frequency or amplitude. A boundary might also absorb part of the ray, reducing the intensity of the reflected and/or refracted echo and dissipating this energy into internal friction.

Less commonly, a boundary surface could also absorb some of the energy and re-emit it at a longer wavelength through fluorescence in a random direction, although in terms of high-frequency GLW in standard structural materials, this case is rare, often negligible, and therefore is not considered in this thesis.

The resulting energy fractions divided between absorption, reflection, refraction, and fluorescence must account for all the incoming energy per ray in the boundary.

### Ray casting

With this information, it is possible to derive a simplified ray casting algorithm, able to study a straightforward energy propagation by applying the GLW theory to propagate the wavefront of an arbitrary signal in a structure.

The idea behind ray casting, the precursor to recursive ray-tracing, is to trace rays from the source and find the closest object blocking the path of that ray. Using material properties to compute the ray propagation, the algorithm could determine the shading of a structural detail to the elastic waves or could serve as a simplified method to estimate the ideal positioning of sensors on a structure.

Ray casting consists in making the simplifying assumption that if a surface faces a wavefront, the wave will reach that surface and either be blocked or in shadow. If a mathematical surface can be intersected by a ray, it can be mapped using ray casting.

### Recursive ray propagation

The basic idea behind ray-tracing involves tracing the path of ideal straight (or curved) rays as they travel through the structure. This process simulates the behavior of these ultrasonic waves considering factors like reflection, refraction, dispersion, and, indirectly shading, by applying a recursive algorithm in order to account for all structural details with all initial and new spawned rays during the wave propagation.

Recursive ray-tracing is a computational technique used in various fields, such as computer graphics, optics, and wave propagation, to model how rays (such as light or sound waves) interact with surfaces or boundaries. In this context, it refers to the process of tracing a ray as it bounces, reflects, or refracts through multiple interactions with different media or surfaces, with each reflection or refraction generating new rays that are also traced recursively.

As described by Nikodym, 2010 and Whitted, 1980, the recursive algorithm may be implemented in a series of steps:

- Ray Generation: Rays are cast from the source into the structure. Each ray represents a potential path that the elastic waves could propagate to.
- Intersection Testing: The rays are traced through the structure to determine if and where they intersect with objects in the virtual environment.
- Reflection and Refraction: In case of an intersection, reflection and refraction of the rays must be accounted for. Reflected rays are traced in the opposite direction from the surface normal, simulating reflective surfaces, as shown in Figure 3.60a. The refracted rays resemble the bending of light as it passes through transparent materials, as shown in Figure 3.60b.

  The path of refracted rays along the structure is governed by Snell's law (Wolf and Krotzsch, 1995), which, at the boundary of two mediums 1 and 2 could be expressed as:

$$\frac{\cos\theta_1}{\cos\theta_2} = \frac{n_2}{n_1} = \frac{v_{p1}}{v_{p2}} \tag{3.7}$$

where $\theta_i$ is the incidence angle of the ray, , $n_i$ is the medium index of refraction and $v_{pi}$ is the phase velocity of the wave pulse on the medium $i$.

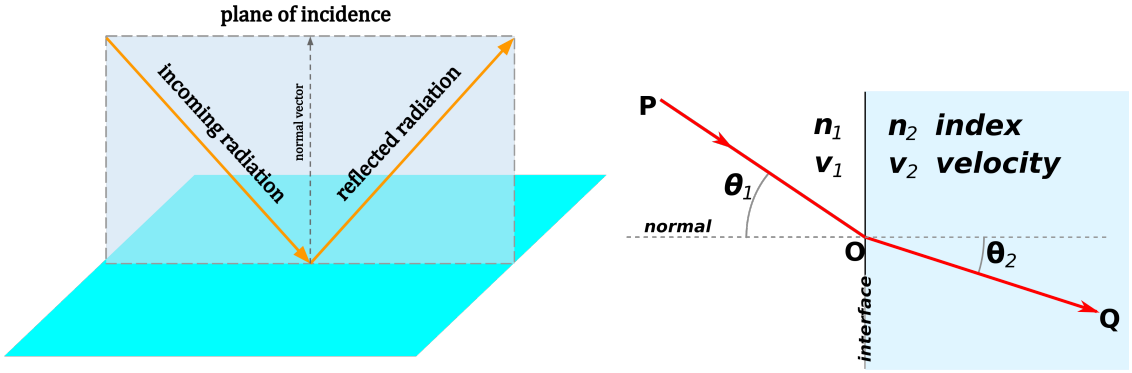


**(a)** Reflection **(b)** Refraction

**Figure 3.60:** Reflected and transmitted rays when encountering a boundary.

When a ray encounters a boundary, a component of the ray energy is reflected and another part is refracted or transmitted. For the particular case in which the ray would reach a segment end (i.e. a corner), the ray is eliminated from the model. This approach is taken as a simplification to reduce computational effort, as the effect is negligible for a sufficiently large number of rays and can be minimized considering initial rays that will not intersect any corners of the model on their first propagation step, for example: by choosing an odd number of initial rays.

Crossing a boundary between two different mediums: $medium1$ and $medium2$ implies that each medium must account for key parameters such as material properties, thickness, and laminate orientations which significantly influence the interaction of the ray at the boundary. The intensity of the reflected ray and the refracted ray is determined by the impedance mismatch between the two materials, which is governed by factors such as density, wave speed, and fiber orientation.

At the boundary, mode changes can spawn additional rays, such as converting a symmetric Lamb wave mode into an anti-symmetric mode, leading to more complex wave behavior. When the boundary represents a element with mass, such as a stringer, these mode changes can also generate echoes, which are secondary waves that spawn at a later time point because of the vibrational modes of the boundary element. Such echoes and mode conversions must be tracked to accurately model wave energy distribution and potential structural damage detection.

The model takes into account the mode conversion phenomena Y. Cho and Rose, 1996; Gunawan and Hirose, 2007 at each boundary, and therefore the transmitted and reflected component energy is divided between the different propagation modes, shown in Figure 3.61.

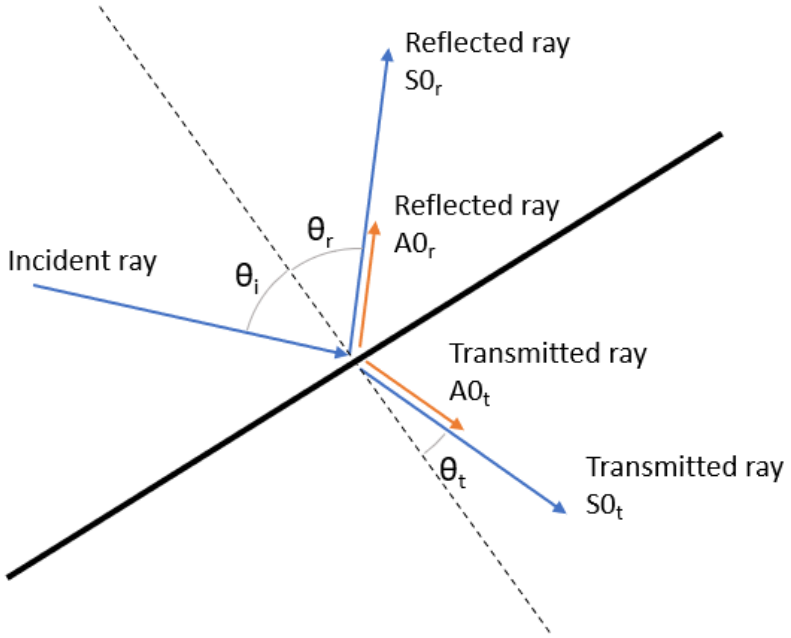


**Figure 3.61:** Generated rays due to the incident ray reflection and refraction after encountering a boundary

Energy losses at the boundary are a critical factor to consider, as a significant portion of the wave energy can be absorbed by the surrounding material or dissipated due to imperfections in the interface, such as roughness or inconsistencies, as well as through internal friction within the material itself. These losses can lead to a reduction in the amplitude of the transmitted or reflected wave, affecting the accuracy of any measurements or predictions.

Additionally, frequency alteration is another important phenomenon to consider. When a wave encounters different layer orientations, changes in material thickness, or transitions between layers of varying properties, its phase and frequency content can be altered. These changes can occur due to the interaction of the GLW with the specific geometric and material characteristics of the structure, which can result in changes in the propagation speed, wavelength and even mode conversion. As a result, the overall signal may exhibit frequency shifts or distortions that need to be carefully analyzed to understand the impact on wave propagation and ensure accurate interpretation of the data.

The incident ray intensity $I_{iray}$ is divided between the potentially four rays originating at the intersection point (reflected, transmitted, and their respective mode changes) and a remnant energy $\varepsilon_E$ that could be lost at the boundary, as follows:

$$I_{iray} = f_1 I_{S0_r} + f_2 I_{A0_r} + f_3 I_{S0_t} + f_4 I_{A0_t} + \varepsilon_E \tag{3.8}$$

where $I_{S0_r}$ and $I_{A0_r}$ represent the energy of the symmetric and anti-symmetric reflected

rays, $I_{S0_t}$ and $I_{A0_t}$ represent the energy of the symmetric and anti-symmetric transmitted rays and the factors $f_i$ represent the wave energy that is distributed between each of the propagation modes, and they are defined in terms of the fraction of energy transmitted through the boundary $f_{tr}$ and the fraction of energy invested in the mode change $f_{mc}$ as follows, assuming an $S0$ incident ray:

$$\begin{aligned} f_1 &= (1 - f_{tr})(1 - f_{mc}) \\ f_2 &= (1 - f_{tr}) f_{mc} \\ f_3 &= f_{tr}(1 - f_{mc}) \\ f_4 &= f_{tr} f_{mc} \end{aligned} \tag{3.9}$$

considering $f_{tr} <= 1$ and $f_{mc} <= 1$. Both factors $f_{tr}$, $f_{mc}$, and the dissipated energy $\varepsilon_E$ must be adjusted based on the medium and the type of boundary encountered.

- Recursive Tracing: To accurately simulate complex wave interactions, the tracing algorithm must incorporate recursive tracing. As mentioned earlier, a reflected ray may produce additional rays to account for secondary reflections, and these new rays are then traced recursively. This recursive process ensures that all subsequent interactions, such as further reflections, refractions, or mode conversions, are captured. The algorithm continues tracing each new ray, monitoring their possible intersections with boundaries and generating even more rays as needed, thereby providing a comprehensive simulation of all wave interactions within the system.

As the algorithm is recursive and the ray propagation is assumed linear, the time increment is only limited by the number of objects in the model, and, for a simple geometry and small number of objects involved, the propagation could be done in a very small number or even a single time increment.

The recursive tracing process continues until certain termination criteria are met, ensuring that the simulation remains computationally efficient and focused on meaningful interactions.

- The energy of the ray falls below a threshold, implying a negligible contribution.
- The ray travels beyond a certain distance or number of reflections.
- The ray exits the system or structure being analyzed.

Following these guidelines, an implementation of the method has been performed with Python that, as an object oriented programming language, each ray can be treated as an independent object, and therefore track its evolution on each increment. The methodology is also easily parallelized, as each ray does not interact with others up to the point of the results reconstruction, where they can be added linearly.

Three basic examples generated in order to demonstrate the effectiveness of this procedure are shown in Figure 3.62

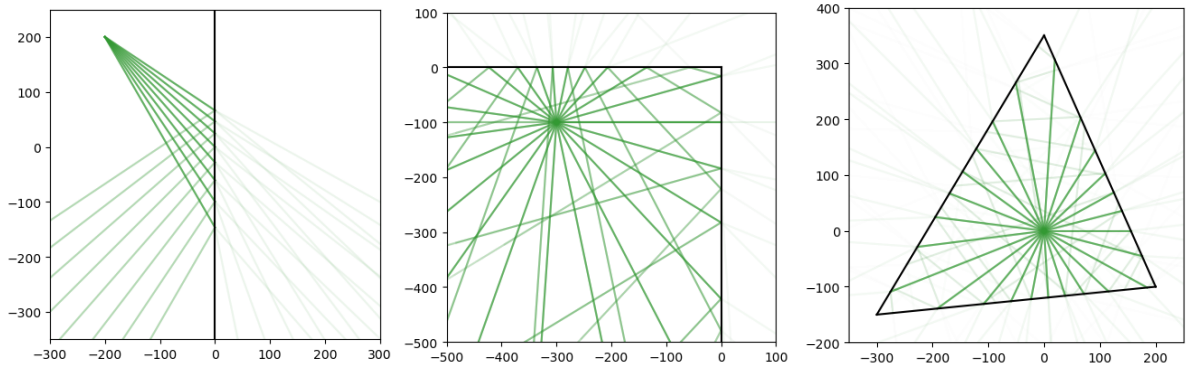

**(a)** Straight line **(b)** Straight corner **(c)** Triangle shape

**Figure 3.62:** Simple geometrical examples of a recursive 2D ray-tracing algorithm implementation

### 3.4.2 Ray signal recovery

#### Acoustic intensity of a ray

The acoustic intensity of a ray, introduced previously, refers to the amount of (sound) energy that is transmitted through a medium per unit area per unit time, in the direction of wave propagation. It is a measure of how much energy is carried by each ray that forms the acoustic wave and can be expressed as the power per unit area, typically measured in watts per square meter $\mathrm{W/m^2}$.

Acoustic intensity can be influenced by several factors, including:

- **Amplitude of the wave ($A$):** Higher amplitude waves carry more energy, resulting in higher intensity.
- **Wave phase speed ($v_p$):** The speed at which the wave propagates through the medium contributes to the rate of energy transfer.
- **Medium properties:** The density ($\rho$) and the elastic modulus of the material ($E$) affect how much energy the wave can carry. More rigid or dense materials typically lead to higher intensities for a given wave.

The mathematical formula for acoustic intensity $I$ in a plane wave is:

$$I = \frac{1}{2}\rho v_p \omega^2 A^2 \tag{3.10}$$

where $\omega$ is the angular frequency of the wave.

For a GLW ray, the acoustic intensity will vary based on how much energy is lost due to absorption, reflection, or scattering at boundaries between different media. Reflected and refracted portions of the wave will carry different intensities based on the impedance mismatch and the energy losses at the boundary.

The signal information is carried independently on each ray in the frequency domain, via a sufficiently large amount of terms of their Fourier transform, and could then be altered as the

ray propagates through the model due to different effects, such as material damping which is considered as a factor over the signal amplitude $A$, following an exponential law:

$$A = A_0 \mathrm{e}^{-\omega \xi t} \tag{3.11}$$

where $\xi$ is the material damping coefficient.

The signal is then recovered at each point applying the time shift property of the Fourier transform:

$$x\left(t - t_0\right) \longleftrightarrow e^{-i\omega t_0} X\left(\omega\right) \tag{3.12}$$

as the signal is dispersive, the phase velocity as a function of frequency $v_p\left(\omega\right)$, estimated in the previous section, is accounted for as follows:

$$x\left(t - t_0\right) \longleftrightarrow \sum_{j=0}^{N} e^{-i\omega_j \frac{d}{v_p(\omega_j)}} X_j\left(\omega_j\right) \tag{3.13}$$

where $d$ is the distance along the ray path where the signal is to be obtained.

To model curvature in a medium with variable material properties, it must be assumed that the power within a ray tube remains constant within it (Officer, 1958), shown in Figure 3.63. And the change in power is only related to the change in the acoustic intensity:

$$\Delta P_0 = I_0 2\pi r_0^2 \cos\Theta_0 d\Theta_0 \tag{3.14}$$

$$\frac{I}{I_0} = \frac{r_0^2}{r} \cos\Theta_0 \left\| \frac{d\Theta_0}{dL} \right\| \tag{3.15}$$

where:

- $r_0$ represents the reference distance,
- $\Theta_0$ is the initial ray angle at the source,
- $d\Theta_0$ is the initial angular separation between two rays,
- $dr$ is the incremental range increase,
- $\Theta$ is the angle at the field point,
- and $dL$ is the with of the ray tube.

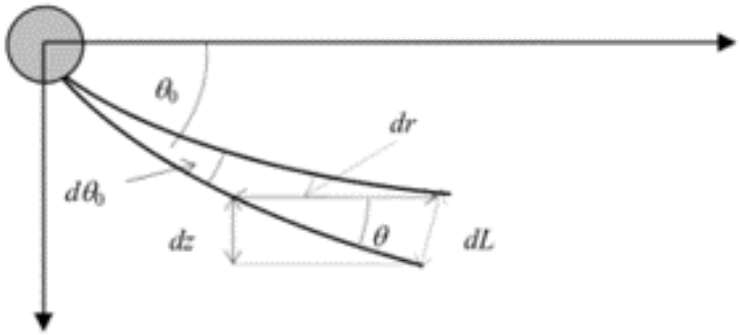


**Figure 3.63:** Curved rays originating from a source. The energy radiated in a narrow tube remains inside the tube (Officer, 1958).

### Area sensors approximation

The method has been developed focusing on the characteristics of a piezoelectric transducer. As explained previously, because of the low weight of the sensors and their ability to generate and measure guided elastic waves, they are ideal for SHM systems. The signals obtained unavoidably contain multiple modes that require complex signal processing techniques to extract useful information. Moreover, PZT sensors may also reveal certain non-linear behavior and hysteresis under high voltages or strains. Brittleness, low fatigue life, etc., may be some other concerns that limit application Schulz et al., 1999.

To include the PZT sensors in the simulation, they are modeled as a circle boundary. This boundary does not interact with the incident rays; however, the intersection time points ($t_i$ and $t_e$) are captured and the ray signal is integrated between the line crossing the sensor area ($s_e - s_i$), as shown in Figure 3.64. This way allows the sensor to act as an integrator of the material strain in the area it coversAyers et al., 2003; Erturk and Inman, 2011, and the solution is obtained by superimposing the integrated signal of all incident rays.

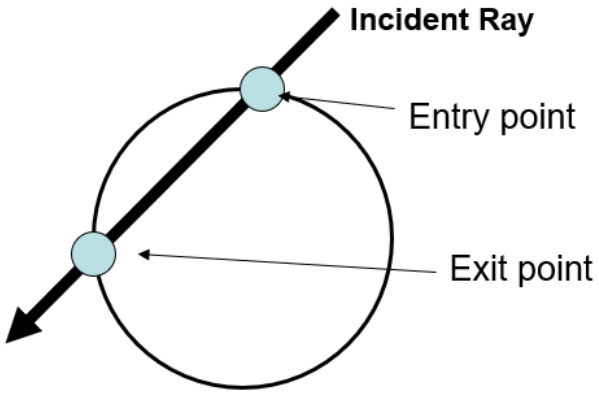


**Figure 3.64:** Schema of the PZT sensors model for the ray-tracing algorithm

There are a number of significant advantages that arise from using this methodology; the main one is being able to avoid the need to calculate eigenrays to the sensors, therefore saving

significant computation time, and being able to obtain a solution with the first iteration of the ray map.

As the sensors act as a signal integrator, the dispersive effect on the signal is inherently captured by modeling its area. This effect is significantly more relevant for cases where the signal wavelength is comparable to the sensor dimensions and may have some noticeable effect on the signal measured.

On the contrary, a larger number of initial rays is needed to achieve a good solution, and later reflections may be captured imprecisely or not be captured at all because of the low number of rays that may cross the sensor, although this could be solved by iteratively increasing the number of rays until achieving a converged solution.

### 3.4.3 Ray propagation in Orthotropic materials

As a ray propagates through an orthotropic material, such as CFRP, its behavior will be different depending on the elastic moduli of the material in each direction, leading to anisotropic wave propagation. This means that the speed of the wave and the distribution of energy will change based on the direction of propagation relative to the principal axes of the material.

The phase speed of the GLW can be solved as $v_p(\theta)$ using the TMM method (Annex D), where $\theta$ is the angle of the ray propagation vector.

# Chapter 4

# Results

## 4.1 Rectangular aluminum plate

This section presents the results obtained using the ray-tracing method to model wave propagation in the aluminum plate specimen, highlighting the strengths and challenges of the ray-tracing approach and providing a foundation for integrating it into broader structural health monitoring frameworks by adjusting experimental factors.

The results of the ray-tracing simulation are visualized as a heat map in Figure 4.1, depicting wave propagation for 1602 initial rays (801 $S0$ rays and 801 $A0$ rays). These results correspond to three representative time points during the simulation run-time and are generated using a 300 kHz BURST-3 signal emitted from transducer PZT1.

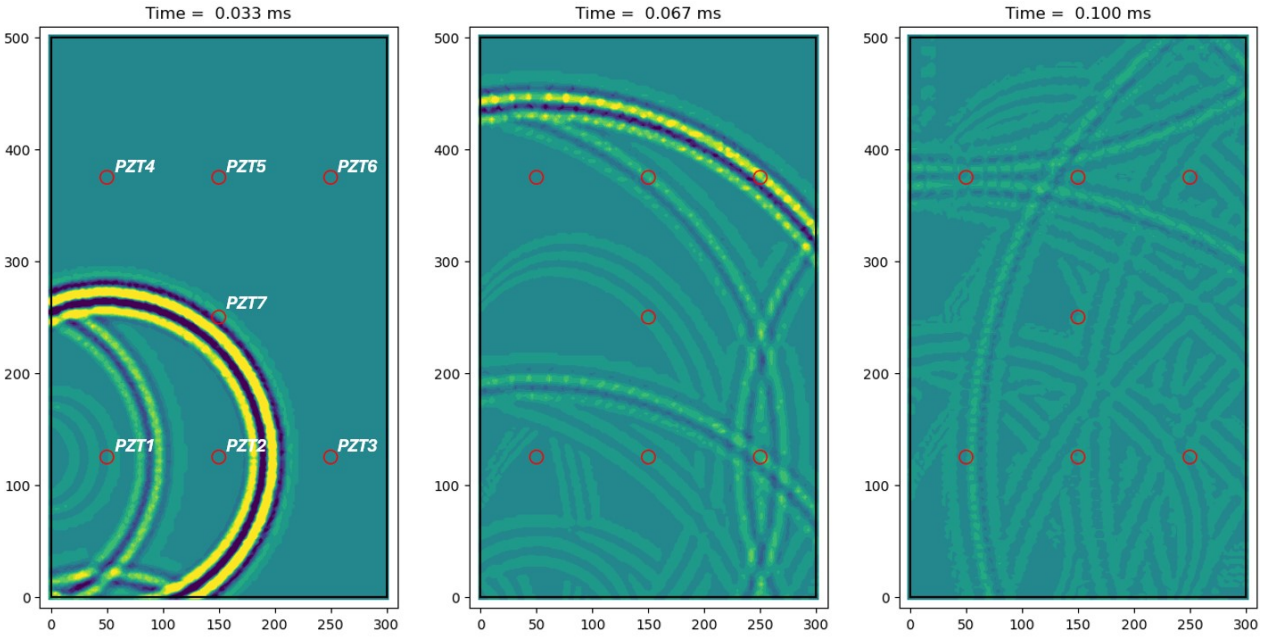


**Figure 4.1:** Rectangular aluminum plate propagation color map of S0 wave at relevant time points.

The heat map shown in Figure 4.1 is calculated by mapping the ray signal on a square grid with a characteristic length of 2 mm. The figure shows how the elastic waves propagate through the plate and interact with each boundary and how the energy is being dissipated after each reflection, highlighting areas of wave concentration and showing patterns of reflection and transmission through the structure.

The number and position of the piezoelectric sensors, defined in section 3.1.1, is also shown in the figure as a reference.

In order to capture the results on a selected transducer, the rays that intersect the sensor must be detected and integrated over its length. As an example, all rays captured by the transducer $PZT6$ when emitting a signal from $PZT1$ at $t = 8 \times 10^{-6}$ s are shown graphically in Figure 4.4b. The signal carried by each ray is then numerically integrated over the length traveled by each ray through the sensor and added together. The results are shown in Figure 4.2, compared to the experimental data.

The amplitude of the Hilbert transform of the signal is plotted along with the sensor signal to aid with its visual interpretation in Figure 4.2.

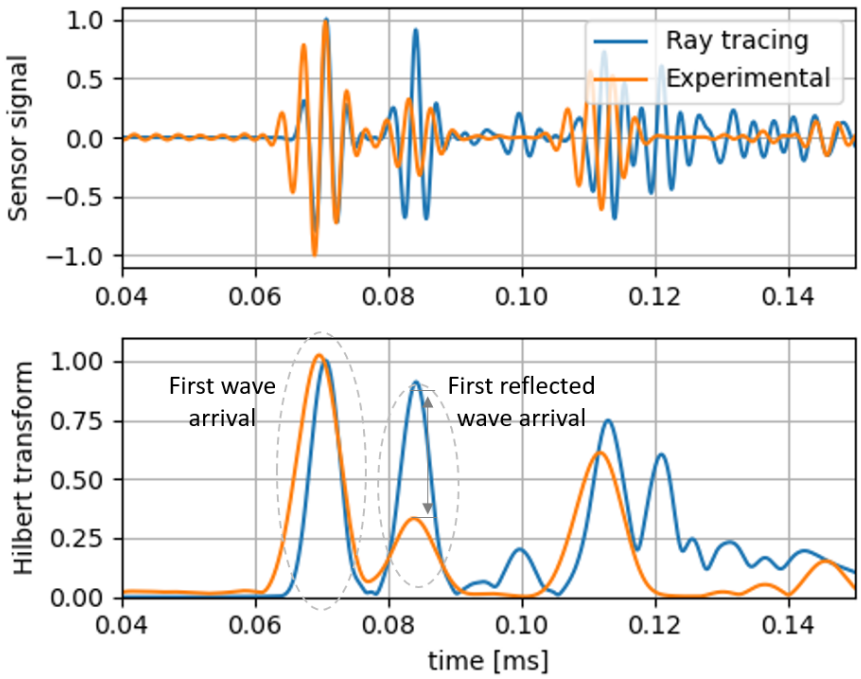


**Figure 4.2:** Result signal and Hilbert transform for path 1-6, normalized with first wave arrival amplitude peak.

Shown in Figure 4.2, the intensity of the first peak of the received signal is related to the amplitude of the input and material properties (damping or guided wave dispersion) during the wave path. However, its absolute value is governed by many different factors such as the piezoelectric characteristics of the sensors or the amplification factor of the acquisition system. These factors, although out of the scope of this study, are assumed to have a linear effect on the signal, and therefore the experimental signal is normalized compared to the simulated

data.

Second and successive peaks on the received signal are related to wave reflections on the plate edges (the A0 wave arrives at the sensor significantly later and at a point where its distinction from other phenomena is not clear from the experimental signal due to its relatively low propagation speed under this condition). Their relative amplitude is therefore governed by the energy dissipated in those reflections. This is taken into account in the simulation by the boundary losses coefficient set at the edges $\varepsilon_E$.

A parametric study is performed evaluating the boundary loss coefficient $\varepsilon_E$ in the interval of $[0, 0.9]$ and the normalized difference of the second peak amplitude is evaluated, with a fixed mode conversion factor $f_{mc} = 0.9$ based on previous experimental experience and FEM model analysis (Sánchez Iglesias et al., 2019), and empirically adjusted to match this test case. As the only boundaries present represent the plate edges, all the remaining energy is reflected, and therefore the energy transmission factor is not taken into account.

The normalized error in the second peak resulting from this study is shown in Figure 4.3, along with its average and standard deviation for each of the sensor paths present on the plate. The average of each measure is combined to highlight the trend of the data.

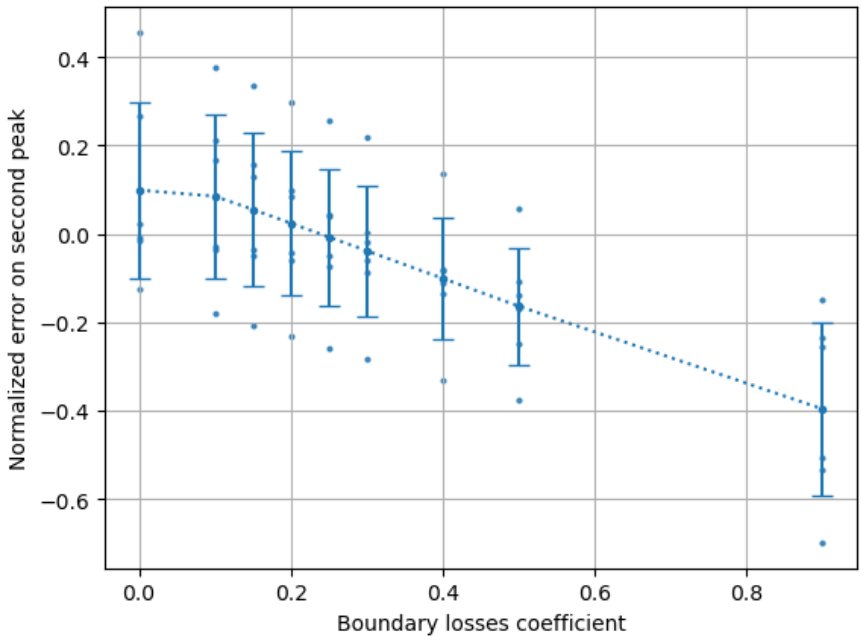


**Figure 4.3:** Aluminium plate error on second peak.

Figure 4.3 shows a significant dispersion in the data; this dispersion has been mainly attributed to factors not considered in the simulation, such as precision in the position and adhesion of the sensor to the plate, imperfections in the material of the plate, sensors and the weight of the cables, and differences in the edges and supports of the plate that are only represented in the simulation as a uniform factor $\varepsilon_E$. However, there is still a clear linear trend that shows an optimal zero average at a value $\varepsilon_E = 0.25$.

Therefore, based on the results of this study, the boundary loss factor $\varepsilon_E$ is fixed at 0.25, as it matches the best the experimental results while taking into account the limitations inherent in the described methodology.

Figure 4.4a displays the contour plot at time $t = 8 \times 10^{-5}$ s, only the $S0$ wave is represented to simplify interpretation. This focused representation highlights the behavior and propagation of the waves within the aluminum plate.

Furthermore, Figure 4.4b illustrates the rays that intersect with the sensor $PZT6$, at the same time-point. This visualization provides insight into the interaction between the wave and the sensor, aiding in the analysis of wave propagation patterns and sensor responses, and its validity.

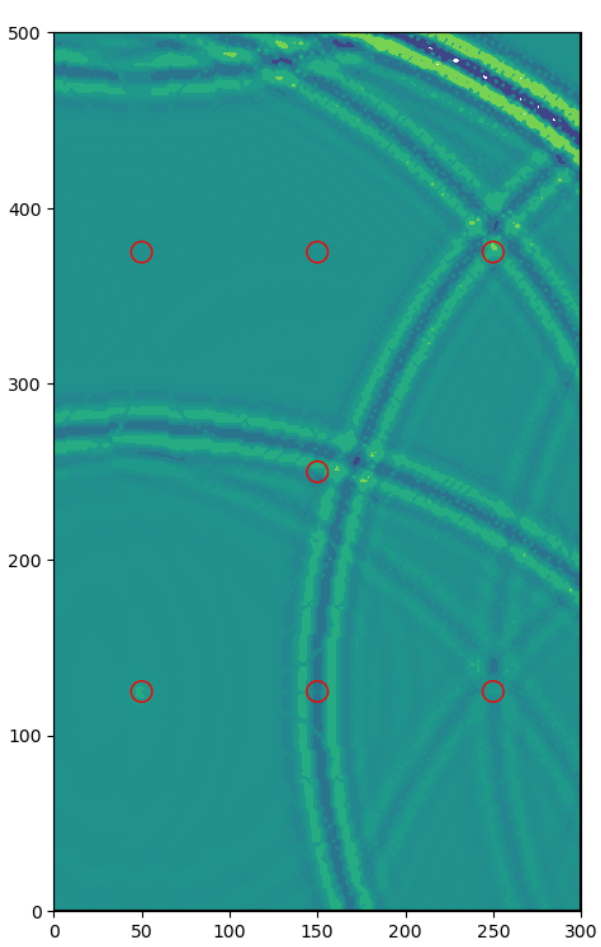


**(a)** Ray signal heat-map.

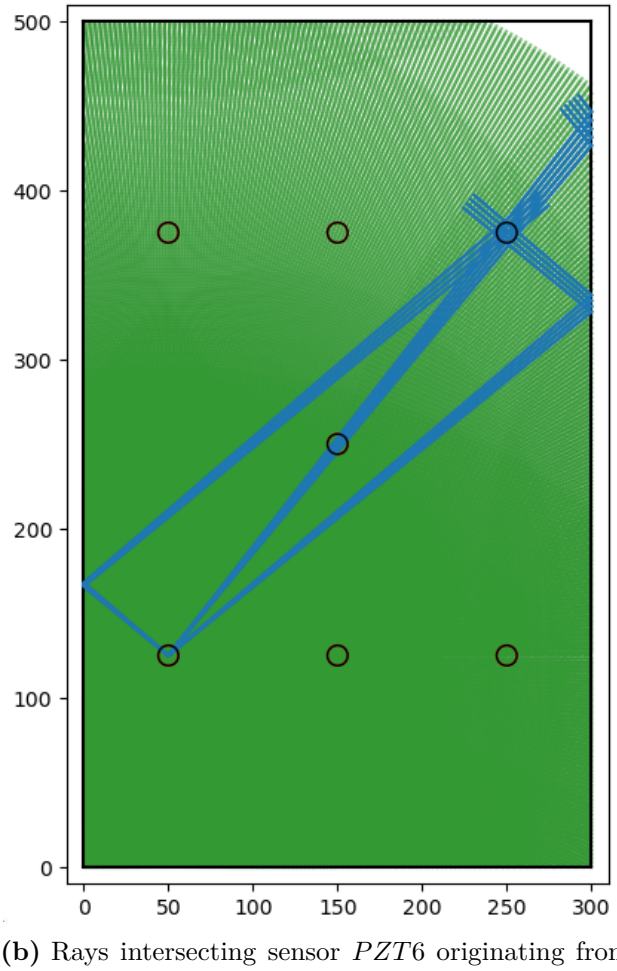


**(b)** Rays intersecting sensor $PZT6$ originating from sensor $PZT1$.

**Figure 4.4:** ray-tracing simulation results on the rectangular aluminum plate at $t = 0.08$ ms.

Figure 4.5 presents the results of the piezoelectric sensor obtained for several significant propagation paths, offering a detailed comparison between the experimental test data and the ray-tracing method. Furthermore, the results of the FEM model, as described n in section 3.2 are also shown in the figure. The results of the ray-tracing simulation were obtained using

1602 rays.

For this simulation, as previously estimated, a uniform boundary loss factor, $\varepsilon_E = 0.25$, was consistently applied along all four edges of the plate to account for energy dissipation at the boundaries.

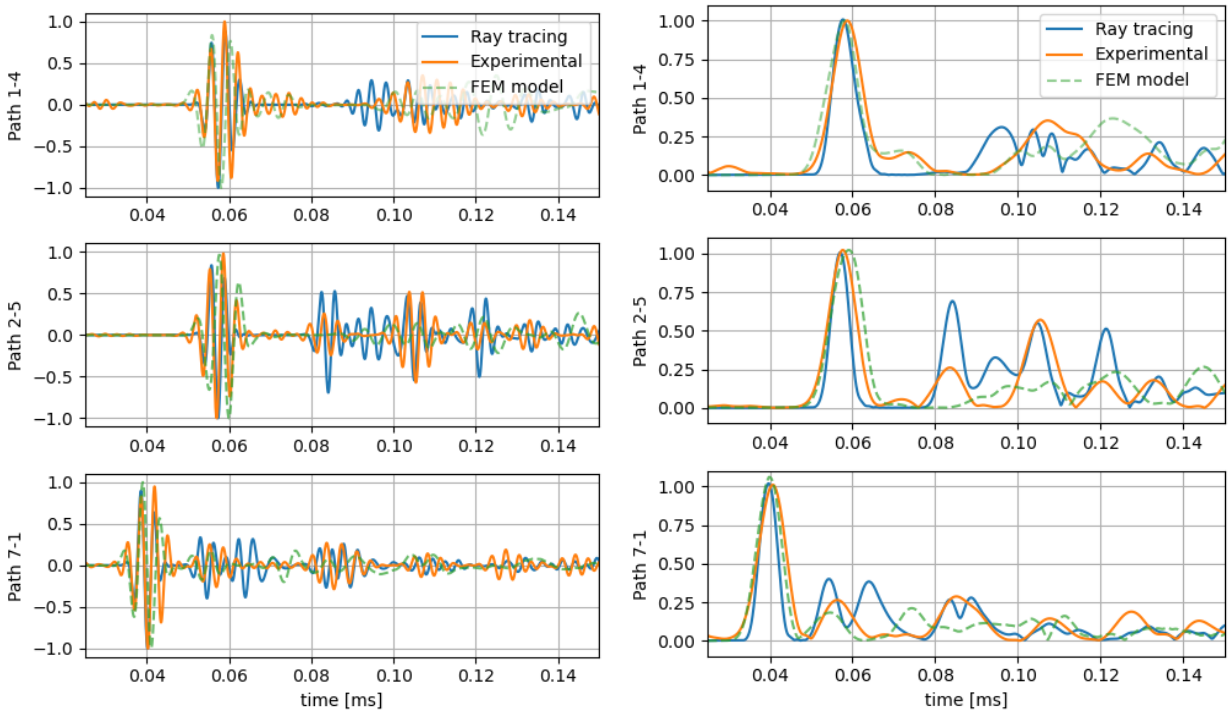


**(a)** Raw signal.

**(b)** Hilbert transform.

**Figure 4.5:** Signal intensity comparison for relevant sensor paths, normalized with first arrival amplitude peak.

The comparison highlights the accuracy of the proposed simulation approach in replicating experimental observations, with a degree of accuracy similar to the predictions of the FEM model, demonstrating its effectiveness in capturing key wave propagation characteristics.

As shown in Figure 4.5a and Figure 4.5b the simulation presents a very good agreement with the experimental data after fitting the boundary loss coefficient, for all the configurations explored. Initial wave packet and reflections appear with precision both in arrival times and amplitude in the simulation results, although some differences can be observed on some of the later reflections that may be explained due to signal error accumulation, sensor positioning and bonding imperfections, geometrical differences or imperfections in the boundaries, materials and sensors and cable and sensors weight.

## 4.2 Composite wing demonstrator

### 4.2.1 Artificial damages simulation

To evaluate simulation behavior in the presence of damage, the methodology is compared with a physical demonstrator of the lower cover of the front left wing of the LIBIS remotely piloted aircraft system (Section 3.1.1).

Artificial damage has been introduced to emulate the effect of a possible delamination in the specimen, these damages are introduced as added masses to alter the dynamic behavior of the structure (Sánchez Iglesias et al., 2023). Three sets of tests were performed considering the intact structure, the structure with artificial damage 01 and the structure with artificial damage 02. The input signal used consists of a BURST3 at 350 kHz at 40 V; test results are presented as an average of 3 runs, as described in Section 3.1.1.

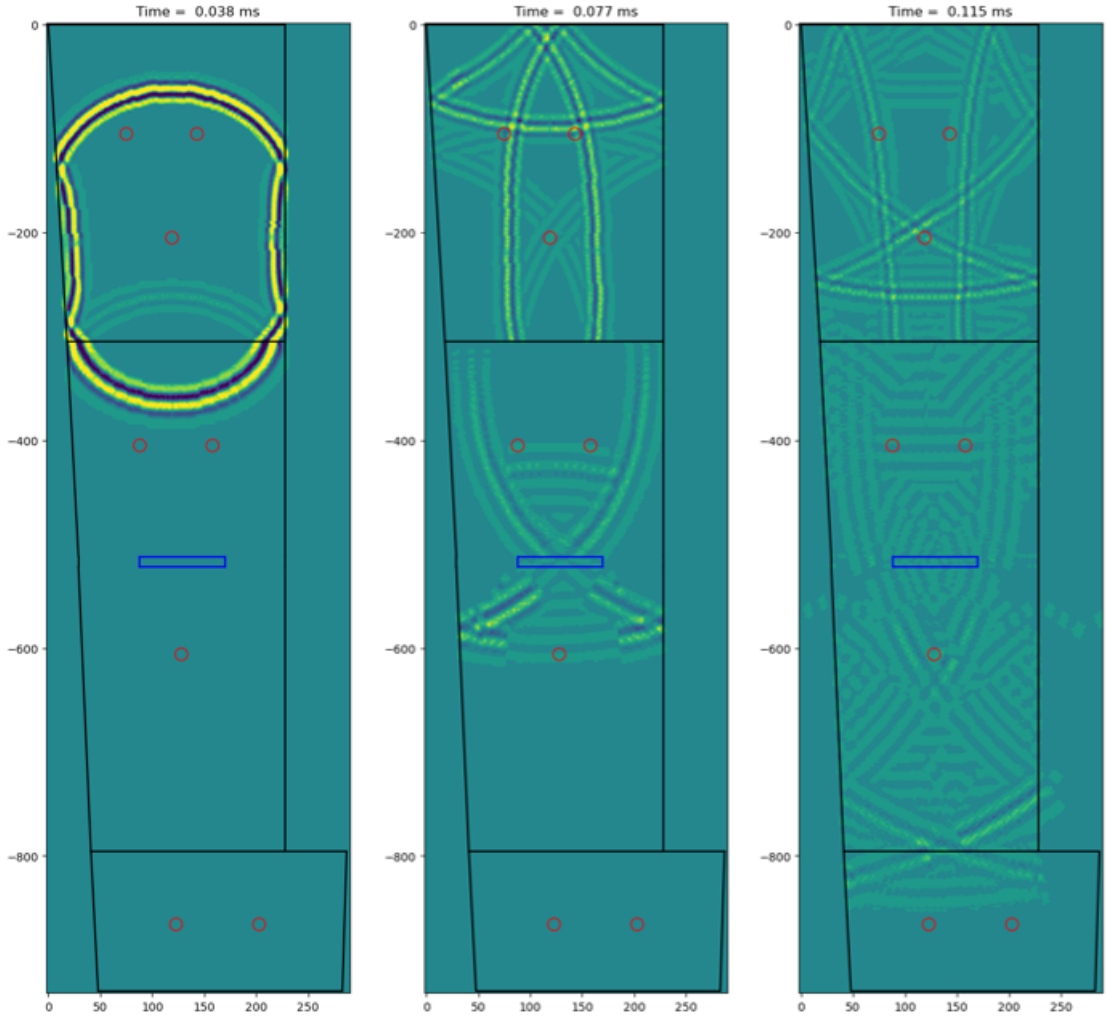


**(a)** Time $t = 0.038\,\text{ms}$. **(b)** Time $t = 0.077\,\text{ms}$. **(c)** Time $t = 0.115\,\text{ms}$.

**Figure 4.6:** Results contours for the LIBIS wing prototype with Artificial damage 01. Origin: $PZT8$.

The ray-tracing simulation contour plot results for the Artificial damage 01 configuration is shown in Figure 4.6. The simulation is run with 1201 initial rays originating from the piezoelectric transducer $PZT8$, artificial damage areas are simulated as linear boundary segments.

The results for each artificial damage configuration at a single time point is shown in Figure 4.7.The intact plate simulation results are shown in Figure 4.7a and Figure 4.7b and 4.7c show the results for artificial damages 01 and 02 respectively.

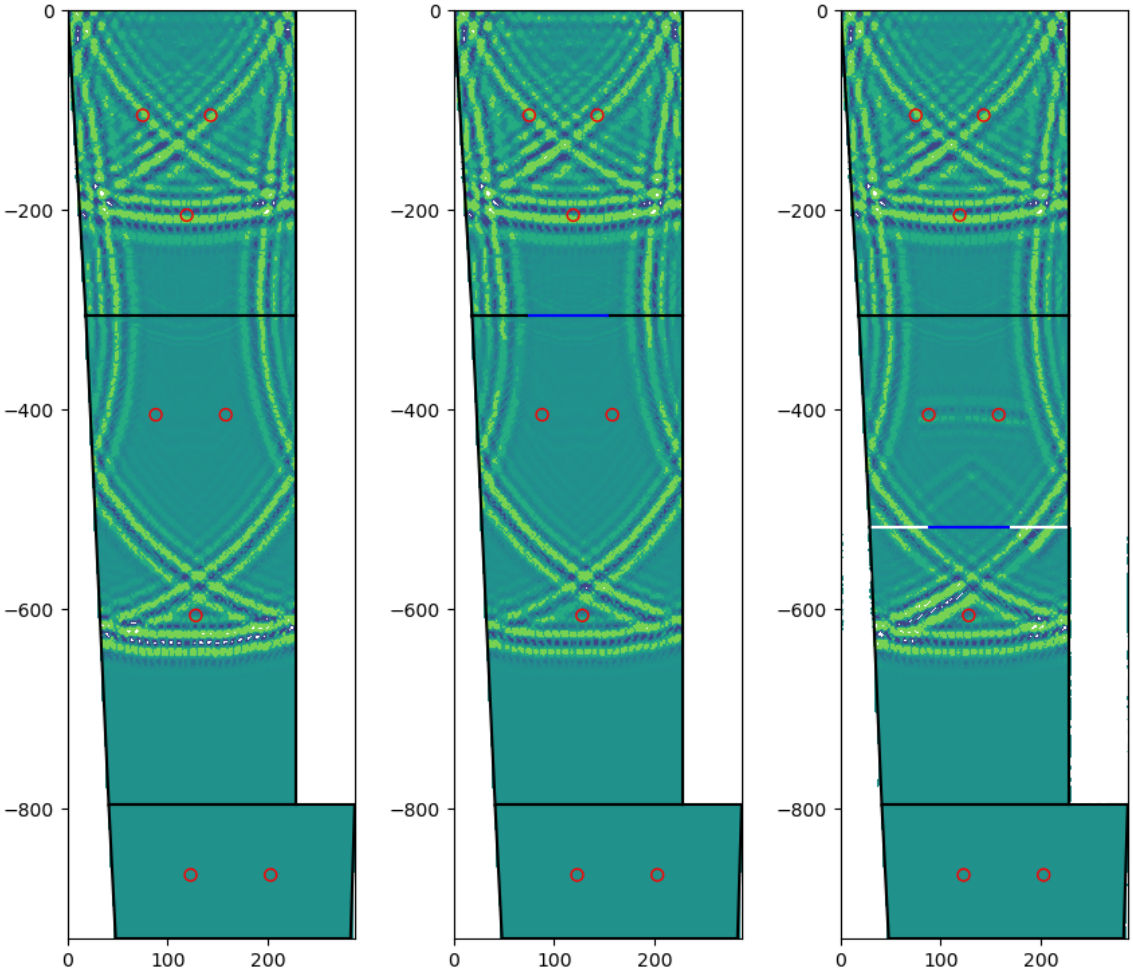


**(a)** Intact configuration. **(b)** Artificial damage 01. **(c)** Artificial damage 02.

**Figure 4.7:** Results contours for the configurations evaluated on LIBIS wing prototype, at $t = 0.5$ ms. Origin: $PZT8$.

The raw signal obtained with the tests is compared with the simulation in Figure 4.8 for the path between$PZT8$ and $PZT6$, both centered on the plate and each located on opposite sides of both artificial damage 01 and 02.

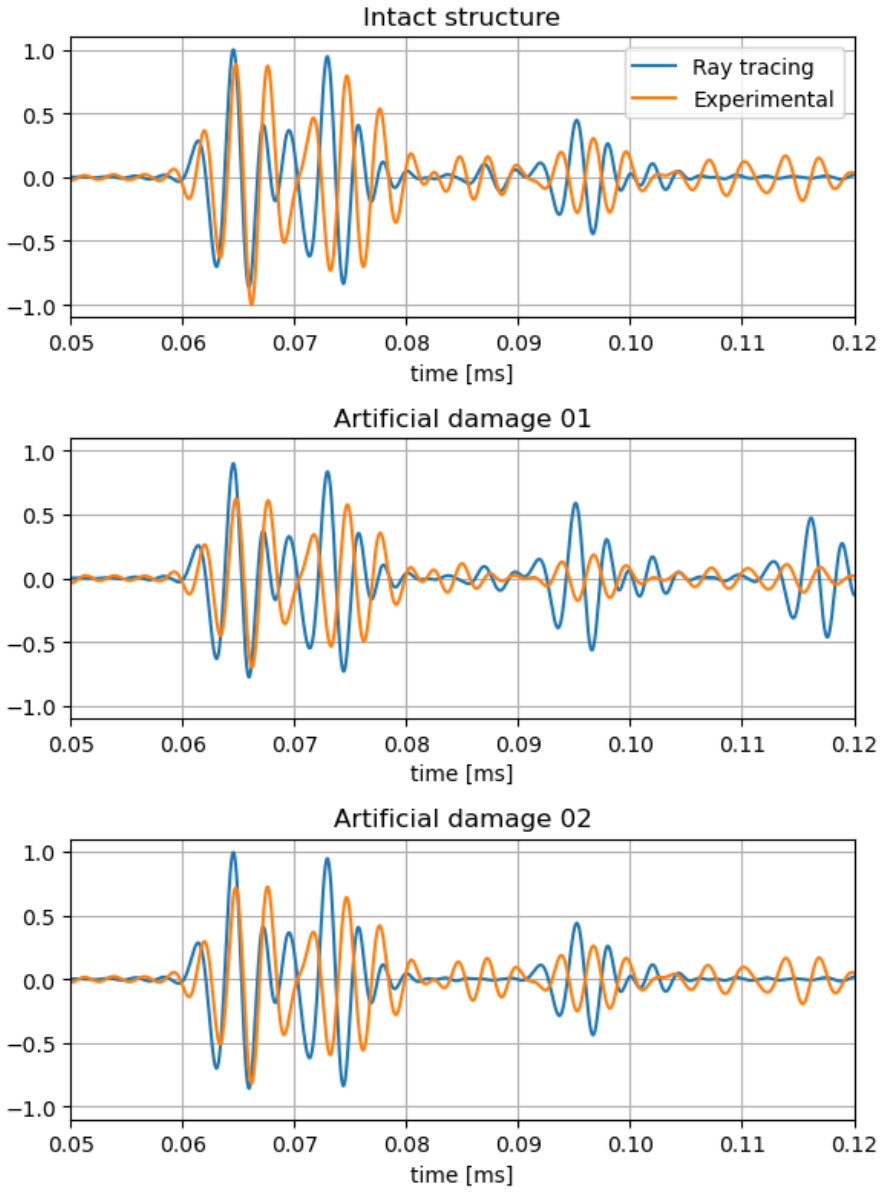


**Figure 4.8:** Simulation vs. Test results raw signal comparison with artificial damages for path 8-6, normalized with first wave arrival amplitude peak.

To effectively quantify the impact of the damage on the system, both the energy reflected and the energy dissipated at the artificial boundary were manually calibrated. This adjustment was based on the shortest linear propagation path, specifically the route between sensors $PZT3$ and $PZT6$. By focusing on this direct path, we aimed to eliminate the potential variability associated with longer or more complex routes, thereby ensuring a more accurate assessment of how the introduced damage influenced the wave dynamics within the system.

This approach allows for a clearer understanding of the energy interactions that occur at the boundary, facilitating a more precise calculation of the energy changes associated with damage. The calibration of the reflected and dissipated energy helps to highlight the extent

to which the damage alters the signal characteristics, ultimately providing valuable insight into the condition of the material. By analyzing the effects observed specifically along this propagation path, it is possible to interpret the underlying mechanisms of wave behavior in the presence of damage, contributing to a more comprehensive understanding of structural integrity in complex geometries (Sánchez Iglesias and Fernández López, 2023).

In this particular case, it is acknowledged that the uncertainties associated with the experimental setup are considerably higher compared to those observed in the case of metallic plates. The variability in the results is more pronounced due to various factors, including the inherent complexities of the material properties and the unpredictable nature of the introduced artificial damage. Despite these challenges, the model predictions remain surprisingly consistent with the experimental data, particularly when it comes to estimating the impact of artificially induced damage on the acoustic signal.

Sensor network data plays a crucial role in this analysis, as it allows for the observation and quantification of signal alterations caused by the presence of the added masses. Through data collection and analysis, it becomes evident that the changes in the signal are not merely theoretical but can be empirically detected and measured. This consistency between the model and the experimental results demonstrates the robustness of the predictive model, even in the face of increased uncertainties and variability.

In addition, the ability to observe and quantify these effects through a well-structured sensor network underscores the importance of integrating advanced monitoring technologies with predictive modeling. It emphasizes that, while uncertainties may pose challenges, they can also serve as opportunities for refining models and improving our understanding of the underlying mechanisms at play. In general, this interaction between experimental data and model predictions reinforces the reliability of the approach, providing confidence in its application to assess structural integrity in more complex materials and conditions.

### 4.2.2 Real impact damages

To evaluate the effect of a real damage, the LIBIS panel is then subjected to a 7 J impact, with a 1 kg steel spherical impactor, using a 70 cm tall drop tower in order to generate a damage representative of an in-service BVID.

**(a)** Impacted side

**(b)** Opposite of impacted side

**Figure 4.9:** 7 J impact damage pictures (Sánchez Iglesias et al., 2024).

Images of the resulting impact are shown in Figure 4.9. As expected, the effects of the damage can be observed more clearly on the opposite side of the impact, appearing as some fiber breakage, shown in Figure 4.9b, while on the impact side (Figure 4.9a) they appear only as a small indentation.

The impact is located in the center of the panel in a location similar to that of artificial damage 01, approximately 6 cm from the trailing edge of the lower cover and it is performed on the outer face to emulate a possible real BVID due to some external damage in service.

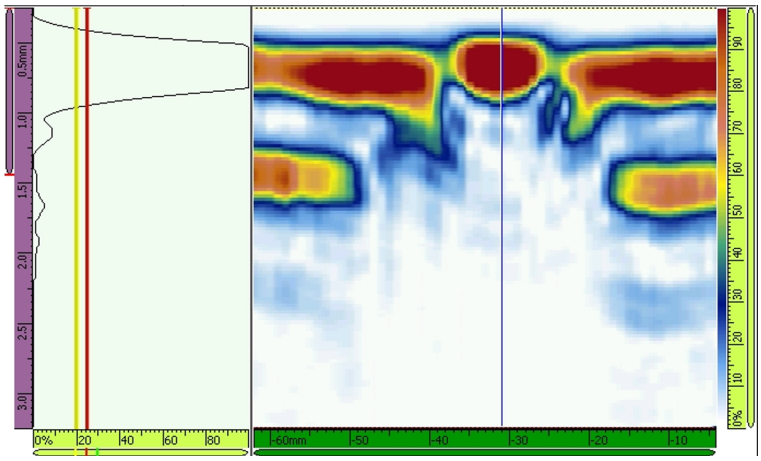

**(a)** A and B-Scan

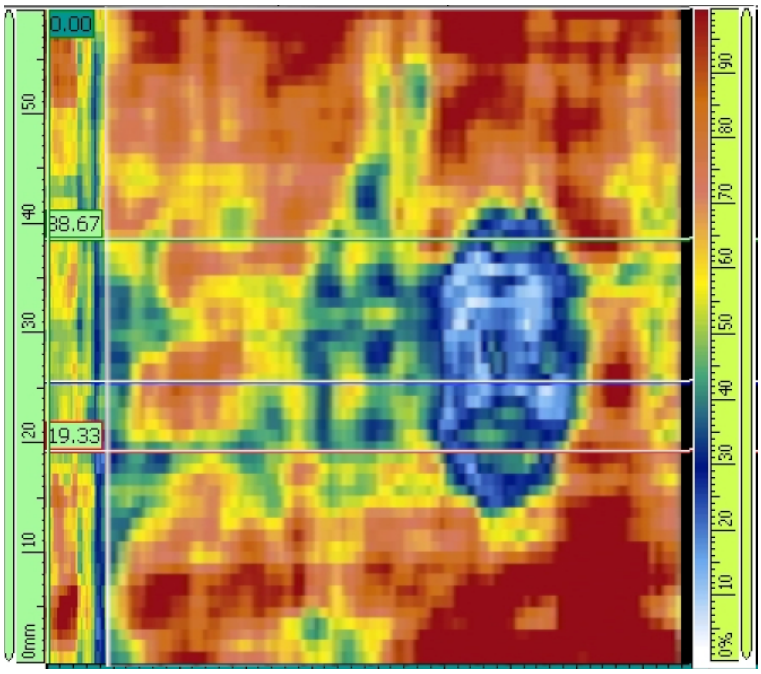


**(b)** C-Scan

**Figure 4.10:** NDT results on damage location (Sánchez Iglesias et al., 2024).

To fully characterize the impact, the damaged area is inspected with an Olympus OmniScan MX2 and its results of A, B, and C scan are shown in Figure 4.10, where significant delamina-

tions and fiber and matrix crackings spanning an approximate area of 23 $cm^2$ and extension of the damage can be observed through the thickness of the entire plate.

The damaged area is then introduced into the simulation, assuming a uniform boundary reflection factor $f_{tr} = 0.1$ and a dissipation factor of $\varepsilon_E = 0.5$.

The instant amplitude difference results of the relevant sensor path $PZT8 - PZT6$, located on both sides of the damaged area, are shown in Figure 4.11. The damage energy dissipation characteristics were adjusted manually in the simulation to match the experiment results.

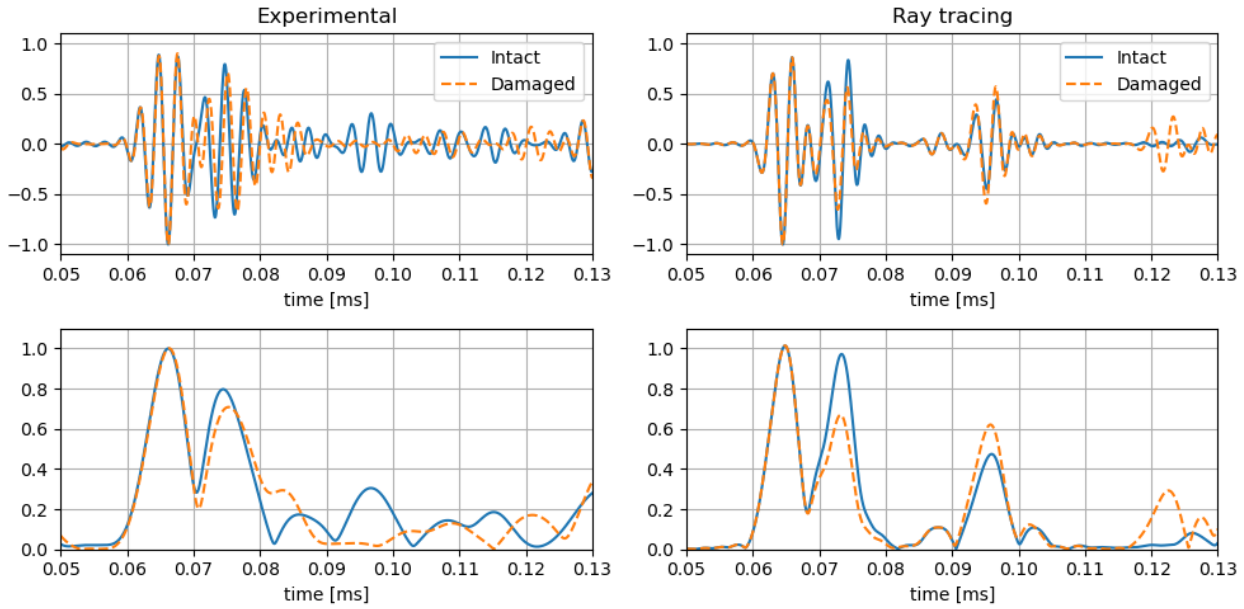


**Figure 4.11:** Results contours for the configurations evaluated on LIBIS wing prototype, at $t = 0.5$ ms. Origin: $PZT8$, normalized with first wave arrival amplitude peak.

As damage is not directly located across the line that joins sensors $PZT8$ and $PZT6$, its effect is clearly visible in the arrival of the second wave packet, while the first wave packet remains unchanged from the intact configuration. Its also pretty obvious from the figures that this damage effect in the signals is significantly more noticeable than the simulated damages shown in the previous section.

Again, the main differences can be explained with the same reasoning as exposed in the previous sections, but additionally this case presents the complications inherent to the damage characterization. A small but appreciable frequency shift is also observed in the experimental results, which does not appear in the ray-tracing simulation as the damage is still modeled as a zero-width boundary.

## 4.3 Stiffened composite panels

To validate the simulations and gain a better understanding of the propagation of GLW in the presence of structural details, a testing campaign has been designed for two different representative structures. A simple, rectangular composite panel with a quasi-isotropic 7 ply layup and the same panel with a representative T-shape stringer along the center. They are both instrumented with an array of 8 piezoelectric sensors, as shown in Section 3.1.1.

Figure 4.12 displays the contour plot results obtained from the ray-tracing model for both panels, offering a visual representation of wave propagation patterns. These results were generated using the same set of parameters as those employed in the previous simulations to maintain consistency and allow for direct comparisons. The uniform application of the modeling parameters ensures that the variations observed in the results can be attributed to differences in the structural configurations of the plates rather than to discrepancies in the simulation settings.

To improve computational efficiency, the number of initial rays used in the stiffened panel simulation was reduced by half compared to the stiffened panel. Despite this reduction, the overall accuracy and reliability of the results remain preserved, demonstrating the robustness of the ray-tracing approach even with fewer rays. The contour plots provide valuable information on the influence of structural stiffening on wave propagation characteristics, highlighting differences in wave reflections, refractions, and energy distributions caused by the geometry of the panel and boundary conditions.

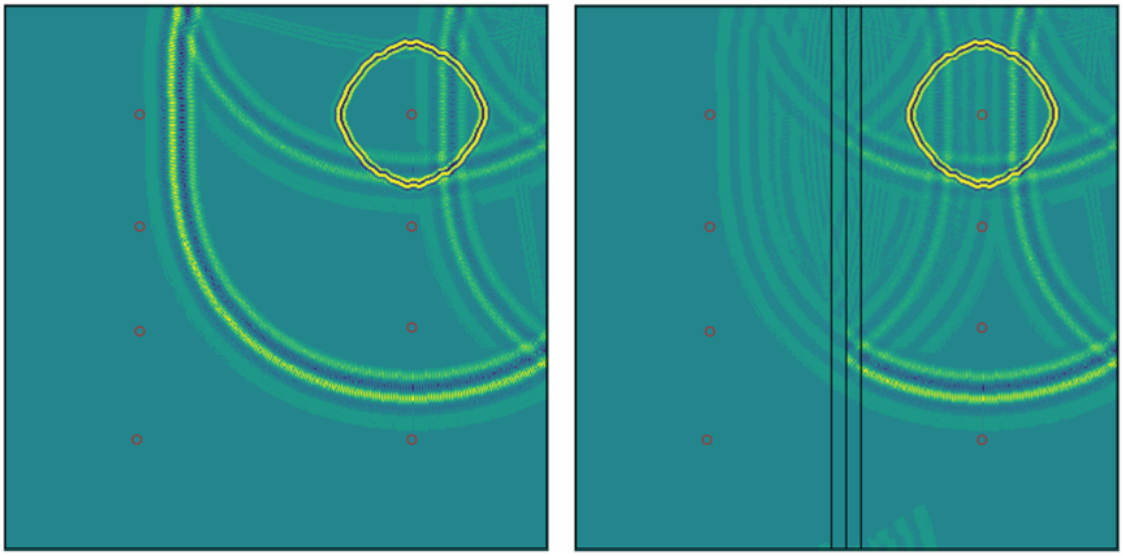

**(a)** Non-stiffened panel **(b)** Stiffened panel

**Figure 4.12:** ray-tracing result contour plot for the stiffened composite panels at $t = 0.07\,\text{ms}$.

The comparison of the results of the piezoelectric sensors between the ray-tracing method and the test results is shown in Figure 4.13. The figure highlights how closely the simulated signals generated by the ray-tracing method align with the experimental measurements recorded by the piezoelectric sensors.

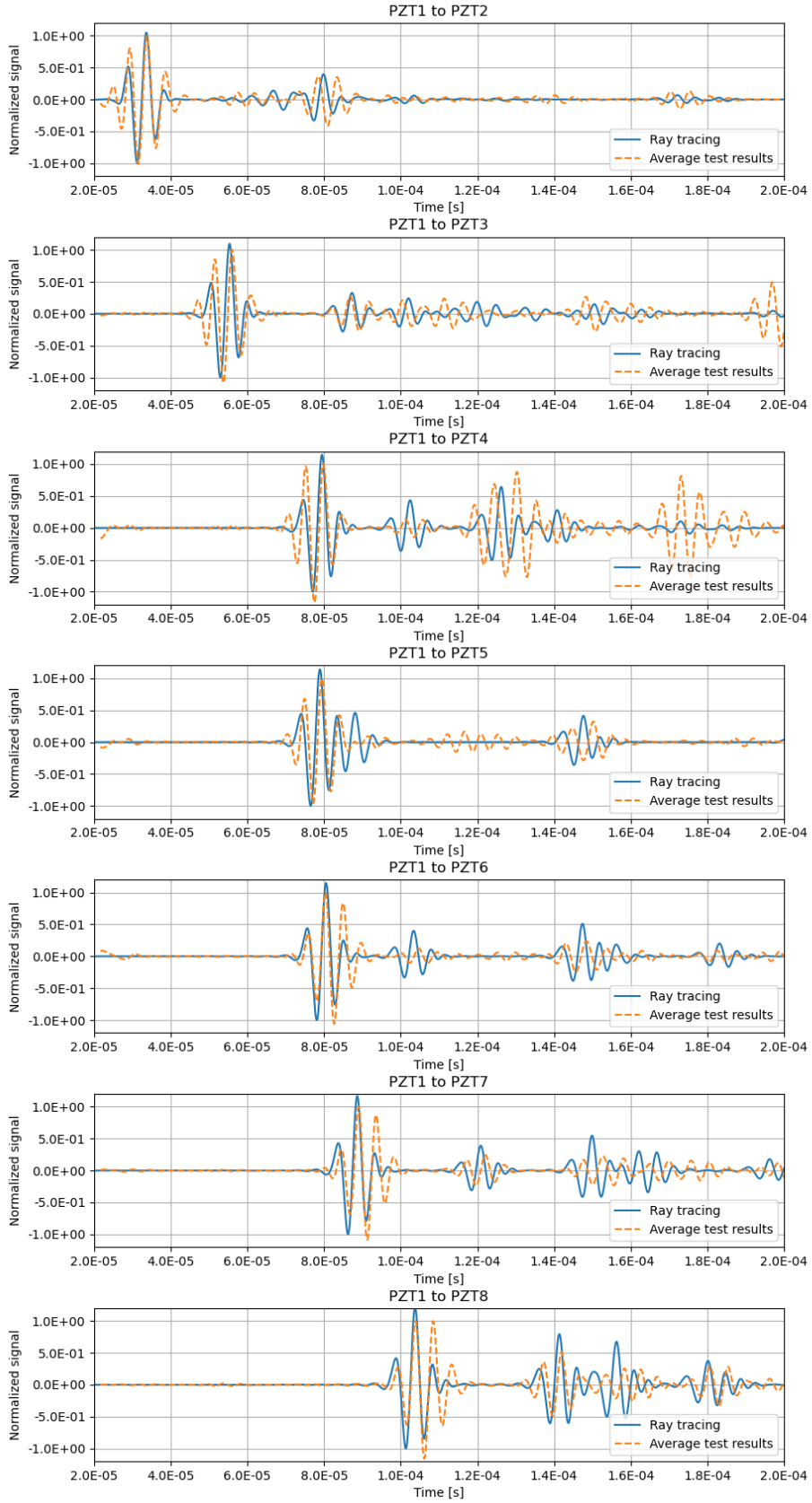


**Figure 4.13:** Test and simulation result comparison of relevant paths from $PZT1$ for the non-stiffened composite panel

# Chapter 5

# Discussion

This thesis presents the development and validation of a ray-tracing methodology to model GLW propagation for lightweight aerospace structures in the context of SHM. The research focuses on improving the efficiency and accuracy of GLW propagation analysis, addressing the limitations of traditional numerical methods such as FEA and developing a methodology suitable for use for machine learning training purposes. Using ray-tracing techniques, the proposed approach models complex wave interactions and is able to accurately represent the signals measured in the SHM system sensors.

The thesis includes an extensive review of the literature that forms the basis for the study. This review explores existing research on guided wave propagation, structural health monitoring (SHM) techniques, and numerical modeling approaches, providing the context and rationale for the proposed ray-tracing methodology. By synthesizing previous work, the review highlights the gaps in current methods, particularly the scalability and computational complexity of modern FEM approaches.

To validate the methodology and improve the understanding of GLW propagation, the study incorporates a comprehensive series of experimental tests. These tests examine both metallic and CFRP specimens, incorporating representative structural features such as stiffeners and joints. The experiments are specifically designed to capture the behavior of GLWs in lightweight structures, providing critical data to benchmark and refine the approach.

Signal analysis plays a vital role in understanding and interpreting the behavior of GLWs. By analyzing wave reflections, mode conversions, and attenuation, it becomes possible to detect, locate, and classify impacts, as well as damage such as cracks and delaminations within a structure. This capability makes signal analysis a cornerstone of effective SHM, enabling early identification of potential problems and supporting preventive maintenance strategies.

This thesis examines accurate signal processing techniques to improve GLW analysis, ensuring reliable damage detection and structural assessment. In addition, it explores the use of time-frequency diagram techniques, which provide a detailed frequency representation of wave behavior over time. These advanced methods allow the extraction of more comprehensive information about the structure and its damage index, providing deeper insights into the condition of aerospace components, and improving the robustness of SHM methodologies.

The methodology is validated through comparisons with both numerical simulations and experimental data, demonstrating its ability to handle dispersion effects and anisotropic material behaviors commonly found in composite structures. A key highlight of the study is the computational efficiency of the approach, making it well-suited for the training of physics-informed machine learning algorithms or other artificial intelligence approaches.

Overall, the research provides a scalable and accurate framework for integrating guided wave analysis into SHM systems that could potentially offer future improvements in safety, reliability, and cost effectiveness for aerospace maintenance strategies.

In this section, the results obtained from the ray-tracing methodology and its correlation with experimental tests and numerical simulations are analyzed and interpreted. The focus is on evaluating the performance of the proposed method, identifying trends, and understanding the discrepancies between the experimental and simulated data.

## 5.1 Ray-tracing methodology development

The development of a ray-tracing methodology for GLW represents a significant advancement in the field of SHM and NDE, particularly for aerospace structures. The method allows for rapid simulation of GLW propagation in aircraft panels, allowing the identification of potential damage locations such as cracks, delaminations, or corrosion and the incorporation of energy-loss mechanisms ensures that the predictions remain accurate even in the presence of complex structural features, making the methodology robust for real-world applications.

The simplicity of the ray-tracing approach is rooted in its reliance on geometric optic principles. By treating guided Lamb waves as rays propagating within the structure, the methodology avoids the need for solving complex wave equations directly. Furthermore, the modularity of the implementation allows for straightforward modifications and extensions, making it adaptable to a wide range of scenarios. By focusing on ray-tracing, this methodology bypasses the computationally intensive nature of full-wave modeling either by FEA, SFEM or analytical methods by reducing the problem to a geometrical approach.

The methodology is able to implement an arbitrary wave speed and attenuation model that can be dependent on the direction, therefore, being able to represent either metal or CFRP structures. Unlike other developments, the material model is not coupled with the propagation engine, this was done in order to improve the versatility but may limit its applicability in some specialized scenarios (Dorn and Kochmann, 2022; Ramos Oliveira et al., 2024).

The choice of a simplified 2D geometrical model is a deliberate design decision aimed at balancing computational efficiency with physical accuracy. Although full 3D models could provide a more comprehensive representation of wave propagation (W. Liu and Hong, 2015), they are often computationally prohibitive even on small structures. The 2D model captures the essential features of GLW propagation while significantly reducing computational requirements and allows for the modeling of arbitrary interfaces between mediums by simply defining the mode conversion and attenuation factors. This flexibility enables the accurate representation of complex wave interactions at material boundaries and structural discontinuities or details.

## 5.2 Method accuracy

Typically, in the field of SHM, the ray-tracing method is not used in the literature due to its accuracy, but rather as a lightweight and fast computation method; and the main intention is the same for the methodology developed in this thesis. However, this thesis has shown that the results of the developed ray-tracing methodology are very close to the experimental data in all the experimental cases studied.

The ray-tracing methodology can achieve a balance between computational efficiency and sufficient accuracy for practical applications. By incorporating detailed modeling of wave interactions, such as mode conversions and dispersion effects, the proposed approach expands the scope of ray-tracing beyond speed alone, making it a viable tool for realistic and reliable GLW propagation in complex aerospace structures. As shown in Section 4.1 on the aluminum plate, by adjusting the boundary attenuation parameters, the method is able to reach the desired solution level at the target senor while following the signal waveform on all other sensors with a dispersion error of less than 10%.

The method can also play a pivotal role in physics-informed ML techniques by providing efficient physics-based data sets for training. Its ability to simulate GLW propagation at a lower computational cost than methods such as FEM makes it ideal for generating labeled data. These data can be used to train ML models to predict damage locations, severity, damage indexes, or other useful metrics while ensuring that the models adhere to physical principles.

By embedding wave propagation physics into the ML framework, ray-tracing enhances the ease of interpretation and reliability of predictions. It can also allow simulation of edge cases or rare damage scenarios, improving the robustness of ML models for real-world SHM applications. Therefore, serving as a bridge between traditional physics-based methods and data-driven approaches, enabling more accurate and efficient hybrid solutions.

Key aspects considered in this discussion include the influence of geometry, material properties, and boundary conditions on wave behavior, as well as the effectiveness of the modeling techniques employed. The role of piezoelectric transducers in the capture and analysis of wave signals is revisited, highlighting their strengths and limitations that can be leveraged in the method to ensure an accurate match with the experimental results.

In addition, potential sources of error, including modeling assumptions and experimental uncertainties, are examined to provide a comprehensive assessment of the approach. Suggestions are also presented to improve accuracy and extend the methodology to more complex structures.

The method effectively fulfills its intended purpose while demonstrating its ability to model GLW propagation accurately. By capturing the essential wave interactions and reflections, it provides results that align with experimental observations. Most importantly, the method successfully detects the same changes in the structure as those observed in the experimental signal, validating its accuracy and practical utility, confirming ray-tracing as a useful tool for analyzing wave behavior and evaluating structural modifications with confidence.

## 5.3 Comparison with FEM results

The correlation with the aluminum plate tests obtained by the ray-tracing method is compared to a dynamic explicit time integration FEM model, run in Abaqus/Explicit version 2020 HF6 following the modeling principles described in Sánchez Iglesias et al., 2019, generated as described in Section 3.2.

To simulate a 300 kHz elastic wave the element size is limited to approximately 1 mm, resulting in 539 reduced integration shell elements, S4R, for the transducers and 370235 reduced integration continuum shell elements, SC8R and a total of 185144 nodes. The stable time increment of the simulation is $5.7611 \times 10^{-9}$ s.

The results of the ray-tracing simulation model are shown in Figure 5.1a and a contour plot of the abs. max. principal membrane strain results from the FEM model are shown in Figure 5.1b.

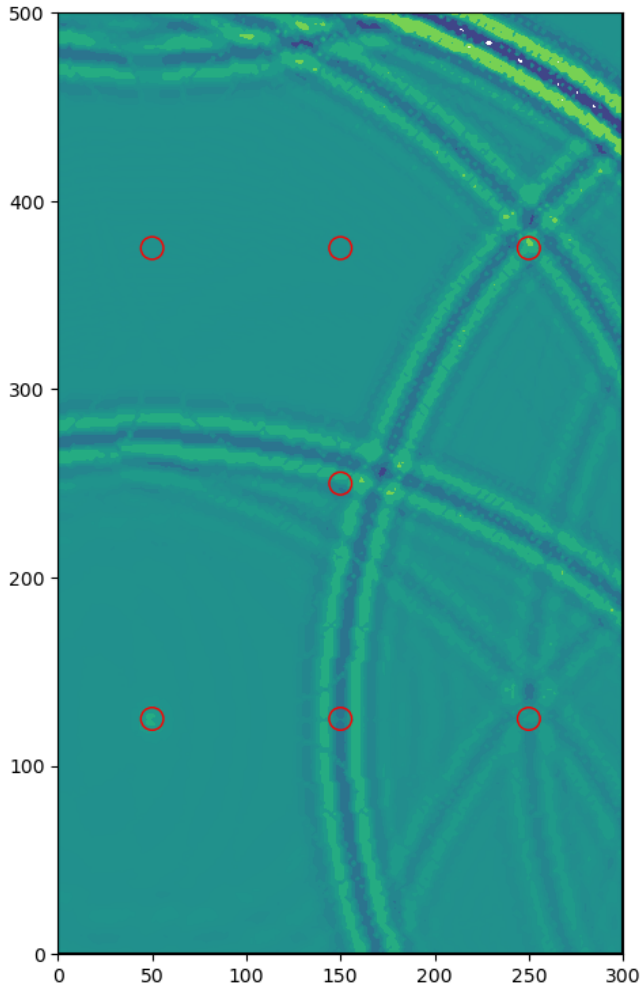


**(a)** Ray signal heat-map.

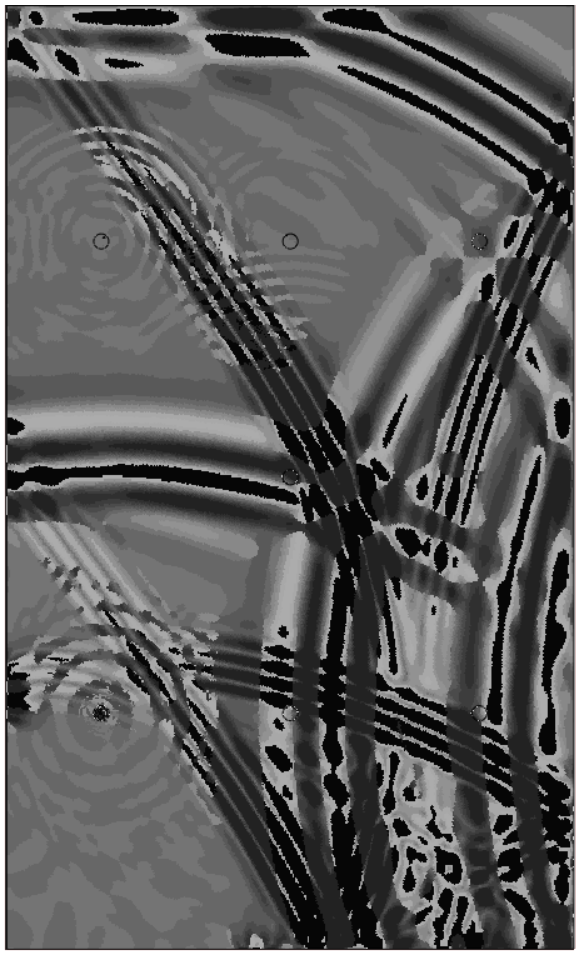

**(b)** FEM model, contour of membrane strains at mid-plane.

**Figure 5.1:** Simulation results (FEM and Ray tracing) at $t = 8 \times 10^{-5}$ s.

The results obtained using FEM and ray-tracing methodology show a high degree of similarity, indicating that both approaches are capable of accurately modeling GLW propagation.

In addition to the aluminum plate, another set of FEM simulations was performed for the stiffened composite panels. As described in Section 3.2, an FEM model has been developed in parallel to act as a benchmark with the ray-tracing simulation for the stiffened composite panels (Sánchez Iglesias et al., 2019). The analysis is done with Abaqus/Explicit version 2017 and the parameters are set as described in Section 3.2.

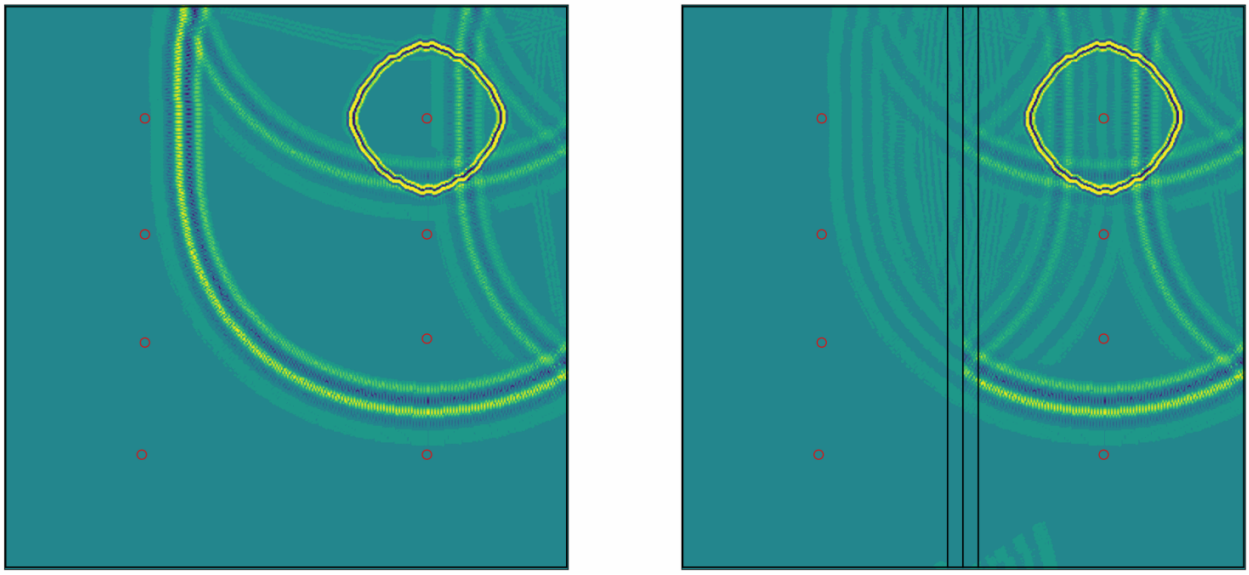

**(a)** Ray tracing model results

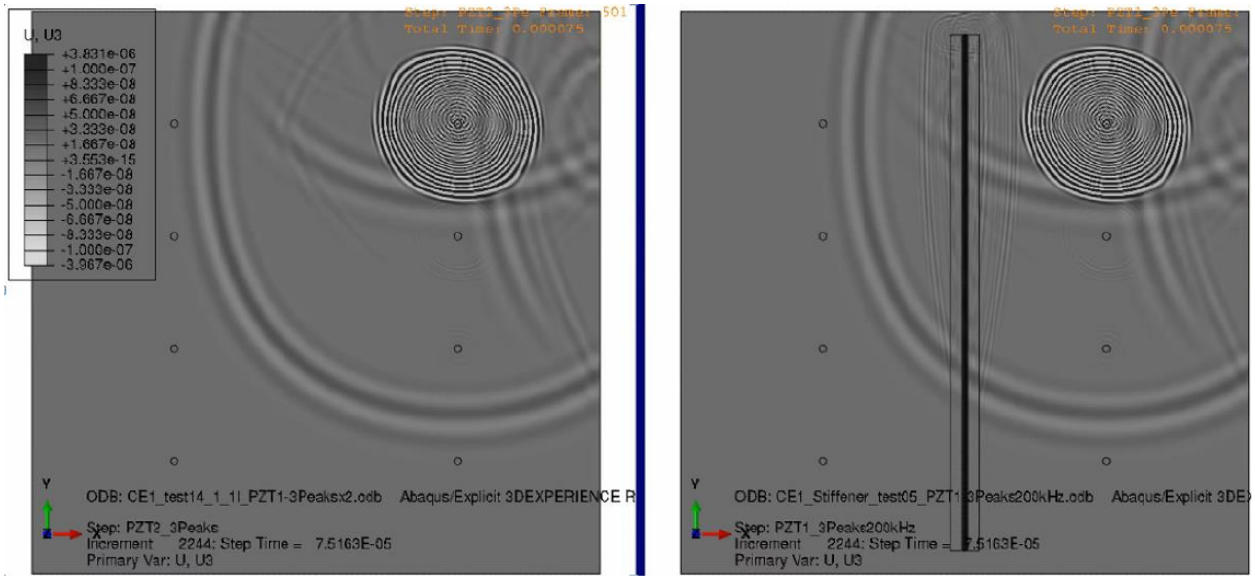


**(b)** Abaqus FEM model results

**Figure 5.2:** Contour plot at $t = 0.07\,\text{ms}$ (Sánchez Iglesias and Fernández López, 2023).

Contour plots are shown in Figure 5.2, compared with the FEM model vertical displacement

results at $t = 0.07\,\text{ms}$. The grid used for the ray-tracing model has a side length of $2mm$. The energy absorption caused by the cohesive stiffener bond is not represented in the FEM model, whereas in the ray tracing model the boundary loss factor is modeled (Sánchez Iglesias and Fernández López, 2023).

Signal results at relevant sensors are shown in Figure 5.3.

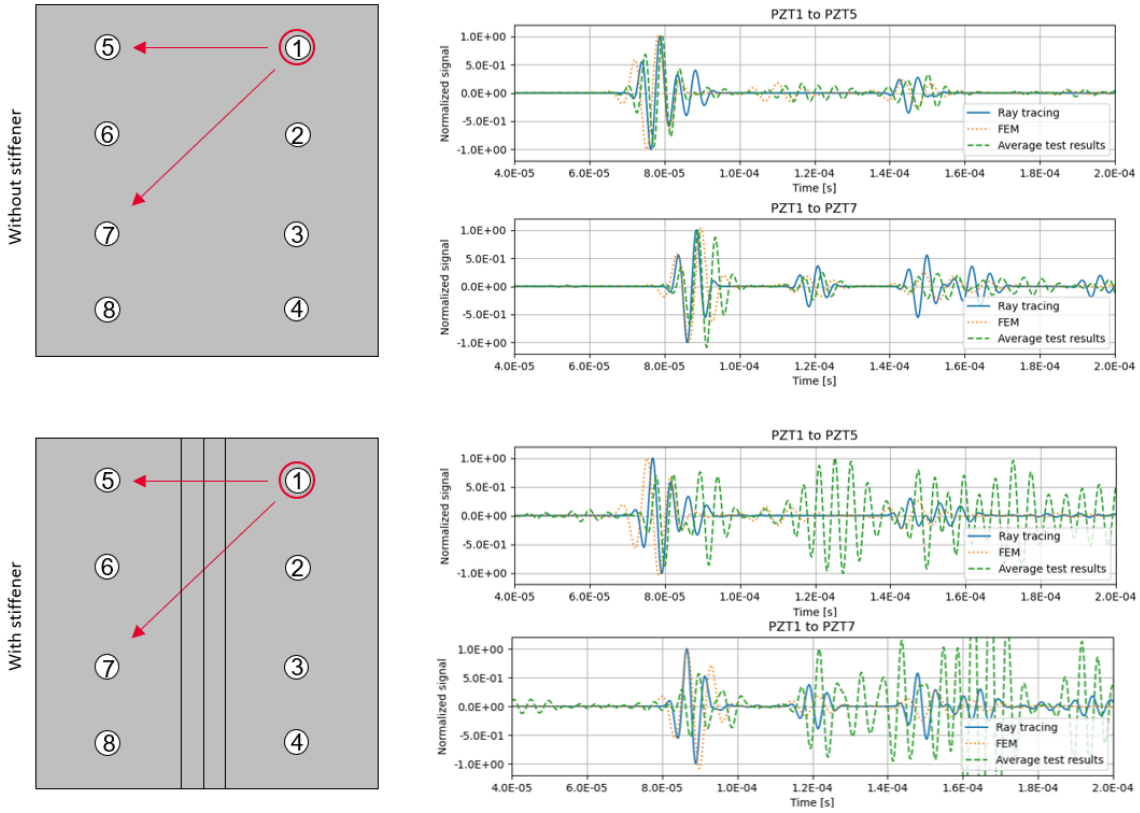


**Figure 5.3:** Result comparison of relevant paths from PZT1 for the composite panels (Sánchez Iglesias and Fernández López, 2023).

The correlation shows that the ray-tracing model can represent the experimental data with a high degree of accuracy, especially when compared with the finite element model, which, although it is more costly computationally, presents a similar accuracy for this problem. As in the previous example, the main differences with the experimental data are due to error accumulation and the wave dispersion model. This alignment in the results validates the reliability of the ray-tracing approach as a computationally efficient alternative to FEM for many applications. Furthermore, the analysis revealed that most potential sources of error, such as inaccuracies in material properties, boundary condition approximations, or simplifications in wave interaction modeling, are common to both methodologies.

These shared sources of error suggest that while FEM and ray-tracing differ in computational complexity and implementation, their underlying physical assumptions and modeling challenges are closely related. This insight underscores the importance of refining the input parameters and improving the representation of complex phenomena, such as dispersion and

mode conversion, to enhance the accuracy of both methods. By addressing these common challenges, both FEM and ray-tracing can be optimized for better performance in SHM and other engineering applications and could even be used with a cross-validation strategy, reducing the number of physical tests.

## 5.4 Computational efficiency

Throughout this thesis, ray-tracing has been shown to be an efficient computational method for modeling GLW propagation, considering reflection, refraction, interference, and damping. Its computational efficiency stems from its ability to trace the paths of individual rays rather than solving complex wave equations across the entire spatial domain.

Although not directly studied in the method presented, it would be trivial to even further reduce the computational load by focusing only on the relevant paths of energy transfer, making it ideal for simulations involving large or complex geometries (Soman et al., 2020; Zhang et al., 2024). Additionally, ray-tracing algorithms can leverage parallel processing, enabling faster computations by handling multiple rays simultaneously. This reduces simulation time while maintaining accuracy. As a result, ray-tracing offers a scalable and practical solution for modeling GLW for SHM.

A comparison of the computation time with FEM is shown in Table 5.1 for the composite panels studied. The calculations of the signal at 1 sensor, $PZT7$ in this example, for a time $t$ =0.3 ms and the time to obtain a contour plot at a time $t$ =0.08 ms are shown in the table, for a different number of initial rays. These results are compared with the computation time of the developed FEM model.

For comparison, the ray-tracing contour plot shown in Figure 5.1a is performed with a grid length of 2 mm, consistent with the FEM model plot shown in Figure 5.1b). The ray tracing model is run in a single processor on a standard work laptop (Intel Core i7-10875H CPU @ 2.30 GHz) and the FEM model is executed with 4 processors on an HPC cluster (Intel Xeon Gold 6136 CPU @ 3.00 GHz).

**Table 5.1:** Computation time comparison: FEM vs. Ray tracing.

| Initial ray number | Total ray number | $PZT7$ signal $t$ =0.3 ms | Contour plot $t$ =0.08 ms |
|---|---|---|---|
| 202 | 2338 | 49 s | 1 min19 s |
| 402 | 4628 | 1 min 53 s | 2 min 42 s |
| 802 | 9231 | 3 min 33 s | 5 min 35 s |
| 1602 | 18454 | 7 min 16 s | 11 min 50 s |
| 3202 | 36864 | 13 min 27 s | 1 h 6 min 49 s |

| FEM model | Computation time for $t$ =0.3 ms |
|---|---|
| `185144 elements` | 4 h 33 min |

It is clear from the results shown that the ray-tracing method provides a significant time advantage over the FEM model (considering the examples used for the method validation of 1602 initial rays, the time difference is nearly of two orders of magnitude); moreover, pre- and post-processing times of the FEM model are not considered in the results shown; however, for a model of this size, this could become a significant time investment.

The ray tracing methodology, while highly effective, necessitates the careful adjustment of a greater number of parameters compared to finite element methods (FEM), particularly when dealing with complex geometrical boundaries. This added complexity arises from the need to account for various interactions, such as reflections, refractions, and mode conversions, which can significantly influence wave propagation. However, despite this increased demand for parameter tuning, the computational efficiency of ray tracing presents a compelling advantage. The time savings achieved through ray tracing are substantial, allowing for the rapid generation of extensive datasets. These large volumes of data points are invaluable, especially in the context of artificial intelligence training databases, where diverse and comprehensive datasets are essential for developing robust machine learning models. Consequently, the efficiency of ray tracing not only facilitates quick data generation but also enhances the potential for innovative applications in the field of structural health monitoring and material characterization.

# Chapter 6

# Conclusions

## 6.1 Recapitulation and original contributions

Condition-based maintenance encompasses a series of activities, inspections, tests, and procedures undertaken in response to damage or failure within a system. This maintenance strategy prioritizes addressing the underlying causes of machine or material failure and implementing solutions only after the problems have been identified. To enable this approach effectively, structural health monitoring (SHM) is essential, as it offers real-time data on the condition of the structure. By continuously monitoring and assessing the state of the material, SHM facilitates timely interventions and informed decision-making, ultimately enhancing the reliability and longevity of the system.

SHM is a vast discipline that covers many areas of engineering, this thesis focuses on a very narrow field of SHM, with a complex numerical simulation able to accurately represent the Lamb waves on composite structure and its possible interaction with structural details, and an application of time-frequency distribution techniques to interpret signals measured at PZT transducers, both due to very low energy impact tests results and active interrogation.

Time-frequency distributions have become a key tool for understanding temporal signals as they can provide a vast amount of information that may be hidden in the signal and visible at first glance. Although the TFD methodology presented may be very costly in terms of computational time and storage, the damping parameters obtained, when applied in the simulations, present a very good agreement with the test results, and therefore a smaller number of tests may be needed in future applications greatly reducing time or cost to adjust this model. Additionally, with this methodology, the anti-symmetric mode dispersion curves appear very clearly and can be used as an alternative method to estimate or validate the material dispersion curves.

In addition, time-frequency distributions have proven to be a very useful tool for studying the system response under low-energy impacts. Using these tools, it is possible to discern the type of impactor with significant accuracy and repeatability. A very significant frequency difference can be observed when the rubber and aluminum impactor; future applications may use this information to assess the possibility of impact damage.

Knowledge of the physical problem is the key to correlated simulations and tests. Having a database of both can help to develop artificial intelligence models to characterize real in-service events. For this, an accurate simulation base is crucial as it will allow us to explore new configurations without the need for testing.

The tests carried out on the metallic plate have proven instrumental in validating the proposed ray-tracing methodology in a representative structure; it enhances the practical applicability of the methodology and therefore increases confidence when applying the validated ray-tracing method to more complex composite structures.

The simulations are able to accurately represent the $S0$ wave, and the wave speed is very accurately captured, although in the case of the $A0$ wave seen in the tests the FEM or ray-tracing models are not able to achieve the same degree of correlation. Moreover, the effect of the stiffener is not fully represented in the simulation and more work may be necessary to include all significant factors to represent it accurately; main reasons for this discrepancy could be due to the effects of the stiffener adhesive that has not been included in the simulation. Future studies may be performed to quantify the energy dissipated in the stringer interface and develop a methodology to include it in the simulation.

The optimization of the boundary dissipation factors has converged to a reasonable low value and is consistent with the expected magnitude for these types of structures. This value is then used for the tests on the CFRP LIBIS wing lower cover demonstrator.

The results in the CFRP LIBIS wing lower cover show a significant match and similar tendencies in the presence of damage between the tests and the numerical analysis. The possibility of damage could be identified and its location and extent could be assessed by analyzing the data with cross-correlation algorithms, or the information could be used to feed an artificial intelligence model.

There will always be differences between the test results and the simulations, as has been discussed before. These discrepancies can arise due to various factors, such as assumptions, simplifications, or unforeseen variables in real-world conditions. However, the key point is not to achieve perfect alignment, but to ensure that the simulations effectively capture the essential trends and changes. As long as the simulations accurately reflect variations and responses to different conditions, they remain valuable tools for analysis and prediction.

Interpreting the results of actual damage can be challenging due to the numerous uncertainties inherent in this analysis. However, the proposed methodology demonstrates a good degree of precision, allowing observation and capture of damping, reflections, and other effects on the signal within the presented results. Although complexities and ambiguities remain, the approach still provides valuable insight into the damage characteristics, highlighting its potential utility in practical applications.

This thesis has explored the complexities of GLW propagation in various test cases and representative aeronautical structures, particularly focusing on the complexities of CFRP and the application of ray-tracing techniques to model these phenomena. The findings emphasize the critical role of advanced simulation methods in understanding how waves behave as they interact with complex geometries and heterogeneous materials,in summary, being able to

reach the following key original contributions:

- **Ray-Tracing methodology Development:** The thesis presents a development of a complete ray-tracing algorithm tailored for GLW propagation, enabling precise modeling of wave reflection, refraction, damping, and mode conversion at structural discontinuities. The methodology incorporates physics-based models to capture dispersion effects and anisotropic material properties common in composite aerospace components.
- **Validation and accuracy analysis:** the accuracy of the proposed methodology is demonstrated by comparing the results with experimental data on a series of representative cases. Evaluates performance in scenarios involving curved geometries, stiffeners, and bonded joints, highlighting the method's ability to handle structural complexities.
- **Computational Efficiency:** the method provides significant reductions in computational costs compared to traditional methods while maintaining high accuracy, making it ideal for artificial intelligence applications.
- **Practical Implementation and Case Studies:** Applies the methodology to representative aerospace structures, such as stiffened composite panels and a representative UAV wing lower cover, showcasing its effectiveness in damage detection and localization. Investigates sensitivity to simulated defects and real BVID, proving robustness under varying conditions.

The validation of ray-tracing simulations against experimental data underscores the effectiveness of these models in accurately predicting wave behavior. Although uncertainties exist, especially in more complex structures, the alignment of simulation results with empirical observations reinforces the reliability of ray-tracing as a tool for analyzing wave propagation.

Furthermore, the integration of ray-tracing and other simulation techniques within an SHM system highlights the potential for proactive maintenance strategies, such as condition-based maintenance. Using real-time data from SHM systems, it becomes possible to detect damage early and respond to underlying issues promptly, ultimately improving the safety and performance of structural systems.

The integration of ray-tracing techniques with PIML presents a groundbreaking opportunity to advance our understanding and modeling of complex physical phenomena. Using the data generated from ray-tracing simulations, considering their small computational cost, it is possible to create highly informative training datasets that enhance the capabilities of neural networks while ensuring adherence to fundamental physical principles.

As we move forward, it will be essential to continue refining these simulation techniques and expanding their applications to a wider range of materials and structures. The interplay between experimental validation and advanced modeling will remain vital for advancing our understanding of wave propagation phenomena and developing effective monitoring solutions. Through ongoing research and innovation in this field, we can pave the way for more robust and reliable structural health monitoring practices, ensuring the integrity and longevity of critical infrastructure.

## 6.2 Future lines of work

Future lines of work could include:

- **Extension to Complex Geometries**, the methodology could be improved to account for more complex structural details, curvature, or other specific features, to improve real-world applicability.
- **Incorporation of scattering effects**, although not very significant for damages in CFRP structures due to the typical high attenuation of the damage boundaries, it could become a relevant effect on sharp edges such as crack growth in metals or other specific scenarios.
- **Experimental Validation**, additional experimental studies could be conducted to compare ray-tracing predictions with real-world GLW propagation covering curvature, material changes or other scenarios, improving the robustness and reliability of the method.
- **Integration with Machine Learning as a physics-informed model**, as it has been discussed during the thesis, the method is ideal to be used for this purpose due to its low simulation time and versatility.
- **Hybrid Modeling Approaches**, combining ray-tracing with FEM or other numerical techniques to achieve a balance between accuracy and computational cost.
- **Integration with Machine Learning for accuracy**, considering a similar approach to the hybrid modeling paradigm, AI-based optimization or deep learning could be used to improve the efficiency and precision of ray-tracing predictions or to use the methodology in inverse problems.
- **Real-Time Implementation on an SHM system**, adapting the methodology for real-time damage detection in aerospace, civil, or mechanical structures by optimizing computational efficiency and using models for real-time data processing.

# References


Aalami, B. (1973). Waves in Prismatic Guides of Arbitrary Cross Section. *Journal of Applied Mechanics*, *40*(4), 1067–1072. https://doi.org/10.1115/1.3423127

*Acess 2.0 user's manual*. (2007). Acellent Technologies, Inc. 835 Stewart Drive Sunnyvale, CA 94085.

Achenbach, J. (1973). *Wave propagation in elastic solids*. North-Holland Publishing Company.

Adams, C. (2012). Hums technology. *Aviation Today*.

Adams, R., & Maheri, M. (1994). Dynamic flexural properties of anisotropic fibrous composite beams. *Composites Science and Technology*, *50*(4), 497–514. https://doi.org/10.1016/0266-3538(94)90058-2

Adams, R., & Maheri, M. (2003). Damping in advanced polymer–matrix composites [Proceedings of the International Symposium on High Damping Materials]. *Journal of Alloys and Compounds*, *355*(1), 126–130. https://doi.org/10.1016/S0925-8388(03)00238-X

Aguilar Redondo, C. L. (2019, June). *Lamb waves analysis for damage detection and identification in composite plate with a t-shape stiffener* [Master's thesis, Universidad Politécnica de Madrid].

Aila, T., & Laine, S. (2009). Understanding the efficiency of ray traversal on gpus. *Proceedings of the Conference on High Performance Graphics 2009*, 145–149. https://doi.org/10.1145/1572769.1572792

Aktepe, B., & Molent, L. (1999). Management of airframe fatigue through individual aircraft loads monitoring programs. *Proceedings of the International Aerospace Congress*.

Allen, J., & Rabiner, L. (1977). A unified approach to short-time fourier analysis and synthesis. *Proceedings of the IEEE*, *65*(11), 1558–1564. https://doi.org/10.1109/PROC.1977.10770

Aloisio, A., Di Battista, L., Alaggio, R., & Fragiacomo, M. (2020). Sensitivity analysis of subspace-based damage indicators under changes in ambient excitation covariance, severity and location of damage. *Engineering Structures*, *208*, 110235. https://doi.org/10.1016/j.engstruct.2020.110235

Application of sfem to shm: Simplified damage models. (2008). In *Spectral finite element method: Wave propagation, diagnostics and control in anisotropic and inhomogeneous structures* (pp. 259–306). Springer London. https://doi.org/10.1007/978-1-84628-356-7_9

Armijo Torres, J. I., Gómez-Escalonilla Martín, J., & García Alonso, J. (2013, March). *Method and system for monitoring a structure* [Patent number: 8855852].

Arnaiz, C. (2002). *Estructuras aeronáuticas: 1ra parte : Cuarto curso (1er. cuatrimestre)*. Escuela Técnica Superior de Ingenieros Aeronáuticos, Sección de Publicaciones.

Arregui-Mena, J. D., Margetts, L., & Mummery, P. M. (2016). Practical application of the stochastic finite element method. *Archives of Computational Methods in Engineering*, *23*, 171–190. https://doi.org/10.1007/s11831-014-9139-3

Artificial neural network tutorial [Accessed: September 2024]. (2024).

Assler, H. D., & Telgkamp, J. (2004). Design of aircraft structures under special consideration of ndt. *Proceedings of the 16th World Conference on NDT*.

Ayers, J. P., Greve, D. W., & Oppenheim, I. J. (2003). Energy scavenging for sensor applications using structural strains. *Smart Structures and Materials*, *5057*. https://doi.org/10.1117/12.482377

Bales, R., Maull, R., & Radnor, Z. (2004). The development of supply chain management within the aerospace manufacturing sector. *Supply Chain Management-an International Journal - SUPPLY CHAIN MANAG*, *9*, 250–255. https://doi.org/10.1108/13598540410544944

Barthorpe, R. J. (2010). *On model-and data-based approaches to structural health monitoring* [Doctoral dissertation, University of Sheffield].

Bartoli, I., Marzani, A., Lanza di Scalea, F., & Viola, E. (2006). Modeling wave propagation in damped waveguides of arbitrary cross-section. *Journal of Sound and Vibration*, *295*(3), 685–707. https://doi.org/10.1016/j.jsv.2006.01.021

Bednarcyk, B. A., Aboudi, J., & Arnold, S. M. (2016). Enhanced composite damping through engineered interfaces. *International Journal of Solids and Structures*, *92-93*, 91–104. https://doi.org/10.1016/j.ijsolstr.2016.04.020

Ben, B. A., Ben, B. S., Kumar, A., & Murthy, B. S. N. (2012). Damping factor of composite plate using lamb wave method. *International Journal of Engineering and Innovative Technology (IJEIT)*, *2*, 65–71.

Benmeddour, F., Treyssède, F., & Laguerre, L. (2011). Numerical modeling of guided wave interaction with non-axisymmetric cracks in elastic cylinders. *International Journal of Solids and Structures*, *48*(5), 764–774. https://doi.org/10.1016/j.ijsolstr.2010.11.013

Bert, C. (1973). Material damping: An introductory review of mathematic measures and experimental technique. *Journal of Sound and Vibration*, *29*(2), 129–153. https://doi.org/10.1016/S0022-460X(73)80131-2

Berthelot, J.-M., & Sefrani, Y. (2004). Damping analysis of unidirectional glass and kevlar fibre composites. *Composites Science and Technology*, *64*(9), 1261–1278. https://doi.org/10.1016/j.compscitech.2003.10.003

Bishop, C. (2016). *Pattern recognition and machine learning*. Springer New York.

Blanchard, J. P. (2003). Elastic waves induced by surface heating in a half-space. *Journal of applied mechanics*, 70(4).

Boashsah, B. (1988). Note on the use of the wigner distribution for time-frequency signal anal-ysis. *Transactions on Acoustics, Speech, and Signal Processing*, *36*, 1518–1521.

Boller, C., & Buderath, M. (2007). Fatigue in aerostructures-where structural health monitoring can contribute to a complex subject. *Philosophical Transactions of the Royal Society A: Mathematical, Physical and Engineering Sciences*, *365*(1851), 561–587. https://doi.org/10.1098/rsta.2006.1924

Bowman, R. D., Bennett, B. A., & Stevenson, M. E. (2003). Radiographic inspection in failure investigations. *Practical Failure Analysis*, *3*, 73–77. https://doi.org/10.1007/BF02715538

Bradford, S. C. (2006, July). *Time-frequency analysis of systems with changing dynamic properties* [Doctoral dissertation, California Institute of Technology].

Brahme, A. (2014, January). *Comprehensive biomedical physics*.

Buchanan, B. G. (2005). A (very) brief history of artificial intelligence. *AI Magazine*, *26*(4), 53. https://doi.org/10.1609/aimag.v26i4.1848

Buckley, T., Ghosh, B., & Pakrashi, V. (2022). A feature extraction & selection benchmark for structural health monitoring. *Structural Health Monitoring*, *0*(0), 14759217221111141. https://doi.org/10.1177/14759217221111141

Burnes, A. (2024, August). Black myth: Wukong out now with full ray tracing & dlss 3 - get the definitive experience on geforce rtx 40 series gpus [Accessed: September 2024].

Cardona, J., Tabuenca, P., & Samartin, A. (2010). A numerical solution of the dispersion equation of guided wave propagation in n-layered media. In C. Constanda & M. Pérez (Eds.), *Integral methods in science and engineering, volume 2: Computational aspects* (pp. 41–53). Birkhäuser Boston. https://doi.org/10.1007/978-0-8176-4897-8_5

Cerqueira, R., Trocoli, T., Albiez, J., & Oliveira, L. (2020). A rasterized ray-tracer pipeline for real-time, multi-device sonar simulation. *Graphical Models*, *111*, 101086. https://doi.org/10.1016/j.gmod.2020.101086

Chandra, R., Singh, S., & Gupta, K. (2002). Micromechanical damping models for fiber-reinforced composites: A comparative study. *Composites Part A: Applied Science and Manufacturing*, *33*(6), 787–796. https://doi.org/10.1016/S1359-835X(02)00019-2

Chandra, R., Singhb, S., & Guptac, K. (2003). A study of damping in fiber-reinforced composites. *Journal of Sound and Vibration*, *262*, 475–496. https://doi.org/10.1016/S0022-460X(03)00107-X

Charles H. Keilers, J., & Chang, F.-K. (1995). Identifying delamination in composite beams using built-in piezoelectrics: Part i – experiments and analysis. *Journal of Intelligent Material Systems and Structures*, *6*(5), 649–663. https://doi.org/10.1177/1045389X9500600506

Chen, H., Feng, Z., Du, Y., Chen, Q., & Miao, H. (2022). Spectral finite element method for efficient simulation of nonlinear interactions between lamb waves and breathing cracks within the bi-potential framework. *International Journal of Mechanical Sciences*, *215*, 106954. https://doi.org/10.1016/j.ijmecsci.2021.106954

Chen, J., Reitz, J., Richstein, R., Schröder, K.-U., & Roßmann, J. (2024). Iot-based shm using digital twins for interoperable and scalable decentralized smart sensing systems. *Information*, *15*(3). https://doi.org/10.3390/info15030121

Cheng, J., & Fomel, S. (2014). Fast algorithms for elastic-wave-mode separation and vector decomposition using low-rank approximation for anisotropic media. *Geophysics*, *79*, C97–C110.

Chiappa, A., Iakovlev, S., Marzani, A., Giorgetti, F., Groth, C., Porziani, S., & Biancolini, M. (2021). An analytical benchmark for a 2d problem of elastic wave propagation in a solid. *Engineering Structures*, *229*, 111655. https://doi.org/10.1016/j.engstruct.2020.111655

Cho, H., & Lissenden, C. J. (2012). Structural health monitoring of fatigue crack growth in plate structures with ultrasonic guided waves. *Structural Health Monitoring*, *11*(4), 393–404. https://doi.org/10.1177/1475921711430439

Cho, Y., & Rose, J. L. (1996). A boundary element solution for a mode conversion study on the edge reflection of Lamb waves. *The Journal of the Acoustical Society of America*, *99*(4), 2097–2109. https://doi.org/10.1121/1.415396

Cohen, L. (1989). Time-frequency distributions - a review. *Proceedings of the IEEE*, *77*(7), 941–981. https://doi.org/10.1109/5.30749

Conry, M. J. (2005, April). Notes on wave propagation in anisotropic elastic solids.

Correa, A., Dorri, A., Rohatgi, P., & Salowitz, N. (2017). Mechanics and design of self-healing materials to complement shm. *Structural Health Monitoring*.

Cross, E. J., Gibson, S. J., Jones, M. R., Pitchforth, D. J., Zhang, S., & Rogers, T. J. (2021, October). Physics-informed machine learning for structural health monitoring. In *Structural health monitoring based on data science techniques* (pp. 347–367). Springer International Publishing. https://doi.org/10.1007/978--3-030--81716--9_17

Curtis, J. M., & Moore, D. R. (1988). Fatigue testing of multiangle laminates of cf/peek. *Composites*, *19*, 446–455. https://doi.org/10.1016/0010-4361(88)90702-1

da Silva, P. A., Dotta, F., & Rulli, R. P. (2014). *Structural health monitoring sensory arrangement integrated within a self-healing system* [Patent No. US9897533B2, application number: 14/309, 484, Filed Jun. 19, 2014, US2015/0369723A1 Dec. 24, 2015].

Dadras Eslamlou, A., & Huang, S. (2022). Artificial-neural-network-based surrogate models for structural health monitoring of civil structures: A literature review. *Buildings*, *12*(12). https://doi.org/10.3390/buildings12122067

d'Alembert, J. l. R. (1747). Recherches sur la courbe que forme une corde tenduë mise en vibration. *Histoire de l'académie royale des sciences et belles lettres de Berlin*, *3*, 214–219.

*Dassault systemes simulia. abaqus v. 2017 documentation.* (2023). Simulia Corp., Providence, RI, USA.

de Luca, A., Perfetto, D., de Fenza, A., Petrone, G., & Caputo, F. (2018). A sensitivity analysis on the damage detection capability of a lamb waves based shm system for a composite winglet. *Proceeding of the AIAS 2018 International Conference on Stress Analysis*, *12*, 578–588.

de Paula S. Ferreira, L., de O. Teloli, R., da Silva, S., Figueiredo, E., Moldovan, I. D., Maia, N., & Cimini, C. A. (2024). Bayesian calibration for lamb wave propagation on a composite plate using a machine learning surrogate model. *Mechanical Systems and Signal Processing*, *208*, 111011. https://doi.org/10.1016/j.ymssp.2023.111011

del Río Velilla, D. (2022, September). *Metodología para el diseño y fabricación de útiles y piezas de material compuesto con catia* [Master's thesis, Universidad Politécnica de Madrid].

del Río Velilla, D., Pedraza, A., & Fernández López, A. (2024). Impact localization in composite structures with deep neural networks. *Structural Health Monitoring*, *0*(0), 14759217241270946. https://doi.org/10.1177/14759217241270946

Diaw, A., McKerns, M., Sagert, I., Stanton, L. G., & Murillo, M. S. (2024). Efficient learning of accurate surrogates for simulations of complex systems. *Nature Machine Intelligence*, *6*, 568–577. https://doi.org/10.1038/s42256-024-00839-1

Donaldson, B. (2008). *Analysis of aircraft structures: An introduction*. Cambridge University Press.

Dorn, C., & Kochmann, D. M. (2022). Ray theory for elastic wave propagation in graded metamaterials. *Journal of the Mechanics and Physics of Solids*, *168*, 105049. https://doi.org/https://doi.org/10.1016/j.jmps.2022.105049

Douglas A. Skoog, S. R. C., F. James Holler. (2007). *Principles of instrumental analysis*. Thomson Brooks/Cole.

Draudviliene, L., Tumsys, O., & Raisutis, R. (2021). Reconstruction of lamb wave dispersion curves in different objects using signals measured at two different distances. *Materials (Basel)*. https://doi.org/10.3390/ma14226990

Duan, W., & Kirby, R. (2019). Guided wave propagation in buried and immersed fluid-filled pipes: Application of the semi analytic finite element method. *Computers & Structures*, *212*, 236–247. https://doi.org/10.1016/j.compstruc.2018.10.020

Dworakowski, Z., Ambrozinski, L., Packo, P., Dragan, K., & Stepinski, T. (2015). Application of artificial neural networks for compounding multiple damage indices in lamb-wave-based damage detection. *Structural Control and Health Monitoring*, *22*(1), 50–61. https://doi.org/10.1002/stc.1659

Ehsani, M., Shamshirsaz, M., Sadighi, M., Sepehry, N., & Loendersloot, R. (2023). Three-dimensional scaled boundary finite element method to simulate lamb wave health monitoring of homogeneous structures: Experiment and modelling. *Ultrasonics*, *129*, 106892. https://doi.org/10.1016/j.ultras.2022.106892

Eisenträger, S., Joulaian, M., Düster, A., & Gabbert, U. (2014). Numerical analysis of lamb waves using the finite and spectral cell methods. *International Journal for Numerical Methods in Engineering*, *99*, 26–53. https://doi.org/10.1002/nme.4663

Elagha, H. A. (2017). Generalized formulas for ray-tracing and longitudinal spherical aberration. *Journal of the Optical Society of America. A, Optics, image science, and vision*, 335–343. https://doi.org/10.1364/JOSAA.34.000335

Erturk, A., & Inman, D. (2011). *Piezoelectric energy harvesting* (1st ed.). John Wiley & Sons, Ltd.

*Esatan-tms 2023 thermal modelling suite* [Accessed: June 2024]. (2024). ITP Aero, ITP Engines UK Ltd.

Fakih, M. A., Chiachío, M., Chiachío, J., & Mustapha, S. (2022). A bayesian approach for damage assessment in welded structures using lamb-wave surrogate models and minimal sensing. *NDT & E International*, *128*, 102626. https://doi.org/10.1016/j.ndteint.2022.102626

Farrar, C. R., & Worden, K. (2006). An introduction to structural health monitoring. *Philosophical Transactions of the Royal Society A: Mathematical, Physical and Engineering Science*, *365*. https://doi.org/10.1098/rsta.2006.1928

Farrar, C. R., Czarnecki, J. J., Sohn, H., & Hemez, F. M. (2002, January). *A review of structural health monitoring literature : 1996–2001*. Los Alamos National Laboratory.

Fausett, L. (1994). *Fundamentals of neural networks: Architectures, algorithms, and applications*. Prentice-Hall.

Fernández Díaz-Maroto, P., Fernández López, A., García Alonso, J., Iglesias Vallejo, M., & Güemes, A. (2018). Buckling detection of an omega-stiffened aircraft composite

panel using distributed fibre optic sensors. *Thin-Walled structures*, *132*, 375–384. https://doi.org/10.1016/j.tws.2018.08.024

Fernández López, A. (2009). *Detección de daño en estructuras aeronáuticas mediante sensores piezoeléctricos y de fibra óptica* [Doctoral dissertation, Universidad Politécnica de Madrid].

Finegan, I. C., & Gibson, R. F. (2000). Analytical modeling of damping at micromechanical level in polymer composites reinforced with coated fibers. *Composites Science and Technology*, *60*(7), 1077–1084. https://doi.org/10.1016/S0266-3538(00)00003-8

Finlayson, R., Friesel, M., Carlos, M., Cole, P., & Lenain, J.-C. (2001). Health monitoring of aerospace structures with acoustic emission and acousto-ultrasonics. *15th World Conference on NDT*.

Firestone, F. A., & Ling, J. D. S. (1945). *Propagation of waves in plates* (tech. rep.). Technical report, Sperry products, Danbury, CT, USA.

Firestone, F. A., & Ling, J. D. S. (1951, January). *Method and means for generating and utilizing vibrational waves in plates* [US Patent 2,536,128].

Frank Pai, P., Deng, H., & Sundaresan, M. J. (2015). Time-frequency characterization of lamb waves for material evaluation and damage inspection of plates. *Mechanical Systems and Signal Processing*, *62-63*, 183–206. https://doi.org/10.1016/j.ymssp.2015.03.011

Frederick, C., & Worlont, D. (1962). Ultrasonic thickness measurements with lamb waves. *Journal of Nondestructive Test*, *20*, 51–55.

Fualdes, C. (2016). Experience and lessons of a full composite passenger aircraft development. *Proceeding of the ICAS 2016 International Conference*.

Furkan Kosova, Ö. A., & Hakk, Ö. Ü. (2024). Structural health monitoring in aviation: A comprehensive review and future directions for machine learning. *Nondestructive Testing and Evaluation*, 1–60. https://doi.org/10.1080/10589759.2024.2350575

Fuse, R., Enya, K., Kameda, S., Kato, H., Osada, N., Ishibashi, K., Ozaki, M., Sakatani, N., Kouyama, T., Suzuki, H., Nakamura, T., Miyamoto, H., Abe, S., Goda, Y., & Murao, H. (2022). Stray light analysis by ray tracing simulation for the wide-angle multiband camera orochi onboard the martian moons exploration (mmx) spacecraft. *Advances in Space Research*, *69*(2), 1236–1248. https://doi.org/10.1016/j.asr.2021.11.011

Galán, J. M., & Abascal, R. (2002). Numerical simulation of lamb wave scattering in semi-infinite plates. *International Journal for Numerical Methods in Engineering*, *53*(5), 1145–1173. https://doi.org/10.1002/nme.331

Galán, J. M., & Abascal, R. (2003). Elastodynamic guided wave scattering in infinite plates. *International Journal for Numerical Methods in Engineering*, *58*(7), 1091–1118. https://doi.org/10.1002/nme.809

Galarza, N., Rubio, B., Diez, A., Boto, F., Gil, D., Rubio, J., & Moreno, E. (2016). Implementation of signal processing methods in a structural health monitoring (shm) system based on ultrasonic guided waves for defect detection in different materials and structures. *8th European Workshop On Structural Health Monitoring (EWSHM 2016)*.

Gangadharaiah, Y., & Sandeep, N. (2021). *Engineering applications of the laplace transform*. Cambridge Scholars Publishing.

García Alonso, J. (2016, January). *Monitorización de estructuras aeronáuticas mediante técnicas de inteligencia artificial* [Doctoral dissertation, Universidad Politécnica de Madrid]. https://doi.org/10.20868/UPM.thesis.39487

Gautschi, G. (2002). *Piezoelectric sensorics: Force, strain, pressure, acceleration and acoustic emission sensors*. Springer. https://doi.org/10.1007/978--3-662--04732--3

Gavrić, L. (1994). Finite element computation of dispersion properties of thin-walled waveguides. *Journal of Sound and Vibration*, *173*(1), 113–124. https://doi.org/10.1006/jsvi.1994.1221

Gavrić, L. (1995). Computation of propagative waves in free rail using a finite element technique. *Journal of Sound and Vibration*, *185*(3), 531–543. https://doi.org/10.1006/jsvi.1995.0398

Gazis, D. C. (1958). Exact Analysis of the Plane-Strain Vibrations of Thick-Walled Hollow Cylinders. *The Journal of the Acoustical Society of America*, *30*(8), 786–794. https://doi.org/10.1121/1.1909761

Ge, Z., & Chen, X. (2008). An Efficient Approach for Simulating Wave Propagation with the Boundary Element Method in Multilayered Media with Irregular Interfaces. *Bulletin of the Seismological Society of America*, *98*(6), 3007–3016. https://doi.org/10.1785/0120080920

Gengembre, N., & Lhémery, A. (2000). Pencil method in elastodynamics: Application to ultrasonic field computation. *Ultrasonics*, *38*(1), 495–499. https://doi.org/10.1016/S0041-624X(99)00068-2

Gibson, R. F., & Hwang, S. J. (1991). Micromechanical modeling of damping in composite including interphase effects. *36th international SAMPE symposium*.

Glisic, B., & Inaudi, D. (2003). Components of structural monitoring process and selection of monitoring system. *6th International Symposium on Field Measurements in GeoMechanics (FMGM 2003)*, 755–761.

Goldstein, H. (1987). *Mecánica clásica*. Reverté.

Gómez Escalonilla, J., García Alonso, J., Cabrejas Portillo, J., & Armijo, J. I. (2007). A full scale parametric-based fatigue monitoring system using neural networks. *Proc. 24th symposium of the ICAF*.

Gopalakrishnan, S., Ruzzene, M., & Hanagud, S. (2011). *Computational techniques for structural health monitoring*. Springer London.

Gorinevsky, D. M., Gordon, G., Kumar, A., & Chang, F.-K. (2005). Design of integrated shm system for commercial aircraft applications. *Proceedings of the 5th International Workshop On Structural Health Monitoring*.

Graff, K. (2012). *Wave motion in elastic solids*. Dover Publications.

Gravenkamp, H. (2014, April). *Numerical methods for the simulation of ultrasonic guided waves* [Doctoral dissertation, BAM, Bundesanstalt für Materialforschung und -prüfung].

Gresil, M., & Giurgiutiu, V. (2014). Prediction of attenuated guided waves propagation in carbon fiber composites using rayleigh damping model. *Journal of Intelligent Material Systems and Structures*, *26*(16), 2151–2169. https://doi.org/10.1177/1045389X14549870

*Guidelines for implementation of structural health monitoring on fixed wing aircraft*. (2021, August). SAE International. Aerospace Industry Steering Committee on Structural Health. https://doi.org/10.4271/ARP6461A

Guinard, S., Allix, O., Guedra-Degeorges, D., & Vinet, A. (2002). A 3d damage analysis of low velocity impacts on laminated composites. *Composites Science and Technology*, *62*, 585–9. https://doi.org/10.1016/S0266-3538(01)00153-1

Gunawan, A., & Hirose, S. (2007). Reflection of obliquely incident guided waves by an edge of a plate. *MATERIALS TRANSACTIONS*, *48*(6), 1236–1243. https://doi.org/10.2320/matertrans.I-MRA2007852

Guo, H., Xiao, G., Mrad, N., & Yao, J. (2011). Fiber optic sensors for structural health monitoring of air platforms. *Sensors*, *11*(4), 3687–3705. https://doi.org/10.3390/s110403687

Gupta, M., Jin, L., & Homma, N. (2004). *Static and dynamic neural networks: From fundamentals to advanced theory*. Wiley.

Haig, A., & Haig, A. (2012). Defect detection for aircraft components : An approach using ultrasonic guided waves and neural networks [European Community's Seventh Framework Programme managed by REA-Research Executive Agency http://ec.europa.eu/research/rea([FP7-SME-2008-1] under grant agreement no [232212]].

Haldar, A., & Mahadevan, S. (2000). *Reliability assessment using stochastic finite element analysis*. Wiley.

Hambric, S. (2006). Structural acoustics tutorial – part 1: Vibrations in structures. *Acoustics Today*, *2*. https://doi.org/10.1121/1.2961142

Han, S. (2007, September). *Finite element analysis of lamb waves acting within a thin aluminum plate* [Master's thesis, Department of the air force Air University. AIR FORCE INSTITUTE OF TECHNOLOGY].

Harris, C. M., & Piersol, A. G. (2002). *Harris' shock and vibration handbook* (5th ed.). McGraw-Hill.

He, L., & Liu, Y. (2005). Damping behavior of fibrous composites with viscous interface under longitudinal shear loads. *Composites Science and Technology*, *65*(6), 855–860. https://doi.org/10.1016/j.compscitech.2004.09.003

He, X., Li, J., Huang, X., & Zhou, Y. (2022). Solving elastic wave equations in 2d transversely isotropic media by a weighted runge-kutta discontinuous galerkin method. *Petroleum Science*. https://doi.org/10.1016/j.petsci.2022.10.007

Heinze, C., Sinapius, M., & Wierach, P. (2014, July). Lamb Wave Propagation in Complex Geometries - Model Reduction with Approximated Stiffeners. In L. Cam, Vincent, Mevel, Laurent, Schoefs, & Franck (Eds.), *EWSHM - 7th European Workshop on Structural Health Monitoring*.

Hexcel Corporation. (2024). Hexply 8552 epoxy matrix (180°c/356°f curing matrix) datasheet.

Heywang, W., Lubitz, K., & Wersing, W. (2008). *Piezoelectricity: Evolution and future of a technology* (Vol. 114). Springer Science & Business Media.

Hovem, J. (2010). *Marine acoustics-the physics of sound in marine environments*. Peninsula Publishing, Los Altos Hills, CA, USA.

Huang, K., & Dong, S. (1984). Propagating waves and edge vibrations in anisotropic composite cylinders. *Journal of Sound and Vibration*, *96*(3), 363–379. https://doi.org/10.1016/0022-460X(84)90363-8

Huang, L., Zeng, L., Lin, J., & Zhang, N. (2020). Baseline-free damage detection in composite plates using edge-reflected lamb waves. *Composite Structures*, *247*, 112423. https://doi.org/10.1016/j.compstruct.2020.112423

Hwang, S., & Gibson, R. (1993). Prediction of fiber-matrix interphase effects on damping of composites using a micromechanical strain energy/finite element approach. *Composites Engineering*, *3*(10), 975–984. https://doi.org/10.1016/0961-9526(93)90005-5

Ihn, J. B. (2013, June). Structural health monitoring overview & aerospace applications [An invited lecture series for ME/MSE 568: Active and sensing materials and their devices.].

Ikeda, T. (1996). *Fundamentals of piezoelectricity*. Oxford University Press.

IOWA State University, c. f. n.-d. e. (2024). Ndt resource center [Accessed: June 2024].

Jacob, P., & L., G. (2002, January). *An explicit finite element primer*.

Jaffe, H. (1958). Piezoelectric ceramics. *Journal of the American Ceramic Society*, *41*(11), 494–498.

Jeon, J.-J., & Shin, Y. S. (1993, March). *Pseudo wigner-ville distribution, computer program and its applications to time-frequency domain problems* [Naval Postgraduate School Report NPS-ME-93–002]. Monterey, California : Naval Postgraduate School.

Ji, D., Gao, F., Liu, Z., Li, H., & Lin, J. (2024). High-precision lamb wave evaluation for corrosion damage with model-based bayesian optimization and gaussian meta-modeling strategy. *Structural Health Monitoring*, *0*(0), 14759217241256272. https://doi.org/10.1177/14759217241256272

Joseph, R., Li, L., Haider, M. F., & Giurgiutiu, V. (2019). Hybrid safe-gmm approach for predictive modeling of guided wave propagation in layered media. *Engineering Structures*, *193*, 194–206. https://doi.org/10.1016/j.engstruct.2019.04.082

Kaliske, M., & Rothert, H. (1995). Damping characterization of unidirectional fibre reinforced polymer composites. *Composites Engineering*, *5*(5), 551–567. https://doi.org/10.1016/0961-9526(95)00028-L

Kalkowski, M. K., Muggleton, J. M., & Rustighi, E. (2018). Axisymmetric semi-analytical finite elements for modelling waves in buried/submerged fluid-filled waveguides. *Computers & Structures*, *196*, 327–340. https://doi.org/10.1016/j.compstruc.2017.10.004

Kamal, A., Gresil, M., & Giurgiutiu, V. (2013). Comparative study of several methods for the calculation of ultrasonic guided waves in composites. *54th AIAA / ASME / ASCE / AHS / ASC Structures, Structural Dynamics, and Materials Conference*. https://doi.org/10.2514/6.2013-1901

Karunasena, W., Liew, K., & Kitipornchai, S. (1995). Hybrid analysis of lamb wave reflection by a crack at the fixed edge of a composite plate. *Computer Methods in Applied Mechanics and Engineering*, *125*(1), 221–233. https://doi.org/10.1016/0045-7825(95)00802-8

Kenny, J. M., & Betti, M. (1995). Elasto–plastic behavior of thermoplastic composite laminate under cyclic loading. *Composite Structures*, *35*, 375–382. https://doi.org/10.1016/0263-8223(95)00052-6

Keshmiry, A., Hassani, S., & Dackermann, U. (2024). 5 - ai-based structural health monitoring systems. In M. L. Nehdi, H. C. Arora, K. Kumar, R. Damaševičius, & A. Kumar (Eds.), *Artificial intelligence applications for sustainable construction* (pp. 151–170). Woodhead Publishing. https://doi.org/10.1016/B978-0-443-13191-2.00008-0

Kessler, S., Spearing, S., & Atalla, M. (2002). In-situ damage detection of composites structures using lamb wave methods. *Proceedings of the First European Workshop on Structural Health Monitoring*, 374–381.

Killedar, M., Lasky, P. D., Lewis, G. F., & Fluke, C. J. (2011). Gravitational lensing with three-dimensional ray tracing. *Monthly Notices of the Royal Astronomical Society*, *420*(1), 155–169. https://doi.org/10.48550/arXiv.1110.4894

Kim, K. B., Nah, M., Kim, B. K., Koo, K., & Kang, J. (2022). The natural frequencies of aisi 316 stainless steel and analytical simulation of a lamb wave excited by a point source. *Wave Motion*, 103085. https://doi.org/10.1016/j.wavemoti.2022.103085

Kim, S.-Y., & Lee, D.-H. (2009). Identification of fractional-derivative-model parameters of viscoelastic materials from measured frfs. *Journal of Sound and Vibration*, *324*, 570–586. https://doi.org/10.1016/j.jsv.2009.02.040

Kirikera, G. R. (2003). *An artificial neural system with distributed parallel processing for structural health monitoring* [Master's thesis, University of Cincinnati, Engineering].

Kirkegaard, P., & Rytter, A. (1994). Vibration based damage assessment of a civil engineering structures using a neural networks. *1st Workshop of the European Group for Structural Engineering Applications of Artifical Intelligence.*, (53).

Kneifl, J., Fehr, J., Brunton, S. L., & Kutz, J. N. (2024). Multi-hierarchical surrogate learning for explicit structural dynamical systems using graph convolutional neural networks. *Computational Mechanics*. https://doi.org/10.1007/s00466-024-02553-6

Knight, S., Salagaras, M., & Trueman, A. (2011). The study of intergranular corrosion in aircraft aluminium alloys using x-ray tomography. *Corrosion Science*, *53*(2), 727–734. https://doi.org/10.1016/j.corsci.2010.11.005

Kocbach, J. (2000). *Finite element modeling of ultrasonic piezoelectric transducers. influence of geometry and material parameters on vibration, response functions and radiated field.* [Doctoral dissertation, University of Bergen, Dpt. of Physics].

Kolsky, H. (1964). Stress waves in solids. *Journal of Sound and Vibration*, *1*(1), 88–110. https://doi.org/10.1016/0022-460X(64)90008-2

Kudela, P., & Ostachowicz, W. M. (2008). Wave propagation modelling in composite plates. *New Trends in Mechanics and Transport*, *9*, 89–104. https://doi.org/10.4028/www.scientific.net/AMM.9.89

Kudela, P., Radzienski, M., & Ostachowicz, W. (2018a). Impact induced damage assessment by means of lamb wave image processing. *Mechanical Systems and Signal Processing*, 23–36. https://doi.org/10.1016/j.ymssp.2017.09.020

Kudela, P., Radzienski, M., & Ostachowicz, W. (2018b). Wave propagation modeling in composites reinforced by randomly oriented fibers. *Journal of Sound and Vibration*, *414*, 110–125. https://doi.org/10.1016/j.jsv.2017.11.015

Kudela, P., Żak, A., Krawczuk, M., & Ostachowicz, W. (2007). Modelling of wave propagation in composite plates using the time domain spectral element method. *Journal of Sound and Vibration*, *302*(4), 728–745. https://doi.org/10.1016/j.jsv.2006.12.016

Lagasse, P. E. (1973). Higher-order finite-element analysis of topographic guides supporting elastic surface waves. *The Journal of the Acoustical Society of America*, *53*(4), 1116–1122. https://doi.org/10.1121/1.1913432

Lamb, H. (1881). On the vibrations of an elastic sphere. *Proceedings of the London Mathematical Society*, *s1-13*(1), 189–212. https://doi.org/10.1112/plms/s1-13.1.189

Lamb, H. (1917). On waves in an elastic plate. *Proceedings of the Royal Society, A: Mathematical, Physical and Engineering Sciences*, *93*, 114–128.

Li, F., Zhao, Y., Cao, P., & Hu, N. (2018). Mixing of ultrasonic lamb waves in thin plates with quadratic nonlinearity. *Ultrasonics*, *87*, 33–43. https://doi.org/10.1016/j.ultras.2018.02.005

Li, J. (2021). *Lead-free piezoelectric materials*. Wiley.

Li, X., Ma, D., Liu, H., Tan, W., Gong, X., Zhang, C., & Li, Y. (2019). Assessment of failure criteria and damage evolution methods for composite laminates under low-velocity impact. *Composite structures*, *207*, 727–739. https://doi.org/10.1016/j.compstruct.2018.09.093

Lin, M., Qing, X., Kumar, A., & Beard, S. J. (2001). Smart layer and smart suitcase for structural health monitoring applications. *SPIE Smart Structures and Materials + Nondestructive Evaluation and Health Monitoring*, *4332*, 98–106. https://doi.org/10.1117/12.429646

Liu, A., Cheung, C., & Martinez, M. (2011). Use of artificial neural networks for helicopter load monitoring. *Proceedings of the 7th DSTO International Conference on Health & Usage Monitoring*.

Liu, G., & Quek Jerry, S. (2003). A non-reflecting boundary for analyzing wave propagation using the finite element method. *Finite Elements in Analysis and Design*, *39*(5), 403–417. https://doi.org/10.1016/S0168-874X(02)00081-1

Liu, S., Du, C., Mou, J., Martua, L., Zhang, J., & Lewis, F. (2013). Diagnosis of structural cracks using wavelet transform and neural networks. *NDT & E International*, *54*, 9–18. https://doi.org/10.1016/j.ndteint.2012.11.004

Liu, W. L., Jen, C. K., Wu, K. T., Kobayashi, M., & Mrad, N. (2011). Flexible ultrasonic transducer arrays for health monitoring of an aircraft component. *Insight*, *53*, 316–320.

Liu, W., & Hong, J.-W. (2015). Modeling of three-dimensional lamb wave propagation excited by laser pulses. *Ultrasonics*, *55*, 113–122. https://doi.org/https://doi.org/10.1016/j.ultras.2014.07.006

Liu, X., Yu, Y., Lomov, S. V., Wang, Y., & Qing, X. (2022). The numerical and experimental investigations for the curing monitoring of woven composites with lamb waves. *Measurement*, *200*, 111604. https://doi.org/10.1016/j.measurement.2022.111604

López, O., López, A., & Crossa, J. (2022). *Multivariate statistical machine learning methods for genomic prediction*. Springer International Publishing.

López, R. F., & Fernández, J. M. F. (2008). *Las redes neuronales artificiales*. Netbiblo.

Lopez-Higuera, J. M., Rodriguez Cobo, L., Quintela Incera, A., & Cobo, A. (2011). Fiber optic sensors in structural health monitoring. *Journal of Lightwave Technology*, *29*(4), 587–608. https://doi.org/10.1109/JLT.2011.2106479

Love, A. (2015). *Some problems of geodynamics*. Cambridge University Press.

Lyle, S., & Salencon, J. (2012). *Handbook of continuum mechanics: General concepts thermoelasticity*. Springer Berlin Heidelberg.

Ma, J., Hu, M., Yang, Z., Yang, H., Ma, S., Xu, H., Yang, L., & Wu, Z. (2023). An efficient lightweight deep-learning approach for guided lamb wave-based damage detection in composite structures. *Applied Sciences*, *13*(8). https://doi.org/10.3390/app13085022

Ma, Z., Chen, J., Li, B., Li, Z., & Su, X. (2016). Dispersion analysis of lamb waves in composite laminates based on reverberation-ray matrix method. *Composite Structures*, *136*, 419–429. https://doi.org/10.1016/j.compstruct.2015.10.036

Maday, Y., & Patera, A. T. (1989). Spectral element methods for the incompressible Navier-Stokes equations. *State-of-the-art surveys on computational mechanics (A90-47176 21-64)*, 71–143.

Malyarenko, E. V., & Hinders, M. K. (2001). Ultrasonic lamb wave diffraction tomography. *Ultrasonics*, *39*(4), 269–281. https://doi.org/10.1016/S0041-624X(01)00055-5

Manbachi, A., & Cobbold, R. S. C. (2011). Development and application of piezoelectric materials for ultrasound generation and detection. *Ultrasound*, *19*(4), 187–196. https://doi.org/10.1258/ult.2011.011027

Marrazzo, M., Sharif Khodaei, Z., & Aliabadi, M. H. F. (2023). Laplace domain boundary element method for structural health monitoring of poly-crystalline materials at micro-scale. *Applied Sciences*, *13*(24). https://doi.org/10.3390/app132413138

Marrel, A., & Iooss, B. (2024). Probabilistic surrogate modeling by gaussian process: A review on recent insights in estimation and validation. *Reliability Engineering & System Safety*, *247*, 110094. https://doi.org/10.1016/j.ress.2024.110094

Marzani, A., Viola, E., Bartoli, I., Lanza di Scalea, F., & Rizzo, P. (2008). A semi-analytical finite element formulation for modeling stress wave propagation in axisymmetric damped waveguides. *Journal of Sound and Vibration*, *318*(3), 488–505. https://doi.org/10.1016/j.jsv.2008.04.028

Matuszyk, P. J. (2017). Modeling of guided circumferential sh and lamb-type waves in open waveguides with semi-analytical finite element and perfectly matched layer method. *Journal of Sound and Vibration*, *386*, 295–310. https://doi.org/10.1016/j.jsv.2016.09.019

Mazzotti, M., Miniaci, M., & Bartoli, I. (2019). A numerical method for modeling ultrasonic guided waves in thin-walled waveguides coupled to fluids. *Computers & Structures*, *212*, 248–256. https://doi.org/10.1016/j.compstruc.2018.11.002

Meadows, L., Reed, S., & Duffield, M. (2009). Operational loads monitoring in military transport aircraft and military derivatives of civil aircraft. In *Encyclopedia of structural health monitoring*. John Wiley & Sons, Ltd. https://doi.org/10.1002/9780470061626.shm201

Megson, T. (2007). *Aircraft structures for engineering students*. Elsevier Science.

Mendler, A., Döhler, M., & Ventura, C. E. (2021). A reliability-based approach to determine the minimum detectable damage for statistical damage detection. *Mechanical Systems and Signal Processing*, *154*, 107561. https://doi.org/10.1016/j.ymssp.2020.107561

Mihailov, S. J. (2012). Fiber bragg grating sensors for harsh environments. *Sensors*, *12*(2), 1898–1918. https://doi.org/10.3390/s120201898

Min, J., Park, S., Yun, C.-B., Lee, C.-G., & Lee, C. (2012). Impedance-based structural health monitoring incorporating neural network technique for identification of damage type and severity. *Engineering Structures*, *39*, 210–220. https://doi.org/10.1016/j.engstruct.2012.01.012

Mindlin, R. D. (1951). Influence of rotatory inertia and shear de-formation on flexural motion of isotropic, elastic plates. *Journal of Applied Mechanics*, *18*, 31–38.

Mo, C., & Davidson, J. (2013). Energy harvesting technologies for structural health monitoring applications. *2013 1st IEEE Conference on Technologies for Sustainability (SusTech)*, 192–198. https://doi.org/10.1109/SusTech.2013.6617319

Modes of sound wave propagation [Accessed: June 2024]. (n.d.).

Moser, F., Jacobs, L. J., & Qu, J. (1999). Modeling elastic wave propagation in waveguides with the finite element method. *NDT & E International*, *32*(4), 225–234. https://doi.org/10.1016/S0963-8695(98)00045-0

Muñoz Chamorro, A. (2018, July). *Design of a damage detection system on an aeronautical composite structure* [Master's thesis, Universidad Politécnica de Madrid].

Nelson, R., Dong, S., & Kalra, R. (1971). Vibrations and waves in laminated orthotropic circular cylinders. *Journal of Sound and Vibration*, *18*(3), 429–444. https://doi.org/10.1016/0022-460X(71)90714-0

Newnham, R. E. (2005). *Properties of materials: Anisotropy, symmetry, structure*. Oxford university press.

Nguyen, A., Kodikara, K. T. L., Chan, T. H., & Thambiratnam, D. P. (2019). Deterioration assessment of buildings using an improved hybrid model updating approach and long-term health monitoring data. *Structural Health Monitoring*, *18*(1), 5–19. https://doi.org/10.1177/1475921718799984

*Ni 6366 device specifications*. (2023). National Instruments.

Nikodym, T. (2010, June). *Ray tracing algorithm for interactive applications* [Master's thesis, Czech Technical University].

Nilsson, N. (2009). *The quest for artificial intelligence*. Cambridge University Press.

Niu, C., & Niu, M. (1999). *Airframe structural design: Practical design information and data on aircraft structures*. Adaso Adastra Engineering Center.

Officer, C. B. (1958). *Introduction to the theory of sound transmission: With application to the ocean.* McGraw-Hill Book Company, Inc.

Ogilvy, J. (1990). A layered media model for ray propagation in anisotropic inhomogeneous materials. *Applied Mathematical Modelling*, *14*(5), 237–247. https://doi.org/10.1016/0307-904X(90)90014-V

Ogilvy, J. (1992). An iterative ray tracing model for ultrasonic nondestructive testing. *NDT & E International*, *25*(1), 3–10. https://doi.org/10.1016/0963-8695(92)90002-X

Okayasu, M., & Bamba, K. (2018). Domain switching behavior in lead zirconate titanate piezoelectric ceramics. *Scripta Materialia*, *146*, 272–275. https://doi.org/10.1016/j.scriptamat.2017.12.003

Ong, W., Rajic, N., Chiu, W., & Rosalie, C. (2016). Adhesive material property evaluation for improved lamb wave simulation. *International Journal of Adhesion & Adhesives*, *71*, 28–38. https://doi.org/10.1016/j.ijadhadh.2016.08.008

Osborne, M. F. M., & Hart, S. D. (1945). Transmission, Reflection, and Guiding of an Exponential Pulse by a Steel Plate in Water. I. Theory. *The Journal of the Acoustical Society of America*, *17*(1), 1–18. https://doi.org/10.1121/1.1916293

Ostachowicz, W., Kudela, P., Krawczuk, M., & Zak, A. (2011). *Guided waves in structures for shm: The time - domain spectral element method*. John Wiley & Sons, Ltd.

Ostachowicz, W., Kudela, P., Malinowski, P., & Wandowski, T. (2009). Damage localisation in plate-like structures based on pzt sensors. *Mechanical Systems and Signal Processing*, *23*, 1805–1829. https://doi.org/10.1016/j.ymssp.2008.10.011

Palacz, M., Zak, A., & Krawczuk, M. (2020). Fem-based wave propagation modelling for shm: Certain numerical issues in 1d structures. *Materials*, *13*(9). https://doi.org/10.3390/ma13092051

Paschotta, R. (2024, October). Fresnel reflections [Accessed: September 2024]. https://doi.org/10.61835/g7b"title="Thislinkwillreloadthecurrentpage.

Patera, A. T. (1984). A spectral element method for fluid dynamics: Laminar flow in a channel expansion. *Journal of Computational Physics*, *54*(3), 468–488. https://doi.org/10.1016/0021-9991(84)90128-1

Pedraza, A., del Río Velilla, D., Bautista Juzgado, V., Fernández López, A., & Sanz Andrés, Á. (2023). Study of the feasibility of decoupling temperature and strain from a $\phi$-pa-ofdr over an smf using neural networks. *Sensors*, *23*(12). https://doi.org/10.3390/s23125515

Peterson, J. R., Jernigan, J. G., Kahn, S. M., Rasmussen, A. P., Peng, E., Ahmad, Z., Bankert, J., Chang, C., Claver, C., Gilmore, D. K., Grace, E., Hannel, M., Hodge, M., Lorenz, S., Lupu, A., Meert, A., Nagarajan, S., Todd, N., Winans, A., & Young, M. (2015). Simulation of astronomical images from optical survey telescopes using a comprehensive photon monte carlo approach. *The Astrophysical Journal Supplement Series*, *218*(1), 14. https://doi.org/10.1088/0067-0049/218/1/14

Philibert, M., Yao, K., Gresil, M., & Soutis, C. (2022). Lamb waves-based technologies for structural health monitoring of composite structures for aircraft applications. *European Journal of Materials*, *2*(1), 436–474. https://doi.org/10.1080/26889277.2022.2094839

Pinello, L., Lomazzi, L., Ghellero, J., Giglio, M., & Cadini, F. (2024). Physics-informed machine learning for structural damage diagnosis in aluminium plates. *proceedings of the 11th European Workshop on Structural Health Monitoring*. https://doi.org/10.58286/29742

Pines, D., & Salvino, L. (2006). Structural health monitoring using empirical mode decomposition and the hilbert phase. *Journal of Sound and Vibration*, *294*(1), 97–124. https://doi.org/10.1016/j.jsv.2005.10.024

Piqueras, J., Pérez-Grande, I., Sanz-Andres, A., & Torralbo, I. (2020). Calculation of linear conductances for thermal lumped models by means of the cmf method. *Acta Astronautica*, *173*, 76–85. https://doi.org/10.1016/j.actaastro.2020.04.004

Pitropakis, I. (2015, June). *Dedicated solutions for structural health monitoring of aircraft components* [Doctoral dissertation, KU Leuven, Science, Engineering & Technology].

Possetti, G. R. C., Kamikawachi, R. C., Muller, M., & Fabris, J. L. (2012). Metrological evaluation of optical fiber grating-based sensors: An approach towards the standardization. *Journal of Lightwave Technology*, *30*, 1042–1052.

Prosser, W. H., Seale, M. D., & Smith, B. T. (1999). Time-frequency analysis of the dispersion of lamb modes. *Journal of the Acoustical Society of America*, *105*(5), 2669–2676. https://doi.org/10.1121/1.426883

Qin, Y.-X., Xiong, X.-M., Chen, Y., & Wang, Y. (2024). Optimization research on defect localization in ultrasonic images of anisotropic and multilayer cfrp structures. *IEEE Transactions on Instrumentation and Measurement*, *73*, 1–14. https://doi.org/10.1109/TIM.2024.3373102

Qing, X., Li, W., Wang, Y.-S., & Sun, H. (2019). Piezoelectric transducer-based structural health monitoring for aircraft applications. *Sensors*, *19*, 545. https://doi.org/10.3390/s19030545

Ramadas, C., Balasubramaniam, K., Hood, A., Joshi, M., & Krishnamurthy, C. (2011). Modelling of attenuation of lamb waves using rayleigh damping: Numerical and experimental studies. *Composite Structures*, *93*, 2020–2025. https://doi.org/10.1016/j.compstruct.2011.02.021

Ramos Oliveira, J. A., Baltazar, A., & Castelán, M. (2024). Classical and lagrangian mechanics in ray tracing: An optimizable framework for inhomogeneous media. *Wave Motion*, *130*, 103391. https://doi.org/https://doi.org/10.1016/j.wavemoti.2024.103391

Ranftl, S., & von der Linden, W. (2021). Bayesian surrogate analysis and uncertainty propagation. *Physical Sciences Forum*, *3*(1). https://doi.org/10.3390/psf2021003006

Rattanawangcharoen, N., Zhuang, W., Shah, A., & Datta, S. (1997). Axisymmetric guided waves in jointed laminated cylinders. *Journal of Engineering Mechanics*, *123*(10), 1020–1026. https://doi.org/10.1061/(ASCE)0733-9399(1997)123:10(1020)

Reshidko, D., Nakanato, M., & Sasián, J. (2014). Ray tracing methods for correcting chromatic aberrations in imaging systems. *International Journal of Optics*, *2014*, 11. https://doi.org/10.1155/2014/351584

Reynolds, L., Twite, R., Khobaib, M., Donley, M., & Bierwagen, G. (1997). Preliminary evaluation of the anticorrosive properties of aircraft coatings by electrochemical methods. *Progress in Organic Coatings*, *32*(1), 31–34. https://doi.org/10.1016/S0300-9440(97)00098-2

Rödel, J., & Li, J.-F. (2018). Lead-free piezoceramics: Status and perspectives. *MRS Bulletin*, *43*(8), 576–580. https://doi.org/10.1557/mrs.2018.181

Royer, D., Morgan, D., & Dieulesaint, E. (1999). *Elastic waves in solids i: Free and guided propagation*. Springer Berlin Heidelberg.

Rucka, M. (2011). Modelling of in-plane wave propagation in a plate using spectral element method and kane–mindlin theory with application to damage detection. *Archive of Applied Mechanics*, *81*, 1877–1888.

Russell, S., & Norvig, P. (2021). *Artificial intelligence: A modern approach, global edition*. Pearson Education.

Russell, S., Russell, S., & Norvig, P. (2020). *Artificial intelligence: A modern approach*. Pearson.

Rytter, A. (1993, April). *Vibrational based inspection of civil engineering structures* [Doctoral dissertation, Aalborg University] [Defended publicly at the University of Aalborg]. Dept. of Building Technology; Structural Engineering.

Saitoh, T. (2024). Convolution quadrature time-domain boundary element method for antiplane anisotropic viscoelastic wave propagation. *Engineering Analysis with Boundary Elements*, *164*, 105753. https://doi.org/10.1016/j.enganabound.2024.105753

Sánchez Galvis, I., Sierra, D., Duarte, C., & Agudelo, W. M. (2017). Simulation of surface seismic waves propagation by 2d finite-difference elastic wave modeling in the presence of complex surface topography.

Sánchez Iglesias, F. (2020, February). *Simulaciones de un sistema de shm basado en ondas de lamb* [Master's thesis, Universidad Politécnica de Madrid].

Sánchez Iglesias, F., Broncano García, P., Tejerina Hernanz, R., Fernández López, A., & Iglesias Vallejo, M. (2019). Elastic waves simulation and damping characterization on composite structures for structural health monitoring applications. *8th European Conference for Aeronautics and Space Sciences (EUCASS 2019)*. https://doi.org/10.13009/EUCASS2019--671

Sánchez Iglesias, F., & Fernández López, A. (2020). Rayleigh damping parameters estimation using hammer impact tests. *Mechanical Systems and Signal Processing*, *135*, 106391. https://doi.org/10.1016/j.ymssp.2019.106391

Sánchez Iglesias, F., & Fernández López, A. (2023). Evaluating structural details' influence on elastic wave propagation for composite structures via ray tracing. *Sensors*, *23*(16). https://doi.org/10.3390/s23167220

Sánchez Iglesias, F., Fernández López, A., & Güemes Gordo, A. (2023). Ray tracing methodology for elastic wave propagation improve simulation applied to aeronautic composite

structures. *Proceedings of the 14th International Workshop on Structural Health Monitoring*. https://doi.org/10.12783/shm2023/36953

Sánchez Iglesias, F., García Alonso, J., Tejerina Hernanz, R., Oslé Dorremochea, E., Iglesias Vallejo, M., Lorente, L., García Etxebarria, J., Fernández, D. A., Lozano, A., Fernández Díaz-Maroto, P., Larrañaga, B., Pozo, A. R., & Fernández López, A. (2017). Numerical simulation and improved correlation techniques for low energy impact detection and damage characterization with elastic waves on composite structures. *Proceedings of the NAFEMS World Congress 2017*, 584.

Sánchez Iglesias, F., García Serrano, A., Pedraza Rodriguez, A., & Fernández López, A. (2024). Validation of a ray-tracing-based guided lamb wave propagation methodology in aerostructures. *Structural Health Monitoring*, *0*(0), 14759217241249056. https://doi.org/10.1177/14759217241249056

Sánchez Iglesias, F., Tejerina Hernanz, R., García Alonso, J., Caffyn, P., & Iglesias Vallejo, M. (2016). Elastic waves simulation on aircraft subcomponent for test correlation using piezoelectric sensors. *8th European Workshop On Structural Health Monitoring (EWSHM 2016)*.

Sasoh, A. (2020). Method of characteristics. In *Compressible fluid dynamics and shock waves* (pp. 229–239). Springer Singapore. https://doi.org/10.1007/978-981-15-0504-1_10

Sbarufatti, C., Manes, A., & Giglio, M. (2013). Performance optimization of a diagnostic system based upon a simulated strain field for fatigue damage characterization. *Mechanical Systems and Signal Processing*, *40*(2), 667–690. https://doi.org/10.1016/j.ymssp.2013.06.003

*Scangenie setup and operation guide*. (2007). Acellent Technologies, Inc. 835 Stewart Drive Sunnyvale, CA 94085.

Schulte, R. T., & Fritzen, C.-P. (2010). Modelling of wave-based shm systems using the spectral element method. *PAMM*, *10*(1), 15–18. https://doi.org/10.1002/pamm.201010005

Schulz, M., Pai, P., & Inman, D. (1999). Health monitoring and active control of composite structures using piezoceramic patches. *Composites, Part B*, *30*, 713–725. https://doi.org/10.1016/S1359-8368(99)00034-7

Schwabacher, M., & Goebel, K. (2007). A survey of artificial intelligence for prognostics. *AAAI Fall Symposium: Artificial Intelligence for Prognostics*.

Sejdić, E., Djurović, I., & Jiang, J. (2009). Time–frequency feature representation using energy concentration: An overview of recent advances. *Digital Signal Processing*, *19*(1), 153–183. https://doi.org/10.1016/j.dsp.2007.12.004

Seno, A. H., Khodaei, Z. S., & Aliabadi, M. F. (2019). Passive sensing method for impact localisation in composite plates under simulated environmental and operational conditions. *Mechanical Systems and Signal Processing*, *129*, 20–36. https://doi.org/10.1016/j.ymssp.2019.04.023

Sensors for aerospace applications [Accessed: June 2024]. (2024).

Shang, L., Zhang, Z., Tang, F., Cao, Q., Pan, H., & Lin, Z. (2023). Cnn-lstm hybrid model to promote signal processing of ultrasonic guided lamb waves for damage detection in metallic pipelines. *Sensors*, *23*(16). https://doi.org/10.3390/s23167059

Shen, Y., & Giurgiutiu, V. (2016). Combined analytical fem approach for efficient simulation of lamb wave damage detection. *Ultrasonics*, *69*, 116–128. https://doi.org/10.1016/j.ultras.2016.03.019

Shen, Y., Jia, Y., Sheng, X., Shen, L., Rogers, J. A., & Giebink, N. C. (2014). Nonimaging optical gain in luminescent concentration through photonic control of emission étendue. *ACS Photonics*, *1*, 746–753. https://doi.org/10.1021/ph500196r

Shivaprasad, S. B., Saini1, A., Purushothaman, P., Balasubramaniam, K., & Krishnamurthy, C. V. (2016). Elastic wave propagation in polycrystalline materials using ray tracing model. *19th World Conference on Non-Destructive Testing (WCNDT 2016)*, *2016–07*.

Silionis, N. E., Liangou, T., & Anyfantis, K. N. (2024). Deep learning-based surrogate models for spatial field solution reconstruction and uncertainty quantification in structural health monitoring applications. *Comput. Struct.*, *301*(100). https://doi.org/10.1016/j.compstruc.2024.107462

Sirohi, J., & Chopra, I. (2000). Fundamental understanding of piezoelectric strain sensors. *Journal of Intelligent Material Systems and Structures*, *11*, 246–257. https://doi.org/10.1106/8BFB-GC8P-XQ47-YCQ0

Sofge, D. (1994). Structural health monitoring using neural network based vibrational system identification. *Proceedings of ANZIIS '94 - Australian New Zealnd Intelligent Information Systems Conference*, 91–94. https://doi.org/10.1109/ANZIIS.1994.396943

Sofi, A., Jane Regita, J., Rane, B., & Lau, H. H. (2022). Structural health monitoring using wireless smart sensor network - an overview. *Mechanical Systems and Signal Processing*, *163*, 108113. https://doi.org/10.1016/j.ymssp.2021.108113

Sohn, H., Worden, K., & Farrar, C. R. (2002). Statistical damage classification under changing environmental and operational conditions. *Journal of Intelligent Material Systems and Structures*, *13*(9), 561–574. https://doi.org/10.1106/104538902030904

Soman, R., Balasubramaniam, K., Golestani, A., Karpiński, M., & Malinowski, P. (2020). A two-step guided waves based damage localization technique using optical fiber sensors. *Sensors*, *20*(20). https://doi.org/10.3390/s20205804

Sony, S., Dunphy, K., Sadhu, A., & Capretz, M. (2021). A systematic review of convolutional neural network-based structural condition assessment techniques. *Engineering Structures*, *226*, 111347. https://doi.org/10.1016/j.engstruct.2020.111347

Speckmann, H. (2007). Shm: History and future. *6th International Workshop on SHM*.

Speckmann, H., & Roesner, H. (2006). Structural health monitoring: A contribution to the intelligent aircraft structure. *9th European Conference on NDT*.

Spencer, G. H., & Murty, M. V. R. K. (1962). General ray-tracing procedure†. *J. Opt. Soc. Am.*, *52*(6), 672–678. https://doi.org/10.1364/JOSA.52.000672

Staszewski, W. J., C., B., & Tomlinson, G. R. (2003, December). *Health monitoring of aerospace structures: Smart sensor technologies and signal processing* (1st ed.). John Wiley & Sons, Ltd. https://doi.org/10.1002/0470092866

Stefanou, G. (2009). The stochastic finite element method: Past, present and future. *Computer Methods in Applied Mechanics and Engineering*, *198*(9), 1031–1051. https://doi.org/10.1016/j.cma.2008.11.007

Stoneley, R., & Baker, H. F. (1924). Elastic waves at the surface of separation of two solids. *Proceedings of the Royal Society of London. Series A, Containing Papers of a Mathematical and Physical Character*, *106*(738), 416–428. https://doi.org/10.1098/rspa.1924.0079

Strutt, J. W. 3rd Baron Rayleigh. (1877). *Theory of sound (two volumes)* (2nd ed.). Dover Publications.

Strutt, J. W. 3rd Baron Rayleigh. (1888). On the free vibrations of an infinite plate of homogeneous isotropic elastic matter. *Proceedings of the London Mathematical Society*, *s1–20*(1), 225–237. https://doi.org/10.1112/plms/s1-20.1.225

Su, Z., Ye, L., & Lu, Y. (2006). Guided lamb waves for identification of damage in composite structures: A review. *Journal of Sound and Vibration*, *295*, 753–780. https://doi.org/10.1016/j.jsv.2006.01.020

Su, Z., & Ye, L. (2005). Lamb wave propagation-based damage identification for quasi-isotropic cf/ep composite laminates using artificial neural algorithm: Part ii - implementation and validation. *Journal of Intelligent Material Systems and Structures*, *16*(2), 113–125. https://doi.org/10.1177/1045389X05047600

Sun, C., Wu, J., & Gibson, R. (1985). Prediction of material damping in randomly oriented short fiber polymer matrix composites. *Journal of Reinforced Plastics and Composites*, *4*(3), 262–272. https://doi.org/10.1177/073168448500400302

Svendsen, B. T., Øiseth, O., Frøseth, G. T., & Rønnquist, A. (2023). A hybrid structural health monitoring approach for damage detection in steel bridges under simulated environmental conditions using numerical and experimental data. *Structural Health Monitoring*, *22*(1), 540–561. https://doi.org/10.1177/14759217221098998

Telford, W., Geldart, L., & Sheriff, R. (1990). *Applied geophysics*. Cambridge University Press.

Theodosiou, A., & Kalli, K. (2020). Recent trends and advances of fibre bragg grating sensors in cytop polymer optical fibres. *Optical Fiber Technology*, *54*, 102079. https://doi.org/10.1016/j.yofte.2019.102079

Tibaduiza, D.-A., Torres-Arredondo, M.-A., Mujica, L., Rodellar, J., & Fritzen, C.-P. (2013). A study of two unsupervised data driven statistical methodologies for detecting and classifying damages in structural health monitoring. *Mechanical Systems and Signal Processing*, *41*(1), 467–484. https://doi.org/10.1016/j.ymssp.2013.05.020

Torres-Arredondo, M.-A., Tibaduiza, D.-A., McGugan, M., Toftegaard, H., Borum, K.-K., Mujica, L. E., Rodellar, J., & Fritzen, C.-P. (2013). Multivariate data-driven modelling and pattern recognition for damage detection and identification for acoustic emission and acousto-ultrasonics. *Smart Materials and Structures*, *22*(10), 105023. https://doi.org/10.1088/0964-1726/22/10/105023

Torzoni, M., Manzoni, A., & Mariani, S. (2023). A multi-fidelity surrogate model for structural health monitoring exploiting model order reduction and artificial neural networks. *Mechanical Systems and Signal Processing*, *197*, 110376. https://doi.org/10.1016/j.ymssp.2023.110376

Treviso, A., Van Genechten, B., Mundo, D., & Tournour, M. (2015). Damping in composite materials: Properties and models. *Composites Part B: Engineering*, *78*, 144–152. https://doi.org/10.1016/j.compositesb.2015.03.081

Tuck, A., & Kekoc, V. (2010). Kc-30 a structural health monitoring system verification and validation.

Tuo, H., Lu, Z., Ma, X., Xing, J., & Zhang, C. (2019). Damage and failure mechanism of thin composite laminates under low-velocity impact and compression-after-impact loading conditions. *Composites Part B*, *163*, 642–654. https://doi.org/10.1016/j.compositesb.2019.01.006

UK, M. A. A. (Ed.). (2019, September). *Design and airworthiness requirements for service aircraft: Part 13: Military common fit equipment* [DEF STAN 00–970: PART 13]. MODUK.

Valdes, J., Cheung, C., & Wang, W. (2011). Evolutionary computation methods for helicopter loads estimation. *2011 IEEE Congress of Evolutionary Computation, CEC 2011*, 1589–1596. https://doi.org/10.1109/CEC.2011.5949805

Van Pamel, A., Sha, G., Rokhlin, S. I., & Lowe, M. J. S. (2017). Finite-element modelling of elastic wave propagation and scattering within heterogeneous media. *Proceedings of the Royal Society A: Mathematical, Physical and Engineering Sciences*, *473*(2197), 20160738. https://doi.org/10.1098/rspa.2016.0738

Vandenplas, S., Papy, J., Wevers, M., & Huffel, S. V. (2004). Acoustic emission monitoring using a multimode optical fibre sensor. *Insight*, *46*, 203–209.

Vázquez, S., Alonso, J., & González, R. (2024). Bird strike test event diagnosis using a hybrid shm system. *e-Journal of Nondestructive Testing*, *29*. https://doi.org/10.58286/29661

Vieira, D. R., & Loures, P. L. (2016). Maintenance, repair and overhaul (mro) fundamentals and strategies: An aeronautical industry overview. *International Journal of Computer Applications*, *135*, 21–29.

Viktorov, I. A. (1967). *Rayleigh and lamb waves: Physiscal theory and applications*. Springer US.

Wahl, T. J., & Bolton, J. S. (1993). The application of the wigner distribution to the identification of structure-borne noise components. *Journal of Sound and Vibration*, *163*, 101–122.

Wang, J., Wang, H., Chen, B., Huang, H., & Liu, S. (2017). A failure mechanism based model for numerical modeling the compression-after-impact of foam-core sandwich panels. *Composites Science and Technology*, *151*, 258–67. https://doi.org/10.1016/j.compscitech.2017.08.027

Wang, Z.-h., Bai, E.-l., Xu, J.-y., Du, Y.-h., & Zhu, J.-s. (2022). Effect of nano-sio2 and nano-caco3 on the static and dynamic properties of concrete. *Scientific Reports*, *12*. https://doi.org/10.1038/s41598-021-04632-7

Wevers, M., Huffel, S. V., Vandenplas, S., & Papy, J. (2007). Acoustic emission monitoring using a polarimetric single mode optical fiber sensor, 148–160.

Whitted, T. (1980). An improved illumination model for shaded display. *Commun. ACM*, *23*(6), 343–349. https://doi.org/10.1145/358876.358882

Wigner, E. (1932). On the quantum correction for thermodynamic equilibrium. *Physics Review*, *40*, 749–759.

Wolf, K. B., & Krotzsch, G. (1995). Geometry and dynamics in refracting systems. *European Journal of Physics*, *16*(1), 14. https://doi.org/10.1088/0143-0807/16/1/003

Worden, K., Farrar, C., & Manson, G. (2007). The fundamental axioms of structural health monitoring. *Proceedings of The Royal Society A: Mathematical, Physical and Engineering Sciences*, *463*, 1639–1664. https://doi.org/10.1098/rspa.2007.1834

Worden, K., & Manson, G. (2007). The application of machine learning to structural health monitoring. *Philosophical Transactions of the Royal Society A: Mathematical, Physical and Engineering Sciences*, *365*(1851), 515–537. https://doi.org/10.1098/rsta.2006.1938

Worlton, D. C. (1961). Experimental confirmation of lamb waves at megacycle frequencies. *Journal of Applied Physics*, *32*(6), 967–971. https://doi.org/10.1063/1.1736196

Wu, S., Zhang, Z., Chen, J., Yao, Y., & Li, D. (2023). Characterisation of stress corrosion durability and time-dependent performance of cable bolts in underground mine environments. *Engineering Failure Analysis*, *150*, 107292. https://doi.org/10.1016/j.engfailanal.2023.107292

Xu, J., Hu, H., Liu, Q. H., Zhan, Q., & Zhuang, M. (2021). Spectral element modeling of elastic wave propagation in an anisotropic background with discrete anisotropic fractures. *Geophysical Journal International*, *227*(2), 832–848. https://doi.org/10.1093/gji/ggab226

Yang, Y., Ng, C.-T., Kotousov, A., Sohn, H., & Lim, H. J. (2018). Second harmonic generation at fatigue cracks by low-frequency lamb waves: Experimental and numerical studies. *Mechanical Systems and Signal Processing*, *99*, 760–773. https://doi.org/10.1016/j.ymssp.2017.07.011

Yoon, H.-S., Jung, D., & Kim, J.-H. (2012). Lamb wave generation and detection using piezoceramic stack transducers for structural health monitoring applications. *Smart Materials & Structures - SMART MATER STRUCT*, *21*. https://doi.org/10.1088/0964-1726/21/5/055019

Yu, F., Shu, Y., Zhen-yu, J., & Zhong, L. (2023). Polarization optical design of 8-meter chinese giant solar telescope. *Chinese Astronomy and Astrophysics*, *47*(3), 659–677. https://doi.org/10.1016/j.chinastron.2023.09.010

Zadeh, L. (1965). Fuzzy sets. *Information and Control*, *8*(3), 338–353. https://doi.org/10.1016/S0019-9958(65)90241-X

Zelenika, S., Hadas, Z., Bader, S., Becker, T., Gljuscic, P., Hlinka, J., Janak, L., Kamenar, E., Ksica, F., Kyratsi, T., Louca, L., Mrlik, M., Osmanovic, A., Pakrashi, V., Rubes, O., Sevecek, O., Silva, J. P., Tofel, P., Trkulja, B., ... Vrcan, Z. (2020). Energy harvesting technologies for structural health monitoring of airplane components-a review. *Sensors*, *20*(22). https://doi.org/10.3390/s20226685

Zeng, X., Liu, X., Yan, J., Yu, Y., Zhao, B., & Qing, X. (2022). Lamb wave-based damage localization and quantification algorithms for cfrp composite structures. *Composite Structures*, *295*, 115849. https://doi.org/https://doi.org/10.1016/j.compstruct.2022.115849

Zhang, S., Yang, J., & Ye, W. (2024). In-situ sparse-array imaging for through-thickness cracks in plates with a0 lamb waves and an efficient waveform inversion algorithm. *Ultrasonics*, *138*, 107247. https://doi.org/https://doi.org/10.1016/j.ultras.2024.107247

Zhao, X., Gao, H., Zhang, G., Ayhan, B., F. Yan, C. K., & Rose, J. (2007). Active health monitoring of an aircraft wing with embedded piezoelectric sensor/actuator network: I. defect detection, localization, and growth monitoring. *Smart Materials and Structures*, *16*, 1208–1217. https://doi.org/10.1088/0964--1726/16/4/032

# Annexes

# Annex A. Time frequency distribution theory

Time frequency distributions (TFDs) allow us to analyze the frequency content of a signal as it changes over time. These distributions capture how a signal's spectral components evolve, representing its energy or intensity across both time and frequency simultaneously. TFDs are commonly used in fields like audio processing, speech analysis, and biomedical signal analysis to visualize and understand the temporal evolution of the frequency components of a signal.

A general equation for a time frequency distribution $w(t, \omega)$ for an input time signal $s(t)$ was derived by Cohen, 1989 as:

$$P(t,\omega) = \frac{1}{4\pi^2} \int\int\int \mathrm{e}^{-i\theta t - i\tau\omega - i\theta u} \phi(\theta,\tau)\, s^*\left(u - \frac{\tau}{2}\right) s\left(u + \frac{\tau}{2}\right) \mathrm{d}u\mathrm{d}\tau\mathrm{d}\theta \tag{1}$$

where:

- $s^*$ is the complex conjugate of the input signal.
- $\phi(\theta, \tau)$ is an arbitrary function that is referred as kernel.
- $t$ is the time.
- $\omega$ is the angular frequency.

All integrals are evaluated from $-\infty$ to $\infty$.

One of the most popular TFD is the generalized spectrogram, based on the Short-Time Fourier Transform (STFT) or Fast Fourier Transform (FFT). Digitally sampled data in the time domain are broken up into chunks which usually overlap, and Fourier transformed to calculate the magnitude of the frequency spectrum for each chunk (Allen and Rabiner, 1977). That is, for a window width $h$ the spectrogram of a signal $s(t)$ would be defined as:

$$\text{spectrogram}(s,h) = |\text{STFT}(s,h)|^2 \tag{2}$$

The size and shape of the analysis window can be adjusted. A smaller (shorter) window improves timing accuracy but reduces the precision of frequency representation. Conversely, a larger (longer) window improves frequency precision but sacrifices accuracy in timing representation.

# Wigner-Vile Distribution

An particular case of TFD is the Wigner-Ville Distribution (WVD), as described in Wahl and Bolton, 1993; Wigner, 1932, it may offer a significant advantage over STFT and Wavelet Transform, as it has a more general application range and is not limited by the uncertainty relationship on simultaneous time and frequency resolution. It was first proposed in physics to account for quantum corrections to classical statistical mechanics and it also usefully serves in signal processing, as a transform in time-frequency analysis. Compared to a STFT, the WVD function provides the highest possible temporal vs. frequency resolution, which is mathematically possible within the limitations of the uncertainty principle.

However, this distribution presents a number of limitations, the most significant being (Prosser et al., 1999):

- The sampling frequency must be four times that of the highest frequency of interest of the signal (Boashsah, 1988) as opposed to the discrete Fourier transform, which requires it to be only two times.
- When more than one frequency component is contained in a signal, it may result in a noisy distribution or the appearance of signal content at frequencies and times not actually contained in the waveform. This *noise* is mostly contained in the cross-terms of the multiple frequency components and could complicate the interpretation of the results.
- The distribution may return negative values. These values do not have a physical meaning and most often appear as a result of interference or *noise* discussed in the previous point.

The kernel function of the Wigner-Ville distribution has a value of 1 (Prosser et al., 1999). Substituting into equation 1 results in the distribution $w(t, \omega)$ as:

$$w(t,\omega) = \int s'\left(t - \frac{T}{2}\right) s\left(t + \frac{T}{2}\right) \mathrm{e}^{-iT\omega} \mathrm{d}T \tag{3}$$

To be able to apply the previous equation to a digitized signal, it must be modified into a discrete form given by:

$$w(m\Delta t, k\Delta\omega) = 2\Delta t \sum_{n=0}^{2N-1} s\left[(m+n)\Delta t\right] s'\left[(m-n)\Delta t\right] \mathrm{e}^{\frac{-i2\pi nk}{2N}} \tag{4}$$

# Pseudo Wigner-Ville distribution

There are many techniques to reduce the noise generated by the Wigner-Ville distributions (WVD), one of the most common approaches is to applicate a smoothing function to the distribution, resulting in the pseudo Wigner-Ville distribution (PWVD). As shown in Jeon and Shin, 1993 this emphasizes the deterministic components and reduces the components due to interference.

According to Prosser et al., 1999, a Gaussian window function ($G(t,\omega)$) is convolved with the Wigner-Ville distribution, where:

$$G(t,\omega) = \frac{1}{2\pi\sigma_t\sigma_\omega} \mathrm{e}^{-\left(\frac{t^2}{2\sigma_t^2}+\frac{\omega^2}{2\sigma_\omega^2}\right)} \tag{5}$$

where both $\sigma_t^2$ and $\sigma_\omega^2$ are greater than zero and $\sigma_t\sigma_\omega >= 0.5$.

The resulting sampled Pseudo Wigner-Ville distribution, $w'(r,m)$ is given by:

$$w'(r,m) = \frac{\Delta t \Delta w}{2\pi} \sum_{p=r-j}^{r+j} \sum_{q=m-k}^{m+k} w(p,q) G(p-r, q-p) \tag{6}$$

# Reduced Interference Distribution

A possible solution to overcome some of the limitations of the Wigner-Ville distribution may be the *Reduced Interference Distribution* (RID), used extensively in the field of civil engineering for the analysis of earthquake signals (Bradford, 2006). In general, a RID refers to any distribution that reduces the expression of the cross-terms relative to the auto-terms in a quadratic Time-Frequency Representation (TFR), significantly reducing the interference or noise caused when more than one frequency component is present in the signal. A particular class of such distributions, $RID(t,\omega)$) with kernel $R_x(t,\tau)$ based on a time series $s(t)$ with analytic associate $x(t)$ can be written as:

$$RID(t,\omega) = \int_{-\infty}^{\infty} h(\tau) R_x(t,\tau) \mathrm{e}^{-i\omega\tau} d\tau \tag{7}$$

And its kernel $R_x$:

$$R_x(t,\tau) = \int_{-|\tau|/2}^{|\tau|/2} \frac{g(\nu)}{|\tau|} \left(1 + \cos\frac{2\pi\nu}{\tau}\right) x\left(t+\nu+\frac{\tau}{2}\right) x^*\left(t+\nu-\frac{\tau}{2}\right) d\nu \tag{8}$$

where $h(\tau)$ is a time smoothing window, and $g(\nu)$ is a frequency smoothing window.

Both the RID and the standard Wigner-Ville distribution are time-frequency distributions of Cohen's general class, but the RID may present some advantages over a WVD, as discussed in Bradford, 2006. The RID can be interpreted as a smoothed WVD by applying a boxcar smoothing filter to reduce the oscillatory interference that tends to appear in the cross-terms.

The study presented in this paper uses a RID formulation for a Hanning window of $[(1 + \cos(2\pi\nu/\tau))/2]$, although other common smoothing kernels may include binomial, Bessel, and triangular (or *Bartlett*) windows.

# Annex B. Elastic wave solutions for the wave equation

The wave equation, firstly postulated by d'Alembert, 1747 as discussed in Section 2, is a second-order linear partial differential equation for the description of waves or standing wave fields such as mechanical waves (e.g. water waves, sound waves, and seismic waves) or electromagnetic waves (including light waves). It arises in fields such as acoustics, electromagnetism, and fluid dynamics.

The problem will be formulated in 1D for an $A0$ wave, taking $u(x,t)$ as the vertical displacement of a plane wavefront propagating in a plate of infinite length. The local membrane force is represented as $T$ and, in order to account for the damping effect in the wave equation, an additional term depending on the rate of change of the vertical displacement is introduced. This term is opposed to displacement and is therefore expressed as $-b\dot{u}$ (Figure 1).

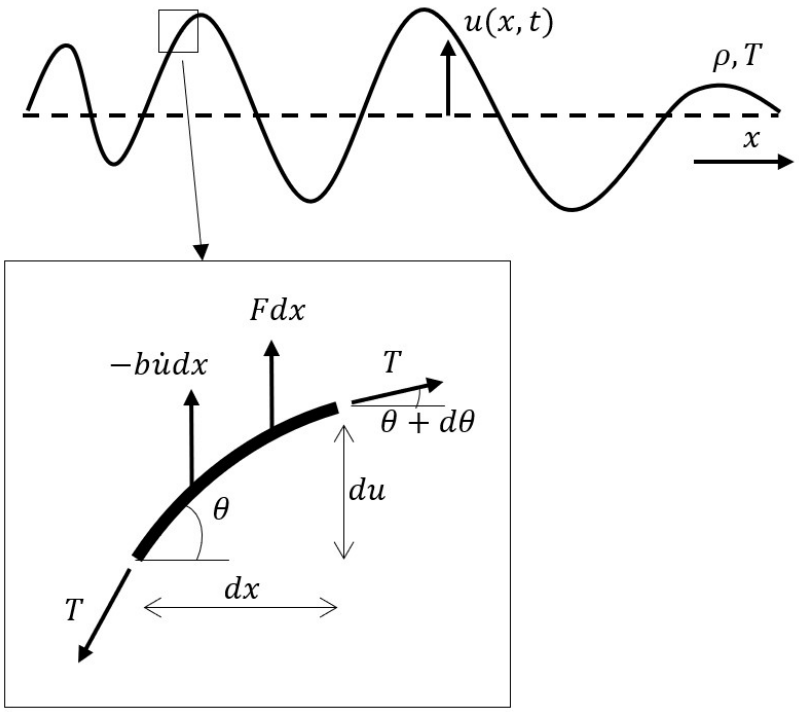


**Figure 1:** Schema of forces applied on a differential slice for a generic wave-shape.

Applying Newton's Second Law ($\sum F = m\ddot{(u)}$) for the differential slice shown in Figure 1 results in (Goldstein, 1987):

$$\rho dx\ddot{u} = -b\dot{u}dx + T\sin(\theta + d\theta) - T\sin(\theta) \tag{9}$$

Considering the small displacements assumption, $\theta \approx \sin(\theta)$ and $\theta \approx \tan(\theta) \approx du/dx$:

$$\rho dx\ddot{u} = -b\dot{u}dx + Td\theta \tag{10}$$

$$\implies \rho\ddot{u} = -b\dot{u} + T\frac{\partial\theta}{\partial x} \tag{11}$$

$$\implies \ddot{u} + \frac{b}{\rho}\dot{u} - \frac{T}{\rho}\frac{\partial^2 u}{\partial x^2} \tag{12}$$

Therefore, the wave equation in one space dimension, considering a damping term $\gamma$, can be written as follows:

$$\frac{\partial^2 u}{\partial t^2} + \gamma\frac{\partial u}{\partial t} = c_T^2\frac{\partial^2 u}{\partial x^2} \quad \text{for all } 0 < x \text{ and } t > 0 \tag{13}$$

were $c_T = \sqrt{T/\rho}$ is the $A0$ wave non dispersive velocity and $\gamma = b/\rho$ is the damping coefficient.

As a practical exercise, we will proceed to calculate the $A0$ wave for the example in Figure 2. Assuming the plate is symmetric and the excitation is applied at the center, we would only be interested in solving the values of $x > 0$.

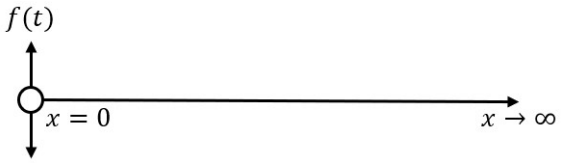


**Figure 2:** 1D model of a traveling plane wavefront on an infinite plate.

The boundary conditions of the problem would be as follows:

$$u(0,t) = f(t) \quad , \quad u(l,t) = 0 \tag{14}$$

Considering that there is no excitation in the plate at the start, the ICs would be as follows:

$$u(x,0) = 0 \quad , \quad u_t(x,0) = 0 \tag{15}$$

The equation would be solved via the Fourier transform in the time domain $\tilde{u}$, expressed as:

$$\tilde{u}(x,\omega) = \int_{-\infty}^{\infty} u(x,t)e^{-i\omega t}dt \tag{16}$$

Applying the Fourier transform to eq. 13:

$$(i\omega)^2\tilde{u}(x,\omega) + i\gamma\omega\tilde{u}(x,\omega) - c_T^2\frac{\partial^2}{\partial x^2}\tilde{u}(x,\omega) = 0 \tag{17}$$

Compressing the previous equation results in:

$$\tilde{u}" + \frac{\omega^2 - i\gamma\omega}{c_T^2}\tilde{u} = 0 \tag{18}$$

That is simply the equation of harmonic motion, where the angular frequency is a complex number. The general solution of this equation could be of the form, where the sub-index $\omega$ refers to a variable that is dependent on the frequency:

$$\tilde{u} = A_\omega e^{iq_\omega x} + B_\omega e^{-iq_\omega x} \quad , \quad q_\omega = \left(\frac{\omega^2 - i\gamma\omega}{c_T^2}\right)^{1/2} \tag{19}$$

The inverse Fourier transform is defined as:

$$u(x,t) = \int_{-\infty}^{\infty}\tilde{u}(x,\omega)e^{i\omega t}\frac{d\omega}{2\pi} \tag{20}$$

Applying the inverse Fourier transform to eq. 19:

$$u(x,t) = \int_{-\infty}^{\infty}A_\omega e^{i(\omega t + q_\omega x)} + B_\omega e^{i(\omega t - q_\omega x)}\frac{d\omega}{2\pi} \tag{21}$$

By examining the terms on the previous equation we can infer that the term: $A_\omega e^{i(\omega t+q_\omega x)}$ physically represents a wave form traveling to the left, while the term: $B_\omega e^{i(\omega t-q_\omega x)}$ represents a wave form traveling to the right. Because of the problem definition, being an infinite plate, the first term of the equation is not physically possible and it can be discarded, resulting in:

$$u(x,t) = \int_{-\infty}^{\infty}B_\omega e^{i\omega\left(t-\frac{q_\omega}{\omega}x\right)}\frac{d\omega}{2\pi} \tag{22}$$

The boundary condition at $x = 0$ specifies that:

$$\int_{-\infty}^{\infty}B_\omega e^{i\omega t}\frac{d\omega}{2\pi} = f(t) \tag{23}$$

The previous equation is of the form of an inverse Fourier integral; therefore, $B_w$ has to be the Fourier transform of $f(t)$: $B_w = \tilde{f}(x)$.

Coming back to the $q_\omega$ expression, which can be rewritten as: $q_w = \frac{\omega}{c_T}\left(1 - \frac{i\gamma}{\omega}\right)^{1/2}$, for the case of light damping conditions, typical of structural materials, where $\gamma << \omega$ for all frequencies present in $\tilde{f}(\omega)$, the binomic expansion of $q_\omega$ results in:

$$q_\omega \approx \frac{\omega}{c_T}(1 - \frac{i\gamma}{2\omega}) = \frac{\omega}{c_T} - \frac{i\gamma}{2c_T} \tag{24}$$

Returning to eq. 22, it yields:

$$u(x,t) = \int_{-\infty}^{\infty} \tilde{f}(\omega) e^{i\omega\left(t - \frac{x}{c_T} + \frac{i\gamma}{2\omega c_T}x\right)} \frac{d\omega}{2\pi} = e^{-\gamma\frac{x}{2c_t}} \int_{-\infty}^{\infty} \tilde{f}(\omega) e^{i\omega\left(t-\frac{x}{c_T}\right)} \frac{d\omega}{2\pi} \tag{25}$$

The previous equation is again of the form of an inverse Fourier integral, therefore, the solution of the vertical displacement could be expressed as:

$$u(x,t) = e^{-\gamma\frac{x}{2c_T}} f\left(t - \frac{x}{c_T}\right) \tag{26}$$

This describes a system with a decaying exponential damping, consistent with what could be intuitively expected. However, the equation does not consider dispersion. In order to do so, the shear force on the differential must also be considered, as shown in Figure 3.

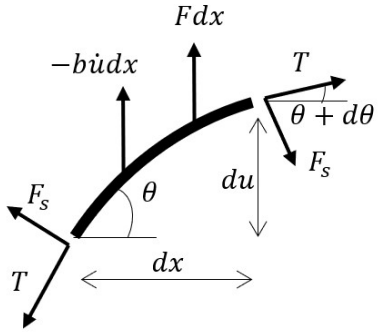


**Figure 3:** Schema of forces applied on a differential slice for a generic wave-shape.

Considering only the membrane and shear forces, the differential equation results in:

$$T\frac{d^2u}{dx^2} - EI\frac{d^4u}{dx^4} = \rho\frac{d^2u}{dt^2} \tag{27}$$

$$\implies \frac{d^2u}{dt^2} = \frac{T}{\rho}\left(\frac{d^2u}{dx^2} - \alpha\frac{d^4u}{dx^4}\right) \tag{28}$$

where $E$ is the elastic modulus of the material, $I$ is the second moment of inertia and $\alpha = EI/T$.

Guessing harmonic motions solutions of the form:

$$u(x,t) = A\cos(kx - \omega t) \tag{29}$$

And applying to eq. 28:

$$-A\omega^2\cos(kx-\omega t) = \frac{T}{\rho}\left[-Ak^2 cos(kx-\omega t) - A\alpha k^4\cos(kx-\omega t)\right] \tag{30}$$

$$\implies \omega^2 = \frac{T}{\rho}\left(k^2 + \alpha k^4\right) \tag{31}$$

As defined previously: $c_T = \sqrt{T/\rho}$, and considering this in the previous equation:

$$\omega = c_T k \sqrt{1 + \alpha k^2} \tag{32}$$

That describes a relationship in which higher frequency sinusoidals move faster, consistent with the results obtained in the dispersion curves derived in (Annex B) and (Annex C).

# Annex C. Elastic wave propagation in metalic plates

Wave propagation in isotropic plates, such as metals, can be understood by the characteristic Lamb wave equations; initially established by Lamb, 1917. They define group and phase velocity for waves propagating in an infinite plate, describing two modes of propagation: symmetric ($S0$) and anti-symmetric ($A0$).

It is possible to derive these equations frome the linear momentum equation, which is simply the Newton's Second Law considering the internal forces of the material:

$$\sigma_{ji,j} + F_i = \rho \ddot{u}_i \tag{33}$$

where:

- $F$ is the driving/applied force vector,
- $\rho$ is the density,
- $u$ is the displacement vector.

If the material is isotropic and homogeneous, the general (or transient) Navier-Cauchy equation is (Kolsky, 1964):

$$\mu u_{i,jj} + (\mu + \lambda) u_{j,ij} + F_i = \rho \ddot{u}_i \quad or \quad \mu \nabla^2 u + (\mu + \lambda) \nabla (\nabla \dot{u}) + F = \rho \ddot{u} \tag{34}$$

where $\lambda$ and $\mu$ are the Lamé parameters describing the elastic properties of the medium (Lyle and Salencon, 2012).

The analysis domain is restricted to a thin plate of thickness $2h$ as shown in Figure 4:

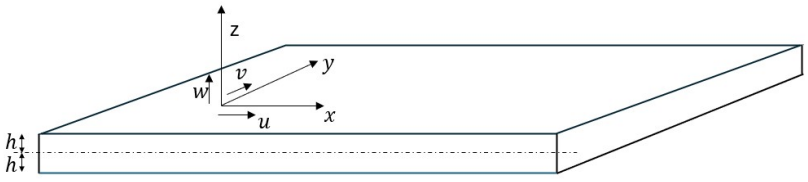


**Figure 4:** Analysis domain for waves traveling on a thin plate.

Imposing the plane stress conditions derived from the analysis domain, on eq. 34:

$$\begin{aligned}\sigma_{xx} = \lambda(u_x + w_z) + 2\mu u_x \implies \sigma_{xx,x} = \lambda(u_{xx} + w_{zx}) + 2\mu u_{xx} \\ \sigma_{xz} = \lambda(u_z + w_x x) \implies \sigma_{xz,x} = \lambda(u_{zx} + w_{xx}) \implies \sigma_{xz,z} = \lambda(u_{zz} + w_{xz}) \\ \sigma_{zz} = \lambda(u_x + w_z) + 2\mu v_z \implies \sigma_{zz,z} = \lambda(u_{xz} + w_{zz}) + 2\mu w_{zz}\end{aligned} \tag{35}$$

According to elastodynamic wave theory (Cardona et al., 2010; Royer et al., 1999), displacements can be derived from the following potentials:

$$\begin{aligned}\bar{U} = (u, v, w) = \nabla\phi + \nabla \wedge \bar{Psi} = (\phi_x, \phi_y, \phi_z) + \nabla \wedge (\psi^1, \psi^2, \psi^3) \\ = (\phi_x + \psi^3_y - \psi^2_z, \phi_y + \psi^1_z - \psi^3_y, \phi_z + \psi^2_x - \psi^1_y)\end{aligned} \tag{36}$$

Because the solution assumes only a plane wave propagating in the $x$ direction:

$$\phi = \phi(x, z) \implies \phi_y = 0 \tag{37}$$

$$\bar{\psi} = \bar{\psi}(x, z) \implies \psi^3_y = 0 \text{ and } \psi^1_y = 0 \tag{38}$$

Therefore, only the displacements in the plane $xz$ are considered ($\Phi^2 = \Phi$), the Lamb traveling wave equations result in:

$$\begin{aligned}u = \phi_x + \psi_z \implies u_x = \phi_{xx} + \psi_{zx}; \quad u_z = \phi_{xz} + \psi zz \\ w = \phi_z - \psi_x \implies w_x = \phi_{zx} - \psi xx; \quad w_z = \phi_{zz} - \psi xz\end{aligned} \tag{39}$$

Substituting these values in eq. 33 and eq. 35:

$$\begin{aligned}\rho\frac{\partial^2}{\partial t^2}\phi = (\lambda + 2\mu)\nabla^2\phi \\ \rho\frac{\partial^2}{\partial t^2}\psi = \mu\nabla^2\psi\end{aligned} \tag{40}$$

General solutions for this differential equation are firstly deduced assuming harmonic solutions in time:

$$\begin{aligned}\phi = \phi(x, z)e^{i\omega t} \implies \frac{\partial^2}{\partial t^2}\phi = -\omega^2\phi(x, z)e^{i\omega t} \\ \psi = \psi(x, z)e^{i\omega t} \implies \frac{\partial^2}{\partial t^2}\psi = -\omega^2\psi(x, z)e^{i\omega t}\end{aligned} \tag{41}$$

Substituting in eq. 40:

$$\begin{aligned}\nabla^2\phi + \frac{\rho\omega^2}{\lambda + 2\mu}\phi = 0 \implies \nabla^2\phi + p'^2\phi = 0 \\ \nabla^2\psi + \frac{\rho\omega^2}{\mu}\psi = 0 \implies \nabla^2\psi + q'^2\psi = 0\end{aligned} \tag{42}$$

where $p'^2 = \frac{\rho\omega^2}{\lambda+2\mu}$ and $q'^2 = \frac{\rho\omega^2}{\mu}$.

Then, assuming harmonic solutions in space:

$$\begin{aligned} \phi = \phi(z)e^{ikx} \implies \nabla^2\phi = -k^2\phi e^{ikx} + \frac{\partial^2}{\partial z^2}\phi e^{ikx} \\ \psi = \psi(z)e^{ikx} \implies \nabla^2\psi = -k^2\psi e^{ikx} + \frac{\partial^2}{\partial z^2}\psi e^{ikx} \end{aligned} \tag{43}$$

And substituting in eq. 42:

$$\begin{aligned} \frac{\partial^2}{\partial z^2}\phi + (p'^2 - k^2)\phi = 0 \implies \frac{\partial^2}{\partial z^2}\phi = p^2\phi \\ \frac{\partial^2}{\partial z^2}\psi + (q'^2 - k^2)\psi = 0 \implies \frac{\partial^2}{\partial z^2}\psi = q^2\psi \end{aligned} \tag{44}$$

where $p^2 = k^2 - p'^2$ and $q^2 = k^2 - q'^2$.

The guessed solutions are applied to eq. 35 on $\sigma_{xz}$ and $\sigma_{zz}$. Both symmetric and anti-symmetric solutions would be searched for these equations:

$$\begin{aligned} \sigma_{xz} = \lambda(\phi_{xz} + \psi_{zz} + \phi_{zx} - \psi_{xx}) \implies \sigma_{xz} = 2i\mu k\phi_z + \mu k^2\psi + \mu q^2\psi \\ \implies \frac{\sigma_{xz}}{\mu} = (k^2 + q^2)\psi + 2ik\phi_z \end{aligned} \tag{45}$$

$$\begin{aligned} \sigma_{zz} = \lambda(\phi_{xx} + \phi_{zz}) + 2\mu(\phi zz - \psi_{xz}) \implies \sigma_{zz} = -\lambda p'^2\phi + 2\mu p^2\phi - 2i\mu k\psi_z \\ \implies \frac{\sigma_{zz}}{\mu} = (k^2 + q^2)\phi - 2ik\psi_y \end{aligned} \tag{46}$$

Firstly, the following symmetric solutions are proposed:

$$\begin{aligned} \phi = A\cosh(pz)e^{ikx} \\ \psi = B\sinh(qz)e^{ikx} \end{aligned} \tag{47}$$

The solutions, along with the plane stress conditions ($z = \pm h \to \sigma_{zz} = 0$ and $\sigma_{xz} = 0$), are applied to the previous equations for $z = \pm h$:

$$\begin{aligned} \frac{\sigma_{xz}}{\mu} = (k^2 + q^2)\psi + 2ik\phi_z|_{z=\pm h} \implies (k^2 + q^2)B\sinh(qh) = 2iApk\sinh(ph) \\ \frac{\sigma_{zz}}{\mu} = (k^2 + q^2)\phi - 2ik\psi_y|_{z=\pm h} \implies (k^2 + q^2)A\cosh(ph) = 2iBqk\cosh(qh) \end{aligned} \tag{48}$$

Dividing both equations results in the solution for the $S0$ Lamb mode:

$$\frac{\tanh qh}{\tanh ph} = -\frac{4k^2qp}{(k^2 + q^2)^2} \tag{49}$$

Then, the following anti-symmetric solutions are proposed:

$$\begin{aligned} \phi = A\sinh(pz)e^{ikx} \\ \psi = B\cosh(qz)e^{ikx} \end{aligned} \tag{50}$$

The solutions, along with the plane stress conditions, are again applied on eq. 45 and eq. 46 for $z = \pm h$:

$$\begin{aligned} \frac{\sigma_{xz}}{\mu} &= (k^2+q^2)\psi + 2ik\phi_z|_{z=\pm h} \implies (k^2+q^2)B\cosh(qh) = 2iApk\cosh(ph) \\ \frac{\sigma_{zz}}{\mu} &= (k^2+q^2)\phi - 2ik\psi_y|_{z=\pm h} \implies (k^2+q^2)A\sinh(ph) = 2iBqk\sinh(qh) \end{aligned} \tag{51}$$

And, dividing both equations results in the solution for the $A0$ Lamb mode:

$$\frac{\tanh qh}{\tanh ph} = -\frac{(k^2+q^2)^2}{4k^2qp} \tag{52}$$

The equation is solved iteratively to estimate the wave propagation speed at any given frequency-thickness ratio, and, as expected, this equation implies that Lamb waves are dispersive in both propagation modes.

# Annex D. Elastic wave propagation in composite materials

Composite materials present characteristic anisotropic stiffness properties that have a significant influence on the propagation speed and media dispersion for elastic waves (Z. Ma et al., 2016). The stiffness transfer matrix method (STMM) has proven to be a good approximation for estimating the wave propagation speed (Kamal et al., 2013; Muñoz Chamorro, 2018), this methodology is well suited for multilayered media as it condenses the system into four equations, eliminating all other intermediate interfaces.

It is ideal to be used for a ray-tracing algorithm, as the wave phase velocity $v_p$ could be calculated for each media before tracing the ray propagation map and the propagation speed of each individual ray can later be interpolated from it based on its traveling direction angle and wave mode.

The method considers a semi-infinite $n$-layered laminate, with layer thickness $h_j$ and wavefront that originates from the origin of the coordinates, as shown in Figure 5.

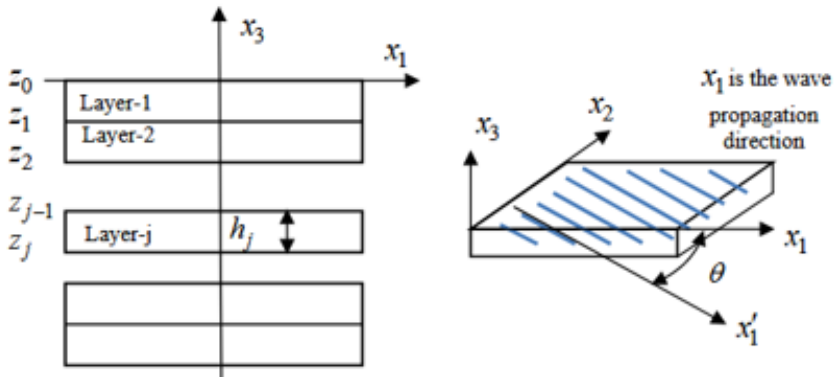


**Figure 5:** Composite material layer orientations (Kamal et al., 2013).

Assuming all composite layers behave as linear orthotropic media and following Hooke's law generalized for a two-dimensional shell, the layer stiffness matrix expressed in the laminate coordinates (rotated around the laminate perpendicular axis, $x_3$) $C$ defines the relation between layer strains and stresses as:

$$\begin{Bmatrix}\sigma_{11}\\ \sigma_{22}\\ \sigma_{33}\\ \sigma_{23}\\ \sigma_{13}\\ \sigma_{12}\end{Bmatrix} = \begin{pmatrix}C_{11} & C_{12} & C_{13} & 0 & 0 & C_{16}\\ C_{12} & C_{22} & C_{23} & 0 & 0 & C_{26}\\ C_{13} & C_{23} & C_{13} & 0 & 0 & C_{36}\\ 0 & 0 & 0 & C_{44} & C_{45} & 0\\ 0 & 0 & 0 & C_{45} & C_{55} & 0\\ C_{16} & C_{26} & C_{36} & 0 & 0 & C_{66}\end{pmatrix} \begin{Bmatrix}\varepsilon_1\\ \varepsilon_2\\ \varepsilon_3\\ \gamma_{23}\\ \gamma_{13}\\ \gamma_{12}\end{Bmatrix} \tag{53}$$

where $\sigma_{ij}$ represent the material stress and $\varepsilon_i$ and $\gamma_{ij}$ represent the strain and shear angles respectively.

Applying Newtons second law to the stiffness matrix from Equation 53 and considering the small linear strain displacement approximation, given by:

$$\varepsilon_{i,j} = \frac{1}{2}\left(\frac{\partial u_j}{\partial x_i} + \frac{\partial u_i}{\partial x_j}\right) \tag{54}$$

the internal forces can be converted into internal stresses, resulting in $\nabla\dot{\sigma} = \rho\ddot{u}$. It is possible to then solve the resulting linear system of equations by imposing a sinusoidal wave solution in displacements of the form:

$$(u_1, u_2, u_3) = (U_1, U_2, U_3)e^{ik(x_1+\alpha x_3 - v_p t)} \tag{55}$$

where $U_1$, $U_2$, and $U_3$ are the amplitudes of the harmonic motions in time and space and $v_p$ is the phase velocity of the wave.

Therefore, the equations of motion can be rewritten in matrix form as:

$$\begin{pmatrix}C_{11} - \rho v_p^2 + C_{55}\alpha^2 & C_{16} + C_{45}\alpha^2 & (C_{13} + C_{55})\,\alpha\\ C_{16} + C_{45}\alpha^2 & C_{66} - \rho v_p^2 + C_{44}\alpha^2 & (C_{36} + C_{45})\,\alpha\\ (C_{13} + C_{55})\,\alpha & (C_{36} + C_{45})\,\alpha & C_{55} - \rho v_p^2 + C_{33}\alpha^2\end{pmatrix} \begin{Bmatrix}U_1\\ U_2\\ U_3\end{Bmatrix} = 0 \tag{56}$$

The system of Equation 56 can only present a nontrivial solution when its determinant equals zero; therefore, it could be studied as an eigenvalue problem to obtain the values of $\alpha$, resulting in a six-order equation with only even coefficients (Conry, 2005; Kamal et al., 2013).

Once solved, the values of $\alpha$ are found to be related in pairs:

$$\alpha_1 = -\alpha_2, \quad \alpha_3 = -\alpha_4, \quad \alpha_5 = -\alpha_6 \tag{57}$$

It is then possible to rewrite the expressions for displacements and layer stresses as a function of $\alpha_j$, as follows:

$$(u_1, u_2, u_3) = \sum_{j=1}^{6} (1, V_j, W_j)\, U_1 e^{ik(x_i+\alpha_j x_3 - v_p t)} \tag{58}$$

$$(\sigma_{33}, \sigma_{13}, \sigma_{23}) = \sum_{j=1}^{6} (D_{1j}, D_{2j}, D_{3j})\, U_1 e^{ik(x_i+\alpha_j x_3 - v_p t)} \tag{59}$$

The values of the matrix terms $V_j$, $W_j$, $D_{ij}$, and $\alpha_j$ can be found in Kamal et al., 2013; they are not written here due to space constraints. Defining a stress displacement vector $\mathbf{s}(x_3) = (u_1, u_2, u_3, \sigma_{33}, \sigma_{13}, \sigma_{23})$, the relation for wave propagation in each layer is as follows:

$$\begin{pmatrix} 1 & 1 & 1 & 1 & 1 & 1 \\ V_1 & V_2 & V_3 & V_4 & V_5 & V_6 \\ W_1 & W_2 & W_3 & W_4 & W_5 & W_6 \\ D_{11} & D_{12} & D_{13} & D_{14} & D_{15} & D_{16} \\ D_{21} & D_{22} & D_{23} & D_{24} & D_{25} & D_{26} \\ D_{31} & D_{32} & D_{33} & D_{34} & D_{35} & D_{36} \end{pmatrix} \begin{Bmatrix} U_{11}e^{k\alpha_1 x_3} \\ U_{12}e^{k\alpha_2 x_3} \\ U_{13}e^{k\alpha_3 x_3} \\ U_{14}e^{k\alpha_4 x_3} \\ U_{15}e^{k\alpha_5 x_3} \\ U_{16}e^{k\alpha_6 x_3} \end{Bmatrix} e^{ik(x_1 - v_p t)} = \begin{Bmatrix} u_1 \\ u_2 \\ u_3 \\ \sigma_{33} \\ \sigma_{13} \\ \sigma_{23} \end{Bmatrix} \tag{60}$$

Having guaranteed continuity by solving Equation 60 at the top and bottom of each layer, it is possible to obtain a relation between the upper and lower surfaces of the plate. Therefore, for a laminate of $n$ layers, the expression would be:

$$\{s_t\} = [T^n][T^{n-1}]...[T^1]\{s_b\} = \prod_{j=1}^{n}[T^j]\{s_b\} = [A]\{s_b\} \tag{61}$$

$$\begin{Bmatrix} \{u_t\} \\ \{\sigma_t\} \end{Bmatrix} = \begin{pmatrix} [A_{uu}] & [A_{u\sigma}] \\ [A_{u\sigma}] & [A_{\sigma\sigma}] \end{pmatrix} \begin{Bmatrix} \{u_b\} \\ \{\sigma_b\} \end{Bmatrix} \tag{62}$$

Stress-free boundary conditions are then guaranteed in the upper and lower layers as $\{s_t\} = \{s_b\} = 0$; therefore, the dispersion curves in terms of the phase velocity $v_p$ can be computed as the solution of the determinant $|A_{u\sigma}| = 0$.

While the phase velocity, $v_p$, determines the speed at which each of the frequency components of the wave travels through a medium, the group velocity, defined as $v_g = \frac{dv_p}{dk}$, refers to the velocity at which the envelope of the wave packet propagates. In simpler terms, it is the speed at which the shape or modulation of a wave moves through space. The group velocity takes into account the entire waveform or wave packet, which may consist of a combination of different frequencies.

In a dispersive medium, where different frequencies of a wave travel at different speeds, the group velocity $v_g$ must be different from the phase velocity $v_p$ and the dispersion relation can be obtained via these two values. In order to trace the ray map for a defined time point the rays are then propagated at the phase velocity corresponding to the central frequency of the wave packet (maximum of the Fourier transform of the signal); this is an approximation, as the signal will be later recovered at the sensors taking into account the complete dispersion curve.

The shear wave propagation mode ($Sh0$) could also be obtained via this method but it is not accounted for in the model, as its usefulness for SHM applications is negligible compared to the other modes and only the $S0$ and $A0$ modes are considered and each is modeled with independent rays.

# Annex E. Testing conditions and transducer installation process

## Testing conditions

WThe aluminum plate specimen serves as the simplest representative benchmark model to evaluate the wave propagation behavior used in this thesis. Provides an isotropic and consistent material platform for analysis. Its uniform material properties, namely density, elasticity, and attenuation characteristics, make it an ideal candidate for investigating elastic wave responses and validating numerical models.

The test setup, using the SCANGENIE DAQ, is shown in Figure 6. PZT instrumentation is described in detail in Section 3.1.1.

**Figure 6:** Aluminum plate and DAQ during active interrogation tests.

To ensure reliable data collection, the aluminum plate is supported with damping materials along its edges. These damping supports are implemented to minimize boundary reflections and simulate free-field conditions. Without proper damping, reflections from the boundaries could interfere with the primary wave signals, complicating the interpretation of results and reducing accuracy; the use of edge damping effectively absorbs the incident waves, preventing their reflection, and allowing clearer observation of wave propagation through the plate.

For the baseline damping setup, three rows of rubber strips, each 45 mm wide, were clamped on both sides of the aluminum plate to dampen reflected GLW. The configuration was compared with a reference case, where the plate was clamped without rubber strips to evaluate the influence of the damping material. To further assess the coupling efficiency between the rubber and the plate, glycerine was applied between the rubber layers, enhancing the damping properties. In addition, a vacuum paste was applied to the edges of the plate in combination with glycerine to improve the sealing and coupling at the boundaries, ensuring consistent wave propagation during testing (Figure 7 & 8).


**(a)** Glycerine coupling **(b)** Vacuum paste coupling

**Figure 7:** The damping material is coupled with glycerine and vacuum paste to improve the elastic wave absorption characteristics.

**Figure 8:** Single edge damped configuration of the aluminum plate for active interrogation tests.

## PZT transducer installation process

Throughout this thesis, all analyzed testing specimens are equipped with PZT transducers, which serve as integral components for both wave generation and detection.

PZTs are used to both generate and detect GLWs in specimens (except for the hammer impact tests performed, where they are only employed to capture the resulting wave signals). This dual functionality, combined with their high sensitivity, makes them reliable tools for structural health monitoring in this research.

The transducers are bonded to the specimen surfaces to ensure effective coupling to generate and detect GLWs. Their placement allows for a detailed analysis of wave propagation and structural responses.

The installation process for a PZT transducer is crucial for accurate wave generation and detection. Proper bonding and positioning ensure that the transducer transmits and receives elastic waves effectively as intended. A detailed explanation of the installation process of the PZT transducer is shown in Figure 9.

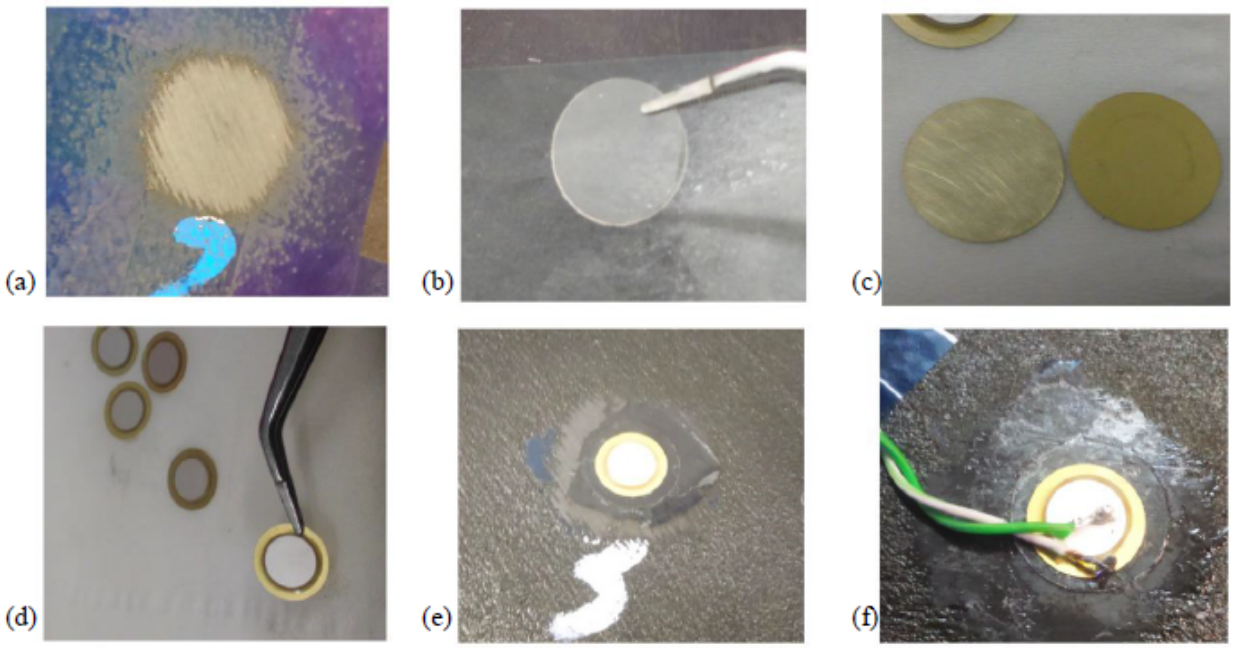


**Figure 9:** PZT sensor installation process. (a) CFRP polished zone, (b) acetate sheet, (c) raw and polished PZT sensor, (d) PZT sensor sample (e) PZT sensor installed and (e) PZT sensor installed with welded wires. (Aguilar Redondo, 2019)

A step by step guide of the installation would be as follows:

- **Surface preparation**: Before installing the PZT transducer, both the surface of the structure where it will be mounted (Figure 9a) and the sensor itself (Figure 9c) must be properly prepared. The area should be cleaned to remove any dirt, oil, or other contaminants that could interfere with the bonding process. This is typically done using

solvents such as isopropyl alcohol; light sanding or polishing may be required to create a smooth and uniform area for the adhesive bond.

- **Acetate film application:** As the surface is electrically conductive (both CFRP and metal), a thin film of acetate is placed on the structure to reduce the signal cross-talk between sensors (Figure 9b). A high-quality cyanoacrylate-based adhesive is used to bond the acetate and later the PZT transducer to the surface of the structure.

  The adhesive is applied evenly in a thin layer to avoid air gaps, which can dampen wave transmission. Care must be taken to prevent excess adhesive from seeping out around the transducer, as it could interfere with wave propagation or sensor readings. Conductive adhesives are sometimes used in cases where electrical contact with the substrate is required.

  Once the adhesive is applied, the PZT transducer is carefully placed on the prepared surface (Figure 9d & e). Light pressure may be applied to ensure proper contact between the transducer and the structure.

- **Electrical Connections** (Figure 9f): After the adhesive has cured, electrical connections are made to the PZT transducer. This involves attaching wires to the electrodes of the transducer to ensure good electrical contact. Soldering is used to secure the wires to the transducer electrodes, performed with care and at low temperature, to minimize the damage to the transducer.

  Once the wires are attached, they are routed carefully to avoid strain or interference during operation. Strain relief measures, such as cable ties or adhesive clips, are employed to protect wires and ensure stable signal transmission.

- **Final Inspection and Testing:** After installation, the PZT transducer is inspected to ensure that it is securely bonded and that the electrical connections are intact. A functional test is performed by applying a known signal to the transducer and monitoring the response. This confirms that the transducer is operating correctly and that there are no issues with the installation.